Contents

The aim of this thesis work is to present complementary techniques for the characterization of functional oxide thin films and heterostructures, in particular of samples based on the strongly correlated $LaMnO_3$ perovskite oxide.
The two paths explored are electrical measurements, including field effect measurements, and spectroscopy.
This work has been developed in the framework of a joint PhD thesis between the physics department "E.R. Caianiello" of Univesity of Salerno, and SIMEM PhD school of ENSICAEN - University of Caen/Basse Normandie.
The work in Italy has been carried on in the laboratory of thin film deposition and magneto-transport properties measurement of the group of prof. L. Maritato, who I thank specially for his guidance. The $LaMnO_3$ thin films studied in this work have been deposited by molecular beam epitaxy and electrically characterized in the facilities of this laboratory.
The host laboratory in France is the electronic equipe of GREYC-ENSICAEN laboratory, under the valuable direction of Dr. L. Méchin, where lithographic techniques have been used in order to engineer devices for electrical characterization of thin films and heterostrustures. To this aim the optimization of oxide thin films such as $SrRuO_3$ and $BaTiO_3$ by pulsed laser deposition was also carried on.
During the period spent in Caen, I also had the precious opportunity to work in the CRISMAT laboratories thanks to Dr. W. Prellier, who gave me access to one of the pulsed laser deposition equipments of his group and to the X-ray diffraction laboratory, for the deposition (mainly of $BiCoO_3$) and characterization of thin films to be employed in the device fabrication in GREYC. The collaboration with this group also concerned the magnetic characterization of the $LaMnO_3$ thin films grown in Salerno, carried on by Dr.s U. Lüders and R.V.K. Mangalam.
I acknowledge the contribution of Dr. C. Adamo for the fabrication of some of the manganite thin films ($La_{1-x}Sr_xMnO_3/Si$) and superlattices ($LaMnO_3/SrMnO_3$) studied in this work.
I also acknowledge Dr. P. Orgiani, of the group of prof. L. Maritato, for $LaMnO_3$ thin film fabrication and for conceiving the X-ray absorption spectroscopy and resonant inelastic scattering experiments carried on at the European synchrotron radiation facility.
Finally I thank Dr. C. Aruta, who patiently taught me all I know about X-ray absorption spectroscopy at transition metal edges and on X-ray diffraction, for her guidance during all my PhD.
I dedicate this work to the memory of prof. Bonaventura Savo, who introduced me to the world of experimental solid state physics.

Chapter 1

Introduction

Fuctional oxides are those transition-metal oxides (TMO) that exhibit properties such as superconductivity, ferroelectricity and piezoelectricity, dielectricity, semiconductivity, orbital and spin ordered phases, fully spin-polarized current.
TMO are characterized by narrow bands, originating by the hybridization of the transition-metal d-orbitals with the oxygen p-orbitals. In such narrow bands the spin, charge and lattice degrees of freedom are coupled due to the strong electronic correlations and overlapping of the atomic orbitals. Their properties together with the possibility of tuning them through strain, chemical doping or application of external fields, make the functional oxides suitable for device fabrication such as micro electrical mechanic systems (MEMS), transistors, field effect devices and so on.
Perovskitic oxides possess a simple crystalline structure that allows the epitaxial growth of thin films of these compounds on other perovskitic structures. This allows to integrate materials with different functionality in thin film heterostructures, in order to exploit coupling effect among the different degrees of freedom or to engineer oxide devices.
New possibilities in thin film fabrication allow controlled growth of unit cell layers of oxides, thus unveiling new perspectives in the study of interface effects in heterostructures and multilayers of strongly correlated materials. As an example, the formation of a 2D electron gas has been studied at several oxide interfaces [1].
Metallic magnetic oxides such as manganites $RE_{1-x}AE_xMnO_3$ have raised interest in the past decades because of the colossal magnetoresistance (CMR) phenomenon. Furthermore the metallic members of the family, such as $La_{0.7}Sr_{0.3}MnO_3$ or $La_{0.7}Ca_{0.3}MnO_3$ are characterized by full spin polarization at low temperature and they can be used as electrodes for spin injection, for the application in spintronic devices.
Also manganite-based superlattices have raised interest. From the theoretical point of view the formation of the 2D electron gas in $LaMnO_3/SrMnO_3$

based superlattices has also been proposed[2]. Further theoretical and experimental works deal with the magnetic and orbital properties of $LaMnO_3/SrMnO_3$ superlattices with different periodicity. The $LaMnO_3/SrMnO_3$ interface charge reconstruction is believed to originate the ferromagnetism in the superlattices whose constituent blocks are insulator antiferromagnets. However, the very complex interactions at work in these strongly correlated materials can also take in account for many different intrinsic ground states (i.e. not dependent from the interface) originated by strain of the unit cell or by oxygen non-stoichiometry.
In this thesis work we will report on different ways to characterize $LaMnO_3$ based thin films and superlattices.
First we will deal with transport measurements. The lithographic techniques developed in order to perform current perpendicular-to-plane (CPP) and field effect measurement on thin films and heterostructures will be described.
Then we will focus on magnetic and orbital properties of $LaMnO_3/SrMnO_3$ superlattices and $La_xMnO_{3-\delta}$ thin films, studied by a state-of-art spectroscopy technique, i.e. near edge X-ray absorption spectroscopy and dichroism.
In the first chapter the physics of doped and undoped manganites will be described, and we will especially refer to the $LaMnO_3$ based compounds. Then in section §1.2.4 we will discuss the issue of $LaMnO_3/SrMnO_3$ superlattices, focusing on both theoretical and experimental reports on such systems.
In section §1.3 the CPP and field effect devices will be described, and the possible application on all oxide systems and manganites will be discussed both in view of applications and basic physics.
For the engineering of the devices, the integration of other oxides with the manganite based layers is needed. In section §1.5 we will describe the properties of $SrRuO_3$, used as base electrode in CPP devices. In section §1.6 we will describe the properties of ferroelectric and multiferroic materials for applications as functional gate insulators in field effect devices.
In the second chapter the experimental techniques will be described: deposition techniques, optical lithography techniques and other techniques for device fabrications and finally characterization techniques. In particular in section §3.6.1 the soft x-ray spectroscopy techniques used in this thesis work will be described.
The third chapter is devoted to the discussion of the results. In the first part of the chapter (sections §3.1 - §3.5) we report on the preliminary work in view of the application of CPP and field effect measurements to $LaMnO_3$ based superlattices and thin film systems.
The deposition and optimization of the oxides needed as base electrode and gate insulator is discussed in sections §3.1, §3.2 and §3.3.
In the next sections §3.4 and §3.5, the issues and problematic arising in the fabrication of the devices are discussed, giving useful hints for further work

in this direction.
The second part of the chapter, sections §3.6 and §3.7, we will report on the orbital and magnetic ordering in $LaMnO_3/SrMnO_3$ superlattices and $La_xMnO_{3-\delta}$ thin films, by the spectroscopic techniques described in section §3.6.1.

1.1 Crystal field theory

As mentioned in the introduction, the properties of transition metal oxides we deal in this thesis work, are dictated by narrow bands that keep a strong d orbital character. Many of these compounds, such as $LaMnO_3$, present orbitally ordered phases, in some cases accompanied by charge ordering (for example in insulating $La_{1-x}Ca_xMnO_3$). On the other hand, hybridization and large bandwidth in metallic compounds leads to orbitally disordered states.
The particular occupation of a specific orbital tunes not only the transport properties, but also the magnetic state of manganites and TMO in general. The orbital occupation is mainly determined by the interaction of the transition metal orbital with the oxygen ligand electrostatic potential, i.e. with the crystalline environment. It is then worth to present the basic ideas of crystal field theory.
The Crystal Field Theory (CFT) is a quantum mechanics model that describes the electronic structure of transition metal in an electrostatic field. The general idea is that, in a strongly correlated system where the charge is tied to the atomic site, the local structure is influenced only by the interaction with its first neighbours [3]. Thus application of the CFT to this material is based on the following assumptions:

- The transition metal compound is stabilised by the Coulomb interaction between a central cation (metal) and the negative charge of several ligands (oxygens).
- The central atom (CA) is considered with its electronic structure while the ligands are assumed to be a spherical, structureless source of electrostatic field.

Considering the simplest case of central ion with 1 d-electron, there are five states associated to the $3d$ orbitals at the same energy. The total orbital momentum is L = 2 and the degeneracy 2L+1 = 5. These five possible states are orbitals with identical radial parts but different angular wave functions. In these hypotheses, the electronic structure of central metal ion will be determinate by the Schr$\acute{}$odinger equation with the Hamiltonian:

$$H = H_{at} + V + W \tag{1.1}$$

where H_{at} is the unperturbed free atom Hamiltonian while, V and W describe the interactions between the ligands, taken as point charges, and the CA electrons and its nucleus respectively. Taking the origin of a polar coordinate system at the CA centre, the coordinates of the N ligand charges

(q) as R and of the n electrons as r, these terms become:

$$V = -\sum_{j=1}^{N}\sum_{i=1}^{n}\frac{q_j e}{|r_i - R_j|} \tag{1.2}$$

$$W = \sum_{j=1}^{N}\frac{q_j Z e}{|R_j|} \tag{1.3}$$

In the considered systems q is negative, so the required energy to stabilise the complex is guaranteed by the W terms, while V, which is positive, destabilises and modifies the energies of the $3d^1$ states.
We will now disregard the W term, as it only represent a shift of the total energy, and consider only the V term.
A way to treat the problem is the perturbative approximation, with the further assumption of V much smaller than the inter-atomic interactions. This is possible only if the resulting splitting obtained in this way is smaller than the energy gap between the free atom solutions H_{at}.
As shown in the equations 1.2 and 1.3, the perturbing potentials are real. It is easy to show that the free hamiltonian eigenfunctions, i.e. the complex Ψ_{nl}^m functions (l=2 for d orbitals) cannot be eigenfunctions of the CFT hamiltonian. However real linear combination of Ψ_l^m with fixed l and different m can be used. In the case of d levels, these orbitals are: $d_{xy}, d_{yz}, d_{zx}, d_{x^2-y^2}, d_{3z^2-r^2}$, represented in figure 1.1. It is opportune to divide these orbitals in two groups, depending on the orientation of the lobes of their distribution: the d_{xy}, d_{yz}, d_{zx} orbitals have their distribution maxima in the region between the coordinate axes, and are referred as t_{2g} orbitals, the $d_{x^2-y^2}, d_{3z^2-r^2}$, that have the maxima along the coordinate axes, as e_g orbitals.

When a transition metal ion (such as Mn in manganites or Ru in $SrRuO_3$) is in octahedral coordination with six identical ligands situated along the cartesian axes, as shown in figure 1.1, electrons in all the five levels are repelled by the negatively charged ligands. It is easy to see that since lobes of the e_g orbitals point towards the ligands, electrons in these two orbitals are repelled to a greater extent than are those in the t_{2g} levels.
In our point-charge hypothesis the energy shift of the orbitals in a d^1 system is the following:

$$E(e_g) = E_0 + \frac{3}{5}\Delta, E(t_{2g}) = E_0 - \frac{2}{5}\Delta, \tag{1.4}$$

where E_0 is the expectation value of the monopole moment of the charge distribution (spherical, i.e. same for all), and Δ (alternatively referred as $10Dq$) is the expectation value of the quadrupole moment (no dipole moment is present if all ligands are at the same distance from the CA).

In the crystal field model the split $3d$ orbital energy levels are assumed to

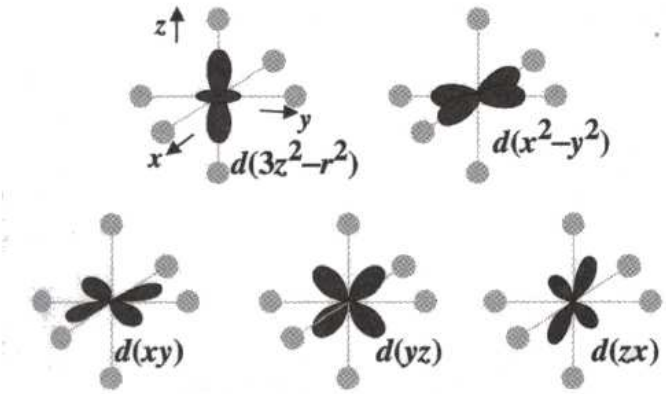

Figure 1.1: $3d$ orbitals of a central atom surrounded by six oxygens in octahedral symmetry. xy, xz and yz are oriented in space such that their distribution maxima fall into the region between the coordinate axes while $3z^2 - r^2$ and $x^2 - y^2$ have their lobes oriented along respectively the z and x, y axes.

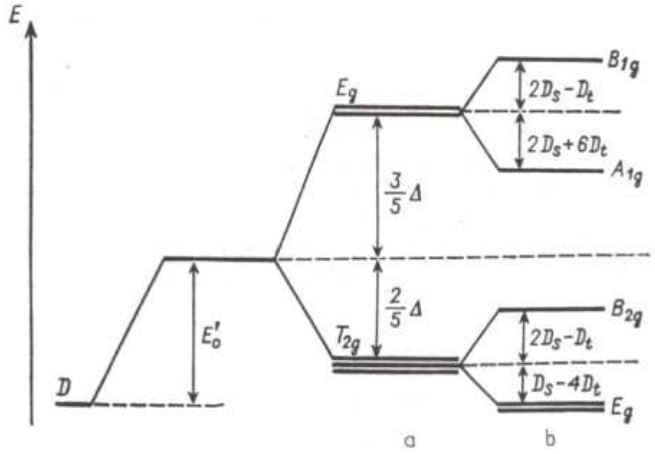

Figure 1.2: Splitting of the energy levels of d states in octahedral field a), and tetragonally distorted (elongated octahedral) field b).

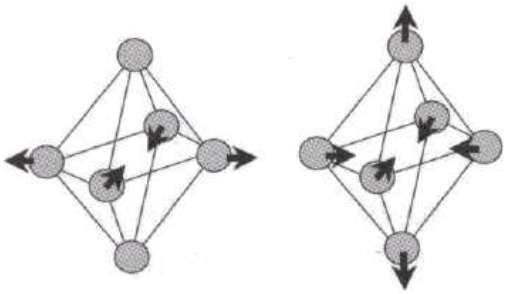

Figure 1.3: Distortions of an octahedral complex. On the left the basal plane axes are inequivalent. On the right a tetragonally distorted octahedron is shown: in this case the octahedron is elongated along the z-axis, but also compression is possible. These deformation remove the degeneracy of t_{2g} and e_g levels.

obey a 'center of gravity' rule, as evident from equation 1.4. This follows from the simple algebraic consideration that the energy of the six electrons in the t_{2g} orbitals is compensated by the energy of the four electrons in the e_g orbitals[4].

As shown in figure 1.2 the residual degeneracy of the energy levels can be removed by octahedral distortions such as the ones shown in figure 1.3. Considering, for example, a tetragonally distorted octahedron by the elongation of the ligand-to-CA distances on the z axis, the energies of the $d_{x^2-y^2}$ and $d_{3z^2-r^2}$ orbitals are no more the same. Also the three t_{2g} states do not remain equivalent: d_{xz} and d_{yz} experience the same lower reduced repulsion from the negative charge than d_{xy}. A twofold degeneracy remains but if the x and y axes become inequivalent, as shown in figure 1.3 left panel, this term splits too.

If the transition-metal ion is in a different coordination than octahedral (such as tetrahedral, dodecahedral or cubic), the d orbitals experience a different splitting, as reported in figure 1.4.

For a metal ion with more than one d-electron the situation becomes more complicated but the idea remains the same: the symmetry of the crystal field influences the energies of the levels and therefore the occupation of the orbitals. When many electrons are present, interactions such as spin orbit coupling (LS), Hund coupling (J_H), and coulomb repulsion (U) have to be taken in account when computing the many-electrons energy levels.

To approach the problem it is necessary to distinguish between two cases: the weak and the strong field approximation. The turning point is the Δ energy: for instance, if the perturbation causes a splitting larger than that of the LS coupling, we cannot determine the ground state by the Hund's rules and it could be that with the lower total spin. On the other hand, under the influence of a weak perturbative field, the states are firstly split by LS coupling, and after by the crystal field addition, so that the term with

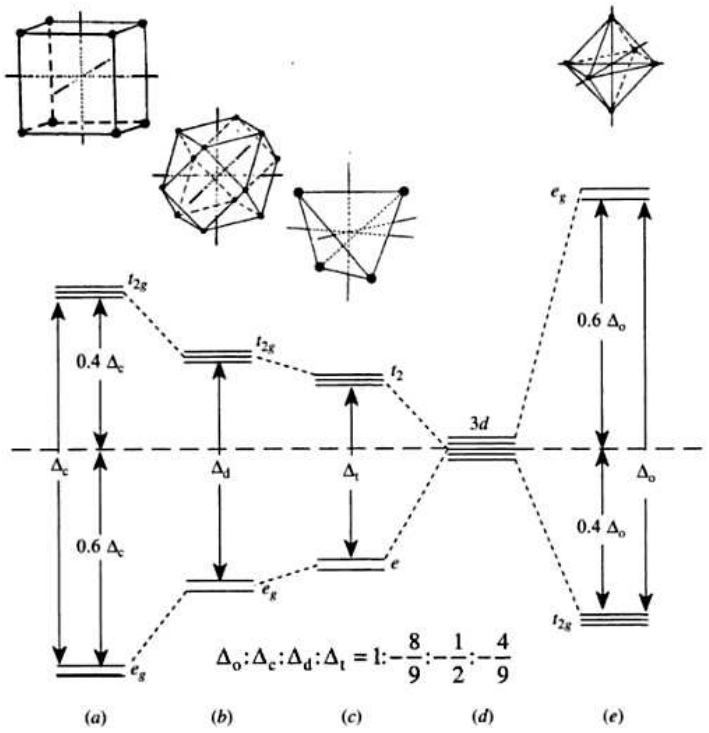

Figure 1.4: Crystal field splitting of transition metal d orbitals in a) cubic, b) dodecahedral (as in perovskite A-site), c) tetrahedral, d) spherical, e) octahedral coordination. The ratio between the splitting parameter for different coordination at fixed CA-ligand distance is also reported. From ref. [4].

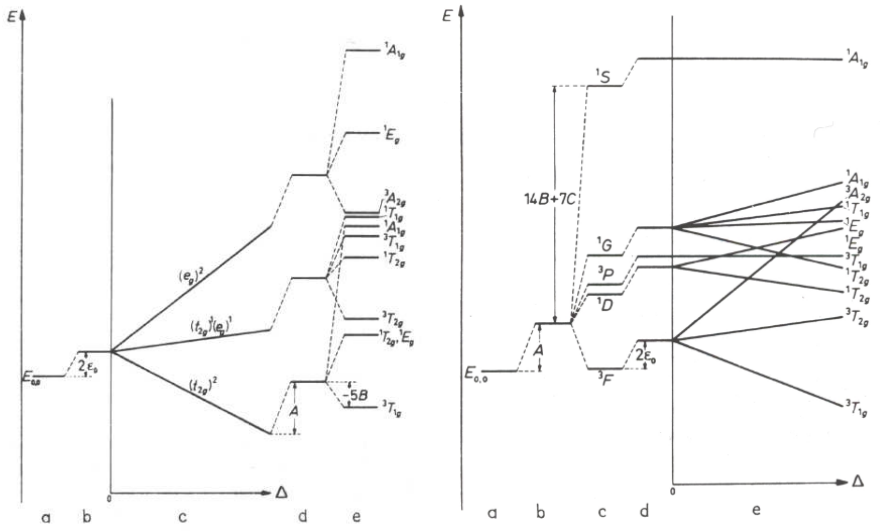

Figure 1.5: Left: splitting of the energy levels for a d^2 system in a strong octahedral field: a) d electron energy; b) ligand field destabilisation; c) ligand field splitting; d) electronelectron interactions. Right: splitting of the energy levels for a d^2 system in a weak octahedral field: a) d electron energy: b) e c) electron-electron interactions; d) ligand field approximation; e) ligand field splitting. From ref. [3]

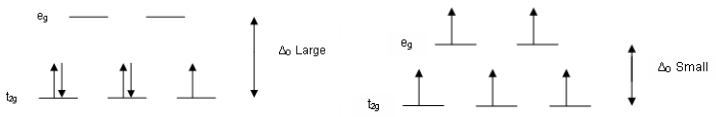

Figure 1.6: Left: d^5 system in low-spin state because of strong octahedral crystal field (for example: Ru^3+). Right: d^5 system in high-spin state because of weak octahedral crystal field (for example: Mn^2+).

highest spin is the ground state.

Typical values of the crystal field splitting in perovskite compounds are about 2-3 eV. While the way the levels split can be easily figured out by geometrical and simple quantum mechanics calculations, exact calculation of the Δ parameter would require the knowledge of the exact radial wavefunction of d orbitals. The value of Δ is obtained directly or can be estimated by spectroscopic measurements[4].

1.2 Properties of CMR manganites: from parent to mixed valence compounds

Since the early 1990s magnetic oxides have raised remarkable interest. In particular many studies have been devoted to manganites, i.e. Mn oxides of the form $RE_{1-x}AE_xMnO_3$, together with the layered compounds of the form $(RE_{1-x}AE_x)_{n+1}Mn_nO_{3n+1}$, where RE is a rare earth and AE is an alcaline earth.
These compounds have a rich phase diagram as a function of AE doping, all composition show magnetic ordering such as antiferromagnetism of different kind (A-type, G-type), spin canting and ferromagnetism. In particular for some composition, the interesting phenomenon of colossal magnetoresistance (CMR) takes place when a magnetic field is applied at temperatures around the Curie temperature of the compound.
In 1950 Jonker and Van Santen[5] characterized the properties of several manganite compounds in policrystalline form, and found that $La_{1-x}AE_xMnO_3$, with AE=Ca^{2+}, Sr^{2+}, Ba^{2+}, showed a striking correlation between the Curie temperature (T_C), the saturation magnetization (M_S) and the electrical resistivity $\rho(T)$.
The $La_{0.7}Sr_{0.3}MnO_3$ samples showed maximum values for the Curie temperature ($T_C^{MAX} \approx 370\ K$) and for the saturation magnetization ($M_S^{MAX} \approx 3.7\mu_B/f.u.$). This situation correspond to the full polarization of all 3d electrons present in the samples.
Furthermore for any of the AE doping and in a certain x range, the resistivity behaviour showed a transition from high-temperature insulating to low temperature metallic state at a metal-insulator transition temperature $T_{MI} \gtrapprox T_C$.
It is around this temperature that the CMR is observed. In figure 1.7 the correlation between the M(T) curve and the $\rho(T)$ curve is showed; in the first and second panel it is evident that the onset of the magnetization together with the metal-insulator transition temperature is pushed to higher temperatures by the application of magnetic field. The magnetoresistance, shown in the bottom panel, is maximum in correspondence of T_C, and in this case it reaches the value of 80%.
Zener proposed a mechanism he called "double exchange" (DE) to explain the simultaneous occurrence of ferromagnetism and metallicity, both as a function of x and T , found by Jonker and van Santen [7]. The FM state is observed only for finite hole concentration where electronic transport is via holes arising from charge exchange between Ca^{2+}, for example, and Mn (hole density = x). For $x < 0.5$ the majority of Mn ions are in the d^4 configuration (Mn^{3+}) which, for octahedral coordination, means a half-filled t_{2g} triplet and a quarter-filled e_g doublet. The minority of sites are d^3 (Mn^{4+}) which corresponds to a half-filled t_{2g} orbital triplet. Hund's rule dictates

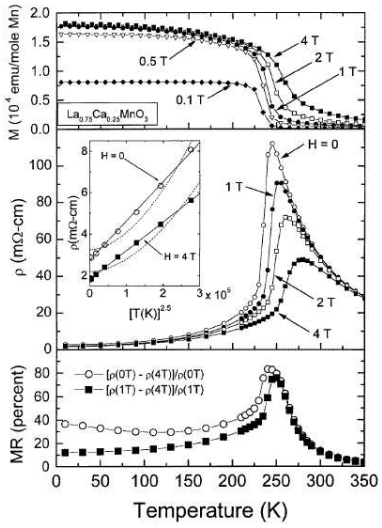

Figure 1.7: Top frame: magnetization against temperature for $La_{0.75}Ca_{0.25}MnO_3$ for various field values. Middle frame: resistivity against temperature. The inset shows the low-temperature resistivity compared to $T^{2.5}$ (solid line) and $T^{4.5}$ (dashed line) behaviour. Bottom frame: magnetoresistance against temperature. Open symbols reflect low-field behaviour and solid symbols reflect the high-field behaviour[6].

that as the hole hops from site to site, it is accompanied by a reduction in S from 2 to 3/2 (Hund's energy $J_H \gg t$, the transfer integral). This hopping is impeded if neighbouring sites are orthogonal, i.e. if spins not parallel. Anderson and Hasegawa showed that the transfer integral varies as the cosine of half the angle between neighbouring spins [8]. As temperature is lowered and spin fluctuations decrease, the combined itinerant/local-moment system lowers its total energy by aligning the spins ferromagnetically and allowing the itinerant electrons to gain kinetic energy.

Millis et al. [9] have shown that a Hamiltonian incorporating only the DE interaction cannot explain the most obvious feature of the manganites, namely the magnitude of the change in resistivity at the FM transition. They proposed, in addition to DE, an electron-phonon coupling term[6].

1.2.1 Crystallographic structure

The crystallographic structure of the (RE,AE)MnO_3 compounds depends from the size of the (RE,AE) ion, as manganites can crystallize in hexagonal and cubic form. Hexagonal structure is typically stabilized by small ions, such as Y. Many hexagonal manganites are of interest because of their magnetic or multiferroic properties.
The compounds we deal in this work are cubic manganites. The cubic struc-

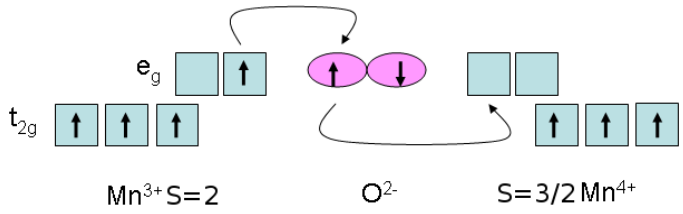

Figure 1.8: Schematic diagram of the double-exchange mechanism. The DE is the simultaneous transfer of electrons from Mn^{3+} to O^{2-} and from O^{2-} to Mn^{4+}. The initial and final configurations are degenerate if the core t_{2g} spins are aligned. The energy is consequently lowered by the hopping of the electrons.

ture is similar to the $CaTiO_3$ cubic perovskite. The large sized RE and AE ion occupy the A-site with 12-fold oxygen coordination. The Mn ions in the mixed valence state Mn^{3+}-Mn^{4+} are located at the centre of the oxygen octahedra, the B-site with 6-fold coordination.
The eventual distortions of the perovskite cell are described by the tolerance factor t, and depends on the dimensions of the actual ionic radii. This factor t, introduced by Goldschmidt, is given by the following relation:

$$t = \frac{(r_A + r_O)}{\sqrt{2}(r_B + r_O)}, \tag{1.5}$$

where r_O is the oxygen ionic radius and r_A,r_B are respectively the ionic radius of the A-site and B-site ions.
For mixed valence manganites, where the A-site is occupied by two species, an average ionic radius is considered: $\langle r_A \rangle$. However also the ionic radius variance $\sigma^2 = (x_i r_{Ai}^2 - \langle r_A \rangle^2)$ has demonstrated to be an important parameter for manganite properties [10].
The perovskite structure is stable when t is in the range $0.89 < t < 1.02$. From equation 1.5, it is evident that $t = 1$ corresponds to the perfect closely packed structure.
However, t is generally different from 1, meaning that the manganites have, typically, a lower symmetry, i.e. rhombohedral or orthorhombic.
In figure 1.9 the undistorted cubic perovskite structure and the distorted orthorhombic structure are reported. The $LaMnO_3$ compound assumes a modified $GdFeO_3$ orthorhombic structure of figure 1.9.
The structural distortion observed in $LaMnO_3$ is a tilting of the MnO_6 octahedra around the $(110)^c$ axis, so that the Mn-O-Mn bond angle is reduced from 180° to about 160°. This phenomenon is originated by the structure factor of $LaMnO_3$ that is different from one. The second type of crystal distortion (not observed in $GdFeO_3$) is the deformation of MnO_6 octahedra caused by the Jahn-Teller effect, originating from orbital degeneracy of quarter filled Mn^{3+} e_g orbitals.
When La^3+ in $LaMnO_3$ is progressively substituted by a divalent AE cation,

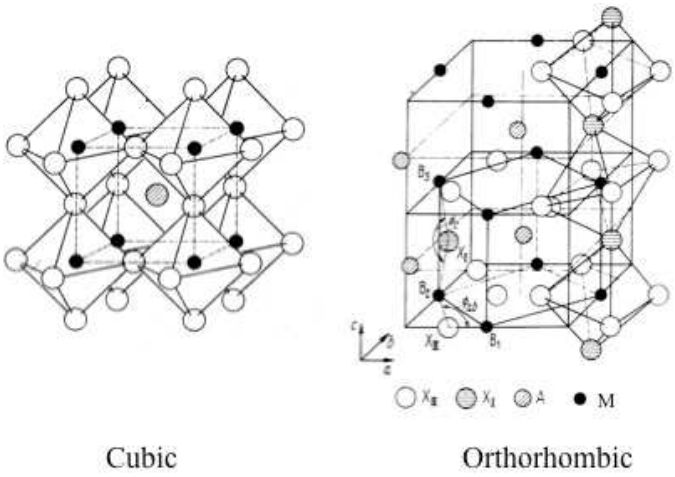

Figure 1.9: The ideal cubic perovskite structure and the principal cooperative octahedral-site rotations in the orthorhombic phase. Here the A atom is in the A-site, the M atom is the B.site atom. Oxygen positions are all equivalent in the cubic phase and represented in white (X-sites), while in the orthorhombic structure the planar and apical oxygens occupy inequivalent sites X_I and X_{II}

the amount of Mn^{4+} increases and the orthorhombic distortion decreases, as Mn^{4+} is not a Jahn-Teller active ion (e_g orbitals are unoccupied).
The different length of the radii of La and the substituting AE ion, produces further distortions of the crystallographic structure because of the t-factor modification.
If the octahedra tilts in the $\langle 111 \rangle$ crystallographic orientation the structure turns into rhombohedral configuration, while a tilting around the $\langle 110 \rangle$ direction yields an orthorhombic structure.
The former distortion is generated if La^{3+} is substituted by a smaller ion, such as Ca^{2+}, the latter if it is substituted by a ion with larger ionic radius such as Sr^{2+}.
The Mn-O distance and the Mn-O-Mn bond angle are the main structural parameters controlling the hybridization strength between Mn and O, hence also the magnetic superexchange interactions and the DE mechanism.
Figure 1.10 shows the variation of the bond angle Mn-O-Mn as a function of the average ionic radius. The mean value of the angle increases while raising the tolerance factor t or equivalently the ionic radius (indicated with R_0 in figure1.10). Conversely, the Mn-O distance is not varying with t, keeping an average value of about 1.9602 Å[11].
In figure 1.11 the T_C variation with $\langle r_A \rangle$ for ferromagnetic manganite compounds is reported, showing influence of the t factor on the DE mechanism. However the T_C is also influenced by the ionic radius variance, as shown in the right panel of figure 1.11.
Similar behaviour is found for the anti-ferromagnetic ordering temperature

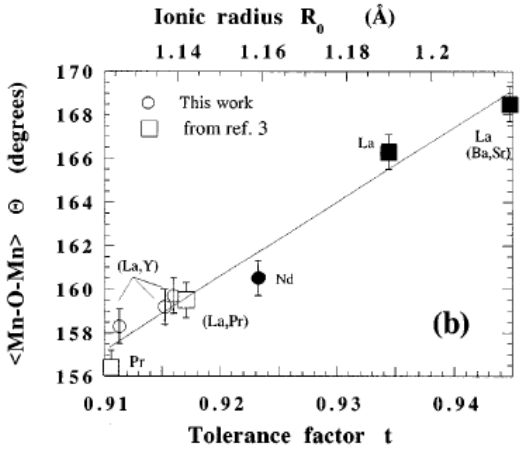

Figure 1.10: Average Mn-O-Mn angle θ as a function of tolerance factor t for several $RE_{1-x}AE_xMnO_3$ composition.Empty and filled symbols correspond respectively to Ca and Sr samples.[11]

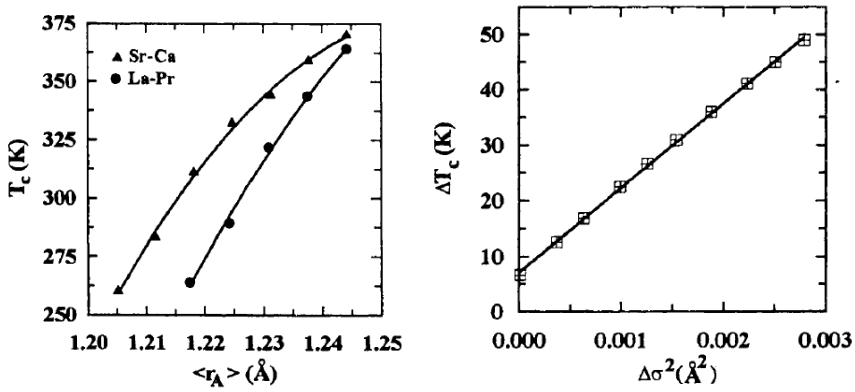

Figure 1.11: Left: Dependence of T_C on $\langle r_A \rangle$ for $La_{0.7-x}Pr_xSr_{0.3}MnO_3$ and $La_{0.7}Sr_{0.3-x}Ca_xMnO_3$. Right: $\Delta T_C = T_C(\langle r_A \rangle, \sigma_i^2) - T_C(\langle r_A \rangle, \sigma_j^2)$ for samples having the same average ionic radius $\langle r_A \rangle$ but different σ^2 plotted versus $\Delta\sigma^2 = (\sigma_i^2 - \sigma_j^2)$. (i, j) stands for pairs of data taken from fixed $\langle r_A \rangle$).[10]

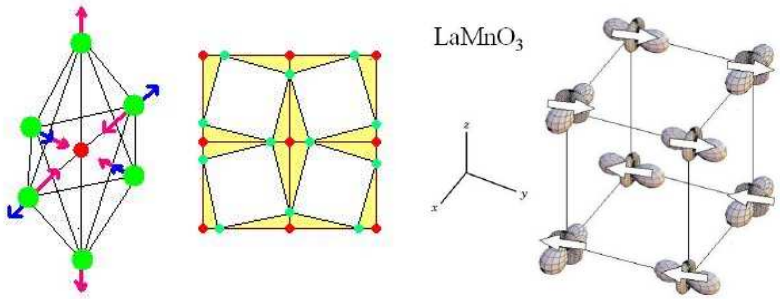

Figure 1.12: The two JT distortion modes of the MnO_6 octahedron. Both distortions are stabilized in $LaMnO_3$, where long and short Mn-O bonds alternate in the xy plane (see figure, with accentuated distortions) and intermediate bonds are along the z axis. The structural distortion stabilises the orbital ordering represented at the extreme left.

in undoped manganites, where antiferromagnetic superexchange interactions dominate[12].

1.2.2 Undoped compounds: $LaMnO_3$ orbital and magnetic properties

The remarkable properties of doped manganites are originated by the mixed valence of Mn^3+/Mn^{4+} and by the interplay of lattice, electronics and magnetic degrees of freedom.
In undoped compounds such as $LaMnO_3$, the Mn valence is simply 3+ (unless non-stoichiometries are present); however the ground state of this compound is already the result of the competition between many degrees of freedom. The result is that the $LaMnO_3$ orbital (orbital ordering: OO) and magnetic state (A-type antiferromagnet: A-AFM) are very peculiar.
The understanding of the $LaMnO_3$ behaviour is crucial to proceed to the study of the behaviour of the hole doped compounds.
The Mn^{3+} is in octahedral coordination, so that the crystal environment breaks the full rotation invariance leading to the splitting of the two e_g and the three t_{2g} states , as discussed in §1.1.
There are four electrons in the d shell that are spin aligned because of the strong Hund's coupling; on average three electrons populate the t_{2g} orbitals at lower energy and one the e_g; the total spin is S=2 as this system is a high spin system ($\Delta < J_H$).
A distortion of the oxygen octahedron lowers the symmetry of the cubic crystal field in such a way that the centre of gravity of the t_{2g} levels and the centre of gravity of the e_g levels is unchanged, as shown in figure 1.2. There is therefore nothing to be gained by Mn^{2+} or Mn^{4+} from such a distor-

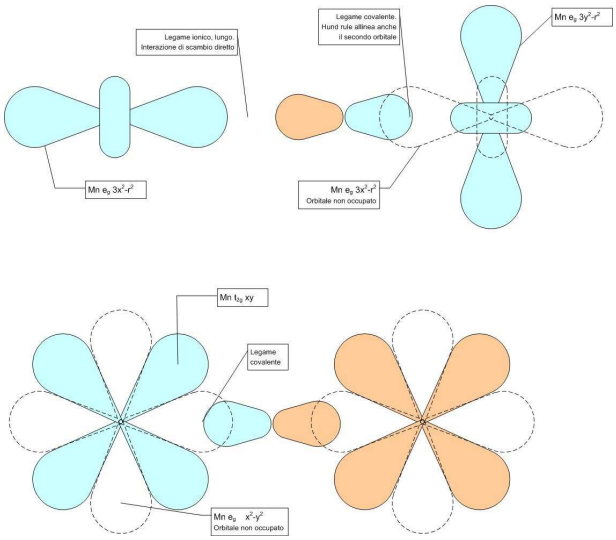

Figure 1.13: Goodenough rule for the oxygen mediated superexchange interaction between Mn ions. Top: semicovalent bond between Mn^{3+} ions in the orbital ordered phase. Bottom: covalent bond between Mn^{4+} ions (for example in $CaMnO_3$ that is a G-type AFM). Orange and blue fillings represent the spin orientation, the small orbital represents oxygen $2p$.

tion, but Mn^{3+} can lower its energy in proportion to the distortion, and the corresponding penalty in elastic energy will scale as the distortion squared, hence we have the marked tendency of d^4 ions to distort their octahedral environment in order to lower their energy. This is the Jahn-Teller effect.
$LaMnO_3$ undergoes to a cooperative Jahn-Teller (JT) distortion at 720°C, leading to a structural transition and consequently to orbital ordering. The orbitals stabilised in this case are supposed to be the $3d_{3y^2-r^2}$ and $3d_{3x^2-r^2}$ ordered as shown in figure 1.12.
The t_{2g} electrons are assumed to be localised because they form a π narrow bond with the ligand oxygens. In fact the superimposition with $2p$ oxygen orbitals is maximum along the coordinate axis and the d_{xy}, d_{xz} and d_{yz} fall into the regions between them. Thus the only levels that hybridise with 2p oxygen states are the e_g and are the only ones involved in the magnetic superexchange process[13].

The magnetic structure of $LaMnO_3$ is A-AFM, as represented in figure 1.12. This magnetic structure is given by ferromagnetic ordering of the spin in plane (say xy) and antiferromagnetic ordering along the perpendicular axis (say z).
This magnetic ordering is naturally obtained by the observed orbital ordering by the application of the Goodenough-Kanamori rules[14]. Goodenough discussed the phase diagram of $(La_{1-x}Ca_x)MnO_3$ in chemical terms, considering the hybridization of manganese orbitals: dsp^2 for Mn^{3+} which forms

square coplanar bonds, and d^2sp^3 for Mn^{4+} which forms octahedral bonds to six near neighbours[13]. These ions can form bonds of different nature with the surrounding oxygens through which magnetic coupling is mediated. In figure 1.13 the different bonds of Mn and O orbitals is represented. For Mn^{3+} a semicovalent bond is formed.
Semicovalence arises when only one out of the two manganese atoms surrounding an O^{2-} has a hybridized orbital available pointing towards the oxygen. In that case, full covalence is not possible since only one side of the O^{2-} orbitals can share an electron with the neighbouring manganese ion. The other bond is ionic, and the oxygen ion is displaced towards the first manganese, with which it forms the covalent bond. One electron is then localized on the oxygen ion to which it confers a magnetic moment that is antiparallel to the spin of the covalent electron (the two electrons sharing the oxygen orbitals have to be antiparallel). Because of the Hund rule, the manganese ion participating in the bond has its moment parallel to the electron shared with the oxygen. On this side of the ionic bond, there is a direct (therefore antiferromagnetic) exchange interaction between the magnetic moment of the anion and that of the neighbouring manganese. The resulting configuration is a ferromagnetic arrangement of the manganese ions.
This is the in-plane situation. The interaction between the orbitals in two neighbouring planes is antiferromagnetic, giving rise to the A-type magnetic structure[13].
From the point of view of electrical transport the $LaMnO_3$ is an insulator, as naturally arises from the orbital and magnetic ordering. As observed by Coey and Viret[13], $LaMnO_3$ can be considered a band insulator whose Fermi level falls in the gap between the two JT splitted e_g orbitals. The importance of the crystal structure is demonstrated by the result that, without the Jahn- Teller distortion (i.e. for a cubic cell), $LaMnO_3$ would be a ferromagnetic metal rather than an A-type antiferromagnetic insulator, as deduced from band calculations. However models not including the JT coupling can also give OO phases by including electron correlations, but do not succeed in reproducing the observed orbitals[15]. However from this point of view $LaMnO_3$ can be considered a Mott insulator, where the particular orbital ordering is stabilised by the electron-phonon interaction.

$LaMnO_3$ thin films: experiments and models

The A-AFM OO ground state is established in $LaMnO_3$ stoichiometric bulk samples. The crystalline structure of $LaMnO_3$ is a distorted $GdFeO_3$ orthorhombic structure, typically indexed as O'[13]. Its point group is Pnma with lattice parameters $a = 0,5655$ nm, $b = 0,7722$ nm, $c = 0,5528$ nm. The underlying pseudo-cubic perovskite structure has in-plane lattice parameter of 0.3954 nm and out-of-plane lattice parameter of 0.3861 nm. When de-

posited on $SrTiO_3$ (001) substrates ($a = 0.3905$ nm), the epitaxial strain leads to a deformation of the cell, that is compressed in plane and elongates in the out-of-plane direction.
Thin films of $LaMnO_3$ are experimentally found to be ferromagnetic, as reported for example in ref.s [16, 17].
Hotta et al.[18] studied the phase diagram of doped and undoped manganites. They used the hamiltonian:

$$H = H_{hop}(t) + H_{Hund}(J_H) + H_{SE}(J_{AF}) + H_{e-ph}(\lambda) + H_{el}, \qquad (1.6)$$

where: H_{hop} is the hopping term, depending from the hopping parameter t, that considers all the hopping process among the different $3d$ orbitals with modulated hopping parameters ($\propto t$); H_{Hund} is the ferromagnetic coupling ($J_H > 0$) between the e_g electrons and the t_{2g} core; H_{SE} is the magnetic superexchange interaction depending by the antiferromagnetic coupling parameter $J_{AF} < 0$; H_{e-ph} is the electron-phonon coupling with the octahedral distortive mode, with coupling parameter λ and H_{el} is the stabilising elastic phonon energy. The Coulomb interaction is not explicitly included in this hamiltonian, but since JT distortions suppress double occupancy, as onsite Coulomb interaction does, a robust λ mimics the effect of interorbital Coulomb repulsion. In addition, a large Hund coupling emulates a large same-orbital Hubbard U term[18].
The authors used Monte Carlo and mean field calculations on 4×4, $4 \times 4 \times 2$ and $4 \times 4 \times 4$ clusters. The results for the larger clusters in the undoped case are resumed in figure 1.14. As we can see from the left panel, the A-type AFM, observed in bulk samples, is only stabilised in a very narrow parameter range, while a OO ferromagnetic phase appears to be much more robust. By decreasing the electron-phonon coupling parameter (λ) this OO phase becomes orbital disordered (indicating a metallic phase, as pointed out previously).

On the basis of these findings and of experimental data, Dong et al. [19] adopted a ferromagnetic ground state for $LaMnO_3$ for the study of $LaMnO_3/SrMnO_3$ superlattices.
A simple explanation for the occurrence of ferromagnetism in $LaMnO_3$ is the following: in the bulk orthorhombic phase, the lattice constant along the c axis shortens compared with those along the a and b axes. For instance, at T =300 K, l_c is only 0.964 l_{ab}, where l_c (l_{ab}) is the nearest neighbour Mn-Mn distance along the c axis (within the $a-b$ plane). Using an empirical formula by Zhou and Goodenough[20], the AFM exchange intensity along c becomes about 1.3 times that on the $a - b$ plane. Thus, this stronger AFM coupling along c will favor the A-AFM state. However, for $LaMnO_3$ thin films on $SrTiO_3$, the lattice is compressed in the $a - b$ plane but it is elongated along the c axis, leading to an almost cubic crystal structure. Therefore, the theoretical phase diagram, derived assuming lattice isotropy[18], should be applicable to the thin films that prefer the FM OO phase instead of the

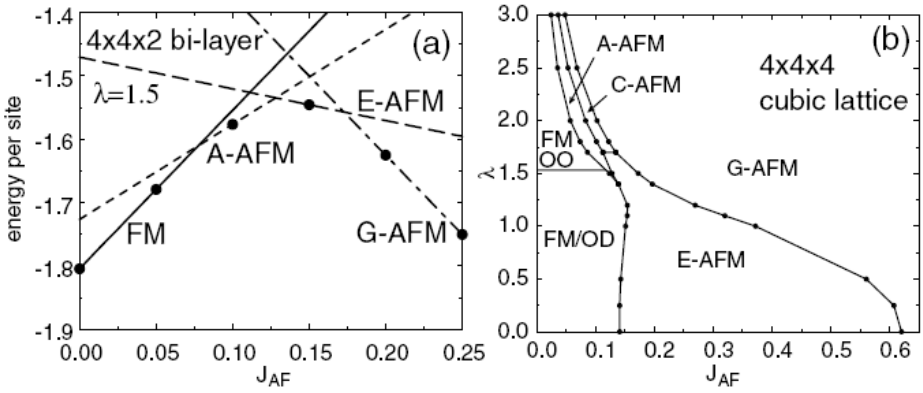

Figure 1.14: (a) Energies of the FM, A-AFM, E-AFM, C-AFM, and G-AFM phases on $4 \times 4 \times 2$ bilayer lattices ($\lambda = 1.5$). Solid circles indicate the results of optimizations, while lines denote the MF results. (b) Phase diagram for the $(4 \times 4 \times 4)$cubic lattice. All solid lines emerge from MF calculations.

A-AFM one[19].
This picture seems to be confirmed in the experimental work by Adamo et al. on superlattices[16]. The single $LaMnO_3$ films on $SrTiO_3$ described in this work have the in plane lattice parameter as the substrate one ($a = 0.3905$ nm), and out-of-plane lattice parameter $c = 0.393$ nm[21]. These films are found to be ferromagnetic with $T_C \approx 150$K and saturation magnetization of about 1 μ_B/Mn, while they are insulators from transport measurements[16]. However also an alternative explanation is proposed for the occurrence of ferromagnetism in these samples, i.e. oxygen non stoichiometry, and in particular oxygen excess[16].
Indeed $LaMnO_3$ compound can allow both for oxygen deficiency and excess. The oxygen excess $LaMnO_{3+\delta}$ is realized by simultaneous vacancies on La and Mn sites, so that the correct formula for this compound is $(LaMn)_{\frac{3}{3+\delta}}O_3$. In order to keep the charge neutrality, some Mn has to oxidize to Mn^{4+}, thus hole doping the sample.
Aruta et al. [17] report on $LaMnO_3$ thin films on $LaAlO_3$ substrates ($a = 0.387$ nm) grown by PLD and cooled under low oxygen pressure (10^-2 mbar). These films experience a remarkable epitaxial strain by the substrate, that is partially relaxed, however the out-of-plane parameter is very extended: $c = 0.399$ nm. The films are found to be in the ferromagnetic insulating phase, with saturation magnetization of about 1.09 μ_B/Mn. Nuclear magnetic resonance measurements confirm the presence of a small quantity of Mn^{4+} ions, and also by Rutherford backscattering results, the chemical formula of the compound is determined as $(La^{3+}_{0.98})(Mn^{3+}_{0.95}Mn^{4+}_{0.05})O^{2-}_3$.
The measured saturation magnetization in both works[16, 17] must be compared with the values of $M_S = 4\mu_B$/Mn expected for Mn^{3+}, of $M_S =$

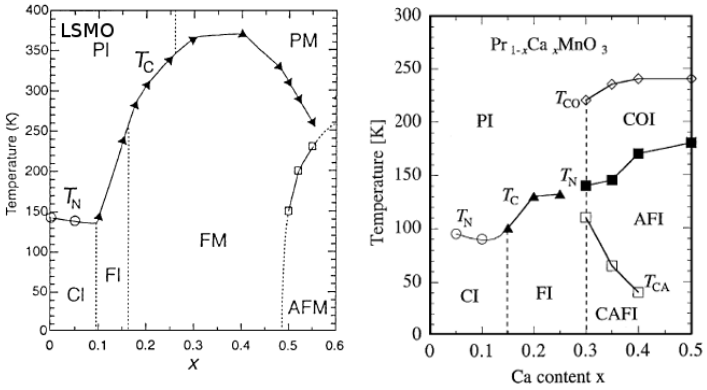

Figure 1.15: Left: phase diagram of $La_{1-x}Sr_xMnO_3$ as a function of Sr content x. Right: the phase diagram of $Pr_{1-x}Ca_xMnO_3$ is reported for comparison. CI stands for canted antiferromagnetic phase, FI for ferromagnetic insulating phase, PI for paramagnetic insulating, FM for ferromagnetic metallic, PM fot paramagnetic metallic, CO for charge ordered. T_N, T_C and T_{CO} represent respectively the Néel, Curie and charge ordering transition temperatures.

$4\mu_B$/Mn in FI doped compositions, and finally with the small magnetization originating by spin canting of $M_S = 0.16\mu_B$ in pure $LaMnO_3$.
Indeed, following Hotta et al [18] and Dong et al. [19], we would expect that the saturation magnetization value is close to the Mn^{3+} one if the ferromagnetic OO phase is realized.
The magnetic properties of the samples are then attributed to the light Mn^{4+} doping, induced by oxygen and/or La off-stoichiometry, and to the stabilization of different structural phases by the epitaxial deposition.

1.2.3 Doped compounds: $La_{1-x}Sr_xMnO_3$ phase diagram.

When AE (valence 2+) is substituted to RE (valence 3+), Mn^{3+} must partially oxidize to Mn^{4+} in order to keep the charge neutrality. This corresponds to introduce holes in the e_g band, so that some charge carriers become available for real hopping processes.
As pointed out in §1.2.1, the Mn^{3+}/Mn^{4+} substitution also reduces the Jahn-Teller static distortion, that is rapidly removed with doping, leading to a "more cubic" structure[13].
A particular attention has to be paid to the $La_{1-x}Sr_xMnO_3$ (LSMO) compounds, which show the strongest ferromagnetic behaviour.
The LSMO phase diagram is relatively simple. At $x = 0$ we have $LaMnO_3$, that is an AFM insulator with $T_N \approx 140$ K, as described in §1.2.2. A small canting angle, presumably due to Dzyaloshinski-Moriya interaction (originating from spin-orbit coupling), is observed from magnetization and

ac susceptibility measurements[22]. Ferromagnetic interaction are already present in the $x = 0$ compound, so that a ferromagnetic phase can be already obtained at low x value ($x \approx 0.1$).
For $0 \leq x \lessapprox 0.1$ an insulating canted AFM structure is stabilised.
The ferromagnetic phase is insulating up to about $x = 0.15$ (FI), and metallic for $0.15 \lessapprox x \lessapprox 0.5$, when the DE mechanism described in §1.2 takes place. One interesting consequence of DE transport mechanism is that at low temperature the carriers are fully spin polarized. This properties naturally arises from the large Hund coupling subtending the DE mechanism, as an electron can be transferred to a neighbouring site only if its spin is parallel to the t_{2g} core spin. In a band picture, this means that spin up and spin down bands are splitted and only one of them crosses the Fermi level.
Adopting a classification from Dagotto and coworkers [23], LSMO is a "large bandwidth" manganite, where the the hopping amplitude for electrons in the e_g-band is larger than in other manganites, as a consequence of the sizes of the ions involved in the chemical composition. For comparison the phase diagram of the $Pr_{1-x}Ca_xMnO_3$ compound, considered a "low bandwidth" manganite is reported. Here a charge ordered (CO) phase is stabilised around $x = 0.5$, where LSMO is FM. CO is induced by the electronic correlation that become important in narrow bands and with increasing carrier density. The Coulomb repulsion localizes the charge in stripes, that can be detected by superstructure peaks in X-ray or electronic diffraction[23].
In LSMO no CO phase is observed, because of bandwidth and also because large samples with $x > 0.6$ cannot be produced. However in the "intermediate bandwidth" compound $La_{1-x}Ca_xMnO_3$, CO phases occupy a wide part of the phase diagram with $x > 0.5$[23].
In the insulating phases such as in LSMO PI phase above T_C, the carriers are localized by lattice distortions, usually described as Holstein polarons, Anderson localization (especially for low carrier density at low x)[23] or Jahn-Teller polarons[13]. In the FM phase the polaronic gap is closed when the ferromagnetic fluctuation are stabilized and DE enlarges the conduction bands.
Given the polaronic nature of the high temperature PI phase, it is clear that electron-lattice coupling is crucial in determining the CMR phenomenon, as anticipated in §1.2. The application of the magnetic field moves the T_C towards higher temperatures, as showed in figure 1.7, so that also the metal insulator transition is shifted, giving rise to the huge resistivity variation.
The effect of magnetic fields on the $Pr_{1-x}Ca_xMnO_3$ CO-state of is remarkable. This is due to the stabilization of a metallic state upon the application of the field. At low temperatures, changes in resistivity by several orders of magnitude can be observed[23].
The CO state is traditionally described as a Wigner crystal, i.e. a charge crystal originated by charge localization on the atomic sites. The orbital ordering accompanying the CO stabilises complex spin structures known as

CE-AFM[23]. However it has been recently suggested by several authors that the CO state in manganites can be described as a charge density wave, i.e. a periodic modulation of charge originated by phonon-mediated electron-hole coupling and provided of excitation modes[24].
Finally for $x = 1$ we have the end-member of the series, the parent compound $SrMnO_3$ or, for Ca doping, $CaMnO_3$.
$SrMnO_3$ stable structure is hexagonal, but the metastable cubic perovskite structure can be stabilized by high pressure or by epitaxial strain.
$SrMnO_3$ is an undistorted cubic perovskite, while $CaMnO_3$ has the $GdFeO_3$ structure with undistorted octahedra.
The Mn^{4+} - Mn^{4+} magnetic interaction is the oxygen mediated superexchange interaction, that, as represented in figure 1.13, is completely antiferromagnetic. The resulting magnetic structure is G-type AFM, i.e. the spin nearest neighbour spins are all antiferromagnetically coupled with a given spin.
$SrMnO_3$ and $CaMnO_3$ are strong band insulators, as the fermi level falls in the wide gap between t_{2g} and e_g 3d electron levels. The crystal field gap in $AEMnO_3$ is even larger than the one in $REMnO_3$, as the crystal field splitting parameter Δ in Mn^{4+} is about 2.5 eV in oxides respect to 1.8 eV in Mn^{3+} [13].

1.2.4 $(LaMnO_3)/(SrMnO_3)$ interfaces and superlattices: experiments and models.

New possibilities in thin film fabrication (as the ones described in the following in §2.1.5) allow controlled growth of unit cell layers of oxides.
This unveils new perspectives in the study of interface effects in heterostructures and multilayers of strongly correlated materials. An example is the $SrTiO_3/LaAlO_3$ interface. As reported by Ohtomo and Hwang[25] in their seminal paper, this interface can be electron doped by the charge reconstruction induced by the polar discontinuity between the two constituent materials. This originates an high mobility 2D electron gas, showing quantum transport properties[25]. Further studies have been performed on this and on relative systems, such as $SrTiO_3/LaGaO_3$ superlattices[26].
It has been argued that the formation of a 2D electron gas may also occur at the $LaMnO_3/AEMnO_3$ interface. For example Nanda and Satpathy [2] studied a theoretical model of $(SrMnO_3)_n/LaMnO_3/(SrMnO_3)_n$ structures and deduced that a 2D electron gas may form in this system and inherit the spin polarization of the alloy compounds.

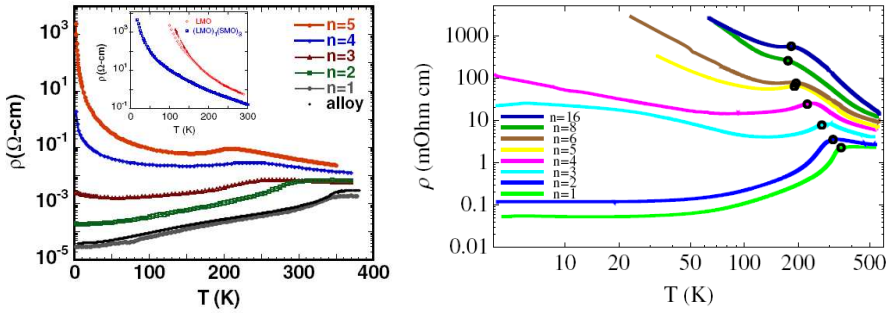

Figure 1.16: Left: Resistivity of $La_{0.67}Sr_{0.33}MnO_3$ random alloy film, and corresponding $(SrMnO_3)_n(LaMnO_3)_{2n}$ superlattices, $1 \leq n \leq 5$. The inset shows the resistivity of a pure $LaMnO_3$ thin film and also the resistivity of a $(SrMnO_3)_3(LaMnO_3)_1$ superlattice for reference (from Bhattacharya et al[27]). Right: Same for the superlattices by Adamo et al[16], as reported in the work by Adamo, Perroni et al. [28]. Black circles indicate the Curie temperatures of the samples (always close to the T_{MI}).

Experimental data

Experimental reports on $((LaMnO_3)_{2n}/(SrMnO_3)_n)_N$ $((LMO)_2n/(SMO)_n)$ superlattices are for example provided by the works of Bhattacharya et al.[27] and Adamo et al.[16].
These superlattices have the same composition of the alloy compound $La_{2/3}Sr_{1/3}MnO_3$, showing the best magnetic and transport properties, as pointed out in §1.2. In particular a part of this chapter will be devoted to the study of the orbital ordering and magnetism by X-ray spectroscopy measurements on the superlattices described in ref.[16].

The striking features of these film samples are the exotic metal-insulator transition (MIT) occurring at $n = 3$, and their magnetic state i.e. bulk antiferromagnetic ordering away from the interface and ferromagnetic ordering at the interface.
A detailed analysis of the transport mechanism is provided by the work of Adamo, Perroni et al.[28]. In figure 1.16 the resistivity versus temperature curves are shown, while in figure 1.17 all the transport mechanism with varying temperature and n are summarised in a diagram.
For $n = 1, 2$ the transport properties are similar to the alloy's ones: the material is a polaronic insulator at high temperature, a DE metal at low temperatures and at intermediate temperatures (around $T \gtrapprox T_{MI}$) Mott variable range hopping takes place, a signature of Anderson localization i.e. localization of narrow-band carriers induced by a disordered potential. The $n = 1$ sample transport properties are quantitatively comparable with the alloy (see figure1.16), and indicate a low disordered system.
For $n = 3$ to 6, Anderson localization takes place at low temperatures, while the metallic transport region is vanishing with increasing n. It is

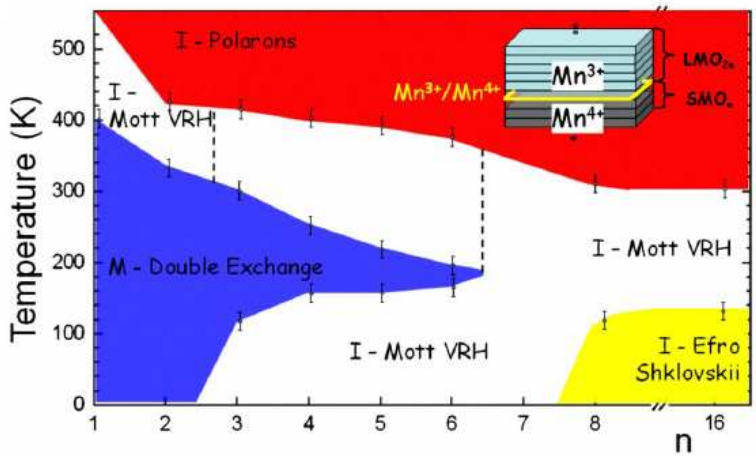

Figure 1.17: A cartoon summarising all the different transport regimes obtained changing n from ref.[28]. M stands for metal, I for insulator, and VRH for variable range hopping.

worth noticing that, for n=3, the size of SMO layers is larger than or on the same order of magnitude as the Thomas-Fermi screening length for manganites. Theoretical calculations[28] indicate that the charge transfer through the interfaces is reduced, implying that the bandwidth becomes very small. Therefore the effects due to disorder are amplified and a MI transition takes place at low temperature.
For $n = 8$ and 16 the low temperature transport is identified as Efros-Shklovskii variable range hopping (ES-VRH) mechanism. This behavior is due not only to the presence of disorder but also to the role of the Coulomb interaction that becomes more effective since the screening is weaker due to a lower carrier density.
Bhattacharya et al.[27] have performed polarized neutron reflectivity (PNR) measurement on their samples. PNR allows to probe the magnetic moment modulations in the layered structure of the samples.
The results for $n = 5$ and $n = 3$ are reported in figure 1.18. As we can see from the magnetic moment as a function of depth, reported in the insets of figure 1.18, the magnetic moment is modulated commensurate to the superlattice period.
In the $n = 5$ superlattice, the magnetic moment is maximum in the LMO close to the interface (its value is 3.8 $\mu_B/f.u.$, close to the alloy saturation magnetization), and it is reduced in the center of the LMO block. In the SMO block the magnetic moment is nearly zero, thus indicating an antiferromagnetic arrangement of the spins.
In the $n = 3$ superlattice, the commensurate modulation is always present, but its amplitude is reduced respect to the $n = 5$ case, i.e. some ferromag-

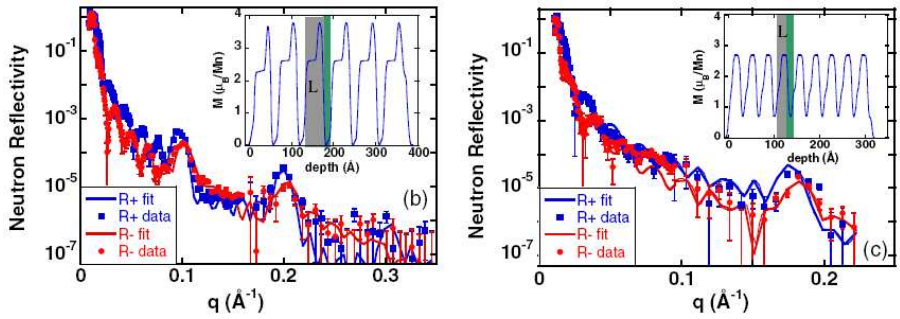

Figure 1.18: PNR measurements for (b) the $n = 5$ superlattice (c) for the $n = 3$ superlattice. Red and blue symbols stand for right polarized and left polarized neutron reflectivity. The inset shows the inferred magnetic structures from the best fit. The gray region is the extent of LMO in one superlattice period, and the green is the SMO[27].

netic arrangement is also present in the SMO block.
Since the Thomas-Fermi screening length is $1 - 3$ u.c., one expects that for $n > 3$ the LMO/SMO interfaces are relatively isolated from one another, and the bulk behaviour is mantained in the inner of the blocks. Conversely, for $n \leq 3$, each interface feels the influence of the others. The transport properties become metallic, consistently with a Mott transitions, and also the magnetic properties become less modulated, i.e. the system is more homogeneous[27, 28].

Models

$(\mathrm{LMO})_{2n}/(\mathrm{SMO})_n$ superlattices have been studied theoretically (among the others) by Dong et al. [19] (as already mentioned in §1.2.2) and by Nanda and Satpathy [31].
Dong et al. used an hamiltonian similar to that used by Hotta et al.[18](equation 1.6):

$$H_{SL} = H_{DE}(t) + H_{SE}(J_A F) + H_{e-ph}(\lambda) + \sum_i (\epsilon_i - \mu) n_i, \qquad (1.7)$$

where H_{DE} is the standard two-orbital large-Hund-coupling DE interaction, n_i is the e_g electron density μ is the chemical potential and ϵ_i the on-site effective potential generated by long-range Coulomb interactions that cannot be neglected in superlattices involving different electronic compositions. Each ϵ_i is be determined by its eight nearest neighbour A-site cation neighbours. More specifically, in the LMO-SMO superlattices, ϵ_i is 0 for those Mn between two LaO planes (LMO region), it becomes V/2 for those between LaO and SrO planes, and finally it is V for those between two SrO planes

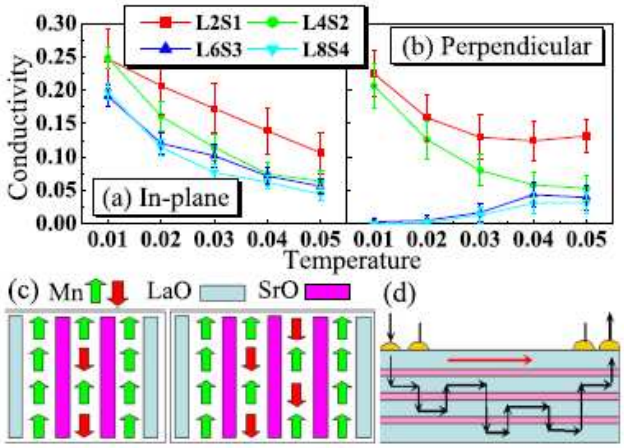

Figure 1.19: (a) In-plane conductivity for the superlattices studied here L2S1 stands for $(LMO)_2(SMO)_1$, and so on. (b) Perpendicular conductivity. (c) Sketch of the spin order at interfaces for L4S2 (left) and L6S3 (right). (d) Sketch of experimental setup for resistance measurements. Pink bars are SMO regions. Typical conducting paths via the DE process (black curves) connect neighbour interfaces, but they will be broken when $n \geq 3$. From ref.[19].

(SMO region).
The authors used Monte Carlo simulations to predict the magnetic and orbital state and the transport properties of the superlattices.
As already mentioned in §1.2.2 the authors assume a FM OO ground state for the LMO. The ground state for the SMO is instead the G-type AFM (completely AF).
For the $n \leq 2$ superlattices, the e_g density results almost homogeneous, regardless from the value of V, while for $n \geq 3$ the e_g density is lower than 0.5 in SMO blocks, accordingly with the findings of[28]. All in-plane conductivities are robust and increase with decreasing T, suggesting metallicity. In contrast, the perpendicular conductivities show metallic behaviour when $n \leq 2$, but insulating behaviour when $n \leq 3$ (see figure 1.19a,b)). To understand this MIT, the spin arrangement at the FM/G-AFM interface should be considered. The authors obtained from their calculations that FM/G-AFM interfaces are almost collinear at low T, namely, the nearest neighbour spins are parallel or antiparallel, as shown in figure 1.19c. Therefore, when there is only one G-AFM layer in each superlattice unit (n=2), the spin-up channels of the G-AFM layer link the neighbouring FM layers, allowing for a good conductance. However, once the SMO layers thickness is 3, the two G-AFM layers cut off the same-spin channels, giving rise to an insulating behavior along the z direction. The experimentally observed MIT can be understood by taking into account the Anderson localization when the DE path becomes exclusively 2D for $n \geq 3$. In this case, insulating behavior

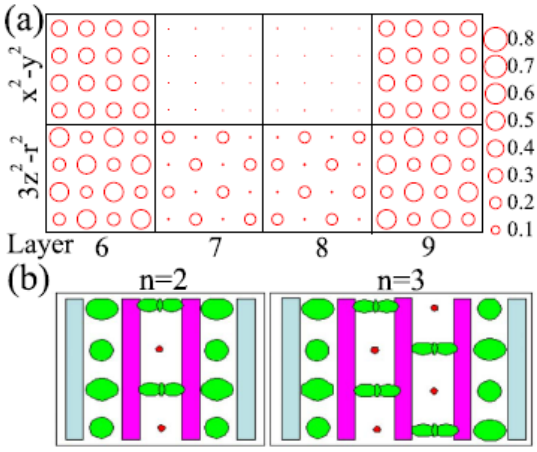

Figure 1.20: (a) Orbital occupation of the sixth to ninth layers for L6S3 when V=0.9 and T=0.01. The sixth and ninth are interface layers between the LaO and SrO layers, while the seventh and eighth are within the SMO region. Here the circle's area is proportional to the local eg charge density. (b) Sketch of orbital ordering at the interface for $n = 2$ and 3. From ref.[19].

may be induced by interface disorder, such as roughness.
In figure 1.20 it is reported the e_g orbital occupation near the interfaces. The authors propose that the parallel spin channels provide another driving force for orbital order in manganite superlattices. Their simulations in the $n = 2, 3$ and 4 cases show that the e_g electrons have more tendency to occupy the $d_{3z^2-r^2}$ orbital than the $d_{x^2-y^2}$ one around the interfaces. However strain or stress due to the lattice mismatch between substrates and LMO/SMO can induce orbital order, even without charge transfer[19].

In conclusion, the authors of ref.[19] successfully explain the MIT transition in long period superlattices ($n \geq 3$). They also describe the magnetic ordering in the system as collinear FM LMO and G-AFM SMO blocks, and the orbital ordering as mainly $d_{3z^2-r^2}$ in LMO blocks and $d_{3z^2-r^2}$-only in SMO blocks.
However, as pointed out in §1.2.2, the hypothesis of LMO being in FM OO phase may be wrong, as the ferromagnetism in LMO films seems to be related to a small concentration of Mn^{4+} ions rather than to a different ground state in a pure Mn^{3+} system.
Nanda and Satpathy[31] studied the same problem assuming a realistic structure for $(LMO)_{2n}(SMO)_n$ superlattices on $SrTiO_3$ substrates. They considered that LMO and SMO must match with the in-plane lattice parameter of the substrate, so that their out of plane lattice parameter is strained from 0.3935 nm and 0.3802 nm to 0.399 nm (LMO) and 0.365 nm (SMO), by volume conservation.

The authors used band calculations (LMTO method) to study the electrostatic potential felt by the electrons and the charge leakage at the interfaces. In order to study the magnetic ground state the authors have calculated the neighboring Mn-Mn exchange interaction energies (J's) for various exchange interactions, and then the energy of various spin configuration was calculated for each superlattice and the energies were fitted with the results of a nearest-neighbour Heisenberg model.

The results of these calculations are the magnetic structures represented in the right panels of figure 1.21. As we can see, for long period superlattices, the bulk magnetic behaviour is recovered in the inner MnO_2 layers, as a consequence of low charge leakage. The calculated behaviour of LMO is A-AFM despite the strain.

In conclusion, in Nanda and Satpathy model, for the short-period superlattice ($n = 1$), the authors find a weak variation in the potential leading to the spreading of the Mn-e_g electrons throughout the superlattice, resulting in a FM structure via the carrier mediated Zener double exchange, much like the alloy compound $La_{2/3}Sr_{1/3}MnO_3$. For higher n there is a potential barrier restricting the electron leakage to the SMO side. For $n \geq 3$, the charge leakage is restricted to just two layers at the interface, beyond which a bulk-like electronic and magnetic structure results[31].

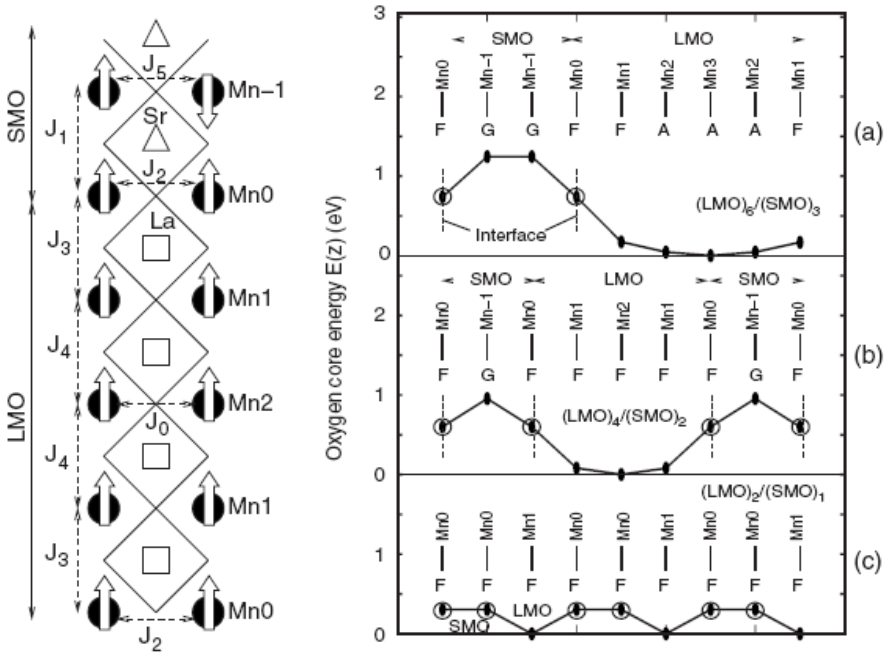

Figure 1.21: Left: Schematic unit cell of $(LMO)_4$ / $(SMO)_2$ superlattice and the magnetic structure as obtained from the DFT calculations. Oxygen atoms occur at the intersections of the checkered lines forming the MnO_6 octahedron. Definitions of all the exchange interactions (J's) considered in the model are reported. Right: (a)-(c) Variations in the oxygen 1s core energy, indicating the electrostatic potential barrier, of each MnO_2 layer, obtained from the layer-projected wave-function characters. Mn atoms of each MnO_2 layer are labelled as shown in the figure. The interfacial manganese atoms (Mn-0), which are sandwiched by the LaO and SrO layers, are shown by open circles with vertical dashed lines, indicating the position of the interface. The magnetic ordering of Mn spins for each layer as obtained from the DFT calculations is shown with the symbols F (FM), G (G-AFM), and A (A-AFM). A potential barrier is clearly seen for the $n = 2$ and $n = 3$ superlattices. From ref. [2]

1.3 CPP and field effect devices: a deeper insight into the transport properties.

In the previous sections, we focused our attention on the properties of $LaMnO_3/SrMnO_3$ (LMO/SMO). In particular the transport properties of such samples have been studied without any patterning of the samples and with the current flowing in the plane of the samples. For the LMO/SMO superlattices, we have seen how the transport and magnetization change with the period of the superlattices, by approaching and increasing the number of LMO/SMO interfaces. Nevertheless the transport could not be probed in the direction perpendicular to the plane, i.e. by a current that crosses the interfaces. The study of the transport in such configuration would be equally interesting for the $La_xMnO_{3-\delta}$ thin films in order to investigate the transport anisotropy in these samples, that show an out-of-plane/in-plane lattice parameter ratio that depends on La/Mn ratio x, as we will see in the following.
The current perpendicular to plane (CPP) measurements, require that the current flows across the film from the bottom to the the top, then the thin film or multilayer has to be grown on a conductive bottom electrode layer or on a conductive substrate. Furthermore a lithographic process is usually needed to access to the bottom electrode layer and define the measurement geometry of the sample. In the CPP measurement a voltage or current is applied in the perpendicular direction and then the current or voltage drop is measured in the same direction.
It is also interesting to see how a voltage applied in the direction perpendicular to plane influences the current flowing in the plane of the film. In this case we are interested in the sample resistance modulation by the applied electric field (i.e. voltage), that is the field effect.
To this aim a field effect device has to be engineered, for example a MOSFET-like structure. The engineering of such field effect devices requires very similar lithographic masks as the ones used for CPP measurements, as shown in section §1.3.2.
The study of the influence of the electric field on the transport properties of manganites and manganite based heterostructures is also a very interesting topic, as demonstrated by several publications [66, 67, 68].
In a MOSFET-like structure, an insulating film is needed for the gate barrier. In oxide field effect devices, epitaxial oxide films can be used. The use of functional oxides allows to provide more functionalities to the devices, and to study the effect of coupling of several degrees of freedom. To this aim we considered the application of ferroelectric and multiferroic oxides as gate insulators.

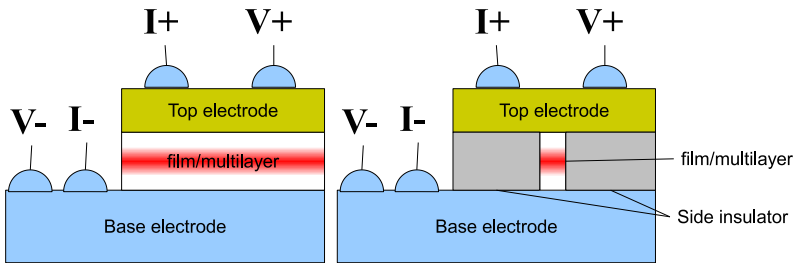

Figure 1.22: Simple schematic of a CPP device. In the first case the top contacts are placed directly on top of the film "square" or "pillar". When the size of the "square" becomes smaller than about 500 μm, the contacts cannot be placed directly on a so small area. It is then necessary to define a larger top electrode, that has to be insulated from the base electrode by means of a side insulator.

1.3.1 Description of the devices: CPP device and electrical polarization measurements

A schematic representation of a CPP device is represented in figure 1.22. As discussed above, electrical contacts have to be placed on the top and bottom electrode. The bottom electrode can be a conductive substrate, such as Nb:STO, or a metallic buffer layer . In the first case, there is no problem to place the electrical contacts, that can be placed on the bottom of the substrate, otherwise the metallic buffer has to be reached for example by etching the overlying film/multilayer to be measured. Even if a CPP measurement structure can be engineered without the use of lithography, it is usually desirable to define the area of the film to be measured. This allows for example to measure the sample resistivity, or to avoid the occurrence of local defects when measuring a large area. In this case, as showed in figure 1f, more lithographic and deposition steps are needed, in order to define the measurement area and insulate the base and top electrode. CPP configuration is commonly used to investigate the transport (and magneto-transport) properties of multilayers, such as GMR multilayers [69], of spin valves [70], or tunnel junctions [71]. Some examples of real devices are reported in figure 1.23.

However the same configuration showed in figure 1f can also be used for dielectric measurements on ferroelectric materials. To measure the electrical polarization of a dielectric or ferroelectric material, we need to fabricate a capacitor structure; then the polarization or dielectric constant can be measured, for example by using the Sawyer-Tower circuit[72], or by complex impedance measurements. Even if large area capacitors can be used, for example for thick films as represented in figure 1.24, large area also increases the possibility of including defects that can generate losses across the film, thus preventing to apply high electric fields and/or to observe the polarization P(E) loop. Furthermore, the possibility to precisely define the capacitor

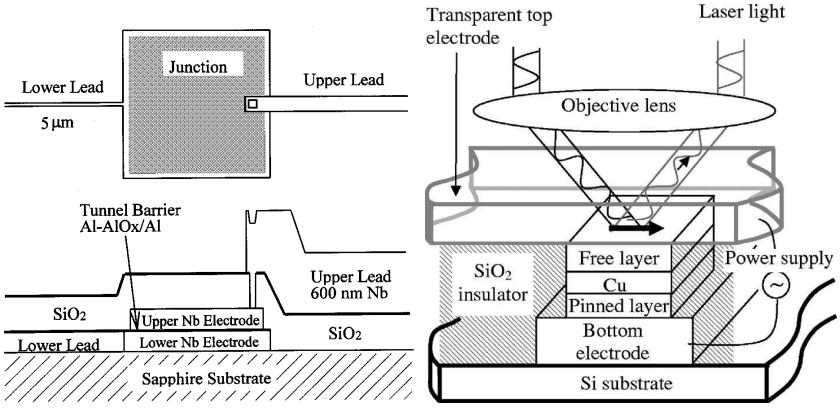

Figure 1.23: Two examples of use of CPP configuration. Left: superconducting tunnel junction of the island type [71]. Right: spin valve with transparent top electrode for magneto optical measurements [70].

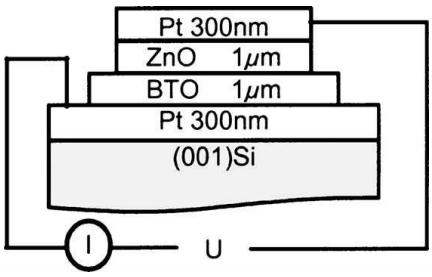

Figure 1.24: Structure for polarization measurement of a BaTiO3/ZnO bilayer grown by PLD by using shadow masks to define the capacitors (from ref. [72]).

area would allow to calculate the dipole moment with high accuracy. Then a structure like the one schematically represented in figure 1.22 would also be suitable for ferroelectric film P(E) measurement, provided that the side insulator allows to apply high voltage and no electrical contact between the top and bottom electrode. Indeed in the case of dielectric measurements even weak electrical losses would perturb the measurement.
Our interest in performing polarization measurements in such configuration resides in the possibility of engineering $LaMnO_3$ based multiferroic multilayers or superlattices. An example is provided by the work of Singh [32] et al. on $BaTiO_3/La_{0.7}Ca_{0.3}MnO_3$ superlattices, or by Murugavel et al. on $La_{0.7}Sr_{0.3}MnO_3/BaTiO_3$ superlattices [33]. However in these work no electrical polarization measurement were performed, as the described superlattices showed a low resistance in the CPP direction.
In this work a CPP measurement configuration technology has been developed on $BaTiO_3/SrRuO_3$ and $BiFeO_3/LaNiO_3$ bilayers for polarization measurements.

1.3.2 Description of the devices: Field effect devices

Field effect is traditionally the modulation effect of an external electric field on the electrical conductivity of a semiconducting channel. Typical field effect devices are the field effect transistors (FET), the most commonly used is the MOSFET (metal-oxide-semiconductor field effect transistors.
The MOSFET (and the CMOS) is the fundamental component used in digital electronic. The structure of the MOSFET is represented in figure 1.25. The general structure is a lightly doped p-type semiconductor substrate, into which two regions, the source and the drain, both of heavily doped n-type semiconductor have been embedded.The symbol n+ is used to denote this heavy doping. Metallized contacts are made to both source and drain. The rest of the substrate surface is covered with a thin oxide film. The gate electrode is laid on top of the insulating oxide layer, and the body electrode in the diagram provides a counter electrode to the gate.

The working principle of the MOSFET is represented in figure 1.26. The p-type doped substrate is only very lightly doped, and so it has a very high electrical resistance, and current cannot pass between the source and drain if there is zero voltage on the gate. Application of a positive potential to the gate electrode creates a strong electric field across the p-type material even for relatively small voltages, as the device thickness is very small and the field strength is given by the potential difference divided by the separation of the gate and body electrodes. Since the gate electrode is positively charged, it will therefore repel the holes in the p-type region. For high enough electrical fields, the resulting deformation of the energy bands will cause the bands of the p-type region to curve up so much that electrons will begin to populate the conduction band. The population of the p-type substrate

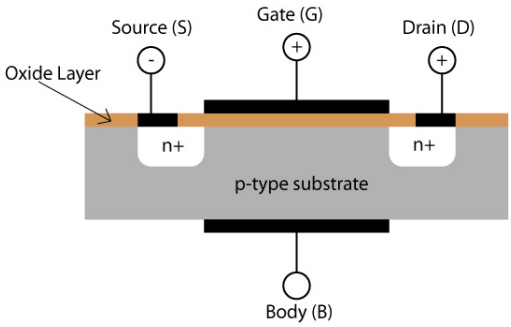

Figure 1.25: General structure of the MOSFET.

conduction bands in the region near to the oxide layer creates a conducting channel between the source and drain electrodes, permitting a current to pass through the device. The population of the conduction band begins above a critical voltage, VT, below which there is no conducting channel and no current flows. In this way the MOSFET may be used as a switch. Above the critical voltage, the gate voltage modulates the flow of current between source and drain, and may be used for signal amplification.
This is just one type of MOSFET, called "normally-off" because it is only the application of a positive gate voltage above the critical voltage which allows it to pass current. Another type of MOSFET is the 'normally-on', which has a conductive channel of less heavily doped n-type material between the source and drain electrodes. This channel can be depleted of electrons by applying a negative voltage to the gate electrode. A large enough negative voltage will cause the channel to be closed off entirely.
The MOSFET technology has reached sub-micrometric dimensions and 32 nm MOSFET technology is actually under development. The miniaturization process has to overcome several problems, such as quantum phenomena, dissipated power and other technological issues. This also requires the use of new materials with better performances than Si and Si oxides (such as high-K -high dielectric permittivity - materials).
The use of functional materials, such as ferroelectric, CMR or piezoelectric materials, can add new functionalities in field effect devices. For example, a ferroelectric gate, thanks to the remnant polarization moment, can keep an electric field in the channel even without the application of voltage. This would be a mean to reduce power consumption and to produce non-volatile memory devices permitting a non-destructive memory readoutscience. For example the ferroelectric perovskite $Pb(Zr,Ti)O_3$ (PZT) can be used as gate oxide, but this material is not highly compatible with a traditional Si channel because of the diffusion of Pb and Ti into silicon and the formation of an intermediate silicate layer at the interface. Therefore, an all-perovskite FET structure has been introduced by using a perovskite semiconducting chan-

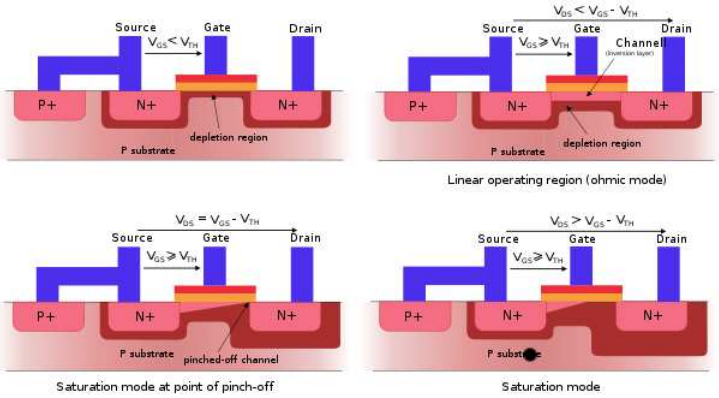

Figure 1.26: A cross section through an n-MOSFET, showing the working principle of the device. When VGS is below the threshold value VTH, electron conduction is null or little from source to drain. Above the threshold, the population of the band near the gate is inverted by the strong electric field, and conduction is possible, and proportional to VDS (linear region). When VDS is strong enough to close the channel near the drain (pinch off), the current reaches its maximum value, being independent from the applied voltage (but it depends on VGS) (saturation mode).

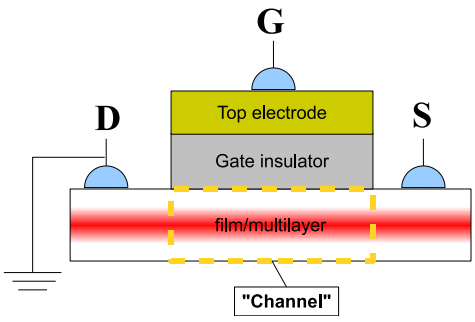

Figure 1.27: Structure of a MOSFET-like field effect device.

nel. Several perovskite semiconductors have been suggested to serve as the channel material, such as $SrRu_xTi_{1-x}O_3$, $SrRuO_3$,$SrCuO_3$, $La_{1-x}Sr_xCuO_3$, $La_{1-x}Ca_xMnO_3$ [74].

In particular CMR manganites are very interesting material for such applications, thanks to the tunability of their transport properties by electric field, magnetic field, strain and chemical substitutions. For example, they present an interesting opportunity to create field effect devices that may potentially be both electrically and magnetically tuned. More in general, the effect of the electric field on the band structure has been studied on several materials, such as high Tc superconductors [73].

The study of the field effect in manganites is a powerful method in itself to explore the scientific nature of the complicated interactions among spin,

charge, orbital, and lattice degrees of freedom in manganites.

1.4 Field effect in manganites

From the fundamental point of view, field effect provide an mean of changing the carrier density in a region of the channel material.
Manganites have a very rich phase diagram as a function of doping: by means of chemical substitutions in the perovskite A-site, the charge carrier density can be tuned and corresponding phase diagrams can be explored. However, the interpretation of the observed phenomenology is fairly complex, as the substitutions of the ions have a manifold effect: they move the Fermi level by doping and modify the band structure by correlation and via changing the structure itself. Indeed, chemical substitutions $RE_{1-x}AE_xMnO_3$ introduce disorder and above all they change the average ionic size in the lanthanide site and the angle of the Mn-O-Mn bond, characterized by the tolerance factor, which determines the double exchange transfer matrix element and consequently the transport properties. On the contrary, field effect appears to be a powerful tool for the study of these strongly correlated systems, as it only changes the charge carrier concentration, leaving unaltered the crystal lattice. Moreover, the carrier density changes induced by field effect are reversible. Thereby, the influence of the carrier concentration on the phase diagram, the transport properties, the magnetic behaviour, and the band structure can be explored.
One practical problem in performing field effect experiments on manganites is that in metallic samples the carrier density is of the order of 10^{21} cm^{-3} (much higher than in lightly doped semiconductor channels) and the electric field penetration is consequently limited to one or two unit cells.
Small resistance changes by field effect have been observed in ferroelectric transistors made of semiconducting $La_{0.7}Ca_{0.3}MnO_3$ [67] and semiconducting $La_{0.87}Ba_{0.13}MnO_3$ [113]. A very large electro-resistance effect is observed in $La_{0.7}Ca_{0.3}MnO_3$/PZT FET, that reaches the value of 76% at 0.4 MV/cm [76]. The device (using inverted configuration) and the resistivity vs. temperature curves for different values of the applied gate voltage are represented in figure 1.28. Such big resistivity modulation cannot be explained by the bare effect of the electric field on an homogeneous metallic channel, as the reduced electric field penetration would not affect the transport in 50 nm thick samples, as the ones used in ref.[76]. The data are then interpreted by the authors as a consequence of inhomogeneous charge ordering in the samples, that are a mixture of metallic and insulating charge ordered phases. In an electronically inhomogeneous channel, partly metallic (M) and partly insulating (I), the E-field would change the relative volume fractions of the M and I regions by accumulation of charge between M and I phases, thereby causing the interface to move. The nature of accumulating charge, holes vs electrons, will depend on field polarity and thereby control the direction of interface movement. As T is lowered, "droplets" of ferromagnetic (FM) metal appear. Applying a negative gate voltage causes electrons to

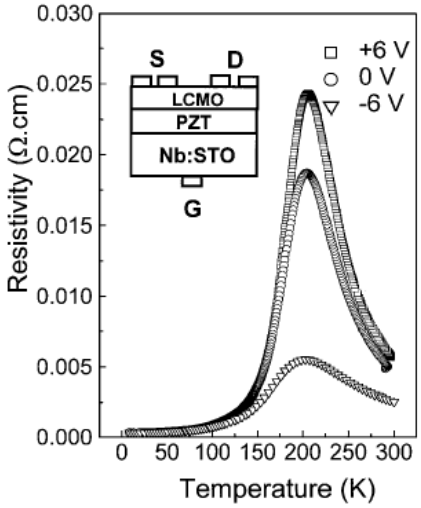

Figure 1.28: Resistivity vs. temperature curve of the LCMO in the ferroelectric field effect device sketched in the inset, with gate voltage +6, 0 and -6 V. From ref. [76]

accumulate at I-M interfaces, which pushes the interfaces away from the electrodes, causing increased metallicity with a nonlinear V dependence. A positive voltage does the opposite, leading to a resistivity which saturates at the intrinsic insulating value for the given T, which is not high.
From figure 1.28 we can also observe that, differently from the CMR phenomenon, the electric field does not influence the position metal-insulator transition peak. Indeed, the application of the magnetic field makes the intrinsic behaviour of the I regions more metallic, while the electric field changes the connectivity of the M regions by modifying the volume fractions of the FM and CO components.
In order to investigate a more homogeneous system, where the carrier density modulation effects are not masked by phase coexistence effects, Pallecchi and co-workers [66] developed a planar field effect device using oxygen deficient $La_{0.67}Ba_{0.33}MnO_{3-\delta}$ on $SrTiO_3$(to reduce the carrier density) with a channel width of 500nm and film thickness from 15 to 80 nm. The planar structure allows to apply up to 100 V to the gate without incurring in the breakdown, and despite the low capacitance of the structure (compared to multilayers), high electric field can be applied to the channel.

In figure 1.29, the channel resistance vs. temperature with different applied field is reported. The magnitude of the effect is smaller than the one observed by the authors of ref [76], but the interesting feature is the modulation of the metal-insulator transition temperature T_{MI}. In particular, a positive gate voltage not only increases the channel resistance by depleting it of mobile holes, but also depresses the T_{MI} temperature. Conversely, a

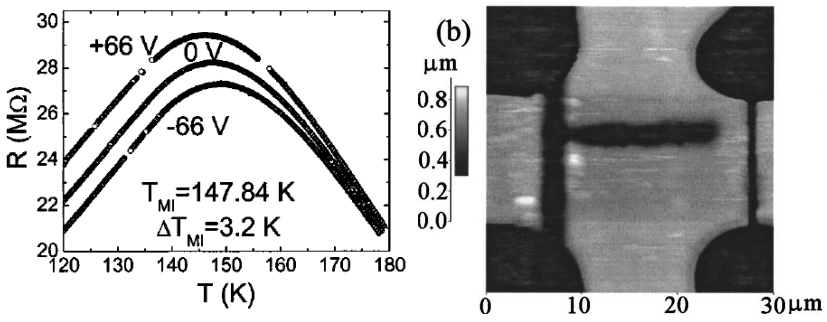

Figure 1.29: Left: Channel resistance versus temperature for different applied gate voltage in the planar field effect device of ref. [66]. Right: AFM image of the device (the gate is the right electrode next to the sub-micrometric channel).

negative gate voltage accumulates holes in the channel and it consequently lowers the channel resistance and enhances T_{MI}.
Interesting effects of electric field can be foreseen in $(LaMnO_3)_{2N}(SrMnO_3)_N$ superlattices, where, especially for large N, the charge density is strongly modulated across the thickness, as shown in section §1.2.4.
In this work the aim is to study the field effect in $La_{0.7}Sr_{0.3}MnO_3$ ultra-thin films on $SrTiO_3$ buffered Si substrates. To this aim Al_2O_3, SiO_2 and ferroelectric $BaTiO_3$ deposited ex-situ on the films have been used as gate insulators.

1.5 $SrRuO_3$: properties and applications

The $SrRuO_3$ compound is a ferromagnetic oxide with a Curie temperature of about 165K[77]. It shows a metallic temperature dependence of the electrical resistivity and thanks to its low resistivity (the single crystal residual resistivity is about 200-300 muOhm cm) it is one of the best conducting metallic oxides [79]. Because of its chemical stability, even at temperatures up to 1200 K, it is a useful candidate as electrode material in all-oxide electronic devices. Furthermore the $SrRuO_3$ structure (discussed in the following) is highly compatible with many functional oxides, such as YBCO or BTO, its growth mechanism has been deeply studied and it is easy to obtain very smooth films.
In this thesis work, we are interested in the application of $SrRuO_3$ as base electrode for our CPP devices. As it will be shown in the last chapter, our aim is to optimize the thin film growth in order to obtain smooth and best conducting films.
Besides the technological applications, the SRO itself is an interesting material for the study of the itinerant ferromagnetism in transition metal oxide systems [81]. Many papers deal with the growth dynamics and microstructure of epitaxial SRO thin films and their relation with the transport properties. Indeed SRO films show higher resistivity, when compared with the single crystals, if strained [82], and the transport properties are often found to be anisotropic [83].

1.5.1 Crystal structure of $SrRuO_3$ and epitaxial thin film growth

The crystal structure of the $SrRuO_3$ at room temperature is a distorted perovskite. Indeed the structure tolerance factor:

$$t = \frac{r_A + r_O}{\sqrt{2}(r_B + r_O)}, \tag{1.8}$$

(where r_A is the covalent radius atom at the A site i.e. Sr, r_O the oxygen one, r_B the one of the atom in the B site i.e. Ru) for this compound is less than one, leading to a rotation of the BO_6 octahedron to accommodate the atoms. The result is an orthorhombic Pbnm structure with lattice parameters $a = 0.55670$ nm, $b = 0.55304$ nm and $c = 0.78446$ nm (analogously we can use the Pnma notation with $a = 0.55670$ nm, $b = 0.78446$ nm and $c = 0.55304$ nm) at room temperature. In the following we will use Pbnm notation. This orthorhombic structure can be obtained from the undistorted perovskite structure by a tilting of the RuO_6 octahedra.
The SRO undergoes two structural phase transitions at 350°C and 600°C to tetragonal and cubic unit cell respectively [86].
It is often useful to refer to the pseudocubic unit cell, with lattice parameter

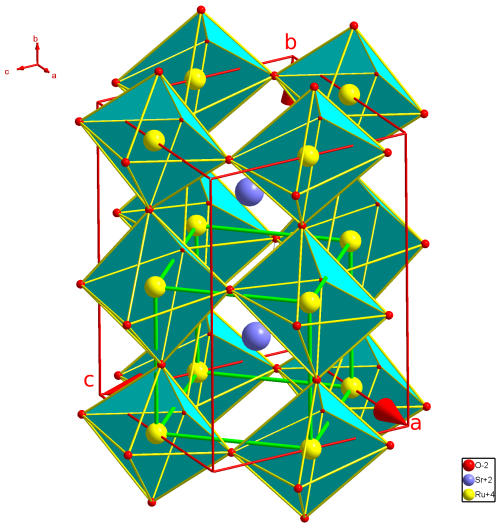

Figure 1.30: $SrRuO_3$ crystal structure in Pnma notation (from ref. [84]). For Pbnm notation y and z coordinates and b and c base vectors have to be exchanged. The Sr is represented by blue spheres, the O by red, the Ru by yellow. The RuO_6 octahedra are shown. To evidence the underlying cubic perovskite structure, the parent cubic cell is drawn in green. The cubic symmetry is broken by the octahedron rotations, that displace the oxygen atoms from the Ru-Ru bonds (green edges) and distort the 90° angles of the cube base (ac plane).

a_{pc} = 0.393 nm at room temperature. The p.c. lattice parameter is very close to the $SrTiO_3$ (STO) one a = 0.3905 nm, the lattice mismatch at room temperature is about 0.64%. Single crystalline epitaxial films of SRO can then be grown on (001) STO [87, 86].
A Pbnm/Pnma orthorhombic unit cell can accommodate on a cubic cell in several (six) different ways. SRO films are cubic during deposition (i.e.: at temperature higher than 600°C), and their epitaxy is "cube on cube" on usual perovskitic substrates [88]. The orthorhombic cell develops during cooling, and it is usually found that epitaxial SRO on (001) STO grows with the $[110]^o$ direction oriented normal to the substrate. Then there are two possible in plane epitaxial domains for such orientation: SRO [001],[-110]//STO[100],[010] and SRO [001],[-110]//STO[010],[100]. The presence of both domains originates in-plane twinning that are responsible for structural disorder [89].

It has been shown that the use of STO vicinal substrates (i.e. substrates with a precise miscut angle between the [001] direction and the crystal substrate) promotes step-flow growth and untwinned structure of the film. It is indeed found that, when the SRO crystal structure undergoes to the structural transition to orthorhombic structure upon cooling, the $[001]^o$ axis of SRO aligns along the step. As a consequence, films grown on exact (non

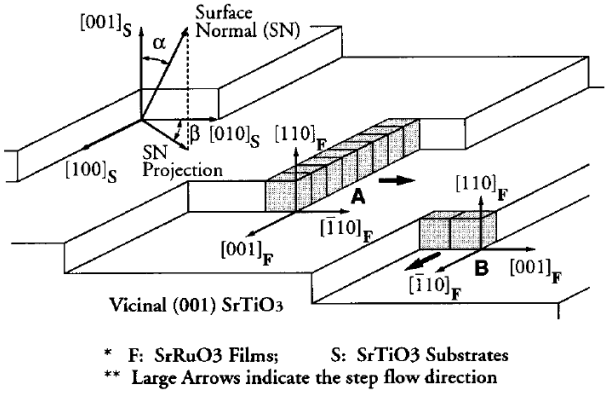

Figure 1.31: Schematic diagram of a vicinal $SrTiO_3$ (001) substrate showing miscut angle, α, and miscut direction, β, as well as the epitaxial arrangement of two types of step flow growth of $(110)^o$ $SrRuO_3$ domains (from ref. [89]).

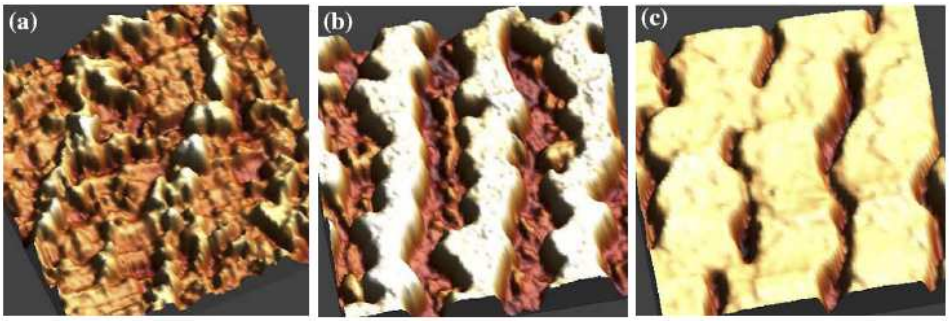

Figure 1.32: AFM topography image, 3D view, from ref. [80]. The image is 1μm x1μm size. (a) 1.7 nm thick film; (b) 3.5 nm thick film; (c) 7 nm thick film. The nucleation of islands along the substrate steps and their coalescence with increasing film thickness is shown.

vicinal) substrates usually contain the same amount of in plane domains, whereas on vicinal substates, the amount of different domains depends on the vicinal direction β (i.e. the angle between the steps and the in-plane [010] direction) [89].

Several works on the growth dynamics of SRO have shown that, in the early stages of growth, 3D or 2D islands nucleate along the substrate steps [80, 87]. Then the islands coalesce first along the step direction, forming fingers-like pattern, and eventually merge together (see figure 1.32). Rijnders et al. [90] observed that in the early stage of growth on TiO_2 terminated STO substrates, the step flow/layer-by-layer steady growth only starts when the SRO surface is entirely converted to SrO; indeed RuO_2 termination is unstable because of the high volatility of ruthenium oxide. The evaporation of ruthenium oxide also promotes the 2D growth by increasing the surface

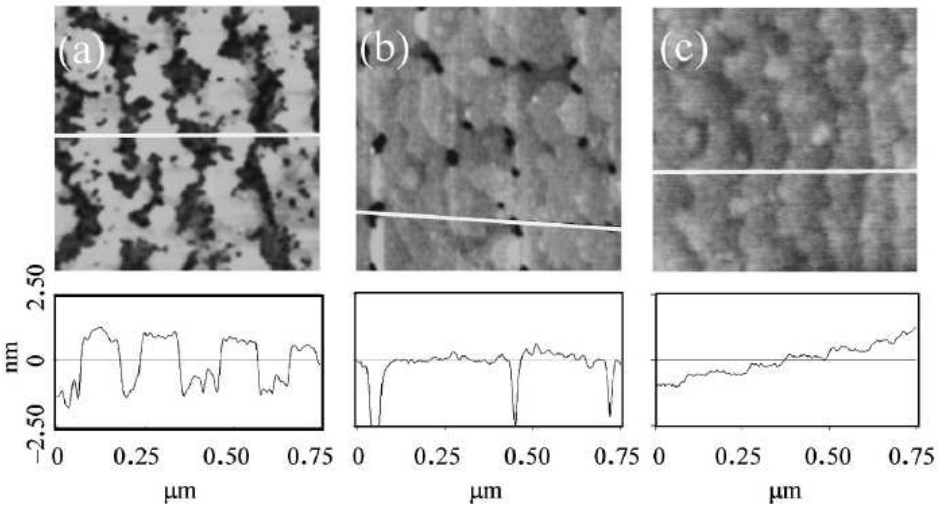

Figure 1.33: Top: AFM topography image of $SrRuO_3$ films with 4nm (a), 8nm (b) and 40 nm thickness. Bottom: height profile for the top measurements taken along the white lines. From ref. [79].

mobility of the ad-atoms.
In conclusion, in order to have single domain, atomically flat SRO thin films, the use of single terminated vicinal substrates is recommended. The use of untreated exact substrates do not allow to attain this limit, but, as we will show in the following, satisfactory results in terms of low roughness can be also obtained in these conditions.

1.5.2 Magnetic and transport properties of $SrRuO_3$ single crystals and thin films

The SrRuO3 compound is an itinerant ferromagnet with saturation magnetization of about 2μB/f.u., whose ferromagnetism is tied to the conduction electrons lying in a $\pi*$ narrow band formed by the overlap of Ru t_{2g} orbitals with the O $2p$ orbitals.
The Ru valence state in the compound is 4+; from the electronic configuration of Ru: [Kr] $4d^7$ $5s^1$, we have that in the compound the 4d orbitals are occupied by four electrons. Because of the octahedral crystal field generated by the oxygen anions surrounding the Ru, the 4d levels split in t_{2g} (xy, yz, zx) and e_g $(3z^2 - r^2,\ x^2 - y^2)$ levels with higher energy. The saturation magnetization value indicates that the Ru is in a low spin configuration, with all the electrons occupying the low energy t_{2g} levels.
The magnetism of $SrRuO_3$ has the same characteristics of the itinerant magnetism of elemental ferromagnets: it is strong and it has the same critical

and low temperature behaviour[91]. On the other hand, from the point of view of transport, strontium ruthenate is considered a "bad metal", in the sense that the product $k_F l$ is O(1) (where k_F is the Fermi wavevector and l is the electron mean free path). Indeed the conduction bands are quite narrow, although the 4d levels are less localized if compared to the 3d ones as in manganites[91]. As a consequence, the effect of the magnetic transition on the electrical resistivity of strontium ruthenate is much stronger if compared to good metallic itinerant ferromagnet (such as iron or nickel), but not as dramatic as in manganites, that show polaronic conduction above T_C. An important source for some of the intriguing properties of $SrRuO_3$ is the relative strength of the spin-orbit coupling of the ruthenium atom (900 cm^{-1} compared to 400 cm^{-1} in iron, for example). This property is the origin of the strength of features such as magneto-optic effects, magnetocrystalline anisotropy, anisotropic magnetoresistance, and the anomalous Hall effect [91].
The resistivity versus temperature $\rho(T)$ curve of $SrRuO_3$ is very peculiar: when crossing the curie temperature the slope $d\rho/dT$ increases, resulting in a knee in the curve. The derivative $d\rho/dT$ diverges at a temperature slightly below T_C, with a critical exponent close to 1 for $T \rightarrow T_C^+$ and a very weak divergence for $T \rightarrow T_C^-$. Such a strong divergence and also the asymmetry of the peak distinguish the behaviour of $SrRuO_3$ from "good metal" itinerant ferromagnets. The expected divergence is expected to be logarithmic for Heisenberg ferromagnets and weak (with a critical exponent of 0.1) for Ising ferromagnets, and in both cases symmetric. These critical transport properties of $SrRuO_3$ indicate that critical spin fluctuations affect the transport much strongly in this material.
It has been observed that in thin films the $d\rho/dT$ peaks at lower temperatures not only than the bulk T_C, but also than the reduced film T_C itself. The discrepancy increases with disorder and decreasing thickness [83].
The low temperature resistivity behaviour, proportional to $\rho_0 + AT^2$ indicates that the dominant scattering mechanism below T_C is the electron-electron interaction. Being an itinerant ferromagnet, majority and minority spin electrons have different effective masses, thus this kind of scattering mechanism happens between heavy and light carriers, and it is more effective than usually observed in metals, where this effect is negligible compared to other mechanisms[91]. In disordered samples, low temperature resistivity minima can be observed, originating from quantum correction to conductivity from electron-electron scattering[83].
The authors of ref. [**?**, 80] observed an in-plane transport anisotropy caused by the microstructure of the films here reported in figures 1.32 and 1.33. As shown in figure 5, the resistivity versus temperature curve is different when the current is injected perpendicular or parallel to the finger-like pattern, and the anisotropy is disappearing in very thick films. In ref. [80] the authors show that the anisotropy is not related to oxygen deficiency at

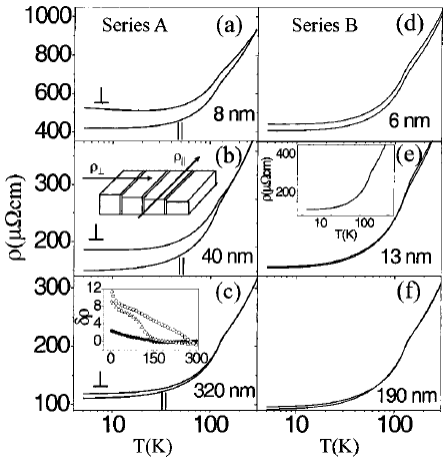

Figure 1.34: resistivity vs temperature curves with injected current perpendicular or parallel to the subtrates steps. (a),(b),(c) films cooled in deposition pressure, with increasing thickness. (d),(e),(f) films cooled in 1bar O2, increasing thickness. The anisotropy is eliminated rapidly with increasing thickness in the second series of samples (from ref. [83]).

the grain boundaries of the finger-like islands, as a post-annealing in oxygen is not reducing it. Instead the anisotropy is eliminated, in a new series of samples, by the cooling after deposition in a higher gas pressure (1bar) than the deposition one (regardless if it is in oxygen or argon). In the experimental set-up of ref. [80], this corresponds to a faster cooling. Indeed, it has been observed, by using x-ray synchrotron radiation, that $SrRuO_3$ undergoes a series of polymorphic phase transformations in a wide range of temperatures[92]. These different phases differ essentially in the tilt of the RuO_6 octahedra, that modifies the Ru-O hybridization, leading to different interactions among the ions, thus affecting the magnetic and transport properties. The modification of RuO_6 tilting also explains the reduction of the Curie temperature in epitaxial thin films on $SrTiO_3$, whose T_C is about 150K. Indeed, because of the epitaxial growth, the pseudo cubic cell of $SrRuO_3$ is distorted to match the $SrTiO_3$ one in the $[110]^o$-$[001]^o$ plane.

1.6 Ferroelectric materials: some properties and applications

Ferroelectricity is a property of certain materials in which they possess a spontaneous electric polarization that can be reversed by the application of an external electric field. The term is used in analogy to ferromagnetism, in which a material exhibits a permanent magnetic moment. Most materials are polarized linearly by an external electric field; nonlinearities are insignificant. Some materials, known as paraelectric materials, demonstrate a more pronounced nonlinear polarization. The electric permittivity, corresponding to the slope of the polarization curve $P(E)$, is thereby a function of the external electric field. In addition to being nonlinear, ferroelectric materials demonstrate a spontaneous (zero field) polarization. Such materials are generally called pyroelectrics. The distinguishing feature of ferroelectrics is that the direction of the spontaneous polarization can be reversed by an applied electric field, yielding a hysteresis loop. Typically, materials demonstrate ferroelectricity only below a certain phase transition temperature, T_c, and are paraelectric above this temperature[93].
The nonlinear nature of ferroelectric materials can be used to make capacitors with tunable capacitance. Typically, a ferroelectric capacitor simply consists of a pair of electrodes sandwiching a layer of ferroelectric material. The permittivity of ferroelectrics is not only tunable but commonly also very high in absolute value, especially when close to the phase transition temperature (see figure 1.36, showing the BaTiO3 relative permittivity). Because of this, ferroelectric capacitors are small in physical size compared to dielectric (non-tunable) capacitors of similar capacitance. The spontaneous polarization of ferroelectric materials implies a hysteresis effect which can be used as a memory function, and ferroelectric capacitors are indeed used to make ferroelectric RAM [94] for computers and RFID cards.
In this work ferroelectric materials find direct application as gate insulator in field effect devices, that can in principle acquire a memory functionality by means of the spontaneous polarization.

1.6.1 Basic principles

For a system of point charges of charge e_i and position $\mathbf{r}_i$, the dipole moment $\mathbf{p}$ is defined as:

$$\mathbf{p} = \sum_i e_i \mathbf{r}_i \tag{1.9}$$

and it is independent of the choice of the coordinate origin, provided that the system is electrically neutral (as it is verified in a crystalline solid). In a macroscopic description of a dielectric, when it is regarded as a continuum, it is convenient to describe the electrical state by introducing the polarization

P, the density of dipole moment per unit volume. This quantity, appearing in the Maxwell equations, is naturally related to charge distribution in a unit cell:

$$\mathbf{P} = \frac{1}{v_{uc}} \sum_{i \in uc} e_i \mathbf{r}_i, \tag{1.10}$$

in the point charge ions approximation, where v_{uc} is the unit cell volume. This polarization density is ill defined, indeed any crystalline solid would have a non-zero dipole moment, but this dipole moment would depend on the choice of the unit cell or, for a macroscopic sample, on the size and shape of the sample. As long as the crystal possess inversion symmetry, the definition 1.10 can give equivalently a dipole moment of equal magnitude but opposite direction. The dipole moment of a symmetric crystal would always be equilibrated by charged defects or charge distribution at the boundaries, and once equilibrated it is zero at any temperature (does not depend on the unit cell expansion)[93]. The measurable polarization is the polarization difference $\Delta\mathbf{P}$ between two states where the inversion symmetry is broken. For example in the pyroelectric effect, with increasing temperature, the charge distribution in the unit cell becomes polar, i.e. the inversion symmetry is broken, giving rise to a measurable polarization:

$$\Delta\mathbf{P} = \frac{1}{v_{uc}} \sum_{i \in uc} e_i \Delta\mathbf{r}_i, \tag{1.11}$$

where $\Delta\mathbf{r}_i$ is the displacements of ions from symmetric position in a high-temperature phase. The ferroelectric phase transition is a structural phase transition, as a result of which a spontaneous polarization occurs in the crystal, which is caused by relative displacements of atoms in each of the unit cells of the crystal and which results in the appearance of a pyroelectric effect in the crystal[93].
More complete treatment would go beyond the point charge approximation and consider the density of the electronic wavefunctions. In this treatment the polarization is no more obtained by the charge density dipole moment, but by the current flowing through the unit cell during the structural transformation (that corresponds to the charge that piles up at the boundaries of the system, finally giving a dipole moment)[95].

1.6.2 Ferroelectric materials: the prototypical BaTiO3

$BaTiO_3$ (BTO) is a well known ferroelectric material. It also possesses other remarkable properties: high dielectric constant, electro optical and non linear optical properties.
The BTO structure is a distorted perovskite one, as represented in figure.

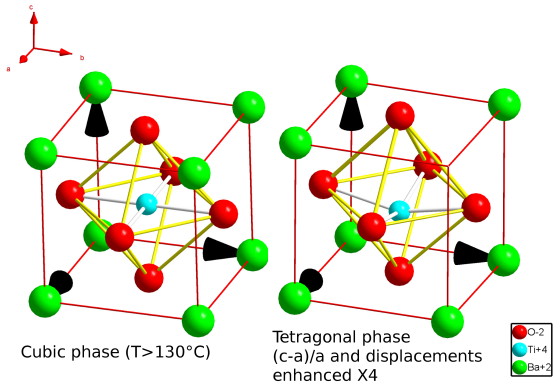

Figure 1.35: BTO structure above and below the structural phase transition giving rise to the electrical polarization. The cell distortion and the atomic displacements have been enhanced for clarity. The tetragonal phase is polar (the inversion symmetry is broken by the relative displacements of the O and Ti ions) and the resulting polarization is directed along the c axis (in this case downward).

The Ti^{4+} is surrounded by an octahedron of oxygen O^{2-} ions and its electronic configuration is d^0. At T=130°C, the material undergoes a structural phase transition from cubic perovskite (Pm3m) with lattice parameter a=0.3996 nm to tetragonal P4mm, with lattice parameter a=0.3994 nm, c=0.4034 nm (see figure 1.35) [96]. In this structure the inversion symmetry is broken by the relative displacements of the O and Ti ions. The hybridization between the filled oxygen p states and the empty Ti d states drives the structural instability that causes ferroelectricity. The resulting electrical polarization vector is directed along the c axis, is the same direction of the Ti ion displacement (downwards for the cell represented in figure c). The saturation value of the electrical polarization of BTO is 0.26 C/m^2. However, the cubic-tetragonal phase transition at 130°C is not the only one occurring in this system.
The structural instability gives rise to several different structures with decreasing temperature; the literature reports: at 5°C a transition to orthorhombic phase (a=0. 3990 nm, b=0.5669 Å , c=0.5682 nm), at -90°C a transition to rhombohedral structure (a=0.4001 nm, α=89° 51') [96]. An alternative interpretation of X-ray diffraction data is given by Yoshimura and co-workers[96], that reports the transition to two phases where a tetragonal and a monoclinic structure coexist, and finally to a tetragonal low temperature phase, as shown in figure 1.36.

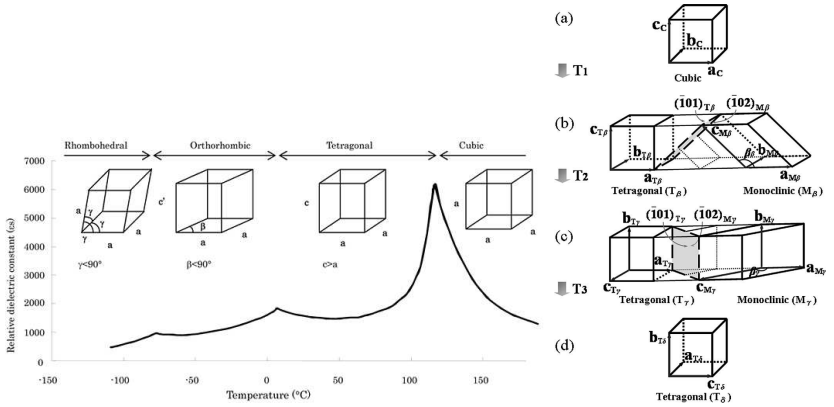

Figure 1.36: Structural transitions of BaTiO3. Left: traditional picture. The behaviour of the relative dielectric constant (permittivity), showing peaks in correspondence of the transition temperatures, is also reported. Right: alternative interpretation by Yoshimura and co-workers: T1=300K, T2=265K, T3=90K.

1.6.3 BTO thin films deposition

Several authors report on BTO thin film fabrication for different applications. For example, to exploit the ferroelectric properties and to measure the electrical polarization of the film, a conductive base electrode is necessary, for the integration of electro-optic function on silicon wafer, an insulating buffer allowing epitaxy, such as MgO, can be used [97].
For ferroelectric application c-axis oriented epitaxial thin films are required (so that the **P** is oriented normal to the substrate), whereas for some optical applications a-axis oriented films (**P** in plane) are needed.
PLD deposition of thin films on different substrates has demonstrated to produce different film orientation depending on the deposition pressure. For example for thin films grown of Pt (polycrystalline but highly (111) oriented) buffered Si, the BTO orientation changes from (110) to (111) to (100) for decreasing deposition pressure[98]. This result is interpreted in terms of the kinetic energy of the ad-atoms reaching the substrate during deposition. At high deposition pressure (0.5 mbar) the mobility of the ad-atoms is low, and the film grows in the highest grow rate direction, that is (110). At intermediate pressure (0.13 mbar), epitaxial growth of (111) oriented film on the (111) Pt is favoured. At low pressure, i.e. at very high kinetical energy, the film growth is along the (100) direction (a-axis), that is an electro-neutral plane[98]. The microstructure of the films also depends on the deposition pressure, indeed smooth films can be obtained at low deposition pressure (10^{-5} mbar).
Other authors report on the growth of BTO on $SrTiO_3$ substrates as a function of deposition pressure[99]. The authors use X-ray diffraction in asymmetric configuration to determine whether the orientation of the films

is (001) or (100); their finding is that films deposited at pressure above 0.12 mbar are (100) oriented, films deposited between 0.12 and 0.07 mbar are cubic and films deposited below 0.07 mbar are (001) oriented. In this case the c-axis orientation is obtained at low oxygen pressure. The SrTiO3 is cubic with lattice parameter 0.3905 nm, then in case of epitaxial growth, c-axis orientation is favoured, as the BTO is less strained in this configuration. In the work reported by Li et al. [99], the c-axis growth is found at lower oxygen pressure, while at high oxygen pressure the growth along the electro-neutral plane (100) is favoured.

Oxygen vacancy and insulation resistance degradation in BTO

For application as dielectric in high dielectric constant capacitors or to measure ferroelectric polarization loops, it is important that the current losses across the dielectric/ferroelectric layer are low. The BTO is an insulator whose resistivity is very high, of the order of 10^{10} Ohm/cm. However defects in grain boundaries in polycrystalline samples or oxygen non stoichiometry reduce the resistance value of real samples.
From studies on reoxidation, it is inferred that the $BaTiO_3$ is an n-type semiconductor, with the major defects resulting from high concentration of oxygen vacancies created during the thermal processing of the devices. Yang and co-workers [100] analyzed polycrystalline BTO capacitors with co-fired Ni electrodes. The first findings is that the most important contribution to resistance is provided by the grain boundaries, while the BTO grains have lower resistance. Using electron energy loss spectroscopy (EELS), an analytical electron microscopy technique combining transmission electron microscopy with spectroscopy, the authors could probe the Ti valence state on nearly atomic scale, and the oxygen vacancies. The effect of ageing of the capacitors is then attributed to oxygen vacancies migration towards the cathode, that reduces the Schottky barrier at the grain boundaries thus degrading the insulation resistance.
The resistivity degradation effect of oxygen vacancies must be much important in single crystalline BTO, where no grain boundaries are present.

1.6.4 Multiferroic materials

According to the original definition, multiferroic materials are materials that combine two or more primary forms of ferroic order, i.e. ferroelasticity, ferroelectricity and ferromagnetism in a single phase. The definition of multiferroics can be expanded as to include non-primary order parameters, such as antiferromagnetism or ferrimagnetism. However most of the recent research has focused in materials that combine some form of magnetic order with ferroelectricity, i.e. magnetic ferroelectrics.

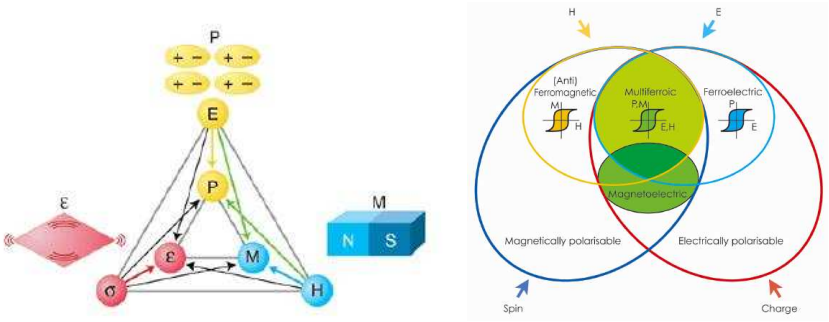

Figure 1.37: Multiferroic materials possess two ferroic orderings simultaneously. Here **E** is the electric field, **H** is the magnetic field, ε is the stress tensor, P is the polarization, **M** the magnetization and ϵ the strain tensor. Coupling between two different degrees of freedom gives rise to magneto-electric effect ($\mathbf{E} \rightarrow \mathbf{M}, \mathbf{H} \rightarrow \mathbf{P}$), piezoelectricity ($\mathbf{E} \rightarrow \varepsilon, \varepsilon \rightarrow \mathbf{P}$), magneto-elastic effect ($\mathbf{H} \rightarrow \varepsilon, \varepsilon \rightarrow \mathbf{M}$).

One of the main issues in magnetic ferroelectrics research is the occurrence of magneto-electric effect in such materials, which is the property that in certain materials a magnetic field induces an electric polarization and, conversely, an electric field induces a magnetization. Such property, coupling magnetic and electric degrees of freedom, together with the memory effect related to the ferroicity, is particularly interesting for device applications.
Traditionally one refers to linear magneto-electric effect, though quadratic or higher order effect is also possible, and for example ferroelectric transition can be induced by magnetic field application application. Not every magnetic ferroelectric exhibits linear magneto-electric effect, and not every material exhibiting magneto-electric effect is also simultaneously multiferroic [101].
Typical multiferroics belong to the group of the perovskite transition metal oxides, and include rare-earth manganites and -ferrites (e.g. $TbMnO_3$, $HoMn_2O_5$, $LuFe_2O_4$). Other examples are the bismuth compounds $BiFeO_3$ and $BiMnO_3$, and non-oxides such as $BaNiF_4$ and spinel chalcogenides, e.g. $ZnCr_2Se_4$. These alloys show rich phase diagrams combining different ferroic orders in separate phases. Apart from single phase multiferroics, composites and heterostructures exhibiting more than one ferroic order parameter are studied extensively.

1.6.5 The prototypical $BiFeO_3$

In usual perovskite-based ferroelectrics like $BaTiO_3$, $PbTiO_3$ or $KNbO_3$, the ferroelectric distortion occurs due to the displacement of B-site cation (Ti, Nb) with respect to the oxygen octahedral cage. Here the transition metal ion (Ti in $BaTiO_3$) requires an empty d shell since the ferroelectric displacement occurs due to the hopping of electrons between Ti d and O p atoms.

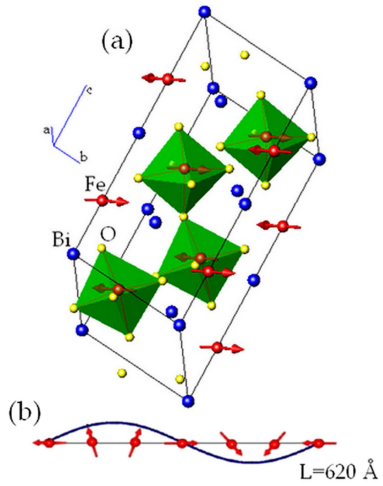

Figure 1.38: (a) Schematic presentation of the BiFeO3 unit cell in the hexagonal setting of space group R3c (a=b= 0.55799 nm, c=13.8670 nm). The Bi, Fe and O ions are shown with blue, red and yellow symbols, respectively. The distorted FeO6 octahedra are shown in green. The (almost) antiparallel Fe3+ magnetic moments are shown with red arrows. The lower part of the figure (b) shows that the magnetic moments' direction changes in a periodic way [103].

This normally excludes any net magnetic moment because magnetism requires partially filled d shells. However, partially filled d shell on the B-site reduces the tendency of perovskites to display ferroelectricity. The ferroelectricity in multiferroic materials is therefore generally caused by a different mechanism than in prototypical ferroelectric materials.
For example in the distorted perovskite $BiFeO_3$ (BFO) the ion responsible for ferroelectricity is not the B-site cation Fe^{3+} that is in d^5 configuration and responsible for the magnetic ordering, but the A-site cation Bi^{3+}.
It is well known in chemistry that cations containing a highly polarisable $5s$ or $6s$ lone pair of valence electrons (such as Bi^{3+} or Pb^{2+}) have a strong tendency to break local inversion symmetry [101].
Bulk BFO is a ferroelectric antiferromagnet (AFM) with a relatively high Néel temperature (320°C) and high ferroelectric critical temperature (810°C). Bulk BFO is known to exhibit G-type AFM ordering, i.e. the magnetic moment of each Fe cation is antiparallel to that of its nearest neighbours. Superimposed to this G-type magnetic order, a long-period cycloidal modulation is observed, where the AFM order parameter (the difference between the two sublattice magnetization) rotates within the (110) plane (see figure 1.38) with a wavelength of about 62 nm[101].
The weak ferromagnetism at room temperature is due to a residual moment from the canted spin structure [102], even though the cycloidal modulation would cancel it. Nevertheless impurities, chemical substitution, application of strong magnetic field or the enhanced anisotropy in strained thin film

would destroy the modulation yielding a net magnetic moment,of the order of 0.05 μ_B/Fe cation[101].
The electrical polarization is directed along the $[111]^c$ direction of the pseudocubic cell, and its spontaneous value measured in high quality single crystal bulk samples is about 60 $\mu C/cm^2$ [104, 101]. The polarization is originated by the relative displacements of all the ionic sublattices along the polar $[111]^c$ direction, and the oxygen octahedra are rotated around the same axis alternately clockwise and counter-clockwise (the cubic symmetry is then broken, yielding the rhombohedral R3c cell represented in figure 1.38).
The spin canting that gives the ferromagnetic moment is induced by the spin-orbit coupling. The microscopic mechanism responsible for canting in weak ferromagnets is the Dzyaloshinskii-Moriya (DM) interaction, that is non-vanishing only if the inversion symmetry is broken between two interacting magnetic centers. Thus, inversion symmetry breaking can cause both ferroelecticity and weak ferromagnetism, and if it is the case, magnetization and polarization would be coupled (magneto-electric coupling), i.e. it would be possible to manipulate the magnetization by an external magnetic field. Unfortunately in $BiFeO_3$ the DM interaction is coupled with an antiferrodistortive mode, not related to the polar distortion, and therefore the weak ferromagnetism in BFO is not controlled by the polarization[101].

1.6.6 $BiFeO_3$ thin films

Thin films can be deposited on buffered Si (with Pt/TiO_2 or $SrRuO_3/SrTiO_3$ base electrode/buffer layer templates) or on $SrTiO_3$ (STO) substrates. Different crystalline structures are found for thin films: the rhombohedral symmetry is only kept in case of STO (111) substrates, while monoclinic or tetragonal symmetries are found by different authors for (100) or (101) substrate orientations [102].
In the case of STO substrates, spontaneous polarization of about 50-60 $\mu C/cm^2$ is reported. It was found that the sensitivity of the electric polarization to strain is surprisingly weak in BFO. The polarization direction is always found to be along the $[111]^c$ direction. The c/a ratio (tetragonality, i.e. the ratio of the long and the short lattice parameter of the pseudocubic cell), that is an important parameter indicating the lattice distortion, is found between 1.032 and 1.014 depending on the deposition conditions[102]. Theoretical calculations suggest that if the BFO is constrained to tetragonal P4mm symmetry (with no octahedral tilts and only a formula per unit cell) it would develop a "super-tetragonality" with c/a ratio of 1.27 and giant electric polarization ($\sim 150\ \mu C/cm^2$)[101]. Tetragonal BFO with giant axial ratio was indeed obtained by epitaxial deposition on $LaAlO_3$ substrates by Béa et al. [105], but the measured polarization value is only 75 $\mu C/cm^2$. Indeed neutron diffraction on the films reveal octahedral rotations causing a

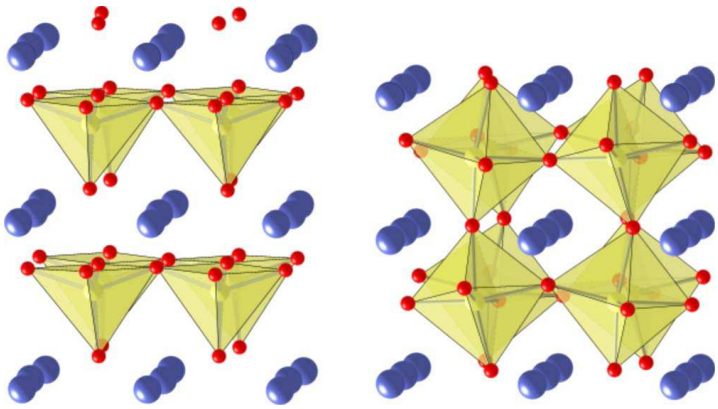

Figure 1.39: Isosymmetric phases of Cc BFO: Left: tetragonal-like T phase; Right: rhombohedral-like R phase [106].

slight monoclinic distortion, in contrast with the assumption of the theoretical calculations. Hatt et al., using density-functional calculation, calculated the strained structure of BFO on (100) substrates for different strain values. Their result, according with Béa et al. experiments, is that above a strain of 4.5%, a nearly tetragonal monoclinic structure, with polarization along the $[001]^c$ (out of plane) direction is obtained (figure 1.39), with c/a ratio of 1.3[106]. Below the critical strain value, a monoclinic structure with the same point symmetry, but more similar to the rhombohedral bulk structure, is obtained, with polarization along the $[111]^c$ direction.

In early studies on BFO, the bulk polarization was believed to be one order of magnitude smaller than the polarization of thin films[102]. Only recently high quality single crystal samples have been produced, revealing that the bulk polarization is very close to the one observed on films. However also in thin films, parasitic phases can be formed because of non optimal deposition condition, such as Fe oxides and Bi_2O_3. Films containing Fe_2O_3 systematically exhibit a ferromagnetic behaviour, in contrast with the weak ferromagnetism of bulk and single phase films. Instead Bi_2O_3 outgrowths create shortcuts through the BFO films, thus preventing their practical use as ferroelectric elements in functional heterostructures[107].

1.6.7 Super-tetragonal $BiCoO_3$ compound

Recent research on magnetic ferroelectrics has focused on perovskite materials with giant axial ratio (c/a), that are believed to possess very high dipole moment respect to traditional ferroelectrics. For example, the axial ratio of $BaTiO_3$ is just $c/a = 1.010$, for rhombohedral-like $BiFeO_3$ $c/a = 1.032 - 1.014$.

$BiCoO_3$ (BCO) is a compound with the same structure of ferroelectric $BaTiO_3$ and $PbTiO_3$, but its tetragonality is $c/a = 1.27$; this suggests very

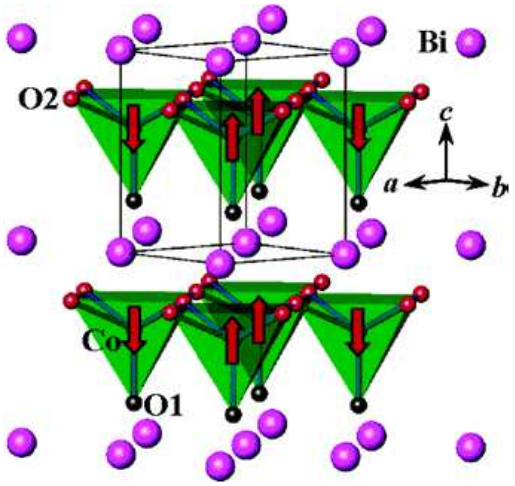

Figure 1.40: Crystal structure of BiCoO3 with solid lines displaying the chemical cell. Arrows show the direction of the magnetic moments below TN = 470 K.

high spontaneous polarization. The BCO contains magnetic Co ions, the magnetic ordering is antiferromagnetic with Néel temperature $T_N = 470K$.

The magnetic structure, determined by neutron diffraction, is of the C-type, i.e. ferromagnetic chains along the c axis are antiferromagnetically coupled (see figure 1.40) [108].

Bulk samples of BCO are produced by high pressure synthesis (6 GPa) and high temperature (1270K), from the work of Belik et al.[108]. The electrical resistivity of BCO exhibited activation-type temperature dependence but was as low as 10^{-2} Ωcm at room temperature. This low value of the resistivity prevented the authors to measure the polarization of the material. It has still to be proved whether such a tetragonal compound is ferroelectric, i.e. it possesses switchable polarization, or just pyroelectric. The low resistivity value is most probably due to the impurity content of the samples, that contain cobaltite Co_3O_4 and $Bi_2O_2CO_3$.

The production of single phase thin film may allow to measure the spontaneous polarization of this material. As many perovskite oxides ($BiMnO_3$, $BiCrO_3$...), bulk samples can only be produced by high pressure synthesis (6GPa)[108]. However, epitaxial stabilization can provide a mean to stabilize these phases in thin films, as found for the $BiMnO_3$ [109] and $BiCrO_3$ [110].

Chapter 2

Experimental techniques

2.1 Deposition techniques

2.1.1 The pulsed laser deposition (PLD) technique

The PLD technique allows the fabrication of thin film samples using stoichiometric targets of the same compound for growth, and it is relatively easy from the applicative point of view. On the contrary the radiation-matter interaction process of evaporation of the target material and the generated plasma dynamic is very complex.
The target material is ablated by focusing, to a spot size of $\sim$1mm^2, short (15-30 ns) and very energetic (50-300 mJ) laser pulses. The laser pulse ionizes and heats the target material, which becomes an extremely hot (7000-20000 K) plasma, that rapidly expands in the vacuum chamber. The matter flux is usually called plume.
The advantages of this technique are:

- The laser source is external to the deposition chamber, so the deposition system is simpler than the one needed for other techniques;
- The deposition pressure is usually of the order of 10^{-6}-10^{0} mbar, so ultra high vacuum is not needed;
- In optimal conditions the target stoichiometry is reproduced in the film, and the reproducibility of the results is very high;
- The particle energy is higher than the thermal energy, therefore particle adhesion to the substrate is enhanced.

The physics of the ablation process has not yet been explained entirely. Many actual studies on the plasma dynamics focus on the speed of the different ablated species, on the braking effect of the background pressure and on their effects on the quality of the films[111, 112, 113]. The target stoichimetry can be transmitted to the plasma if the thermal diffusion time

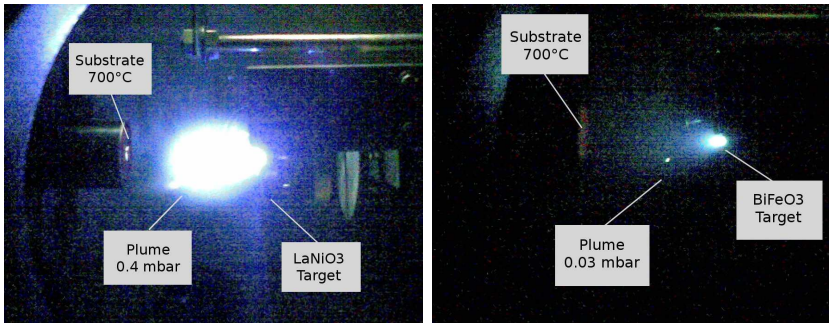

Figure 2.1: Left: Laser ablation of $LaNiO_3$, plume expansion in a background pressure of 0.4 mbar. Right: Laser ablation of $BiFeO_3$, plume expansion in a background pressure of 0.03 mbar. The braking effect of the deposition atmosphere leads to a more anisotropic expansion, that can lead to a higher arrival rate of particles on the substrate. On the other hand the particles reaching the substrate at higher pressure lose more of their kinetical energy.

is large compared to the laser pulse duration. In this case the heating of the internal region of the target can be neglected, and the ablated material comes directly from the surface, reproducing its composition. As the radiation absorption length is inversely proportional to the wavelength, short wavelength and short duration pulses are necessary.
For power, short duration pulses and short wavelength, excimer lasers are widely used, thanks to monochromatic pulses with a wavelength between 350 and 150 nm, duration of some tenths of ns and high power.

The plasma plume is characterized by a strongly anisotropic expansion. The plume shape is ellipsoidal, and the dependence of the thickness of a deposited film by the angle θ between the target normal and the substrate is $(\cos\theta)^{8\div12}$. As a consequence the PLD technique is not suitable to uniformly cover wide surfaces, and it is usually limited to 5x5 mm^2 substrates.
Another inconvenience of the technique is that droplets and particulates can be ablated by the target and deposit on the film. Their occurrence can be avoided by adjusting the laser energy and the target-substrate distance.

2.1.2 The PLD deposition system of GREYC laboratory

$SrRuO_3$ and $BaTiO_3$ thin films have been grown in the PLD system of GREYC laboratory of University of Caen-Basse Normandie. This PLD system is made up of an excimer laser using KrF excitation medium, a deposition vacuum chamber equipped with a primary rotary and a secondary turbomolecular vacuum pump, a substrate holder with a radiative heater for high temperature deposition, a carousel target holder allowing to rotate

and switch up to 5 different targets, a mass flow controller and a Baratron pressure gauge for O_2 pressure control during deposition.
The KrF excimer laser is one of the most widely used PLD lasers thanks to its high efficiency (high power) short wavelength, and relatively low cost of the gas mixtures. In our case the Kr and F_2 gas mixture is mixed with He, an inert gas, and Ne, a buffer gas. The laser wavelength is 248 nm (corresponding to the excimer dissociation energy), its pulse duration is about 20 ns, with an energy up to 300 mJ and the emission rate ranges from 1 to 10 Hz. The laser beam is focused by a lens and enters the deposition chamber by a Pyrex optical window, hitting the target with an incidence angle of 45°.
The vacuum chamber reaches a vacuum of 10^{-3} mbar if the rotary pump is used and of about 10^{-5} mbar if the turbomolecular pump is used. The pumps are connected to the chamber by high vacuum electro-valves, operated by manual switches. An Alcatel Pirani-cold cathode vacuum gauge is used to measure the pressure. During the deposition of oxides, O_2 is introduced by the mass-flow valve, operated by a Baratron controller to set the deposition pressure. For deposition pressures of the order of 10^{-1} mbar, only the primary pump is used.
The target is held by a 5 target carousel, allowing to rotate the target on its axis by a continuous rotation motor and to switch among the targets by a stepper motor. The stepper motor also shifts continuously the target during the deposition to allow the laser beam to scan the target surface.
The sample holder is a plate with a hole allowing the insertion of a 10x10 mm^2 substrate or two 5x10 mm^2 substrates, that are fixed by two hooks. The hole allows the sample to be heated by a radiative heater, located behind the sample holder. For the radiative heating to be effective for transparent substrates, a $YBaCuO_3$ deposition is done on the back of the substrates, in order to have a dark layer to absorb the radiation. The substrate temperature is measured by a thermocouple positioned on the plate holder, as close to the substrate as possible. The heater is controlled by an Eurotherm temperature controller, that allows to set temperature dwells and ramps.

2.1.3 The PLD deposition system of CRISMAT laboratory

$BiCoO_3$ and $BiFeO_3/LaNiO_3$ thin films have been deposited in the multitarget PLD system of CRISMAT laboratories in Caen. This PLD system is equipped with a pump station equipped with a rotary pump and a turbomolecular pump, that reach a vacuum of the order of 5×10^{-7} mbar.
During the deposition an oxygen pressure is established in the chamber. In order to keep this oxygen pressure, the oxygen enters the chamber by a needle valve, while the principal pump-chamber connection is closed and a low conductance by pass is used to pump in the chamber. In the chamber two

vacuum gauges are used: a wide range one, connected to the pump station security, and a narrow range one (1 Torr - 10^{-3} Torr) used to control the pressure during the deposition. Because of the deposition set-up, the lowest oxygen pressure that can be kept in a controlled way in the chamber is about 10 mTorr.
The multi-target carousel is controlled by a PC, together with the excimer laser, so that multilayers and superlattices can be fabricated, by setting the number of shots to fire on each target and the number of repetition. The PC also controls the energy and pulse rate of the laser. The laser is a KrF excimer laser, allowing to tune the energy from 250 mJ to 150 mJ, and shot frequency up to 10 Hz.
The sample holder can be heated up to 700°C in oxygen, and its temperature is controlled by a PID temperature controller, that allows to set temperature dwells and heating and cooling ramps at fixed rate. The target-substrate distance and the substrate position can be changed by a (x,y,z) manipulator.

2.1.4 Molecular beam epitaxy (MBE) deposition technique.

Several techniques are used to grow thin films under high vacuum conditions. These techniques can be divided into two categories depending on whether the species are physically or chemically transported from the sources to the substrate.
In the physical deposition techniques, the compounds are vaporized from policrystalline or amorphous sources at high temperatures and transported through the vacuum reactor to the substrate without producing any chemical reaction. Conversely in chemical deposition techniques, the species, often in non-elemental form, undergo to chemical reactions to form the reactants which will make the film growing on the surface of the substrate crystal.
Both these deposition modes can be employed in a MBE system.
The distinguishing feature of MBE technique and its main advantage respect to other deposition techniques is the possibility of high precision control over the deposition parameter and over the molecular flux of the evaporated species.
In MBE the species are evaporated in form of molecular beams by high temperature crucibles of a particular kind, known as effusive cells or Knudsen cells, represented in figure 2.2. However, for high evaporation temperature materials, electron guns evaporators are also used. Knudsen cells are preferable thanks to the higher stability of the flux rate[29].

The molecular beams travel across the system in ballistic regime thanks to the high vacuum conditions, and reach the substrate region, where the beams interact with each other and with the gases that can be introduced in this region of the chamber, creating a gaseous phase surrounding the whole substrate. Finally the condensation of the crystal on the substrate, typically

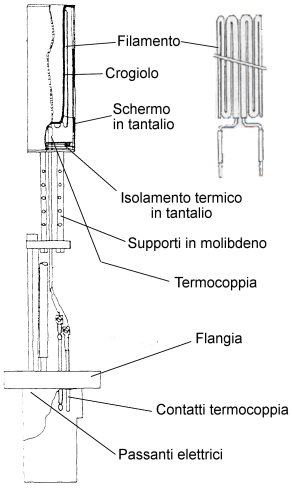

Figure 2.2: Effusive cell used in the University of Salerno MBE deposition system. The filament is made in tantalum. The effusive cells are closed by shutters that can be manually or computer controlled by pneumatic actuators.

kept at high temperature, takes place.
In order to obtain the growth of the desired phase, the evaporation rate of each constituent of the material and the substrate temperature have to be monitored. For the effusive cells, the flux rate is determined by the crucible temperature and by the external pressure, and by geometrical factors such as the aperture area of the cells and its position respect to the substrate. As most of these parameter are fixed during the deposition, the rate can be very precisely controlled by the cell temperature[29].

2.1.5 Reflection High-Energy Electron Diffraction (RHEED) in-situ diagnostic

Compared to other deposition techniques, the MBE has the advantage of allowing in-situ control by surface diagnostic methods such as RHEED. This methodology can be applied thanks to the ultrahigh vacuum conditions characteristic of the growth environment.
RHEED uses electron having energy in the 5-50 keV range, that are produced by an electron gun and focused and collimated to impinge on the substrate/sample at a variable glancing angle, usually less than 5°. The diffraction of the incident primary beam on the 2D lattice of the film surface, leads to the appearance of streaks (or rods) on the fluorescent screen used as detector, that is placed opposite to the electron source.
This configuration, the forward scattering geometry, is the most suitable for the deposition control, since the electron beam is at grazing incidence on the sample, while the molecular beams impinges almost normally on the

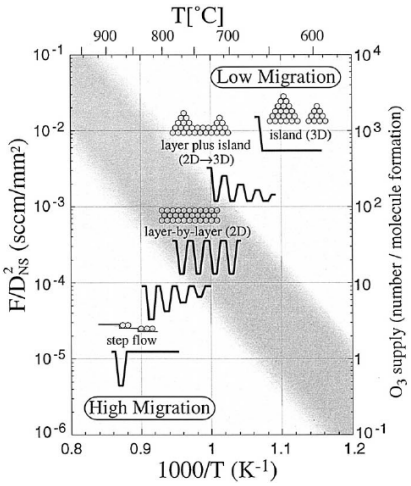

Figure 2.3: Phase diagram showing the growth mode of homoepitaxial $SrTiO_3$ as a function of the deposition parameters. For any growth mode the observed intensity modulation of the RHEED pattern is reported[30].

substrate.

The streak position on the phosphor screen is related to the film in-plane lattice parameters, as the lattice can be considered 2D because of the low incidence angle of the electrons. The distance between two adjacent streaks is given by:

$$d = \frac{Lg_{||}}{k}, \tag{2.1}$$

where L is the distance between the substrate and the phosphor screen, $k = (2\pi/h)\sqrt{2mE}$ is the is the wave vector of the primary beam of energy E and $g_{||} = 2\pi/r_0$ where r_0 is an in-plane lattice vector.

If during the growth 3D islands are formed, the electron beam can be transmitted through the island leading to an additional spot pattern, so that the film growth mode can be identified by the qualitative change of the diffraction pattern.

The central spot in the streak pattern is the specular spot (SS) is the mirror like reflection of the electron beam. The SS definition gives information about the flatness and the flatness and the quality of the surface. The SS and the higher order streaks are all originated by the elastic scattering of the electron beam. They can be used to interpret the surface morphology. In particular the intensity of the RHEED features shows an oscillatory behaviour which is directly related to the growth rate, as summarized in figure 2.3. In the case of layer-by-layer 2D growth, the intensity of the signal is maximum when a unit cell layer is completed, and minimum when the roughness is maximum i.e. when half of the layer is completed. However the intensity is also modulated by the chemical composition of the surface

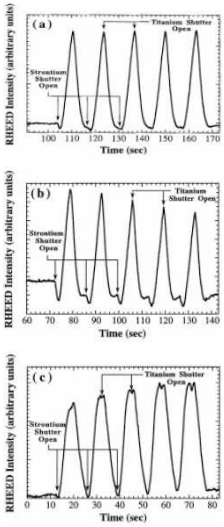

Figure 2.4: RHEED intensity oscillations of the entire central diffracted streak (oo rod) as the strontium and titanium are deposited in a sequential manner. (a) Stoichiometric full monolayer of both strontium and titanium deposited. (b) Strontium dose held constant, but titanium dose increased by 3% from a full monolayer. (c) Strontium dose held constant, but titanium dose decreased by 3% from a full monolayer[34].

layer.
This was first demonstrated by Haeni et al.[34] that used shuttered MBE deposition for homoepitaxial $SrTiO_3$ growth.
The shuttered deposition is an alternative technique to co-deposition of multicomponent oxides. In co-deposition all the component of the oxide are evaporated at the same time. In shuttered deposition a monolayer of each component of the oxide is deposited in order to complete a unit cell.
The variation in the intensity of the oscillations in the diffracted spots, the presence of beatings or of double peaks are related to the stoichiometry of the deposited compound and to the exact completion of the unit cells. This technique then allows to use the RHEED not only for morphology but also for stoichiometry control.

2.1.6 The MBE equipment

In figure 2.5 the University of Salerno MBE system is represented. The system is composed of three different chambers. The chamber 1 and 2 are separately used thanks to different pumping system which mantains the chambers in ultra high vacuum ($< 10^{-9}$ Torr).
Both the chambers are supplied by a RHEED system for the control of the growth process (see §2.1.5).
The intro chamber allows to load the samples without breaking the vacuum

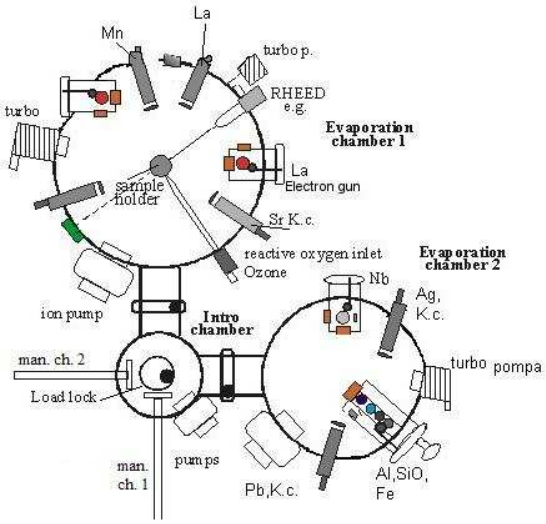

Figure 2.5: A schematic representation of the Salerno MBE system.

in the growth chambers.
In both chambers the evaporation of the elemental materials is performed through effusion (Knudsen) cells and electron guns.
The electron guns are mainly used in evaporation chamber II. In the electron guns an electron beam is generated by a hot filament, then it is accelerated by an electric field and focused on a water-cooled crucible containing the material to evaporate.
Because of the small evaporating surface, the deposition rate cannot be easily controlled.
The chamber I is dedicated to the fabrication of oxide materials, such as $La_{1-x}Sr_xMnO_3$. In this chamber three effusive cells are used: one is the high temperature effusive cell for the deposition of La and the others are the effusive cells for Sr and Mn.
Regular effusive cells have a pyrolytic BN crucible and can reach temperatures of 800°C. High temperature effusive cells have Ta crucibles and a water cooled shield, so that temperatures of about 1400°C can be reached. High temperature effusive cells have progressively substituted electron guns for a wide range of materials.
Oxygen and a mixture of oxygen and 5% ozone can be introduced in chamber for the oxide formation.
The chamber I sample holder can be rotated during the growth and can be heated to temperatures up to 800°C.
The rate of evaporation can be monitored by quartz crystal thickness monitors.

2.2 Device fabrication techniques

2.2.1 Optical lithography techniques

Optical lithography is a technique that allows to define a pattern on a flat surface by means of a light sensitive resin (photoresist) and by the exposition by light of a certain wavelength (usually in the UV range) through an optical mask, where the pattern is delineated. This technique is widely used in the thin film micromachining, thanks to its reliability and high reproducibility. The resolution that can be attained by this technique is ideally limited by the diffraction of light. Other factors, such as the uniformity of the resist layer, the flatness of the surface, the type of etching used on the thin film, can further reduce the resolution.
The disadvantages of this technique is that it requires flat surfaces and clean operational conditions, and it is not very effective in creating non-flat patterns.

Working principle

The working principle of optical lithography is exposed in figure 2.6. The sample (film or substrate) is covered by a thin layer of photoresist, and a pattern is exposed by UV radiation passing through an optical mask. The solubility of the photoresist is changed by the interaction with the radiation: a positive photoresist becomes soluble in bases after exposition (while the unexposed is insoluble), a negative photoresist conversely becomes insoluble. Then the photoresist is developed in a basic solution (developer solution) and the positive or negative image of the pattern is left. The successive step of machining can be etching, i.e. the non protected film is removed, or lift off, i.e. a film is deposited all over the sample, then the resist is removed leaving the film only in the non-protected zones. These steps have usually to be repeated several times to obtain the final structure or device, including both etching (dry or wet) and deposition (of metallic contacts, insulating layers...).

There are two different exposition methods: contact lithography and projection lithography. In contact lithography the mask is a 1:1 reproduction of the pattern, and it is brought in contact (as close as possible) with the photoresist to be exposed. This technique does not present focusing problems, then a large area can be exposed at the same time. It is also easy to align the substrate parallel to the mask, and expose samples of different thickness without requiring calibrations. The equipment used for the contact lithography exposition is called mask aligner. The disadvantage of this technique is that true contact can be prevented by particulates or non-uniformity of the resist layer, leading to a non-perfect transfer of the pattern. Furthermore the mask can be damaged by particulates included in the resist or resist traces can stick and damage the successive expositions.

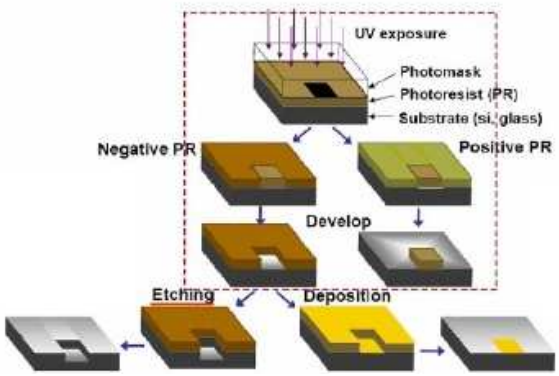

Figure 2.6: The light passes through the mask where the pattern (the black square) is reported, and exposes the photoresist (PR). Positive and negative PRs give complementary patterns after development (positive or negative image of the mask). Two different techniques are then illustrated: etching, where the non protected film is removed, or lift-off, where the film is deposited only in the non protected zones.

In projection lithography the mask is far away from the samples, and contains an enlarged pattern. The light passing through the mask is focused on the sample by lenses, that also reduce the pattern to the right scale. This technique experiences focusing problems on large areas, and also special care has to be taken in order to have the sample surface exactly perpendicular to the incident light and at the focal distance. Projection lithography is mainly used in industrial application, because the pattern can be reproduced several times on the same sample (for example a large wafer) with subsequent expositions, and the mask is less wearied, because no mechanical contact is required. For our purposes, contact lithography is used, also thanks to its higher flexibility for research purposes (adaptability to different kind of samples), and to the simpler equipment needed for the expositions.

Photoresist

The photoresist is a solution composed by a polymer, a sensibiliser and a solvent. Its main characteristic is to change its solubility when exposed to light, but besides that, other properties are needed: it has to cover the surface with a thin, homogeneous and adherent layer, that has to protect the film below from chemical and physical etchants, and it has to be possible to remove it from the pattern without damaging the sample.
The polymer is the main ingredient of the resist. In the case of a positive resist, it is a polymer with inactive bonds, that can be activated to form long insoluble chains. The sensibiliser is a light sensitive substance that, with light of a certain wavelength, activates the bonds of the polymer, then

changing its solubility. The solvent keeps sensibiliser and polymer in solution.
The resist used in this work is the positive tone photoresist Shipley 1813.
The photoresist has to be spread on the sample. This is commonly done by spinning the sample at a speed of about 2500-4500 rpm. During this process part of the solvent evaporates, and a thin layer of resist, whose thickness depends on resist density and on spinning speed, remains on the sample. The manufacturer of the Shipley 1813, reports that, at a speed of 3500 rpm, the resulting resist thickness is 1.3 um. Another important parameter in the spinning process is the acceleration used to reach the chosen speed, that determines the uniformity of the thickness. The resist layer is more uniform when a high acceleration is used. Other factors determining the thickness and uniformity of the resist layer are the surface adhesion (on Si primers are used to enhance it) and the size and shape of the samples (on the edges and on corners resist is usually thicker).
After the application of the photoresist, a pre-exposition bake, or soft bake, is usually performed to evaporate the remaining solvent. Usually the sample with the resist is heated on a hot plate at about 90-120°C for some minutes. Excessive baking can originate fogging, a phenomenon consisting in the partial development of the resist, that becomes partly insoluble/soluble.

Exposition

The light sources used for standard UV lithography are high pressure Hg arc lamps. A sketch of the optical part of a mask aligner is represented in figure 2.7.
During the exposition process the light is absorbed by the photoresist, that changes its properties. The photoresist is usually sensitive to light in the UV region (157 - 436 nm), the correct exposition wavelength depends on the properties of the particular resist. The best exposition wavelength is chosen by the requirements of having an high absorbance by the unexposed resist and a low absorbance by the exposed one (so that the exposed resist is transparent to the radiation and the underlying resist can be irradiated). The difference of the absorption coefficients is called the resist contrast. Exposing the resist with a wavelength corresponding to low contrast yields sloped profiles in the pattern. The exposition time (of the order of some seconds) depends on the resist characteristics and thickness. Over exposition results in smaller details respect to the ones reported in the mask and in irregular profiles.

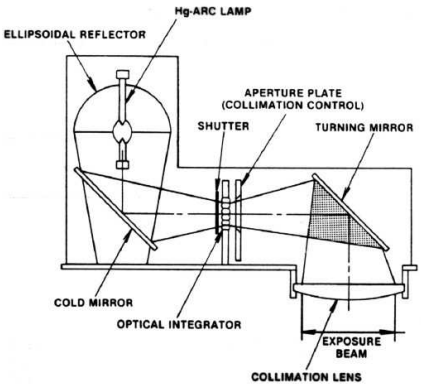

Figure 2.7: Optical part of the mask aligner. The light produced by the arc lamp is collimated by the optical elements in order to have a plane wave beam perpendicular to the mask and sample

Development

The development is done by soaking the exposed resist in a developer solution, that is designed on purpose for the kind of resist. The developer melts the soluble fraction of the fotoresist. The development time has to be carefully calibrated. Excessive development would damage also the residual non-soluble resist.
After the development a second baking, post exposure baking, is performed on the samples. The post exposure baking hardens the resist for the successive steps of fabrication (such as etching), removes the residual solvent and improve the quality of the profiles. Indeed, in the exposition, standing waves, formed between the resist and the film surface, can give a rippled profile of the edges that is reduced by post exposure baking.

Resolution

The resolution that is possible to attain by optical lithography is determined by the diffraction of light. We define the resolution in the following way: we consider a grating of equal lines of width b and separated by a distance b, and the maximum resolution correspond to the minimum value of b for which is possible to reproduce the grating pattern.
In the case of contact lithography, the mask-film pattern is very small, then the diffraction is described by the Fresnel pattern reported in figure 2.8. The minimum resoluble grating step, $2b_{min}$ is given by:

$$2b_{min} = 3\left[\lambda\left(S + \frac{d}{2}\right)\right]; \tag{2.2}$$

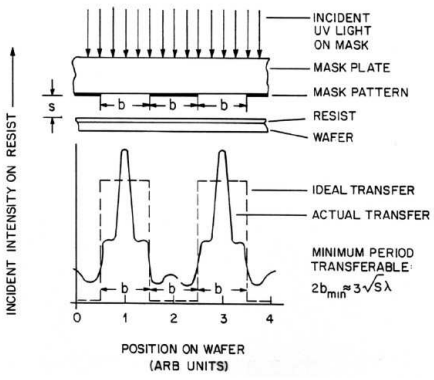

Figure 2.8: Real pattern transfer by Fresnel diffraction of a grating of equal lines of step 2b. The mask-resist distance is S, the resist thickness is d.

where λ is the light wavelength, S is the mask-resist distance, d is the resist thickness (as illustrated in figure 2.8). In case of true contact $S = 0$. The resolution is higher for smaller wavelength and for thinner resist.
Nevertheless it is not possible to reduce the resist thickness below a certain limit, because the resist layer has to protect the sample in the successive machining steps, and because it is more likely to have an inhomogeneous layer at lower thickness. Even if in principle it is possible to achieve a higher resolution by smaller wavelength, this cannot be reduced to any value, because the resist sensitivity is λ dependent, and it steeply decreases at small wavelengths.
For example, for a 405 nm wavelength, a resist layer of 0.5 um (very thin) and ideal contact, the limiting resolution is 0.48 nm. In practice it is impossible to achieve ideal contact, because of particulates and non homogeneous resist.

Mask

Lithographic masks are fabricated with flat transparent supports, such as glass or quartz, and a pattern is reproduced on one side, that will be in contact with the photoresist during exposition. There are two kinds of masks: photographic masks and metallic film mask.
Photographic mask are covered with a thin film of photographic emulsion, where the pattern is exposed by projection (and reduced to the desired size) or drawn by an electron beam. Metallic film masks are covered on the contact side by a thin metal film, usually chromium, because of its chemical stability and adhesion.
An important parameter for a mask is the optical density D, i.e.:

$$D = \log_{10}\left(\frac{I_0}{I_t}\right), \tag{2.3}$$

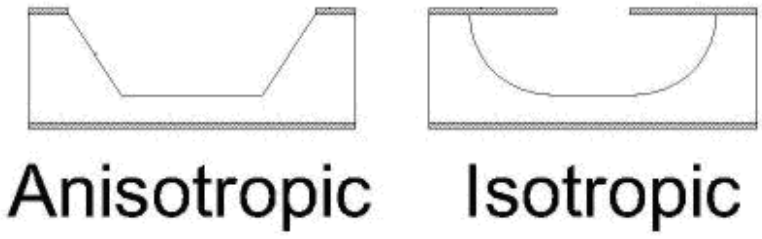

Figure 2.9: Pattern profiles obtained by anisotropic and isotropic etching. Because of the isotropic etching, usually the thinnest line that can be obtained by wet etching techniques, cannot be thinner than twice the thickness of the film.

where I_0 is the incident intensity and I_t the transmitted one. The optical density must be high in the dark zones and low in the clear ones, furthermore the transition region between dark and light zone has to be very small. Metallic film masks have higher optical density compared to photographic masks. Usually the formers are obtained by the latter by contact lithography. There is no gain in resolution, but the transition region can be reduced from the photographic to the metallic film mask by operating with care.
Metallic film masks are also more resistant to wearing compared to the photographic masks, whose emulsion layer can be easily damaged.

Etching

The etching can be performed by chemical or physical methods.
Chemical methods use chemical reaction to decompose the material. Thanks to their nature they are selective methods, i.e. they can be used to etch only a particular material. Among chemical methods wet and dry etching techniques can be distinguished. Wet etching uses liquid solution of etchant (usually an acid or a salt) and a solvent, usually water. On the contrary dry chemical etching uses a ion bombardment by reactive gas (as in RIE: reactive ion etching, that uses low energy RF sputtering in reactive atmosphere).
Physical methods use ion bombardment from non reactive gas, for example ion etching (or ion milling, a physical method used in this work) that uses a beam of neutralized accelerated argon ions, or sputtering.
An important difference between wet and dry etching is the resulting profile of the pattern. Indeed wet etching, excepting some special cases, is isotropic, i.e. the material is etched with the same speed in all directions. The resulting profile is represented in figure 2.9, that shows that part of the material below the protective resist is also removed (underetching). The size of the pattern elements is also reduced. Wet etching is then not suitable to define very precise width lines or deep holes and trenches.

Dry etching uses directional ion bombardment, and especially the physical methods are highly anisotropic. RIE combines chemical etching and sputtering, then the etching is not completely anisotropic; the etch conditions depends on different parameters, such as pressure, concentration of the reactive ions and RF power.

2.2.2 High Resolution Ion Beam Coater

The system used for metallic contact and insulator deposition is a high resolution ion beam coater produced by Gatan Inc. This system produces continuous, ultra thin, amorphous coatings free of thermal artifacts. This is an important advantage over traditional coating techniques such as thermal evaporation, magnetron or RF sputtering that produces coarse deposition structures. The ion sources are two Penning ion guns with miniature rare earth magnets, that produce high sputtering rates. A third Penning ion gun is directed towards the sample, for etching and cleaning. The ion beam energy varies from 1 to 10 kV, with a maximum current density of 10mA/cm2 and a diameter of about 1 mm. The feeding gas is argon (also iodine gas can be used for reactive etching).
The ion beam is directed on the target material, that is evaporated and deposited on the sample. The system allows to mount four target on two target holder, so that multiple layer deposition can be performed without breaking the vacuum. The deposition rate is approximately 0.5 Å/sec for Carbon and 1.5 Å /sec for Chromium at 10.0keV (very high). An oscillating quartz thickness monitor is used to measure the deposited thickness and the deposition rate.
The sample is introduced by a load-lock system, that allows to charge the samples without exposing the system to the atmosphere. The sample can be continuously rotated during the deposition (10-60 rpm), it can be tilted (0°- 90°) and rocked with variable speed (5°/sec - 36°/sec). The coating is uniform up to 1 inch of diameter.

2.2.3 Ion etching system

The ion etching (ion milling) system is composed by a vacuum chamber equipped with a ion beam source and a mass spectrometer. The ion beam source uses Ar to provide the neutral ion beam to etch the sample and the mass spectrometer is used to control the etching process. The sample is mounted on a rotating holder tilted of 45° respect to the incident ion beam, and the mass spectrometer is again at 45° respect to the sample normal. A sketch of the system is reported in figure 2.11. The ion source is represented schematically in figure 2.12. The principle of operation is the

Figure 2.10: A high resolution ion beam coater system like the one used in Caen. The two sputtering ion sources are the yellow cylinders at the sides of the deposition chamber, while the etching gun is the one on top.

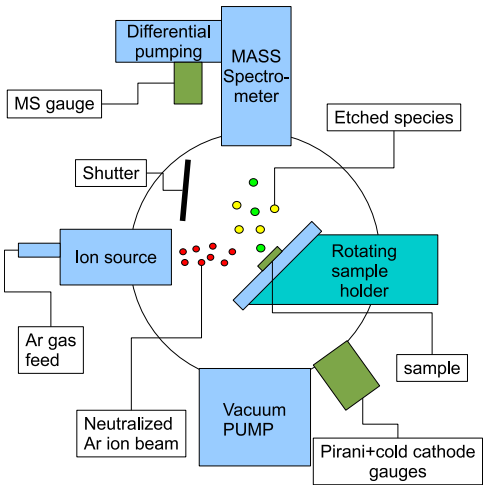

Figure 2.11: Schematic diagram of the ion etching system used in this work. The vacuum chamber pumping is provided by a turbomolecular secondary and a rotative primary pump. Mass spectrometer operation needs higher vacuum respect to the chamber one (2×10^{-4} mbar during etching). The differential pumping is provided by a turbomolecular+membrane pumps. The vacuum is monitored by gauges connected to the main chamber and the mass spectrometer. A gate valve separates the pumping station from the chamber, and an air inlet is used for venting (not represented). The rotating sample holder is water cooled during operation to prevent overheating of the sample.

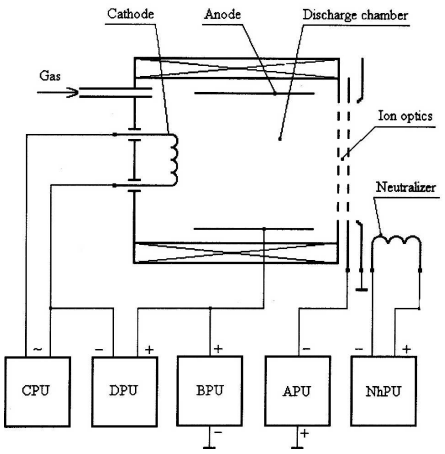

Figure 2.12: Diagram of the ion source. It consist of a filament cathode, a discharge chamber, an ion optics and a cathode neutralizer. The discharge chamber contains a frame, anode and a magnet system. The ion optics includes a screen and an accelerator grid. CPU = cathode power unit, DPU = discharge power unit, BPU = beam power unit, APU = accelerator power unit, NhPU = neutralizer heating power unit.

following. Inert gas (Ar) is fed to the discharge chamber, voltage is applied to the cathode filament and between cathode and anode (by the discharge power unit in figure 2.12). With suitable voltage and low gas pressure, the discharge appears: electrons emitted by the cathode and proceeding in the magnetic field ionize the gas and finally come to the anode. Ion from plasma fall down on walls in the discharge chamber and in holes of the screen grids of the ion optics. By applying a positive potential to the beam power unit (see figure 2.12) and a negative potential to the accelerator grid, the ions are accelerated passing through the holes in grids. The neutralizer filament is immersed in the ion beam, and is fed by current to emit electrons by thermionic emission, thus neutralizing the ion beam space charge. The specific values of power unit voltage and current depend by the system and by the desired beam energy. In our case the etching was performed by adopting the same beam conditions. The beam energy is fixed by the beam power unit voltage equal to 600 V, while the beam current is about 7-8 mA.

When the beam result stable, the shutter is open and the argon ions impinge on and etch the sample, that is kept in continuous rotation to provide uniform etching. The etched species are collected by the mass spectrometer, that is kept at lower pressure than the main chamber.

The mass spectrometer (MS) is an instrument that measures the mass-to-charge ratio of charged particles. It is widely used for several purposes such as determining masses of particles, for determining the elemental composition of a sample or molecule, and for elucidating the chemical structures

of molecules. The MS principle consists of ionizing chemical compounds to generate charged molecules or molecule fragments and measurement of their mass-to-charge ratios. In our case the molecules are provided by the sample that is etched by the argon ion beam. The MS is provided by a quantitative detector, that measures the signal from ions having a determined mass-to-charge ratio. It can either scan over a mass range or detect the signal from a particular mass value. During the ion etching, the MS is set to follow the signal of some species that allow to discriminate the layer of material that is being etched.
However not all elements can be detected: the average signal decreases with ion mass, so that in our system, the heaviest ion that can be detected is Sr. Furthermore Fe, Ni, Cu and Al cannot be followed because they are present in the chamber and in the sample holder, so that ions coming from the sample cannot be distinguished.
In our case the pattern to etch in the sample is masked by a resist layer. In the condition used in this work the resist layer (nominally 1.3 μm) is completely etched in 40'. Furthermore the ion bombardment can heat the sample, and degrade the resist, making the removal impossible or very difficult. To avoid sample overheating the sample holder is cooled by water flux.

2.3 Characterization techniques

2.3.1 X-ray diffraction technique for thin film characterization.

X-ray diffraction (XRD) is a powerful tool to investigate the crystalline structure of materials, thanks to the X-ray wavelength, that is the same order of magnitude of the interatomic distance in crystals.
Several different set up are used, depending on the type of samples under investigation (powders, polycrystals, single crystals, thin films), using monochromatic or polychromatic radiation, point detectors, photographic films. In this section I will describe the commonly used X-ray technique for thin film characterization.

XRD kinematical theory.

The X-ray interact with the atoms composing a crystal through electron-photon scattering. In the kinematical theory the Thompson scattering of the incident photons with the crystal electrons is considered; the scattered photons from different ions of the crystal interfere. Consider an ideal crystal of dimension N_1a, N_2b and N_3c in the direction of the primitive lattice vectors $\mathbf{a}$, $\mathbf{b}$, $\mathbf{c}$ and a radiation with incident wave vector $\mathbf{k_0}$ and scattered $\mathbf{k}$; the diffracted intensity is:

$$I \propto |F(\mathbf{Q},\lambda)|^2 \frac{\sin^2(N_1\mathbf{Q}\cdot\mathbf{a}/2)}{\sin^2(\mathbf{Q}\cdot\mathbf{a}/2)} \cdot \frac{\sin^2(N_2\mathbf{Q}\cdot\mathbf{b}/2)}{\sin^2(\mathbf{Q}\cdot\mathbf{b}/2)} \cdot \frac{\sin^2(N_3\mathbf{Q}\cdot\mathbf{c}/2)}{\sin^2(\mathbf{Q}\cdot\mathbf{c}/2)}; \quad (2.4)$$

Where $\mathbf{Q} = \mathbf{k} - \mathbf{k_0}$ and $F(\mathbf{Q},\lambda)$ is the structure factor, that depends from the wavelength λ, and contains the contribution from the atomic form factors (scattering from the electrons of each atom in an unit cell) and from the position of any atom in the unit cell.
In this approximation the scattered intensity is a Fraunhofer pattern modulated by the structure factor. Intensity maxima are given by the conditions: $\mathbf{Q}\cdot\mathbf{a} = 2h\pi$; $\mathbf{Q}\cdot\mathbf{b} = 2k\pi$; $\mathbf{Q}\cdot\mathbf{c} = 2l\pi$, with h,k,l integers. This is the Laue condition for constructive interference, that states that constructive interference is given when the difference among the scattered and incident vector $\mathbf{Q} = \mathbf{k} - \mathbf{k_0}$ equals a reciprocal lattice vector $\mathbf{K}$ (defined by the condition $\mathbf{K}\cdot\mathbf{R} = 2n\pi$, where $\mathbf{R}$ is any crystal lattice vector, $\mathbf{R} = n_1\mathbf{a} + n_2\mathbf{b} + n_3\mathbf{c}$). Laue condition for constructive interference is equivalent to Bragg formula, more commonly used. In this formulation we consider the crystal as composed by parallel plans of ions, separated by a distance d. If we imagine that the X-ray are reflected by the planes, constructive interference of the beam reflected by successive plans is given when the optical path difference is an integer number of λ:

$$n\lambda = 2d\sin\theta, \quad (2.5)$$

where n is the order of reflection and θ is the incidence angle of radiation on the considered family of planes.
Knowing λ and θ, the plane distance d can be obtained. As a crystal can be divided in planes in infinite ways, infinite reflections are possible; in practice only a finite number of reflections is accessible to measurement, depending by the radiation wavelength and by the measurement setup.

Configuration for thin film measurements

For the study of thin films the Bragg configuration is used. In this configuration monochromatic radiation is used and the incident and diffracted beam are on the same side of the sample (no transmission). The incident beam is collimated by narrow slits to hit the sample surface with a precise angle ω. A detector, also provided with slits of different width, measures the reflected intensity from the surface of the sample at angle 2θ respect to the incident beam direction. In the simple case of a two circle diffractometer, these are the only degrees of freedom. In a three circle diffractometer the sample can be rotated along an axis perpendicular to its surface; the rotation angle is identified as ϕ. A four circle diffractometer allows to tilt the sample by an angle ψ around the axis in the sample plane belonging to the incidence plane of the radiation. There are also five and six circle diffractometers, that are used for grazing angle and surface diffraction. In our case a three circle (at the university of Naples and at the CRISMAT laboratory of Caen) and a four circle diffractometer (at the TASC laboratory of Trieste) have been used for the characterization of our samples.

$\theta - 2\theta$ scan

To perform this scan, the incidence angle ω is set to θ. In this case the scattering vector $\mathbf{Q}$ is perpendicular to the sample surface, or analogously we are looking for the specular reflection of the crystalline planes parallel to the sample surface. If the film is single oriented, we can only determine the measure of the lattice parameter perpendicular to the surface. If the crystal planes are well aligned along all the sample thickness, interference fringes reproducing the intensity profile 2.4 are detectable. The thickness of the sample t can be estimated by the position of the relative maxima:

$$t = \frac{(i-j)\lambda}{2(\sin\theta_i - \sin\theta_j)} \tag{2.6}$$

where i and j are the order of the maxima, and θ_i, θ_j the maximum position.

Rocking curve: ω-scan

This kind of measurement is performed by fixing the 2θ angle in correspondence of a reflection of the film, and then scanning the ω around the incidence angle θ for the reflection. This measurement requires alignment of the sample in order to assure that ω is the true incidence angle of radiation on the sample surface. To this aim an alignment procedure is usually performed on a substrate peak, as the lattice parameter and the quality of the substrate crystal are well known.
Scanning ω, a peak, centred at the ω value where the constructive interference condition is fulfilled, is obtained. For example, if the film planes are tilted respect to the sample surface, the peak would be centred around $\omega \neq \theta$.
An important parameter for thin film characterization is the width of the rocking curve. In case of a single, flat crystal, the width of the peak is determined by the instrumental resolution only; on the contrary, if there is some spread of the cell orientations, interference can take place also for some range of ω, leading to an enlargement of the peak respect to the ideal case. The resulting curve is called the rocking curve. The width of the rocking curve is identified by the full width half maximum FWHM, that is usually compared with the substrate one.

Texture measurement: ϕ-scan

This kind of measurement allows to verify the film epitaxy. This kind of information cannot be obtained by the only $\theta - 2\theta$ scan. Indeed, even if the film displays a single orientation in the direction perpendicular to the plane, in-plane axes can be randomly oriented in plane. It is then necessary to assure that they are coherently oriented respect to the substrate axes.
This kind of measurement is performed by individuating a particular family of planes intercepting one of the in-plane lattice parameter, finding the peak maximum and then rotating the sample around the normal to plane, i.e. scanning the ϕ angle. If the sample has cubic or tetragonal symmetry, by rotating the sample, four peaks will be found each 90° due to the four-fold symmetry of the structure. This is possible only if most of the cells are oriented in the plane; some variation of the in-plane orientation, would lead to a broadening of the peaks. Depending on the cell symmetry, we can have four peaks separated by 90° for cubic or tetragonal symmetry, four peaks at angles different from 90° for trigonal structures, two peaks at 180° for orthorhombic structures...

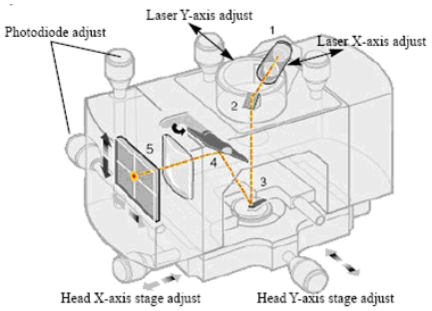

Figure 2.13: SPM head of the Veeco multimode SPM equipment used in Caen. Major components are: laser (1);mirror (2); cantilever (3); tilt mirror (4); photodetector (5).

Reciprocal space maps

Reciprocal space maps are two axes measurements $(2\theta, \omega)$. This kind of measurements are usually used in non symmetric configuration ($\omega \neq 2\theta/2$) to determine the in-plane lattice parameter of the films. It usually requires a careful alignment around the substrate peak close to the film reflection, ϕ (and sometimes ψ) alignment to match the reflection are usually required.

2.3.2 Tapping mode atomic force microscopy

Atomic force microscopy (AFM) or scanning force microscopy (SFM) is a very high-resolution type of scanning probe microscopy, with demonstrated resolution on the order of fractions of a nanometer in the vertical direction.

The AFM consists of a cantilever with a sharp tip (probe) at its end that is used to scan the specimen surface. The cantilever is typically silicon or silicon nitride with a tip radius of curvature on the order of nanometers. When the tip is brought into proximity of a sample surface, forces between the tip and the sample lead to a deflection of the cantilever according to Hooke's law. Depending on the situation, forces that are measured in AFM include mechanical contact force, van der Waals forces, capillary forces, chemical bonding, electrostatic forces, magnetic forces... The sample surface is scanned by the probe using piezoelectric actuators that allow very precise tiny movements.

Typically, the tip deflection is measured using a laser spot reflected from the top surface of the cantilever into an array of photodiodes. A feedback mechanism acting on the vertical movement of the tip is used to keep the deflection or the oscillation amplitude of the tip (depending on the measurement mode) constant, thus keeping the tip-sample distance at fixed height. The tip vertical displacement z is then registered as a function of the horizontal coordinates x and y, thus giving a topography of the sample.

The AFM can be performed in contact mode, non-contact mode and tap-

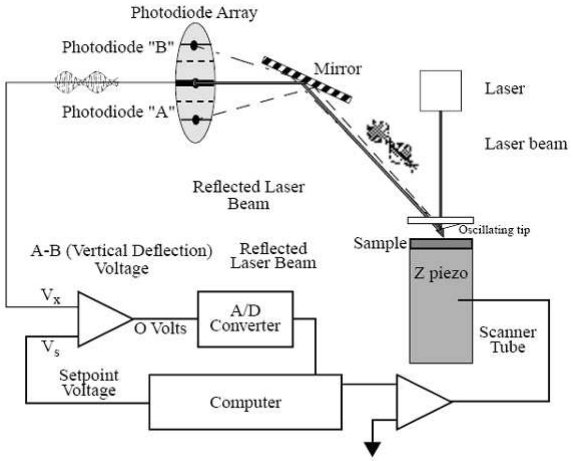

Figure 2.14: Operation of tapping mode AFM. The RMS value of the photodiodes (A-B) oscillating voltage is measured and compared to the setpoint voltage. The difference between the two voltages is converted in vertical movement of the Z piezo by the PID parameters, and the sample-tip distance is kept constant.

ping mode.
In contact mode the tip is static and in contact with the sample (i.e. feeling the repulsive forces). The vertical and horizontal deflection of the tip are measured,and the vertical deflection is kept constant.This technique can often damage the sample surface.
In non-contact mode, the tip of the cantilever does not contact the sample surface. The cantilever is instead oscillated at a frequency slightly above its resonance frequency where the amplitude of oscillation is typically a few nanometers ($< 10nm$). The van der Waals forces, which are strongest from 1 nm to 10 nm above the surface, or any other long range force which extends above the surface acts to decrease the resonance frequency of the cantilever. This decrease in resonance frequency combined with the feedback loop system maintains a constant oscillation amplitude or frequency by adjusting the average tip-to-sample distance. Measuring the tip-to-sample distance at each (x,y) data point allows the scanning software to construct a topographic image of the sample surface. In this case the sample is not degraded by the tip, but this technique is not suitable in ambient conditions as a liquid meniscus usually forms between the tip and the sample, making difficult to avoid the tip sticking on sample.

In ambient conditions (as in our case) tapping mode AFM is more suitable. In this technique the tip-sample contact is intermittent. In tapping mode, the cantilever is driven to oscillate up and down at near its resonance frequency by a small piezoelectric element mounted in the AFM tip holder similar to non-contact mode. However, the amplitude of this oscillation is

greater than 10 nm, typically 100 to 200 nm. Due to the interaction of forces acting on the cantilever when the tip comes close to the surface, Van der Waals force, dipole-dipole interaction, electrostatic forces, etc. cause the amplitude of this oscillation to decrease as the tip gets closer to the sample. This method of "tapping" lessens the damage done to the surface and the tip compared to the amount done in contact mode.
An important parameter to characterize the surface of thin films is the roughness. The rms (root mean square) roughness is the standard deviation of the Z values in a given area. For atomically flat surfaces, a roughness value of the order of the out-of-plane lattice parameter is expected.

2.3.3 Electric polarization measurements

As described in the beginning of the chapter, the electric polarization is the vector field that expresses the density of permanent or induced dipole moments in a dielectric material.
The bound charge density in a dielectric is given by:

$$\rho_b = -\nabla \cdot \mathbf{P}. \tag{2.7}$$

At the surface of the polarized material, the bound charge appears as a surface charge density:

$$\sigma_b = \mathbf{P} \cdot \hat{n}_{out}, \tag{2.8}$$

where $\hat{n}_{out}$ is the normal unit vector of the given surface. For constant polarization, the surface charge density is the only bound charge. In ferroelectrics, a static dipole moment is present, thus resulting in a static bound charge at the sample surface, that is usually compensated by a free charge density. However in ferroelectric materials the polarization can be reversed by the application of electric field, and in the switching process the polarization difference between the two states can be measured.
The Sawyer-Tower (S-T) circuit is the simplest circuit to measure ferroelectric hysteresis loops. In figure 2.15 the simplest implementation of the S-T circuit is represented. The ferroelectric material is between the armatures of a capacitor, and voltage is cycled by the signal generator. Its direction is reversed at high frequency, and the voltage across the reference capacitor is measured. The charge on the reference capacitor must be the same as the charge over the ferroelectric capacitor, as they are in series. This means the charge on the ferroelectric can be found by:

$$Q = C_{ref} \times V \tag{2.9}$$

where C_{ref} is the capacitance of the reference capacitor, and V is the voltage measured over this capacitor. Then the P is proportional to the charge Q by the ferroelectric capacitor area. We can therefore represent the polarisation of a material in an oscillating electric field, by plotting the voltage applied

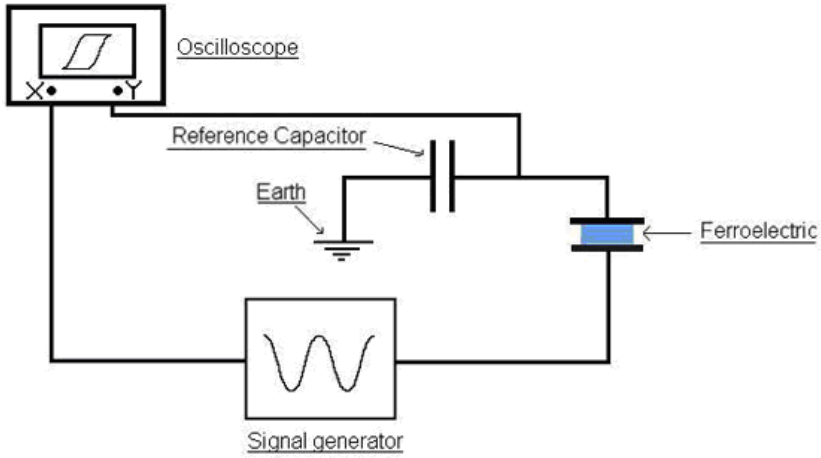

Figure 2.15: simple S-T circuit for polarization loop measurements.

to the material on the x-axis of the oscilloscope, and the surface charge on the y-axis. The capacitance of the reference capacitor must be much higher than the capacitance of the ferroelectric, so that most of the voltage lies over the ferroelectric.

However in this simple circuit there is no mean to take into account losses across the ferroelectric or the linear capacitance contribution of the ferroelectric capacitor. To take into account these phenomena, several modification on the S-T circuit have been performed, as reported by Ornelas-Arciniega et al. [78], or different circuits such as the Diamond-Drenk-Pepinski circuit (figure 2.16).

In this work a Radiant Technologies Precision Materials Analyzer has been used. The hysteresis loop measurement is performed by the instrument by applying a waveform as the one represented in figure 3. The waveform begins at 0.0 volts and steps to a maximum value of the assigned voltage. It then proceeds to step to the negative of the assigned maximum. Finally it steps back to zero volts. At each voltage step, the current induced in the sample by the voltage step is integrated and the integral value is captured and converted into Polarization ($\mu C/cm^2$) by:

$$\frac{\mu C}{cm^2} = \frac{Q}{Area} = \frac{CV}{Area} = \frac{IntegratorVolts \times SenseCapacitor}{Area}. \qquad (2.10)$$

The standard duration of the waveform is 1 ms. The short duration of the measurement reduces the influence of loss current that would be integrated and summed to the total charge.

The instrument also performs leakage and I(V) measurements, that allow to determine the resistive contribution to the measured hysteresis loops and to correct it.

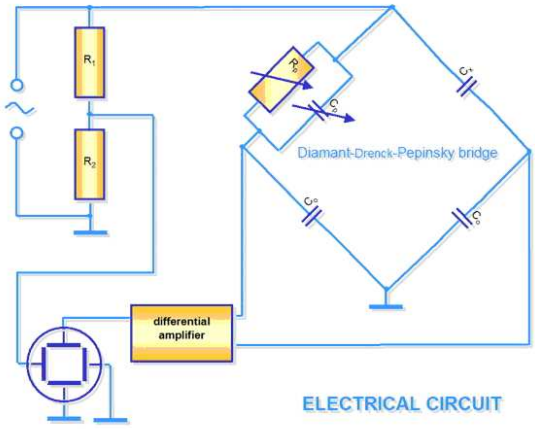

Figure 2.16: Diamant-Drenk-Pepinsky bridge. The ferroelectric sample is the capacitor C_x. The variable resistor and capacitor are used to compensate the resistive losses and the linear capacitance contribution. The reference capacitors are indicated by C_0.

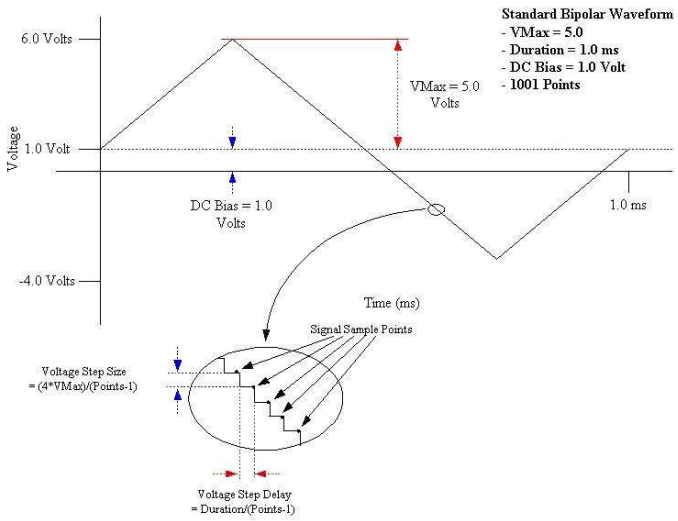

Figure 2.17: Excitation waveform used in the Radiant Technologies Precision Materials Analyzer P-loop measurement. The description of the parameters that can be set for the measurement is reported. In the enlargement, the sampling points are indicated by arrows.

However high value of the leakage current, not only can mask the polarization switching, making impossible its detection, but it also prevents to apply high enough voltage to switch the ferroelectric domains, as the instrument power limit can be overcome because of the flowing current, or the sample itself can be damaged by the excessive power dissipation.
Another inconvenient we can incur during polarization loop measurement is the electrical breakdown of the ferroelectric sample, when applying an elevate voltage. The breakdown can permanently change the insulating properties of the material, thus preventing further measurements.

Chapter 3

Results

In the first part of this chapter we will present the results on the fabrication of CPP and field effect devices.
Our interest in these devices resides in the applicability of such devices in the transport characterization of $LaMnO_3$ based thin films and heterostructures.
In particular the CPP measurements would allow to probe the transport across the interfaces in the LMO/SMO superlattices described in section §1.2.4.
However to this aim the superlattice has to be grown on a conductive base electrode or at least on a conductive substrate. The base electrode has to be a compatible material with the film and present a smooth surface to allow epitaxial growth of low roughness interfaces.
In the beginning of the chapter we report on the growth and optimization of $SrRuO_3$ thin films for application as base electrode of oxide thin films and heterostructures.
In this work the $SrRuO_3$ has been used, for example, as base electrode for $BaTiO_3$ thin films, whose growth is also described.
The field effect, as explained in section §1.4, can be used on manganites in order to tune the carrier density. However the electric fields penetrates in the metallic phase only for few unit cells, while large field effect is observed in phase separated manganites, where the electric field can penetrate in the insulating regions and change their metallicity.
In the following we will discuss on LSMO channel field effect devices, where ultrathin films have been employed. However we can consider the perspective of the study of the field effect on superlattices, where the metallic phase can reduce to a few unit cell interface.
Ferroelectric oxides can e employed in field effect devices in order to exploit the high dielectric constant values and the memory effect of these materials. To test the ferroelectric properties of our $BiFeO_3$ and $BaTiO_3$ thin films, the CPP geometry has been used. This also allows to test the applicability

of this geometry for polarization measurements.
In the second part of the chapter the magnetic and orbital properties of LMO/SMO multilayers and of non-stoichiometric LMO thin films will be investigated. This issue will be mainly treated with a completely different approach, i.e. by spectroscopic techniques. In particular two X-ray absorption spectroscopy experiments were performed by synchrotron radiation at the European synchrotron radiation facility. The technique employed, soft X-ray absorption spectroscopy by polarized light, allows to gain unaccessible information with other (non spectroscopic) techniques (as described in §3.6.1-§3.6.3).
Our data allow to complete the picture of magnetic order and orbital ordering tuned by the electronic reconstruction at LMO/SMO interfaces.
For the non-stoichiometric LMO films, the information obtained by transport and magnetization measurements is completed by the XAS measurements, so that the mechanisms at work in these self-doped compounds can be enlightened.

3.1 Growth and optimization of $SrRuO_3$ thin films for base electrode applications

3.1.1 $SrRuO_3$ deposition

The SRO thin films have been deposited on 5 mm x 10 mm x 1 mm SrTiO3 (001) untreated exact substrates. The deposition was carried in an oxygen pressure ranging from 0.1 and 0.5 mbar, at temperatures between 700 and 740°C. The target-substrate distance was fixed at 50 mm. The substrate was brought to the deposition temperature by a ramp rate of 15°C/min; after the deposition, an oxygen pressure of 700 mbar was introduced in the chamber, and the sample was cooled at the rate of 10°C/min. The laser energy ranged from 150 to 200 mJ, with a frequency between 1 and 3 Hz.
The samples were measured by X-ray diffraction to determine the crystalline orientation and the SRO lattice parameter; by tapping mode AFM to study the surface and the growth mode; and by electrical transport measurement in liquid nitrogen to measure the R(T) curve in the temperature range [77, 300] K.
The AFM characterization of the growth mode and of the surface roughness is very important in view of applications as a base electrode. Indeed, to promote the ordered epitaxial growth of other layers, it is important to produce base electrodes with smooth surfaces. The lower limit of roughness is to reach a value of the order of the out-of-plane lattice parameter, indicating we have only one unit cell steps. This is only possible if we can achieve a layer by layer or a step flow 2D growth, and, in our experimental condition it has not been possible to reach this limit, most probably because of the

use of non-vicinal and non-single terminated substrates.

3.1.2 $SrRuO_3$ thin films

The best films in terms of low roughness are obtained in the following conditions:

- T = 730°C
- P_{O2} = 0.2 mbar
- Laser energy: EGY = 170 mJ
- Pulse frequency: f = 2 Hz
- Cooling in 700 mbar O_2 at -10°C/min

The characteristics of these films are the following:

- Thickness: 23 nm for 1500 shots
- Roughness: 0.84 nm
- Lattice parameter: d_{110}: 3.955 Å

The aim, in optimizing the deposition, was to minimize the surface roughness and have an homogeneous and ordered crystal. Then the transport properties of the samples were studied, to check the metallic conduction, the resistivity and the absence of any transport anisotropy.
We can divide our samples in two series. The second series was produced after a cleaning of the chamber and of the optical window, that resulted in an increased rate of deposition. So the first series is a "low rate" one, while the second is an "high rate" one.

First series of samples

In the first series of samples, the temperature and pressure were varied, while keeping the laser energy and frequency fixed at 200 mJ, 3Hz. The sample thickness could be calculated in most of the samples by the size effect oscillations in the XRD symmetric $\theta - 2\theta$ scans. Nevertheless, in some samples, because of large thickness or because of structural disorder, the size effect oscillations could not be observed.
In the first series of samples, the temperature and pressure were varied, while keeping the laser energy and frequency fixed at 200 mJ, 3Hz. The sample thickness could be calculated in most of the samples by the size effect oscillations in the XRD symmetric $\theta - 2\theta$ scans. Nevertheless, in some samples, because of large thickness or because of structural disorder, the size effect

Sample	T(°C)	P(mbar)	EGY(mJ)	f (Hz)	Shots
G365[1]	700	0.35	200	3	2000
G393[1]	720	0.20	200	3	2000
G394[1]	720	0.50	200	3	2000
G396	720	0.10	200	3	2000
G398	720	0.20	180	3	2000
G405	720	0.10	200	3	2000
G406	720	0.20	200	3	2000
G410	720	0.10	170	2	2000
G416	730	0.20	170	2	1500

Table 3.1: Deposition parameters of all the samples described in the text. The first series samples are identified by the superscript 1.

Sample	Thick.(nm)	der.peak(K)	*c*-axis(Å)	Rock.c.(°)	Rough.(nm)
G365[1]	-	152.5	3.932	-	5.5
G393[1]	26.8	133	3.957	0.29	0.75
G394[1]	30.0	136	3.956	-	1.2
G396	57.8	127	3.963	0.34	-
G398	38.8	133	3.956	-	-
G405	55.5	126	3.963	0.31	1.4
G406	35.9	139.3	3.950	0.29	1.5
G410	45.1	143.7	3.952	-	1.8
G416	22.9	133	3.955	-	0.84

Table 3.2: Properties of the samples whose deposition parameter are reported in table 3.1. In particular "der.p." stands for the position of the dR/dT peak,"*c*-axis" stands for the out of plane lattice parameter and "Rock.c." stands for the full width half maximum of the rocking curve.

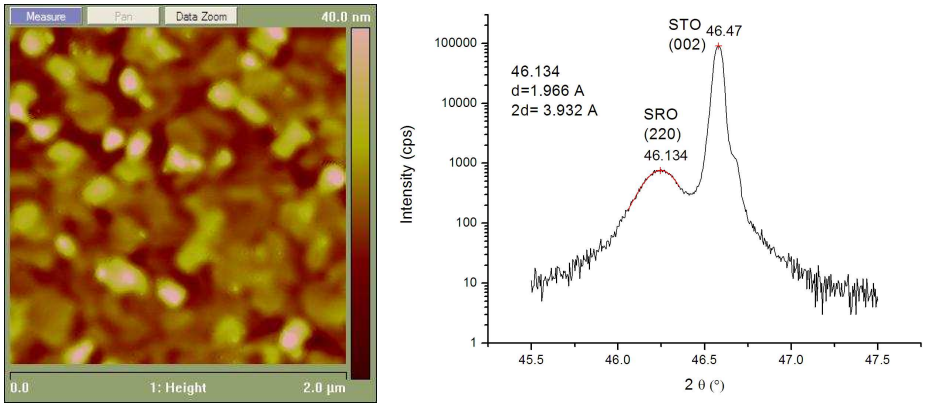

Figure 3.1: Left: AFM topography image of the sample G365, showing 45° oriented grains respect to the substrate [100]-[010] directions, having the size of the order of 100 nm. Right: XRD scan around the (002) STO peak, no size-effect oscillations are detectable.

oscillations could not be observed.
For example, sample G365, grown at T=700°C, P=0.35 mbar, shows a relaxed bulk-like out-of-plane lattice parameter of 3.932 $\AA$, no size-effect oscillations and an high roughness (5.5 nm rms). An AFM topography image, showing rectangular grains oriented at 45° respect to the substrate [100]-[010] directions, is reported in the left panel of figure 3.1. The best sample of the low-rate series is the sample G393, deposited in the following conditions:

- T = 720°C
- P_{O2} = 0.2 mbar
- Laser energy: EGY = 200 mJ
- Pulse frequency: f = 3 Hz
- Shots: 2000
- Cooling in 700 mbar O_2 at -10°C/min

The AFM topography image shown in the left panel of figure 3.2, shows an ordered step-like pattern of the sample surface, while the rms roughness is 0.75 nm.

The step pattern indicates against a 2D step flow growth, because the height of the steps is much bigger than the unit cell height, as shown by a section in the direction perpendicular to the step shown in figure 3.3. The pattern most likely originates by the coalescence of finger-like islands nucleated along the substrate steps, as reported in ref. [80]. Indeed a measurement of the miscut angle of the substrate and of the film gives a value of

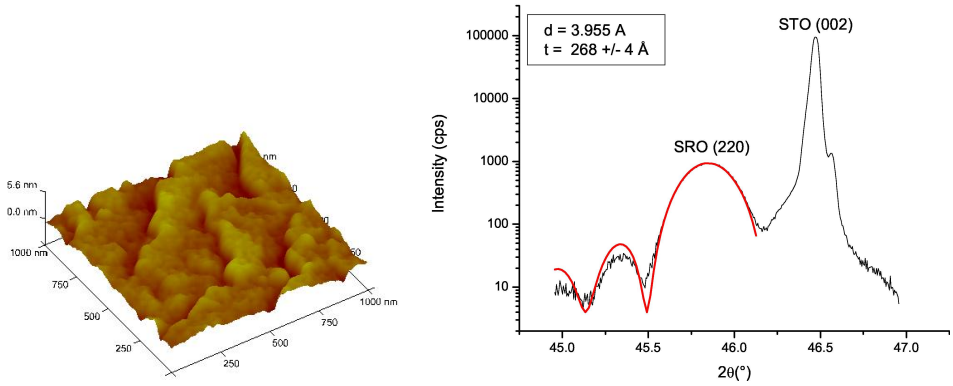

Figure 3.2: Left: AFM topography image, 3D view, of the sample G393. A step pattern is clearly visible in the 1um·1um image. Right: XRD symmetric scan around the STO (002) peak. The size-effect oscillations are clearly visible. A fitting of the data yields a thickness of about 27 nm.

$\alpha = 0.11$, indicating a small vicinality that may be the origin of the pattern.

By the thickness measurement, 27 nm, and by the number (2000) and frequency (3Hz) of the laser shots, we can obtain the deposition rate per shot, 0.15 Å/shot, and the deposition rate per second, 0.40 Å/s.

Second series of samples

In the second series of samples, the rate is higher with the same deposition conditions, probably because of the higher laser fluence reaching the target, thanks to the cleaning of the optical window. As a result the roughness of the samples also increases[30].

For example the G406 sample, deposited in the same condition as the G393 sample, but after the cleaning of the system, is thicker (see table 3.2). The deposition rate is increased from 0.40 Å/s to 0.54 Å/s (and the rate per shot is increased to 0.18 Å/shot). The out-of-plane lattice parameter $d_{(110)}$ is decreased from 3.955 Å for the G393 sample to 3.950 Å, implying the film structure is less strained. This structure relaxation may also originate by the larger thickness of the sample.

The rms roughness of the film is about 1.5 nm.

In this new condition, several trials were made in order to recover the low roughness of first series of samples, by reducing the oxygen pressure to 0.1 mbar, or the deposition rate by decreasing the laser energy or the pulse frequency; finally the deposition temperature was varied from 720°C to 730°C.

A common feature of all the samples is that, in the same growth conditions, thicker samples are smoother than thinner ones. This is counterintuitive for epitaxial growth, but it is in agreement with that of ref. [80, 79] indicating

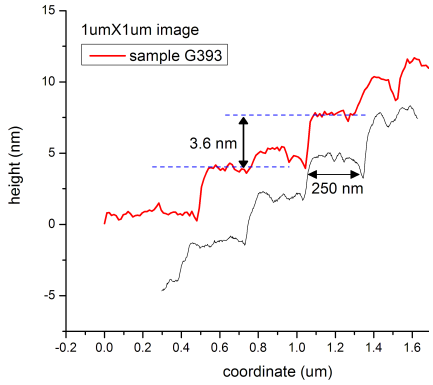

Figure 3.3: Height profile along a line perpendicular to the step pattern in the G393 sample. The step height is about 3 nm, i.e. 7-8 unit cells. A linear background has been subtracted from data.

that the growth mode of SRO is by nucleation and coalescence of 3D islands, as described in the previous sections.
The samples grown at 0.1 mbar have a higher growth rate with respect to their 0.2 mbar counterparts. The film microstructure is constituted by small islands, with roughness comparable or higher than the 0.2 mbar samples (see table 3.2). The out-of-plane lattice parameter of the 0.1 mbar samples strongly depends by the deposition rate. Indeed the high rate samples (as G405) have an elongated lattice parameter of (3.963 $\pm$ 0.002) Å, while the G410 sample has $d_{(110)}$=(3.952 $\pm$ 0.001) Å. The attempt to obtain smooth samples at 0.1 mbar by reducing the deposition rate failed, as the low rate sample has a higher roughness than the high rate sample, as shown in figure 6d. Instead, for the 0.2 mbar samples, G409 (170mJ, 2Hz) has lower roughness (1.2 nm) than the G406 (200mJ, 3Hz). Finally a low roughness was obtained by increasing the deposition temperature to 730°C (sample G416). Further attempts to reduce laser energy or frequency yielded much rougher samples: using 150mJ/ 3Hz, I obtained a roughness of 5.3 nm; using 170mJ/1Hz, I obtained a roughness of 7.25 nm. This last result also confirms that the important factor to quantify is the rate per second and not the rate per shot, as the rate per shot would be the same with the same energy.

3.1.3 Structural characterization of $SrRuO_3$ films by XRD

As shown in the previous section, all films were characterized by $\theta - 2\theta$ scans in order to determine the out of plane lattice parameter. The films are always showing a single crystalline orientation. Most of the samples show size effect oscillations, indicating that the crystalline planes are well aligned throughout the whole thickness of the film. For example, samples

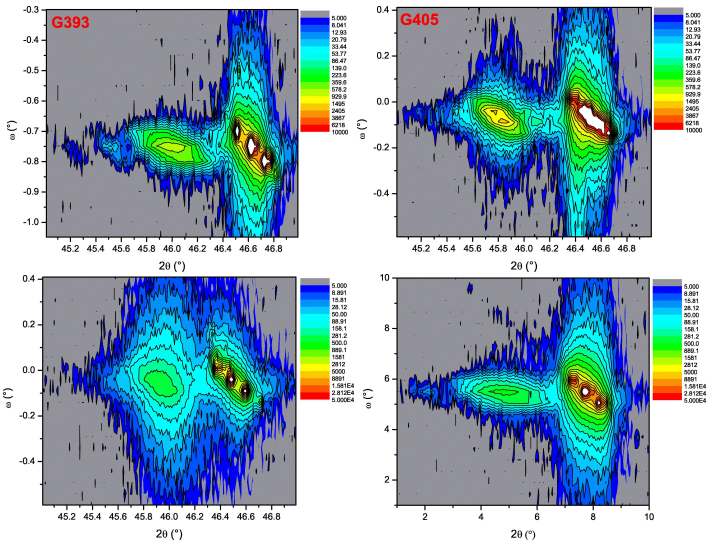

Figure 3.4: Reciprocal space maps around the (002) peak of STO, showing the (220) SRO peak (symmetrical reflection) for samples with different deposition conditions. The G393 and G416 samples are the optimized ones of first and second series respectively. The G405 and G410 samples are grown in 0.1 mbar O_2 with 200mJ/3Hz and 170mJ/2Hz respectively. The ω values, not ranging around zero, account for the misalignment of the sample in the instrument.

with high roughness value and bulk-like (relaxed) lattice parameter, such as the G365 (figure 3.1), do not show any oscillation, because of relaxation and loss of coherence of the crystalline structure during the growth. More information is provided by $(2\theta, \omega)$ reciprocal space maps in symmetrical and asymmetrical configuration.

The reciprocal space maps around the (002) reflection, in figure 3.4, give information on the out of plane lattice parameter, on the film-substrate alignment respect to the substrate c axis and on the film rocking curve width.

The G393 and G416 optimized samples have a narrow rocking curve compared to the other samples.

The samples grown at 0.1 mbar, G405 and G410, have very different characteristics depending from the laser fluence. The high fluence sample G405 has the largest lattice parameter (3.963 Å) among the series, and a rocking curve slightly larger than the optimized samples. On the contrary, the G410 lattice parameter is even smaller than the one of 0.2 mbar samples (3.954 Å), but the rocking curve is much wider, thus indicating a high degree of structural disorder in this sample.

The asymmetric scans have been performed around the (103) peak of the substrate. Because of the orthorhombic symmetry of the SRO cell, the (103) STO peak is close either to the (332) or to the (420) reflection of the film

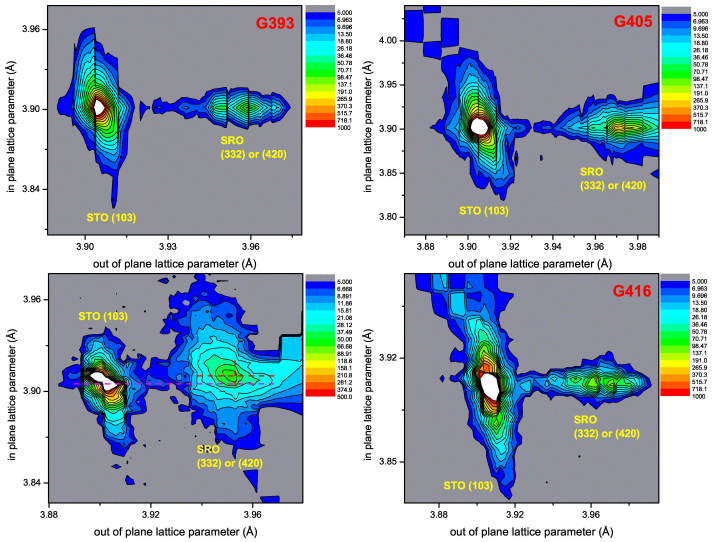

Figure 3.5: Reciprocal space maps around the (103) substrate peak of STO. The map has been converted to real space lattice spacing. For the G410 sample, the pink dashed line represents the substrate in-plane lattice parameter, and the red cross the position of the film peak. The film in-plane lattice parameter is not matching the one of STO.

(for (110) oriented SRO), depending on the in plane orientation of the SRO cell respect to the STO one [88]. With the asymmetric reflection, we can probe both the out of plane and the in plane lattice parameter. In figure 3.5, the asymmetric maps are reported; the coordinates have been converted to real space units.

The in plane lattice parameter of the samples is matching the substrate one for the samples G393, G405 and G416, whereas the sample G410 is partially relaxed, with an in plane lattice parameter of about 3.91 Å. This also explains the rocking curve width and the roughness of the surface for this sample, as the structure has lost coherence with the substrate and is evolving to bulk parameters and disordered growth.

3.1.4 Transport properties of $SrRuO_3$ thin films.

The transport properties of the samples have been investigated by performing resistance versus temperature, R(T), measurements in liquid nitrogen. The measurements have been performed in the GREYC laboratory by using four probe technique with in line contacts, and in Salerno by using the van der Pauw [**?**] technique to estimate the sample resistivity. As the van der Pauw technique requires to make measurements along the two sides of the sample, also the presence of transport anisotropy can be observed. In our

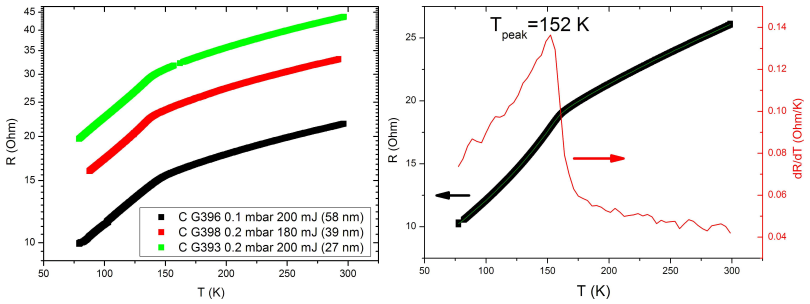

Figure 3.6: Left: R(T) curves of three samples deposited in different conditions, showing the characteristic knee at about 160 K. Right: R(T) and dR/dT curves of a relaxed sample (G365), showing the derivative peak in corrispondence of 152K, corresponding to the Curie temperature usually observed in thin films.

case, we did not observe any transport anisotropy, even in the sample with steps G393. We can argue that the cooling of the samples was fast enough to avoid the formation of metastable phases at the grain boundaries, as described in ref. [79], that may originate transport anisotropy in samples with oriented grain boundaries such as the G393.
The 77K resistivity of the lowest roughness samples G393 and G416 has been estimated to (0.14 ± 0.01) mOhm cm. The value is low if considered that the residual resistivity of single crystal samples is reported to be about 0.2 mOhm cm; we can argue that the van der Pauw technique underestimates the sheet resistance, or that the thickness obtained by size effect oscillations is underestimate.

It is interesting to look at the behaviour of the derivative dR(T)/dT, and correlate it to the structural information we have. For example, the peak temperature T_P shows a linear correlation with the out of plane lattice parameter of the film, as shown in the left panel of figure 3.7.

The critical behaviour of the derivative has also been investigated by fitting the data with the expressions:

$$\frac{dR}{dT} = a + K\left(\frac{|T - T_P|}{T_P}\right)^{\eta} \tag{3.1}$$

$$\frac{dR}{dT} = a + K' \ln\left(\frac{|T - T_P|}{T_P}\right) \tag{3.2}$$

,using the Levenberg-Marquardt fitting routine of the Origin software (a, K and K' are additional fitting parameters). The first expression has been used to fit the data at $T > T_P$. The second expression has demonstrated to better fit the data at $T < T_P$; this has been verified by the lower value of the average square residual returned by the fitting routine.
The value of the critical exponent can then be obtained as a fitting parameter. As reported by ref. [85], the divergence is strong with critical exponent

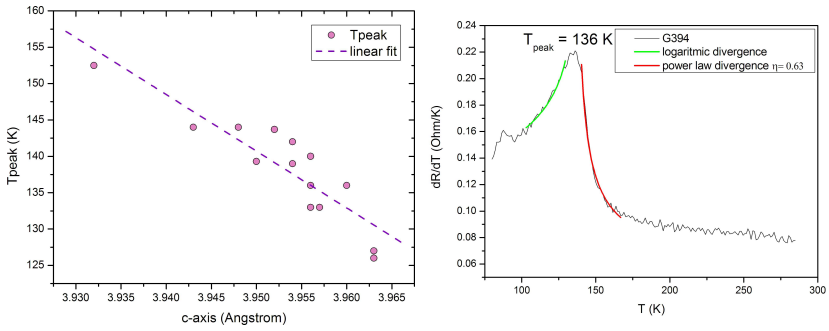

Figure 3.7: Left: Scatter plot of the derivative peak temperature as a function of the out of plane lattice parameter. The data show linear correlation, as evidenced by the linear fit (dashed line). Right: Example of the fitting of the critical behaviour of dR(T)/dT.

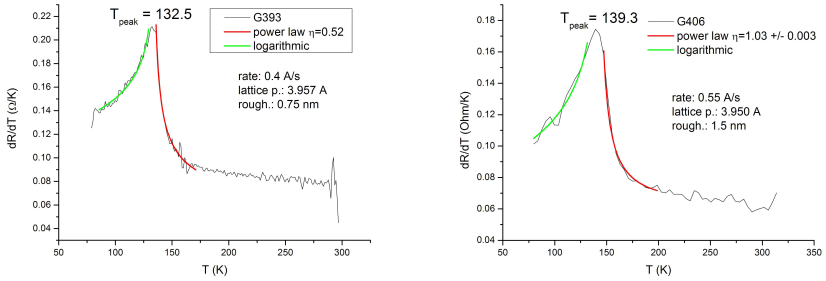

Figure 3.8: Resistance derivative for the G393 sample (left) and the G406 sample (right), deposited with the same parameters in the first series condition and in the second series condition respectively. The critical exponent and the other different features of the samples are also reported in the graphs.

between 0.5 and 1 for $T \to T_P^+$, and logarithmic (weak) for $T \to T_P^-$.
For the films grown in the low rate condition (first series) the critical exponent is closer to 0.5 for all the samples. For the optimized sample G393 we have $\eta = 0.52 \pm 0.07$.
For the films of the second series, the critical exponent for $T > T_p$ is always closer to 1, for both 0.1 and 0.2 mbar samples, excepting for the less rough optimized sample G416 (grown at higher temperature than the other samples of the second series), whose $\eta = 0.430 \pm 0.005$. It has already been remarked that the samples of the second series have an higher deposition rate than the samples of the first series, thanks to the higher laser fluence through the optical window; this results in increased roughness. It is interesting to note that not only the quality of the surface of the samples is changed, but there is also some modification in the electron-spin interaction or in the critical spin fluctuations, leading to a different value of η. The samples grown at 0.1 mbar also show an interesting feature in the dR/dT

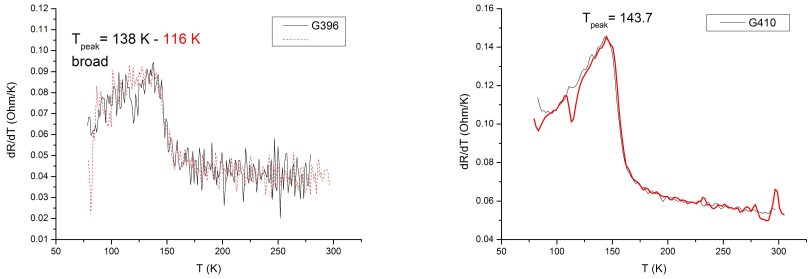

Figure 3.9: Left: dR(T)/dT curve of a 0.1 mbar sample with lattice parameter of 3.963 Å; Right: same curve for a sample with lattice parameter of 3.952 Å (for this sample η=0.78).

curves. Indeed those samples characterized by an elongated out-of-plane lattice parameter (3.960-3.963 Å) show a broadened peak for $T < T_P$; the curve cannot be fitted by any critical behaviour function as the ones described above. The broadening of the peak corresponds to a smearing of the knee in the R(T) curve, as showed by sample G396 in the left panel of figure 9. On the other hand, the G410 sample, also grown at 0.1 mbar (at low energy), but having a lattice parameter of 3.952 Å, shows a narrow peak, as reported in figure 3.9. The broadening of the peak is not simply related to structural disorder; indeed the G410 sample has a wider rocking curve than the G396 one: it is rather related to the elongation of the lattice.
The elongation of the lattice parameter may be related to oxygen deficiency in the samples, that are grown at higher rate than the relaxed G410, thus disfavouring the oxygenation. Nevertheless the oxygenation of the samples mainly takes place in the cooling after deposition, when the chamber is filled up with a pressure of 700 mbar.
Several works report on a different orthorhombic phase of SrRuO3 films with expanded in-plane and out-of-plane lattice constants [114, 115]. In particular Maria et al. find that this phase is appearing in thin films whose deposition condition favours the energetic ion bombardment, for example by a low (20 mTorr) deposition pressure. This phase has an out of plane lattice parameter of 4.02 Å; a slightly smaller lattice parameter (4.00 Å) is found by the authors of ref. [115], that instead study the occurrence of a second phase by changing the deposition temperature. The latter cell is described as a strained cell with extended pseudo-cubic lattice parameters of 3.95 Å. In both cases these authors find larger lattice parameters than our findings. In conclusion, we cannot discriminate the reason why the lattice parameter of most of 0.1 mbar samples is elongated; both oxygen deficiency or stabilization of a different phase by energetic ion deposition are possible explanations. The resulting broadening of the dR/dT peak may result from band narrowing because of oxygen ligand vacancies or octahedron rotations,

that hamper the magnetic and/or transport properties of $SrRuO_3$.

3.2 Growth and optimization of (001) oriented $BaTiO_3$ thin films.

Barium titanate thin films have been deposited in the PLD deposition system of GREYC laboratory. Our aim is to use this ferroelectric thin films for the gate of field effect devices.
The films were deposited on SrTiO3 substrates, on $SrRuO_3$ buffered $SrTiO_3$ and finally on $La_{0.7}Sr_{0.3}MnO_3/SrTiO_3$ thin films on Si.
The microstructure of the films was probed by XRD and AFM measurements, while the film thickness was determined by profilometer measurements. Finally the electrical properties of a BaTiO3/SrRuO3 thin film was tested by means of the CPP technology developed in this work.

3.2.1 $BaTiO_3$ deposition.

In order to find the optimal deposition conditions for BTO, both BTO and BTO/SRO thin films have been deposited in different oxygen pressure and changing the post-deposition cooling procedure. Indeed, following the literature [99, 98] as discussed above, different crystalline orientations are expected as a function of pressure.
All BTO/STO samples have been deposited at substrate temperature of 720°C and with laser energy of 200 mJ and frequency 3Hz. The oxygen pressure during deposition was varied from 0.1 mbar to 0.005 mbar. The cooling was carried on in 700 mbar oxygen with cooling rate of 10°C/min, for some samples an in situ annealing of 1 hour at 500°C was performed during the cooling.
The resulting XRD $\theta - 2\theta$ diffraction patterns show the evolution of the out of plane lattice parameter with decreasing oxygen pressure. The measurements are shown in figure 3.10, together with the peak positions for the different structures of bulk (unstrained) BTO as found in the literature[96].
The values of the out of plane lattice parameters are reported in the table. As we can observe from figure 3.10, the 0.05 and 0.03 samples clearly show two diffraction peaks.

deposition pressure (mbar)	out-of-plane lattice parameter (nm)
0.1	0.402
0.05	0.419-0.406
0.03	0.421-0.416
0.005	0.412

Some of the films contain differently strained or differently oriented phases. The polymorphism of BTO can also contribute to the different lattice spacing detected by XRD. The samples deposited at 0.1 mbar and the sample deposited at 0.005 mbar show a single peak, but very different lattice parameters. The lattice parameter of the high pressure sample is very close to

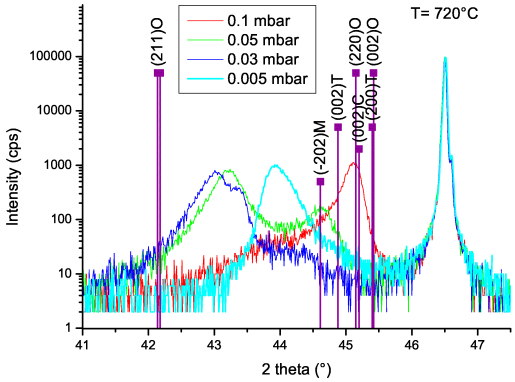

Figure 3.10: XRD symmetric scans of BTO/STO samples deposited at different oxygen pressures around the (002) STO peak. All the samples have been deposited with 3000 laser shots. The vertical lines are the peak positions of cubic (C), tetragonal (T), orthorhombic (O) and monoclinic (M) phases, by literature data [96]. The weak peak around 44° comes from the sample holder.

the bulk values found for different symmetries. If we suppose that our films are tetragonal, the 0.1 mbar sample seem to be a-axis oriented or cubic, accordingly to the findings of Li et al. [99]. Indeed the film is subject to compressive strain by the STO substrate, and an expansion of the out of plane lattice parameter is then expected. However, a measurement of the in-plane lattice parameter is needed to clarify this point.
The sample deposited at 0.005 bar shows a single peak with a large lattice parameter. The lattice parameter of the 3000 shots sample is 0.412 nm, that has to be compared with the bulk lattice parameter of the tetragonal BTO: a=0.3994 nm, c=0.4034 nm. However the Poisson ratio, obtained by assuming in-plane matching of film and substrate, is $\nu = 0.32 \pm 0.05$, close to typical values found in perovskite films ($\nu = 0.3 - 0.4$), so that the elongation of the out-of-plane lattice parameter can be explained in terms of epitaxial strain.
The elongation of the out of plane lattice parameter can also originate by oxygen vacancies. A 3000 shots sample has been fabricated and then post-annealed in situ at 500°C for 1 hour in to try to increase the oxygen content. If more oxygen is included in the structure, we would expect a reduction of the lattice parameter, as found for example in manganites[55]. Surprisingly the lattice parameter of the annealed sample is (0.415 ± 0.001) nm, i.e. it does not show any lattice parameter contraction with oxygenation. We can suppose that the annealing at 500°C changes the strain relaxation process, yielding a more strained film. We cannot then determine if the annealing procedure is successful in providing higher oxygen content to the sample.
The thickness of the 0.005 mbar samples has been measured by profilometer, and it is found to be (85 ± 5) nm for 3000 shots and (30 ± 5) nm for 1000

shots.
On the 1000 shots sample an AFM measurement was also performed, revealing a smooth surface with roughness less than 0.5 nm rms.

3.3 $BiCoO_3$ thin film deposition

$BiCoO_3$ has never been synthesized as thin film. Bulk samples are only synthesized at high pressure, but, as found for $BiMnO_3$ and $BiCrO_3$, there is the possibility that epitaxial strain can stabilize the structure in thin films. However the $BiCoO_3$ (BCO) structure is highly distorted ($c/a = 1.27$), and the in-plane lattice parameter is $a = 0.373$ nm (while $c = 0.472$ nm), then small compared to the substrates usually employed for perovskite oxide deposition such as $SrTiO_3$ (cubic, $a = 0.3905$ nm), $NdGaO_3$ (orthorhombic, pseudocubic $a = 0.386$ nm), $LaAlO_3$ (rhombohedral, in plane $a = 0.379$ nm).
In the beginning of the work, LaAlO3 (LAO) substrates have been used, so that the resulting strain on the (001) oriented BCO would be 1.6% tensile. This value is quite high, so $SrLaAlO_4$ (SLAO) and $YAlO_3$ (YAP: yttrium aluminium perovskite) substrates have been used too.
SLAO is a layered perovskite having tetragonal structure with in plane $a = 0.3756$ nm and out of plane $c = 1.263$ nm, so that the tensile strain is reduced to 0.7%. YAP has an orthorhombic structure similar to NdGaO3, (110) oriented substrates have in plane lattice parameter of 0.370-0.368 nm, thus providing compressive strain of 0.8%.

3.3.1 Thin film deposition

To find the best deposition condition several parameters were widely varied, such as oxygen pressure, deposition temperature, cooling procedure, target stoichiometry. In order to check the sample structure and the phases present in the film, $\theta - 2\theta$ XRD scans were performed in the [10, 80]° range.
Three different target have been used, prepared by sintering Bi and Co oxides with the following Bi:Co ratios: 1:1 , 1.1:1 and 1.2:1. Indeed the Bi forms extremely volatile oxides, so that films produced with stoichiometric targets turn out often to be Bi-deficient. This is the case of BiMnO3 and BiCrO3 thin films produced by PLD, that are usually grown by bismuth enriched targets [116, 117, 110].
BCO phase turned out to be very difficult to stabilize. For example at pressure of the order of 100 mTorr, no BCO associated peaks are detected in XRD; only Bi and Co oxides of different oxidation state are detected by the XRD.
The window in the parameter space for BCO stabilization turns out to be very narrow. We succeeded in obtaining some samples containing BCO

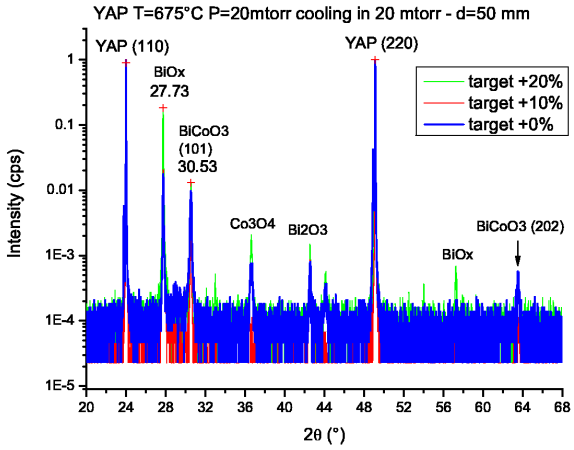

Figure 3.11: XRD scan of three samples deposited in the same conditions, but from different targets. The spectra are normalized to the substrate peak intensity. The best target is the 0% one (i.e. Bi:Co=1:1), giving the higher ratio between the BCO and impurities intensity.

phase, but no single phase films could be obtained. In the XRD spectra, only the peaks associated to the (101) reflection, i.e. the 100% intensity reflection, are detected.

The BCO phase is only present in thin films grown between 675°C-20 mTorr and 650°C -10 mTorr. No detectable BCO phase is formed at 700°C, or at 650°C - 20 mTorr. In figure 3.11 the XRD of samples deposited on YAP is reported for the following growth conditions: T=675°C, P=20 mTorr, substrate-target distance d=50 mm. The cooling for these samples has been performed at -10°C/min at deposition pressure.

The cooling procedure also influences the phase formation. Indeed a thin film deposited in the same condition of the ones of figure 3.11, but postannealed for 2h at deposition pressure and temperature shows a reduced intensity of the BCO peaks.

Cooling in higher oxygen pressure (100-300 mTorr) enhances the formation of Bi oxides. However further investigation is needed about the best cooling procedure to promote the BCO phase.

The BCO (101) peak has been detected both on YAP and SLAO substrates, in thin film deposited in the same conditions, regardless of the tensile or compressive strain.

In conclusion we were not able to grow single phase BCO films, and the impurity content seem to be predominant in our samples. We were able to identify the deposition condition for some BCO phase to appear, but we have no hint about the way of reducing the impurity content in these samples. Further investigation, probably at lower oxygen pressure, is needed,

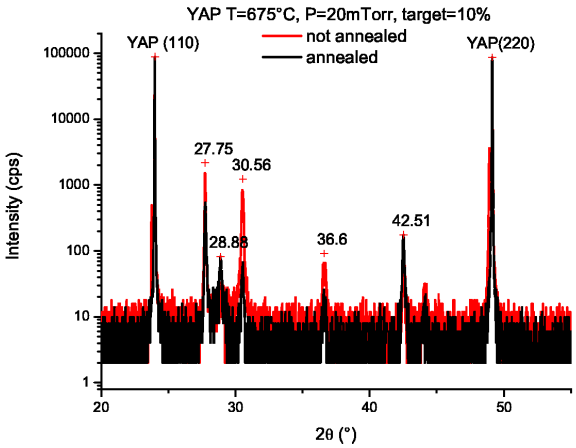

Figure 3.12: XRD scan of two samples, the first grown in the same conditions of the samples reported in figure 1, the second has been postannealed for 2h in deposition pressure at the deposition temperature. The BCO peak intensity is reduced after the annealing procedure.

but this was beyond the limits of the employed equipment.
The BCO phase may be stabilized also by chemical doping, for example by stabilizing the phase by means of Co-Mn[119] or Co-Fe [118] substitution. However this would lead to a reduction of the tetragonality of the system.

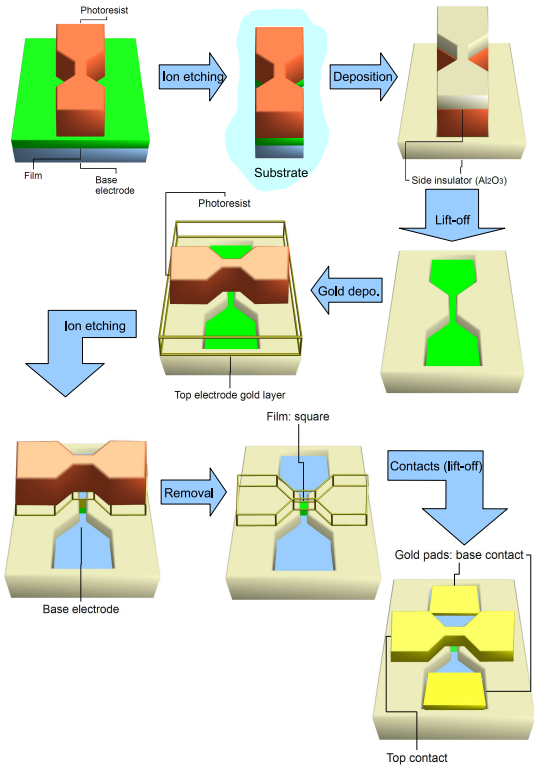

Figure 3.13: Lithographic process to define the CPP measurement geometry in the configuration chosen in this work.

3.4 CPP devices fabrication

All the CPP devices have been fabricated on thin films deposited on a base electrode film such as $SrRuO_3$ and $LaNiO_3$. At the beginning of this work two equivalent configuration and mask sets were tested, and finally the more successful one was chosen.

Figure 3.13 represents all the fabrication steps for the definition of the CPP structure. The first step consists in the definition of the base electrode: the film plus the base electrode layer are etched to the substrate. The second step is the deposition of the side insulator, that has to prevent electrical contact between the top and base electrode. A thick layer (thicker than the total etched thickness) of Al_2O_3 is deposited all over the sample, and then the photoresist is removed (lift-off). In this way there are no alignment problems (self-aligned geometry) and the possibility of shortcuts between top and bottom electrode is then reduced. However the lift-off can be difficult (especially for very thick insulator layer) or not perfect, and cracks can form along the sides of the base electrode.

Then the top electrode gold layer is deposited all over the sample, and the

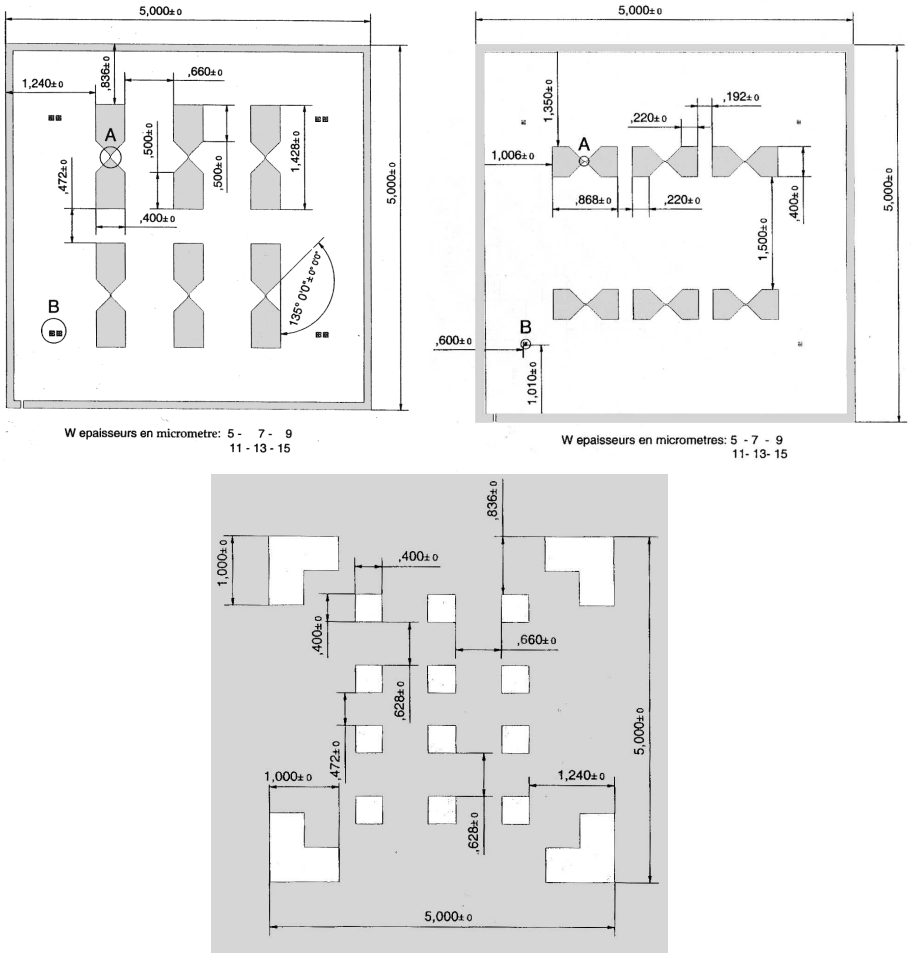

Figure 3.14: Lithographic masks for the CPP structure patterning. The size of the elements are indicated in millimetres. The first one is the base electrode, the second one the top electrode and the third one the base electrode contacts. The circles labelled A and B in the first two patterns indicate respectively the measurement and alignment geometries. Dark zone are represented in grey, while transparent zones are represented in white.

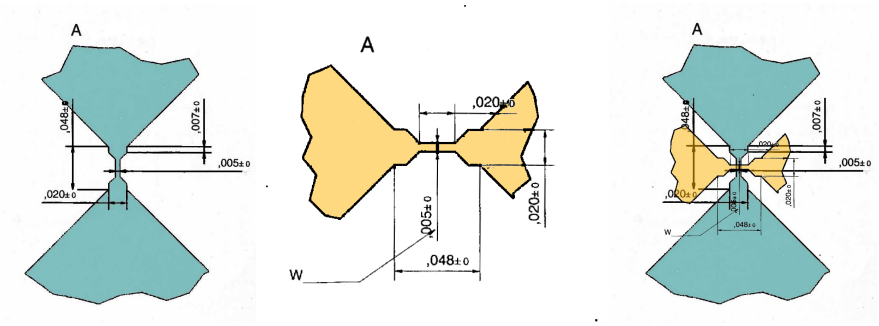

Figure 3.15: Enlargement of the base electrode(blue) and top electrode (yellow) thin lines (labelled A in figure 3.14), with sizes in millimetres. The measurement area is given by the superimposition of the base and top electrode lines (in this case 0.005×0.005 mm).

top electrode is delineated in the photoresist. The subsequent etching process is the most delicate one, as it has to pattern the top electrode and, at the same time, etch all the film down to the top electrode in order to define the measurement area. In this step the control of the ion etching, that is non-selective, is crucial. Finally, the gold pads on the base contact are defined by lift-off.
Therefore the two delicate steps in the process are the insulator lift-off and stopping the second ion etching in the base electrode.

3.4.1 The lithographic mask

The lithographic mask is a metallic film mask. To define the geometry three patterns are superimposed. The plans of the three mask elements are represented in figure 3.14.
As showed in figure 3.13, the film measurement area is defined by the crossing of the base electrode and top electrode thin lines (marked by the circles labelled A in figure 3.14). Each pattern contains six elements, with line width of 5, 7, 9, 11, 13 and 15 μm respectively.
An enlargement of the lines (in particular the thinnest one) and the resulting superimposition is reported in figure 3.15. In order to correctly align the different levels of the mask on the sample, alignment geometries are drawn on the four corners of the mask (in the circles labelled B in figure 3.13). The alignment geometries of the base electrode are transferred on the sample and patterned in the film. When the top electrode pattern has to be exposed on the resist coated sample, the alignment geometries on the mask have to be centred on the alignment geometries on the sample, as shown in figure 3.16. As shown in the schemes, the smallest detail in the mask is 5 μm, a standard size for optical lithography.

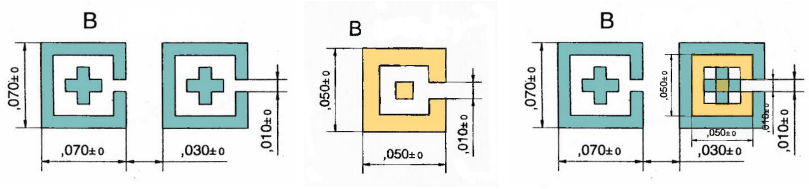

Figure 3.16: Enlargement of the alignment geometries (labelled B in figure 3.14), with sizes in millimetres. The correct aligment of bottom and top electrode is realized when all the top alignment geometries fit in the bottom ones as shown in the third image. However the geometry is drawn to tolerate some misalignments.

3.4.2 $BiFeO_3/LaNiO_3$ devices

$BiFeO_3/LaNiO_3$ thin films

The BFO/LNO thin films on STO have been deposited in the PLD multi-target deposition system of CRISMAT laboratory (Caen), using the deposition condition optimized by Ranjit et al. for a work on BFO/STO superlattices [120].
$LaNiO_3$ (LNO) is a perovskite oxide exhibiting paramagnetic metallic behaviour. It is widely used highly conductive electrode for ferroelectric thin-film devices, including non volatile memories [121]. The LNO crystal structure is distorted from cubic to rhombohedral R-3c by the rotation of NiO_6 octahedra. However we can refer to the pseudocubic structure with lattice parameter 3.838 Å, that makes this oxide highly compatible with STO and BFO, together with many functional perovskite oxide such as manganites [122].
The deposition conditions are the following:
$LaNiO_3$ deposition:

- T=700°C;
- P(O_2) = 300 mTorr;
- Laser EGY/f = 180 mJ/3Hz;
- d(target-substrate)= 63 mm;
- 10 min annealing at deposition P, then $BiFeO_3$ deposition.

$BiFeO_3$ deposition:

- T=700°C;

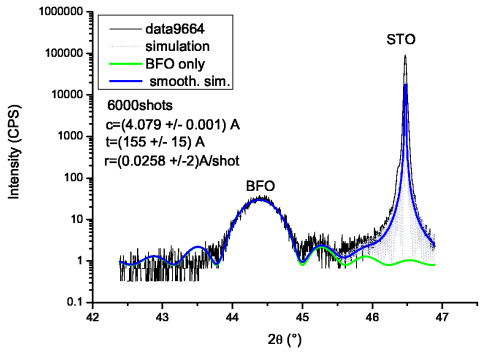

Figure 3.17: XRD $\theta - 2\theta$ scan of the sample PBF091218 (9664). The diffraction pattern has been simulated by kinematical theory. The BFO lattice parameter and thickness have been estimated.

- P(O_2) = 20 mTorr;
- Laser EGY/f = 180 mJ/3Hz;
- d(target-substrate)= 63 mm;
- Cooling in O2 at -10°C/min; at 680°C increase pressure to 300 mtorr; at 400°C fill the chamber with 300 mbar.

In order to determine the BFO layer thickness, a single BFO thin film (PBF091218-9664) has been deposited on $SrTiO_3$. The XRD of the sample is reported in figure 3.17.

The thickness has been estimated by the XRD and by profilometer measurements. The profilometer measurement has been performed by defining a step by lithography and by etching the unprotected film by 10% HCl in H_2O for 5 min. The profilometer yields a thickness of 20-25 nm, whereas by XRD the estimated thickness is (15.5 ± 1.5) nm. However the profilometer precision is low for thickness less than 50 nm.
From the XRD thickness we can calculate the deposition rate per shot, that results (0.0258 ± 0.0002)Å/shot.

The BFO/LNO bilayers have also been measured by XRD.
For all the samples the XRD diffraction spectra do not show any impurity peaks such as Bi2O3 or ferrites. In figure 3.18 the $\theta - 2\theta$ scan of the sample PBF091211-9660 is reported. The estimated BFO thickness is (13.4 ± 1.5) nm corresponding to 5000 shots. The calculated deposition rate is (0.0268 ± 0.0005) Å/shot, accordingly with the findings on the BFO single layer.

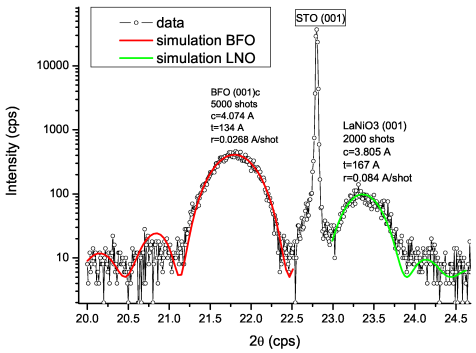

Figure 3.18: XRD scan of the BFO/LNO bilayer on STO PBF091211 (5000shots/2000shots) around the STO (001) peak. The measured lattice parameters, thickness and deposition rate for the BFO and LNO are also reported.

Lithographic process

Here it is reported a detailed outline of the process for these samples:

1. The bilayers are covered by a protecting gold layer. This can be deposited by PLD or ion beam deposition (Gatan system). The PLD deposition is used to avoid to deoxygenate the BiFeO3, that may be damaged by the energetic Gatan deposition. The Gatan system is provided of a quartz microbalance to measure the deposited thickness, while the PLD thickness is obtained by a calibration.

2. The base electrode is defined by lithography and then the full sample is etched by ion milling down to substrate.

3. Keeping the photoresist from the previous step, Al_2O_3 is deposited as side insulator by Gatan system. The photoresist is removed (by soaking in aceton with ultrasonic agitation) and Al_2O_3 is lifted-off.

4. A layer of gold thick enough to connect the top of the base electrode and the top of the insulating layer is deposited by Gatan.

5. The top electrode is defined by lithography and then the remaining part of the film is etched down to the $LaNiO_3$ by ion milling. In one case the gold was removed by KI (wet chemical etching) before the ion milling.

6. The contact pads are defined by lithography (lift-off) and then 200 nm of gold are deposited on $LaNiO_3$ by PLD.

Several technical problems have been encountered during the device fabrication, especially during the ion etching. During the ion etching, the mass

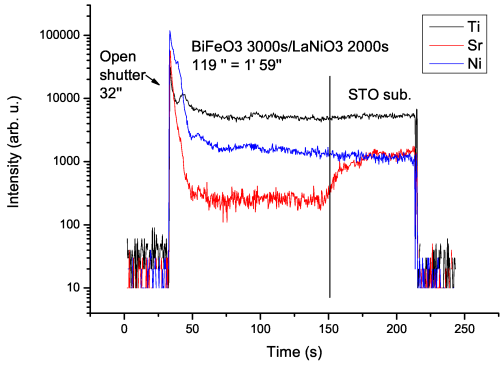

Figure 3.19: Mass spectrometer signal for Sr^+, Ti^+ and Ni^+ ions recorded during the ion etching of a BFO/LNO sample on STO. The Ni^+ signal does not show any variation during all the etching, whereas an increase of the signal during the LNO layer etching is expected.

signal by some chosen elements is detected by the mass spectrometer, allowing to determine the material that is being etched. However, for BFO/LNO the Bi and La signals are not detected because their masses are beyond the limit of the system, and Fe and Ni are already present in the vacuum chamber and sample holder. For example the mass spectrometer signal of Sr^+, Ti^+ and Ni^+, during the etching of a BFO/LNO bilayer in standard conditions, is reported in figure 3.19. Then stopping in the base electrode layer can be very difficult, as we have no marker element to determine when the LNO layer is reached. The etching time of a single BFO/STO thin film has been measured in order to obtain a calibration, resulting in 1'03" for a 6000 shots film. However, even with a calibration, the etching is very difficult to control, as the etching rate is subject to changes with the ageing of the ion source filaments.
Another problem encountered is related to the Al_2O_3 lift-off step, especially when the insulator layer is very thick (300 nm). Cracks at the insulator edges are often formed, providing shortcuts between the top and bottom electrode, as shown in figure 3.20. These cracks can be avoided by reducing the side insulator thickness and by gentle removing of the photoresist (by long soaking in aceton and short time in ultrasonic agitation).

Electrical measurements

All the CPP devices have been tested on the room temperature probe station of GREYC laboratory. The probe station is equipped with 6 probes and an optical microscope, in order to access the contacts of patterned films having size of some hundreds of microns (as in our case). The DC measurement system is composed by a stabilized current source, a preamplifier

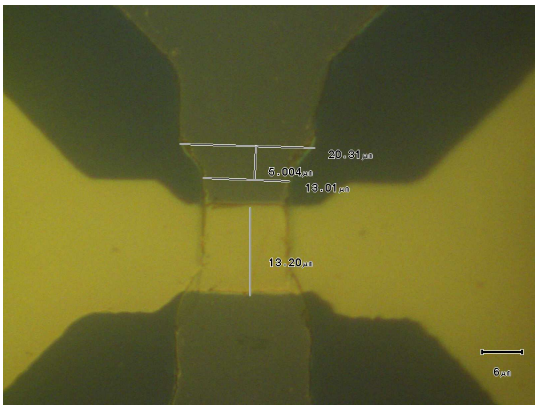

Figure 3.20: Optical microscopy image of one of the CPP devices fabricated on the sample PBF091210. Cracks in the side insulator layer are evident, and shortcuts between the bottom and top electrode are formed.

(with amplification 10) and a multimeter for voltage measurements. All the measurements have been performed in four probe configuration.

The resistance of the base electrode has been tested in order to verify that the base electrode is conductive. The result for the PBF091210 sample is reported in figure 3.21. For the base electrode resistance measurements voltage and current probes have been placed on the two base electrode contact pads, so that the contact resistance has also been measured.

Furthermore the transport has been probed also in the CPP configuration to verify that there are no losses in the structure and if the ferroelectric film is insulating, as no electrical polarization can be measured if the leakage current is too important.

The results are reported in figure 3.22. The devices show very different resistance values, that may originate from defects in the device structure. The highest value is recorded for the 13 μm line, i.e. for the 13 μm x 13 μm square. However this resistance value is not high enough to allow the polarization switching by electric field and P loop measurements. The film resistivity can be calculated by using the film thickness of 14 nm, and the square size measured by optical microscope (11.4 μm x 12.4 μm), assuming that no parasitic losses across the structure are present. The resistivity value obtained is $13 \times 10^5 \Omega$cm, that is much lower than the value reported in literature of about $10^{10} \Omega$cm [123]. However the thickness of our films is very small, and the process is not fully controlled, especially during the ion etching. To better clarify this point, the same lithographic process has been applied on $BaTiO_3/SrRuO_3$ bilayers.

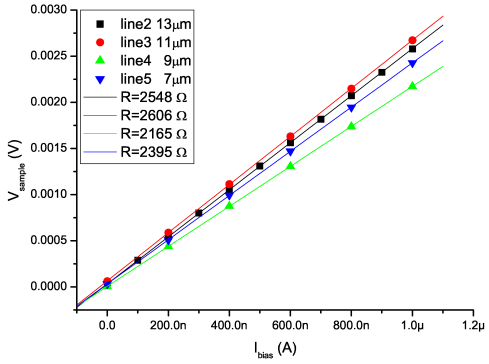

Figure 3.21: V(I) curves of the base electrodes of sample PBF091210. The resistance is not scaling with line width, probably the contact resistance contribution is more important and not constant for all lines. The lines are labelled from 1 to 6 from the thicker (line1=15 μm) to the thinner (line6=5 μm)

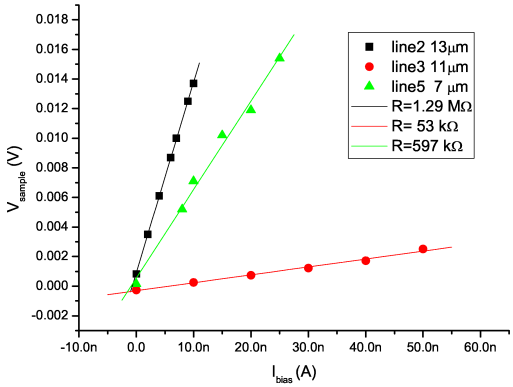

Figure 3.22: V(I) curves of sample PBF091210 in CPP configuration. Line 4 (9 μm) could not be measured as the top electrode contact was interrupted.

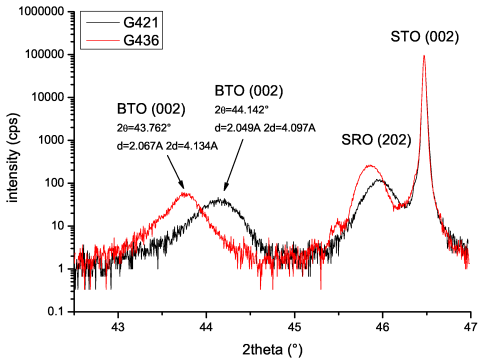

Figure 3.23: $\theta-2\theta$ scan around the (002) STO peak of the G421 and G436 bilayers.

3.4.3 $BaTiO_3/SrRuO_3$ devices

BTO/SRO bilayers present the advantage of allowing to control the ion etching, as Ti and Sr ions can be detected by the mass spectrometer. In this case we report the process on the sample G421, 85nm BTO on 30nm SRO.

$BaTiO_3/SrRuO_3$ bilayers on $SrTiO_3$

The bilayers were deposited by using different deposition conditions for the SRO and BTO layer. In most of the samples SRO was deposited using the optimized condition, and subsequently the BTO was deposited in the conditions described for the single layers in section §3.2.1.
In figure 3.23 the XRD scans of the G421 and G436 bilayers are reported.

The G421 bilayer was fabricated by depositing the BTO at 0.005 mbar. This sample is the one used in the fabrication of the CPP device. The G436 bilayer was annealed in situ, and as found for the single BTO films, its lattice parameter is larger than the one of the G421 sample, not annealed. An AFM measurement has been performed on the G417 bilayer, deposited in the same conditions of G421 sample but with BTO 1500 shots on SRO 2000 shots. The roughness of the sample is 2.2 nm rms, a very high value if compared to the single layer BTO film. This confirms that low roughness base electrodes are crucial in order to keep low roughness in the overlying film.

Device fabrication

In figure 3.24 the Sr and Ti signals from the mass spectrometer during the first ion etching step is reported. As we can see, the etching of the base

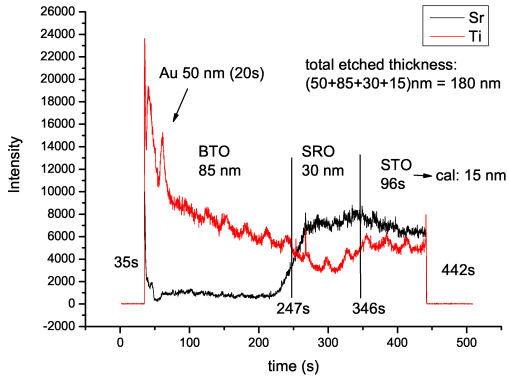

Figure 3.24: Mass spectrometer signal from Sr^+ and Ti^+ ions. The etching of the BTO, SRO and STO is recognizable by the signal intensity variations. The STO etched thickness is estimated by a calibration (etching rate 9.6 nm/min), even if the real rate may be different.

electrode is accompanied by the marked rise of the Sr signal, that can be used to stop the second ion etching step.

Because of the sample thickness, a thick Al_2O_3 layer has been deposited as side insulator. To promote the lift off and to avoid degradation of the insulator edges, we used RIE (reactive ion etching) in oxygen to try to remove the phootoresist.

RIE is a dry chemical etching technique using low energy RF sputtering in a reactive gas that chemically interacts with the material and removes it. Oxygen is used to etch the photoresist. In this case the etching lasted 10', a long etching time to remove the Shipley photoresist (usually removed in 5').

After the RIE the Al_2O_3 and residual photoresist was removed by ultrasonic agitation in acetone for 1h. Despite the long time in ultrasound, the insulator profiles are not damaged, as shown in figure 3.25.

Electrical measurements

The testing of the geometry has been performed in the same condition of the BFO/LNO bilayers. The base electrode V(I) curves are reported in figure3.26, show that the resistance increases with decreasing width of the lines. The resistance scales almost linearly with the inverse line width. The resistance values for the SRO base electrode are comparable with the LNO ones (however the film thickness is different).

The CPP resistance could not be measured with the same technique because of its high value, then the measurement was performed by a HP4156B semiconductor parameter analyzer. The measurement was performed by voltage

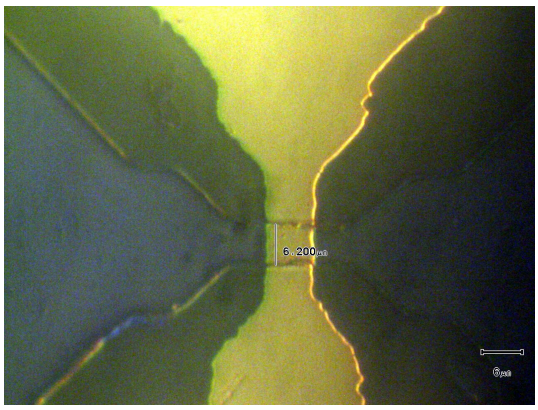

Figure 3.25: Optical microscope image of one geometry on G421 sample (thinner line). The bottom electrode profiles are sharp. On the other hand, because of to high developing time in the lithography step 6, the top electrode profiles are irregular.

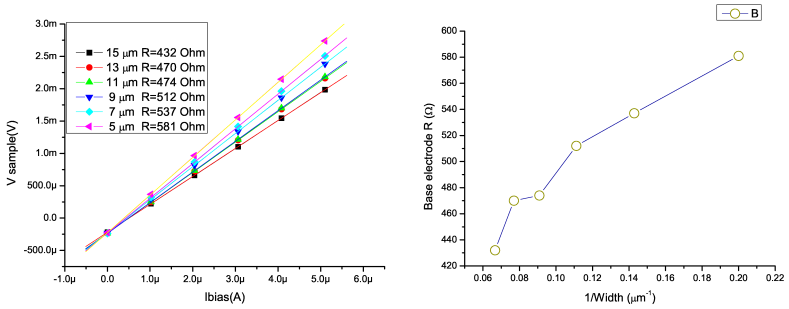

Figure 3.26: V(I) curves of the base electrodes in G421 sample. The resistance values as a function of the inverse width are also reported. The contact resistance contribution is always present, as in the case of BFO/LNO structures.

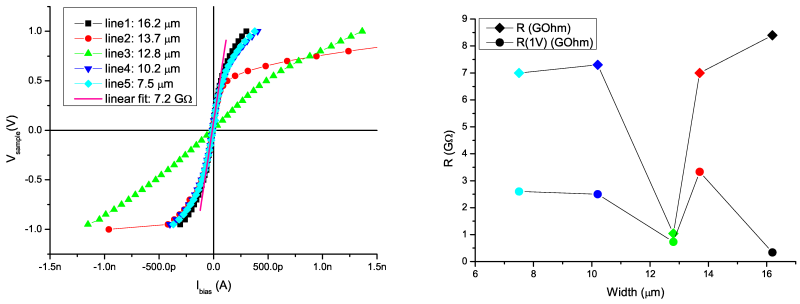

Figure 3.27: V(I) curves of the G421 sample (side of the sample labelled B). The line 6 (6.2 μm, measurement not reported) has very low resistance, probably due to shortcuts. One of the lines (line 2) shows a diode-like V(I) curve. The red line is a linear fit on line 1 data around zero. The resistance values obtained by the linear fit around zero and by the V/I ratio at 1V. There is no scaling with the measurement area.

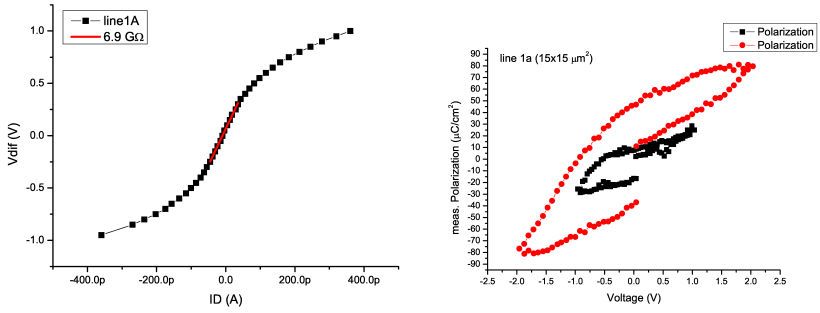

Figure 3.28: V(I) curve and polarization loop measurement at frequency 1kHz. The shape of the P(V) loops is typical of lossy dielectrics.

biasing the sample and measuring the current flow by the source monitor units, that allow to measure very weak currents and apply up to 100 V. The voltage drop across the CPP structure has been measured by the voltage measurement units of the analyzer.
The resulting V(I) curves are reported in figure 3.27. The measured resistance value is very high if compared with the previous geometries, and the V(I) curves are non linear. However we cannot observe any scaling with the measurement area, the resistance values are very close to each other, excepting for the line 3 sample that has lower resistance.

On this sample P-loop measurements have also been performed using a Radiant Technologies Precision Materials Analizer at CNRT Matériaux laboratory in Caen. However the polarization loops yield unphysical values of the polarization (saturation polarization of BTO is 26 $\mu C/m^2$), and a show the typical shape of lossy dielectrics.

In conclusion, the BTO appears lossy. This is in agreement with the find-

ings of Trithaveesak et al.[125] that measure the polarization of BTO films of different thickness (from 300 to 100 nm), and find increasing losses with decreasing thickness, so that the polarization of the 100 nm sample could not be measured. However they find that at the temperature of -150°C the losses are reduced and P loops of the 100nm sample can be measured.
As we do not see any scaling with the measurement area, we cannot determine if the losses come from defects in the BTO layer or from defects in the patterned structure. It is interesting to remark that one of the V(I) curves in figure 15 has a diode-like shape. This is also observed by other authors [125][126] on BTO/SRO and BTO/La_2CuO_4 lossy capacitors, and it is attributed to the bottom electrode/BTO interface pn junction.

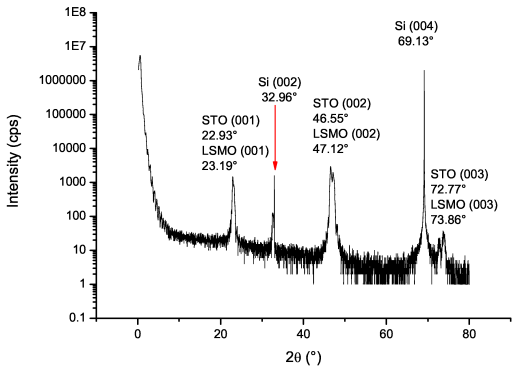

Figure 3.29: XRD $\theta - 2\theta$ scan of the LSMO/STO sample on Si CA662. The STO c-axis is 0.390 nm while the LSMO one is 0.385 nm.

3.5 Field effect devices fabrication

Field effect devices have been fabricated by optical lithography on ultrathin 15 nm $LaSrMnO_3$ films on $SrTiO_3$ buffered Si. The fabrication of such samples, with 20 nm STO buffer directly deposited on Si, is a very challenging issue, as usually use of more than one template layer is necessary in order to grow $SrTiO_3$ on silicon. Such samples have been deposited by DR. C. Adamo at the Pennsylvania State University (USA) by using the Molecular Beam Epitaxy layer-by-layer technique. This technique allows the growth of epitaxial $SrTiO_3$ on Si substrates, and then to use it as template layer to deposit on silicon all the different oxides traditionally deposited on STO substrates.

3.5.1 The lithographic mask

The lithographic mask is a photographic film mask. This kind of mask has lower resolution respect to the metallic film mask used for the CPP devices and is easily damaged by contact. However copies of the mask (both positive and negative, as we will see in the following) on chromium coated glass substrates have been fabricated to be used in place of the original mask. The pattern size is 5mm?10mm, and contains 24 devices. The device is composed of 3 levels: the channel, the gate and the contact pads. The disposition of the devices in the pattern and a sketch of the three levels is reported in figure 3.30.
The mask was designed for the following process:

1. The film is coated by the gate oxide layer (for example Al_2O_3 deposited by ion beam deposition in the Gatan system, or PLD $BaTiO_3$).

2. The oxide gate pattern (mask level 2 - named: Mask FET A) is exposed

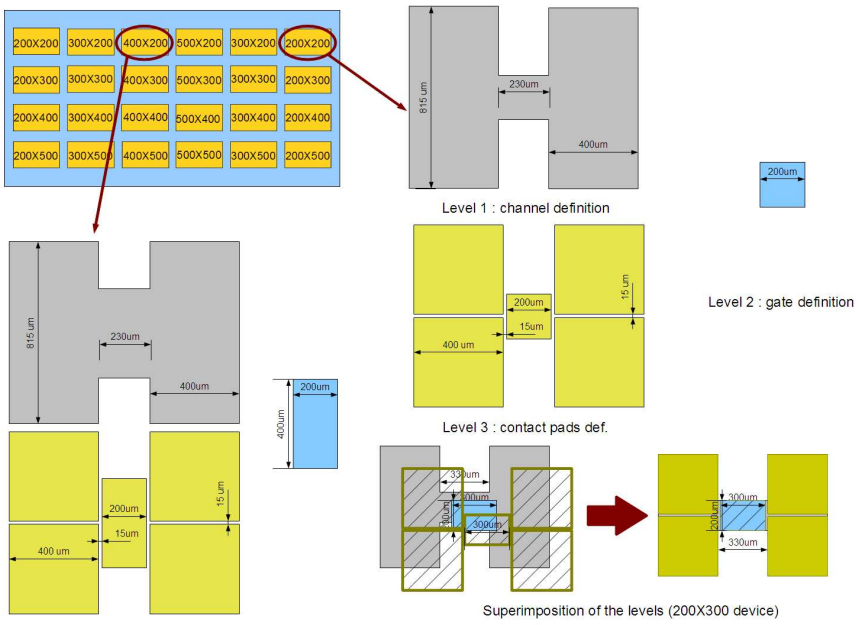

Figure 3.30: Sketch of the device disposition on the sample (each device is identified by its channel width×length) and of the three mask levels. In the original mask all the levels are positive images of the patterns. However a negative image of level 2, containing the oxide gate, has been prepared in order to define the gate by lift-off. Finally the superimposition of the three levels to give the device is represented. Grey colour represents the LSMO/STO film, light blue the oxide layer and yellow (or black hatching) the gold.

on the photoresist coated sample.

3. The oxide is etched, for example Al_2O_3 is selectively etched by RIE or $BaTiO_3$ is etched by ion milling until the film is reached (monitoring the etching by mass spectrometer).

4. The mask level 1 (Mask FET B) is aligned to the gate and exposed on the sample.

5. The film is etched down to the substrate by ion etching.

6. A gold layer is deposited on the sample.

7. The contact pattern (mask level 3 - Mask FET C) is exposed on the sample (carefully aligned on the underlying structure) and the gold is chemically etched in KI.

In order to avoid to cover all the film with Al_2O_3, as the ion beam deposition has been proved to deoxygenate the sample, a negative image of the level 2

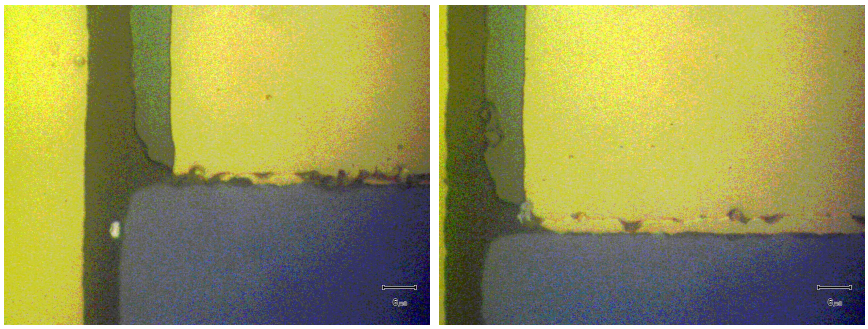

Figure 3.31: Enlargement of the edges of the gate electrodes of some devices of sample CA662-9A.

of the mask has been produced. Then the gate has been defined by lift-off instead of etching. The only problem with the negative image of the mask is that the whole mask is inverted, and some of the geometries (the central ones as reported in figure 2) do not match with the gates.
This process could not be applied to $BaTiO_3$ gates, as the deposition of this material is performed at high temperature (as described before), then the photoresist would become insoluble and could not be removed in acetone to lift-off the oxide layer.
As shown in figure 2 the size of the devices (in particular the channel size) is large. This allows to access directly to the gate contact with the measurement probes. However, it is usually desirable to reduce the size of the channel (and consequently of the gate) as in large gate areas local defect can be easily included and degrade the gate insulation.
The design of the mask has a disadvantage, as the gate contact pad has the same size as the gate. In this way any misalignment of the mask levels can give rise to shortcuts between the gate electrode and the channel, thus preventing the measurement of many devices, as showed in figure 3.31.

3.5.2 Al_2O_3 and SiO_2 gate devices

Our aim is to test manganite based field effect devices employing ferroelectric (or multiferroic) gates. However, as shown in the previous section, we were not able to obtain ferroelectric loops with $BiFeO_3$ and $BaTiO_3$ thin films, even if we obtained better results with $BaTiO_3$ (high resistance).
At the beginning of the work, to test the geometry and verify the field effect in our ultrathin manganite films, we prepared some samples using well known oxides such as SiO_2 and Al_2O_3. The gate oxide in these samples was defined by lift-off. The lithographic process was modified: the negative image of the Mask FET A is exposed at first, then the gate oxide and a metallic layer (Ag/Au) is deposited and finally lifted-off. The steps 4-7 follow as described in the previous section.

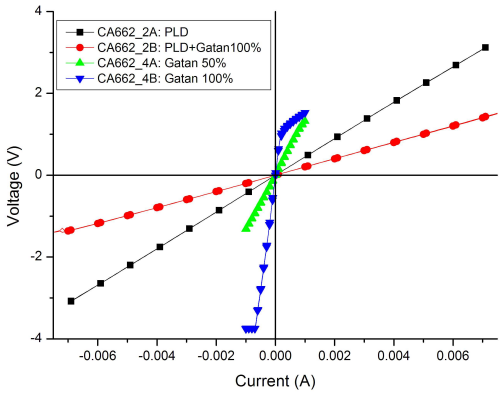

Figure 3.32: V(I) curves of LSMO/STO on Si samples belonging to the same wafer of the sample used for the devices (i.e. CA662 wafer, LSMO 15 nm). On the samples four gold contacts have been deposited with different techniques and conditions (as reported in the legend), and the four probe measurement has been carried on.

However in this procedure the gate is often lifted off together with the excess, so that only few devices could be measured.
The first processed samples are the CA662-7-1 with Al_2O_3 gate and Ca662-7-2 with SiO_2 gate. A first problem encountered in these samples is the non-linearity of the V(I) curves of the LSMO channel, as we will show in the following.

To find the origin of such non-linearity, some tests have been performed on 15 nm LSMO thin films with four gold contacts deposited in different conditions. The V(I) curves, four probe measurement, are reported in figure 3.32. In particular in figure 3.32, blue symbols indicate the V(I) curve obtained with gold contacts deposited with ion beam deposition (Gatan system) and full power (100% indicates V=10kV, the energy of the beam). As we can see, the corresponding V(I) is non-linear. Then the gold deposition can effectively damage the LSMO film. We tried to reduce the energy of the beam (5kV), obtaining a linear V(I) curve, but still a high resistance.
We then tried to deposit a gold layer by PLD on the film.
The contacts obtained by PLD (black symbols) do not damage the sample (linear V(I)), but the gold layer is thin (here 2000 shots, corresponding to 20 nm), and PLD gold has a very rough surface. We then deposited 200 nm of gold at full power with ion beam deposition on the PLD gold (red symbols), and we verified that the PLD gold acts as a protective layer. Indeed the V(I) curve keeps its linear characteristic and yields a lower resistance, thanks to the better adhesion and connectivity of the contacts.
We remark that this non-linearity problem is particularly important in ultrathin films, while in thin films the LSMO results less damaged.
By our results on Au/LSMO contacts we decided deposit a PLD protective

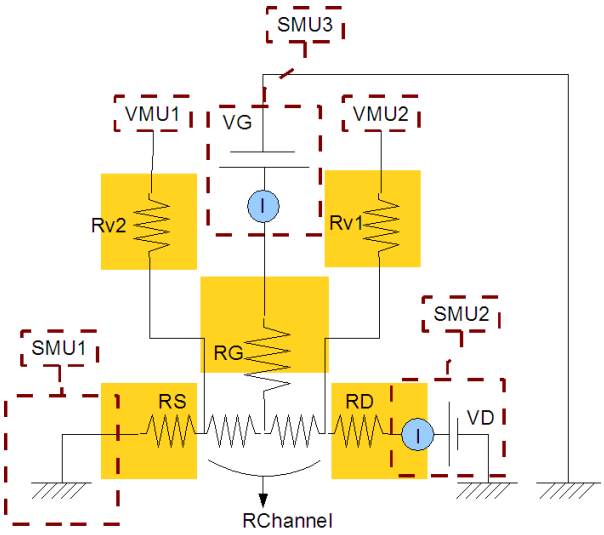

Figure 3.33: sketch of the electrical connections of a field effect device to the HP4156B instrument. The contact pads on the sample are sketched in yellow. RS, RD, Rv1 and Rv1 represent the contact resistance of the four channel contacts. RG represent the gate insulation resistance, that must be very high (ideally infinite). The gate junction must ideally be a capacitor (not represented for clarity). RChannel represents the channel resistance.

gold layer before step 6 (samples CA662-9A with Al_2O_3 gate and CA662-9B with SiO_2 gate), so that direct ion beam deposition of gold on the LSMO layer is avoided.

Electrical measurements

All the electrical measurements have been performed using the HP4156B semiconductor parameter analyzer and the room temperature probe station of GREYC laboratory.

The electrical connections of a device with the instrument are schematically represented in figure 4. The semiconductor parameter analizer contains voltage sources, current sources, voltage monitors, and current monitors that can be programmed via a menu-driven user interface. The HP4156B contains four SMUs (=Source Monitor Units). Each of these can be programmed to be a voltage source, a current source, or a ground. If the source is programmed to be a voltage source, the current can be monitored and vice versa.

The instrument contains also two independent voltage monitor units (VMU) and two programmable voltage sources (VSU). In our case two SMU (SMU2 and SMU3) are used in voltage source mode, and a third (SMU1) as ground (common). These three terminals are connected to the gate contact (G) and to two of the channel contacts, labelled source (S) and drain (D) in analogy

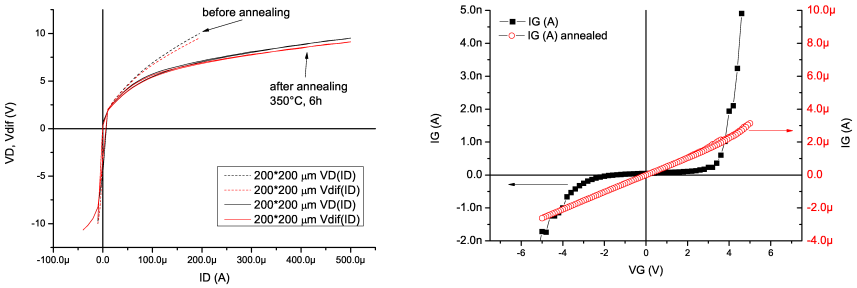

Figure 3.34: Sample CA662-7-1, 200*200 μm device. Left: Two probe VD(ID) and four probe Vdif(ID) characteristics of the channel (see figure 4 for the definition of the quantities). Vdif is defined as VMU2-VMU1. Right: current versus voltage characteristic of the gate IG(VG). Black symbols represent the characteristic before annealing, showing very low leakage currents for voltages between [-2, +2]V. After the annealing (red symbols) the gate resistance is degraded (notice the different scale).

to MOSFET connections, as shown in figure 3.33. In order to measure the 4 probe resistance of the channel, the VMUs are connected to the remaining two channel contacts.
During the test measurements only the necessary probes were connected to the devices (for example during the VD(ID) measurement, the gate contact tip was disconnected.
The 4 probe channel resistance of the CA662-7-1 sample is reported in figure 3.34. The measure has been performed by voltage biasing the sample, even if it is reported as V(I). As we can see, the curve shows a diode-like shape. We believe that the LSMO loses oxygen during the ion beam deposition of gold, thus becoming semiconducting, and that the Au metal contact forms a Schottky diode on the semiconducting LSMO. In order to restore the correct oxygen content in the sample, an annealing of 6h at 350°C has been performed in 500 mbar of oxygen. The annealing seem to reduce the Schottky barrier, but the curve remains diode-like. Furthermore, from the IG(VG) graph reported in figure 3.34, we can see that the gate insulation resistance is degraded by the annealing. In figure 3.35 the electrical measurements on a device of the sample CA662-9A show that, even if we removed the problem of non-ohmic Au/LSMO contacts, the current versus voltage curve is still similar to the diode characteristic. Furthermore, in this case there is little or no difference among the 4 probe and 2 probe measurement, (compare the VD and Vdif in figure 3.34 and 3.35).
Then the non-ohmic characteristic of the channel may be originated by the Al_2O_3 deposition on LSMO that can damage the ultrathin film as well as gold deposition. All the SiO_2 devices show worse performances than the Al_2O_3 ones in terms of gate insulation.

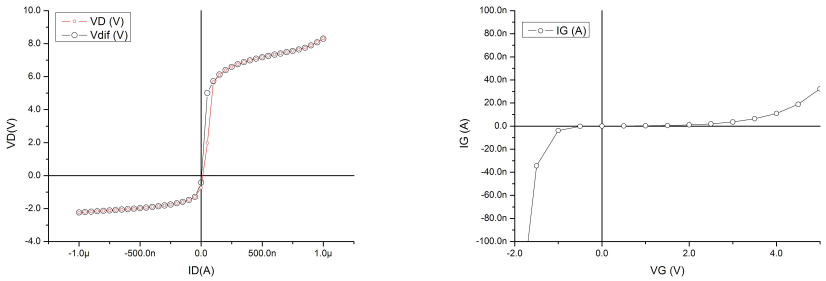

Figure 3.35: Sample CA662-9A, 200μm*200μm device. Left: Channel 2 probe and 4 probe V(I) curves. The curves are diode-like also in this case. There is very little difference between the 4 and 2 probe measurement. Right: the IG(VG) curve is similar to the one of the previous sample in shape, but the current values are higher.

3.5.3 $BaTiO_3$ gate devices

These devices have been fabricated by employing BTO/LSMO/STO on Si trilayers.

$BaTiO_3$ deposition on $La_{0.7}Sr_{0.3}MnO_3/SrTiO_3$ thin films on Si

The $La_{0.7}Sr_{0.3}MnO_3/SrTiO_3$ (LSMO/STO) thin films on Si were deposited by dr. C. Adamo at the Pennsylvania State university (USA) by the same MBE layer-by-layer technique employed to deposit the $LaMnO_3/SrMnO_3$ superlattices described in the first chapter. The STO layer thickness is 20 nm, and the LSMO layer thickness is 15 nm.
The BTO has been deposited by PLD, using the same deposition conditions of the BTO/STO thin films. After the cooling, a gold layer was deposited in situ at room temperature to protect the BTO during the photolithographic processing.
In figure 3.36 the XRD scans of two BTO samples are reported. The first sample was deposited at 0.1 mbar, and its out-of-plane lattice parameter is (0.400 ± 0.001) nm, whereas the second sample was deposited at 0.005 mbar and its out-of-plane lattice parameter is (0.414 ± 0.001) nm, accordingly with the value found on BTO/STO thin films.
As the film studied by CPP technique (G421) did not show high resistance values, we decided to use a BTO film deposited at high oxygen pressure and one deposited at low oxygen pressure, and to postanneal in situ both samples at 500°C in oxygen in order to enhance the oxygen content and consequently the insulating properties. The deposition of the BTO samples by PLD

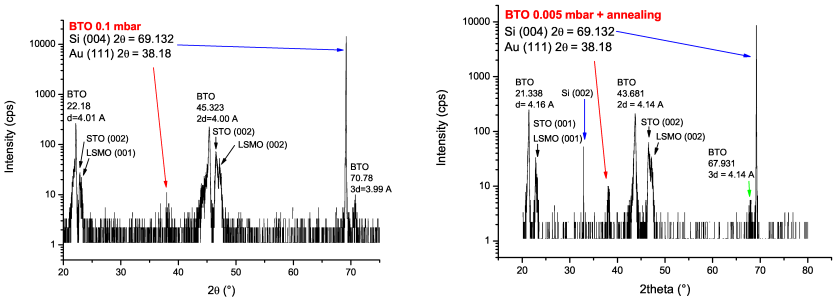

Figure 3.36: XRD scans of the gold coated BTO samples deposited on LSMO/STO bilayers on Si. Both samples were deposited at 720°C with laser energy/frequency 200mJ/3Hz. The sample deposited at 0.005 mbar was annealed for 1h at 500°C during the cooling process at -10°C/min, 700 mbar O_2 for both samples.

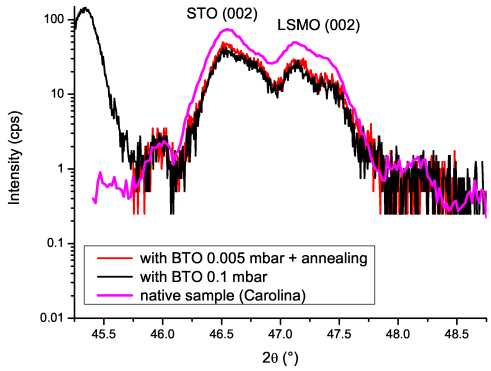

Figure 3.37: $\theta - 2\theta$ scans around the (002) STO/LSMO peaks for the two BTO samples and the native LSMO/STO bilayer, measured in a different instrument.

at high temperature seem to not damage the structure of the underlying LSMO/STO bilayer. Indeed, as shown by figure 3.37, the STO and LSMO (002) peak positions and relative intensities are not modified by the BTO deposition.

Device fabrication

For these devices the original process and masks (i.e. positive images of the masks) were used. In order to solve the problems that may arise with misalignments, longer exposition time and longer Au etching time in KI were employed for the contact pads definition step, in order to reduce the pad area and avoid the occurrence of shortcuts.
We prepared two samples, the first one CA662-8A with BTO at high oxygen pressure (0.1 mbar), the second one CA662-8B at low oxygen pressure (0.005 mbar). As explained in the deposition section, both samples were covered

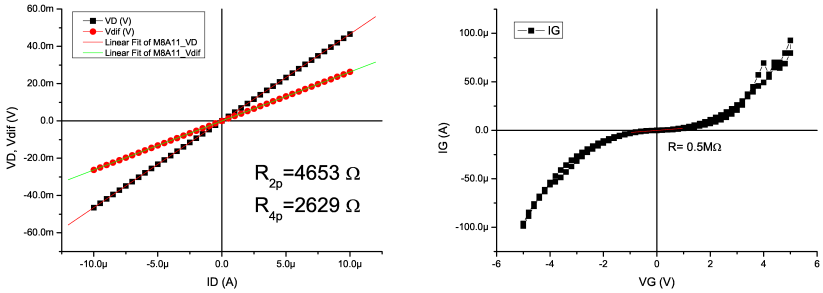

Figure 3.38: Sample CA662-8A Left: 2 probe (VD) and 4 probe (Vdif) voltage versus current curves of the 400μm*200μm device channel. Right: gate current versus voltage (IG(VG)) curves for the same device. The curve is non-linear, the resistance value around zero is 0.5 MΩ.

in situ by a protective layer of Au by PLD.
Furthermore, before depositing the gold for the contact pads (step 6), a protective gold layer was deposited by PLD (2000 shots).
The ion-etching of the BTO layer has been monitored by ion milling, by following the intensities of Ti (in the BTO layer) and Sr (in the LSMO layer).

Electrical measurements

The electrical measurements on these samples were performed in the same configuration of the CA662-7 and 9.
The V(I) curves of the channel are reported in figure 3.38 and 3.39, showing that in this case the V(I) are linear for both samples. In figure 3.40 the resistance values of channels with different length and constant width are reported, and from the linear fitting of the data the resistivity value of the LSMO is calculated. The obtained values, (1.3 ± 0.1) mΩ cm and (1.5 ± 0.1) mΩ cm are very close to the room temperature resistivity of LSMO (2 m Ω cm). However the gate resistance is found to be low in both samples.

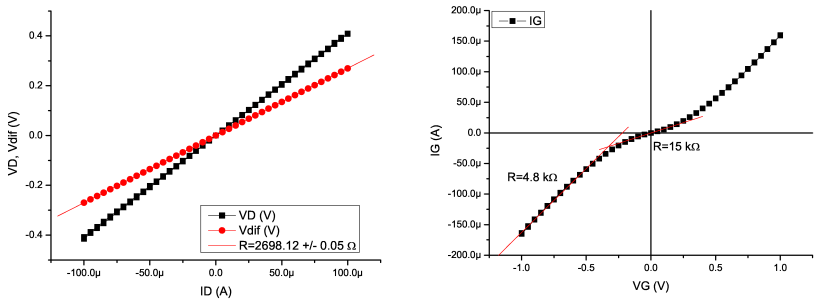

Figure 3.39: Sample CA662-8B Left: 2 probe (VD) and 4 probe (Vdif) voltage versus current curves of the 300μm*300μm device channel. Right: gate current versus voltage (IG(VG)) curves for the same device. The curve is non-linear, but the gate resistance has always low values.

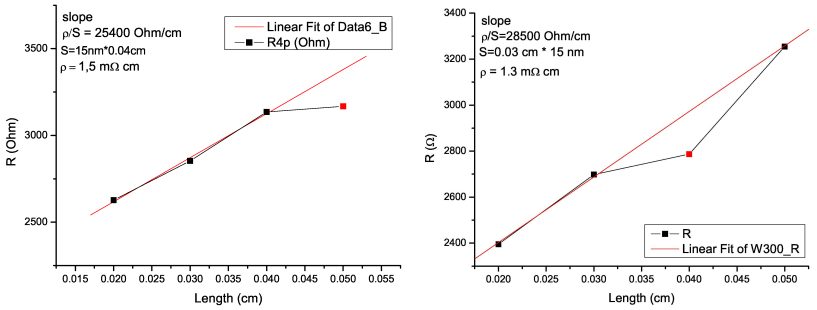

Figure 3.40: Left: sample CA662-8A: channel resistance as a function of channel length for devices with channel width of 400 μm. Right: sample CA662-8B: same thing for devices with channel width of 300 μm. From the linear fitting of the data the LSMO resistivity is estimated.

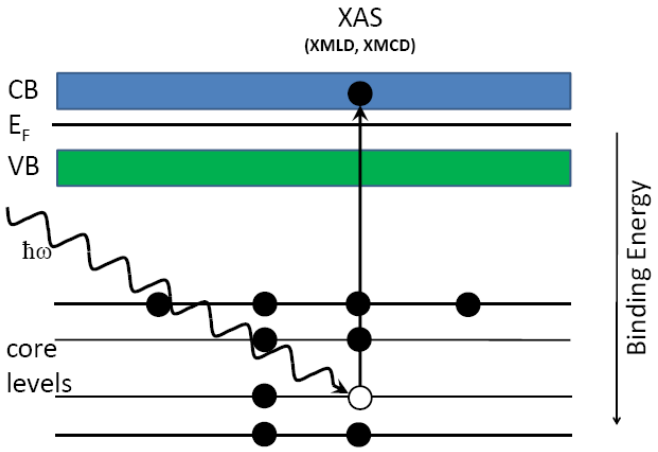

Figure 3.41: Scheme of the x-ray absorption process.

3.6 Magnetic phases and orbital occupation in $(LaMnO_3)_{2n}(SrMnO_3)_n$ superlattices

The magnetic and electronic modifications induced at the interfaces in $(LaMnO_3)_{2n}(SrMnO_3)_n$ superlattices have been investigated by linear and circular magnetic dichroism in the Mn $L_{2,3}$ X-ray absorption spectra.
These technique allows to probe the average orbital occupation of selected ions (Mn) by natural linear dichroism, and by combining the circular and linear magnetic dichroism informations, the presence of ferromagnetic and antiferromagnetic phases and their orientation (in-plane or out-of-plane of film) can be probed.
In this sense linear and circular magnetic dichroism are a precious source of information to compare with the results of theoretical works[19, 28, 31], or for further modelling.

3.6.1 The technique: X-ray Absorption Spectroscopy (XAS).

In the x-ray absorption spectroscopy (XAS) a core electron is excited to an unoccupied state above the Fermi level. A schematic illustration of XAS can be seen in figure3.41. The required energy E_{abs} is:

$$E_{abs} = h\nu = E_{final} - E_{initial} \tag{3.3}$$

Here E_{final} is the energy of the final state with the core electron excited into the conduction band. $E_{initial}$ is the energy of the not excited initial state. Due to the dipole selection rules only transitions which change the angular momentum quantum number l by one occur in the process ($\Delta l = \pm 1$). While

the spin s is conserved ($\Delta s = 0$), the z-component of the orbital momentum m has to change by zero or one ($\Delta m = \pm 1; 0$). In particular, $\Delta m = \pm 1$ for left and right hand circularly polarized light and $\Delta m = 0$ for linear polarized light. There are quadrupole transitions which allow $\Delta L = \pm 2; 0$, but these transitions are hundred times weaker than the dipole transitions.
With XAS one probes site specifically the unoccupied density of states. This means that the electrons are excited from a specific core level to the unoccupied states, whereby only one atom sort is excited because each element has individual excitation energies for its levels.
To determine different states in the conduction band one has to use a tuneable source, e.g. the radiation of a synchrotron. The transition intensity can only be determined indirectly. In transmission or reflection experiments one measures the remaining intensity and calculates the absorption. For the metals one can measure the drain current from the sample which is proportional to the XAS signal. This is called total electron yield (TEY). If the sample is an insulator one can measure the intensity of radiant recombination which is called partial or total fluorescence yield (PFY- or TFY-mode). The XAS can be divided into two spectral regions, the so called near edge x-ray absorption fine structure (NEXAFS) which reflects excitations of the photoelectron into the unoccupied states, and the so called extended x-ray absorption fine structure (EXAFS). Here the photoelectron treated as a wave is excited into the continuum, and its superposition of backscattered waves from neighbouring atoms leads to characteristic features in the XAS, usually at photon energies well above the corresponding NEXAFS threshold.

Theoretical Description of the Absorption of X-rays.

The x-ray absorption spectroscopy process is an excitation of a system, initially in a ground state Ψ_i, into a final state Ψ_f . The theoretical description of this process by Fermi's Golden Rule is the following:

$$\omega = |\langle \Psi_f | \hat{e}\mathbf{r} | \Psi_i \rangle|^2 \delta(E_f - E_i - h\nu), \tag{3.4}$$

where ω is the transition probability and $|\hat{e}\mathbf{r}|$ is the dipole matrix element coupling initial and final state. The electric quadrupole transition is some hundred times smaller than the dipole transition and is therefore neglected (dipole approximation). The wave functions Ψ_i and Ψ_f are not exactly known, and for practical calculations of the x-ray absorption cross section one can make an approximation of a one-electron process. This means an assumption that all other electrons do not participate in the transition from initial to final state. Then the initial state wave function can be rewritten as a core wave function c, and the final wave function as a free electron wave function ϵ. It is possible to rewrite the matrix element in 3.4 to a single electron matrix element M, which often is constant or slowly varying

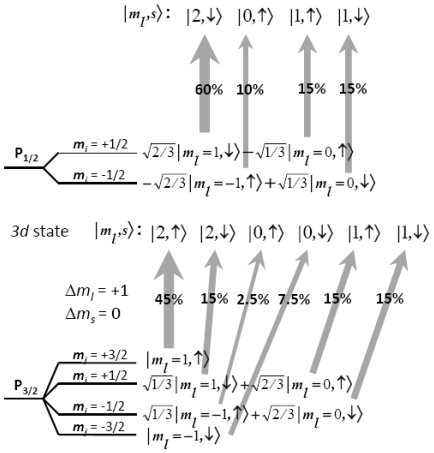

Figure 3.42: Absorption of a right-hand circular polarized photon by $p_{1/2}$ and $p_{3/2}$ multiplets. The excitation probability is given by Clebsch-Gordan coefficients.

in energy.
One observes the density of empty states (ρ) which is implied by the delta function. This leads together with the one-electron approximation to the following intensity:

$$I_{XAS} \propto M^2 \rho(E_f) \tag{3.5}$$

The dipole selection rules dictate that the dipole matrix element is non zero if the orbital quantum number of the final state differs by 1 from the initial state ($\Delta l = \pm 1$) and the spin is conserved ($\Delta S = 0$). That means that for example transitions like $s \rightarrow p$ and $p \rightarrow s$, $p \rightarrow d$, etc. are allowed when additionally the spin is conserved. The neglected quadrupole transitions follow other selection rules ($\Delta l = \pm 2$ or 0) where transitions $s \rightarrow d$, $p \rightarrow f$, $s \rightarrow s$ and $p \rightarrow p$, etc. are allowed.

3.6.2 X-ray Magnetic Circular Dichroism (XMCD).

The excitation with circular polarized light in XAS measurements leads to different absorption probabilities for different spin directions. This difference is measured by the spin dependent absorption coefficients μ^+ and μ^- for circular polarized light with parallel (+) and antiparallel (-) helicity with respect to the majority and minority spin, respectively.
For example for the $2p_{3/2}$ state excited with right-hand circular polarized light, just taking into account the core hole excitation, the ratio between the excitation of spin up and spin down electrons is 62.5% to 37.5%. The ratio for the $2p_{1/2}$ state is 25% to 75% (see figure 3.42).

By means of x-ray magnetic circular dichroism (XMCD) one can anal-

yse the magnetic moments element specifically and moreover separated into their spin and orbital moments. It was first verified by Schütz et al. [35] in 1987. In the following decade it became an often used method for the characterization of magnetic materials. For the XMCD effect it is assumed that the spin dependent dichroism in the absorption process corresponds to the difference between the number of spin up and spin down holes of the conduction band, which gives the magnetic moment.
For a maximum XMCD effect in the experiment, the photon angular momentum L_ph has to be collinear to the magnetization direction M. The dichroism is then given by the difference spectra of a measurement with the right-hand polarized light ($q = +1$, L_{ph} points in the direction of wavevector **k**) and the lefthand polarized light ($q = -1$, L_{ph} points in the direction of wavevector **-k**). The same effect can be achieved with a fixed light helicity, when the magnetization is switched in the opposite direction. The XMCD is described as a linear combination of the absorption of circular polarized light $I_{right} - I_{left} = I^+ - I^-$.
In figure 3.43 the XMCD process is schematically presented. The d-band is split into spin up and spin down bands. Firstly the absorption of circularly polarized xray photons leads to a spin polarization of the photoelectrons due to the spin orbit coupling ($j = l \pm s$). In a second step the d valence band acts as a spin detector. At the L_3 edge ($j = l + s$) left hand circularly polarized x-rays mainly probe the unoccupied spin up d states with respect to the direction of the magnetization. The effect reverses at the L_2 edge due to the opposite sign of the spin-orbit coupling ($j = l - s$). For $2p \rightarrow 3d$ transitions the magnetic moments can be calculated by applying the so called XMCD sum rules found by Thole et al. [36, 37]. Here the sum rules modified by Chen at al. [38] are reported:

$$m_{orb} = -\frac{4\int_{L_3+L_2}(\mu^+ - \mu^-)}{3\int_{L_3+L_2}(\mu^+ + \mu^-)}(10 - n_{3d}) \tag{3.6}$$

$$m_{spin} = -\frac{6\int_{L_3}(\mu^+ - \mu^-) - 4\int_{L_3+L_2}(\mu^+ - \mu^-)}{3\int_{L_3+L_2}(\mu^+ + \mu^-)}(10 - n_{3d})\left(1 + \frac{7\langle T_z\rangle}{2\langle S_z\rangle}\right) \tag{3.7}$$

Here m_{orb} is the orbital magnetic moment and m_{spin} is the spin magnetic moment in units of μ_B/atom. The indices L_3 and L_2 of the integrals refer to the integration over the whole L_3 and L_2 peaks. $(\mu^+ - \mu^-)$ is the XMCD spectrum and $(\mu^+ + \mu^-)$ is the sum of the XAS spectra excited with left and right circularly polarized light. n_{3d} is the number of 3d electrons in the corresponding ion. $\langle T_z\rangle$ is the ground state expectation value of the magnetic dipole term originating from the expectation value of the magnetic dipole operator and $\langle S_z\rangle$ is the corresponding spin operator. Usually for bulk cubic crystals $\frac{\langle T_z\rangle}{\langle S_z\rangle} \ll 1$ and can be neglected.
There were some simplifications made during the derivation of the sum rules.

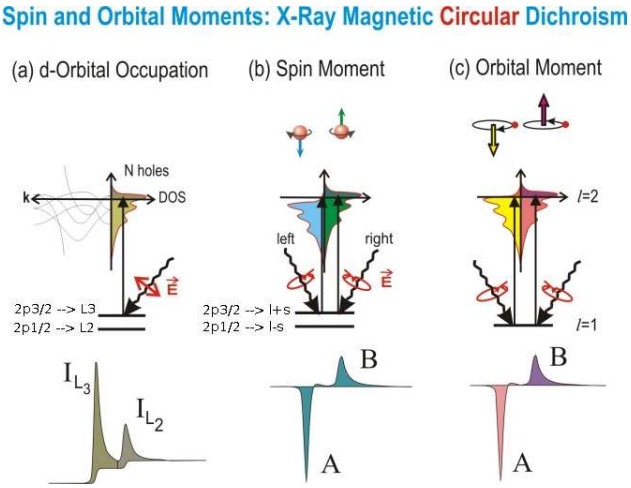

Figure 3.43: Electronic transitions in conventional L-edge x-ray absorption (a), and x-ray magnetic circular x-ray dichroism (b,c), illustrated in a one-electron model. The transitions occur from the spin-orbit split 2p core shell to empty conduction band states. In conventional x-ray absorption the total transition intensity of the two peaks is proportional to the number of d holes (first sum rule). By use of circularly polarized x-rays the spin moment (b) and orbital moment (c) can be determined from linear combinations of the dichroic difference intensities A and B, according to other sum rules.

It is considered that the $2p \rightarrow 3d$ transitions take place between free atoms. Secondly the L_3 and L_2 edges should have a complete energetic separation for the purpose of getting exact results for the integrals. Problems occur for lessthanhalf-filled band of 3d transition metals.
The sum rules can be used for the late 3d transition metal ions with a small deviation, but for the earlier transition metals a correction factor is needed to handle the mixing of the TM L_2 and L_3 edge. This factor was found by Teramura et al. [39] for different valence states of Ni, Co, Fe and Mn. For the less influenced Ni ions the factor is around 0.92, but for the Mn^{4+} ion a factor of around 0.59 was found. Without this correction the magnetic spin moments extracted from XMCD experiments by the sum rules are underestimated for early and intermediate transition metals.
A two-step model describes the XMCD effect. In the first step a photoelectron with a spin and an orbital momentum from a localized atomic inner shell is generated by circularly polarized light. In the second step, the 3d shell acts as a detector of the spin and the orbital momentum of this photoelectron. The amount of dichroism depends on three important parameters: the degree of circular polarization P_{circ}, the expectation value of the magnetic moment of the 3d shell $\langle m \rangle$ and the angle Θ between the directions of the photon angular momentum L_{ph} and the magnetic moment m. Then the

XMCD intensity is casted to the following dependence:

$$I_{XMCD} \propto P_{circ}\langle m\rangle cos\Theta. \tag{3.8}$$

With this dependence the effects of partly polarized light and experimental geometries deviating from the ideal case can be taken into account.

3.6.3 X-ray (Magnetic) Linear Dichroism (XLD and XMLD)

The X-ray absorption of linear polarized light changes with the geometry of the experiment. This gives a dichroic signal for different orientations of the polarization of the light. Two types of linear dichroism can be distinguished. The first is the x-ray natural linear dichroism (XNLD) which is also abbreviated with XLD. Here the polarization plane is either perpendicular or parallel to the crystal axis of a not magnetized single crystal. The second is the x-ray magnetic linear dichroism (XMLD) where the geometry is similar to the XNLD, but the magnetization of the sample is either perpendicular or parallel to the polarization plane. There is a complex angle dependence between magnetization, crystal axis and polarization plane, which is examined in detail by Arenholz et al. [41] for Ni^{2+} $L_{2,3}$ XMLD in cubic lattices.
For linear polarized light the electric field vector E acts like a searchlight for the occupation of orbitals because the transition intensity of the absorption process is directly proportional to the number of empty valence states in the direction of E. That means that orbitals lying perpendicular to the electric field vector are not excited. For spherical orbitals, no natural linear dichroism appears.
For example the split 3d states, e_g and t_{2g}, of an octahedral crystal field are spherical, but if the orbitals d_{xy}, d_{xz} and d_{yz} (t_{2g}) or $d_{x^2-y^2}$ and $d_{z^2-r^2}$ (e_g) are differently occupied, a natural linear dichroism will appear. With this technique an orbital ordering can be observed.
For the magnetic linear dichroism the sample is magnetized by an external magnetic field. In this case the charge density is distorted and elongated along the spin axis. This is due to spinorbit interaction, whereby the atomic spins are axially aligned by the exchange interaction. This effect is present for ferromagnetic, ferrimagnetic and antiferromagnetic configuration. This is the advantage of XMLD with respect to XMCD. The XMLD effect does not vanish for antiferromagnetic coupling.
The XMLD spectra can be described as a combination of the absorption of circularly and linear polarized photons $I^{||} - I^{\perp} = I^0 - (I^+ + I^-)/2$.
It is important to note that the natural linear dichroism is additionally present in the magnetic linear dichroism experiment. Both linear dichroism effects are due to a charge asymmetry[40].

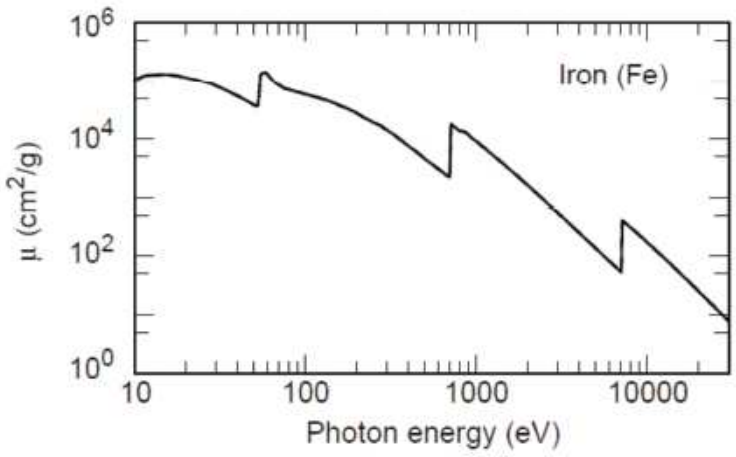

Figure 3.44: Iron absorption mass coefficient μ/ρ as a function of the energy in eV.

3.6.4 L edge in 3d transition metal compounds

In figure 3.44 the attenuation coefficient μ of iron (a 3d transition metal) is reported. The attenuation coefficient is defined by the Lambert-Beer law of transmitted intensity of radiation $I = I_0 e^{-\mu t}$, where I_0 is the incident radiation intensity, t is the material thickness and $\mu = \mu(\lambda) = \mu(E)$ is the attenuation coefficient, that depends on the radiation wavelength i.e. energy.
An interesting feature of the $\mu(E)$ coefficient efficient is the presence, on top of a slow decreasing evolution vs energy, of sharp absorption edges corresponding to the excitations of core electrons into empty valence states, i.e the process described above for the XAS. XAS is indeed the study of the spectral fine structure near the absorption edges of a given element.
Figure 3.44 clearly shows three edges. In particular two of them are below 1000 eV and correspond to the two possible transitions to a 3d state: from the 3p orbitals, below 75 eV and called $M_{2,3}$ edge, and from the 2p in the soft x-ray range known as $L_{2,3}$ edge. The third edge at higher energy (about 7 keV) arises mainly from the $1s \rightarrow 3d$ transition (K edge) and its cross section is about one hundred time lower than that of the M and L edges.
$L_{2,3}$ are the most probable absorption processes, as we can see from the μ graph in figure 3.44 also. Here we will focus on the $2p \rightarrow 3d$ process because it is the strongest resonance and shows several specific advantages.
For such absorption process the presence of a 2p hole can drastically affect the XAS structures because of the strong Coulomb interactions with the other atomic charges, both electrons and holes. The single electron approximation breaks down and multiplet effects have to been taken into account: we have to consider a many electron model with all their possible interac-

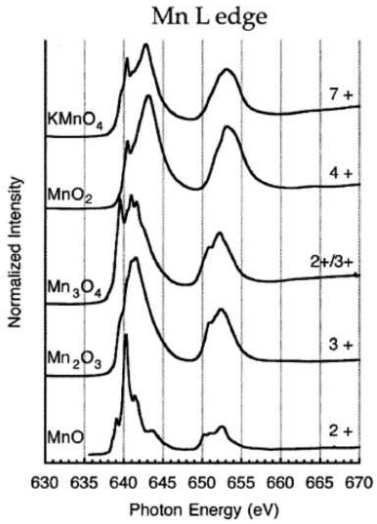

Figure 3.45: Multiplet structure for different oxidation state of Mn. As the number of valence electrons varies, the electron-electron interaction drastically changes as well as the unoccupied density of state. From ref.[42]

tions to understand the XAS structure.

As we can see in figure 3.45, the spectral shape for the same Mn element shows several features that definitely change when the oxidation state, and thus the number of valence electrons, is different. However if one transfers the atomic multiplet theory to the solid state it is necessary to deal also with the different local symmetry and with a more itinerant electronic behaviour. The Ligand Field Theory developed by T. Thole, G. Van der Laan and Butler, approaches the problem of the symmetry thanks to the Crystal Field theory, while the effect of delocalised charges is described using the charge-transfer multiplet method which consist of two or more configurations interaction.

Summarising, at the $L_{2,3}$ the X-ray absorption can be described as the transition of the absorbing atom from $2p^6 3d^n$ to $2p^5 3d^{n+1}$ state. The final state is split into a wide multiplet by the electron-electron interaction, according to the LS coupling, and it is influenced by the inner hole because of its excitonic character. In addition, this multiplet structure is assembled in two different edges called L_3 and L_2, due to the large core-hole spin-orbit interaction in the $2p$ shell. For such compounds this interaction is of the order of some electronvolts: from about 5 eV in Sc to 23 eV in Zn. Therefore the $2p_{1/2}$ and the $2p_{3/2}$ states are well separated and that results in two different edges called L_3 and L_2 respectively, as we can see in figure 3.45. Moreover the $2p$ core hole lifetime broadening is mainly under 300 meV, which means that sharp peaks are visible[43].

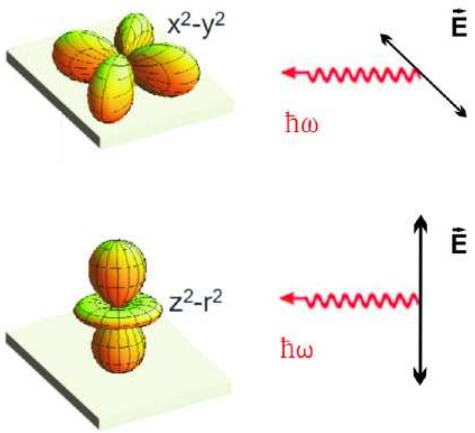

Figure 3.46: How the orbital anisotropy influences the x-ray absorption: if one free orbital is aligned to the photon electric vector, the photoexcited electron will preferentially undergo a transition towards it. In the upper part the $x^2 - y^2$ orbital and the polarisation lies in the plane while below the configuration is orthogonal for the $3z^2 - r^2$ state. From ref.[43]

3.6.5 Crystal field effect on the X-ray linear dichroism

The spherical symmetry of an atom can be broken by an electric field, in particular the non-spherical Coulomb potential generated by negatively charged ligands. As we know from the crystal field theory (§1.1) the central metallic ion strongly interacts with the negative charge at the oxygens sites and the anisotropy in their dispositions, rising from the crystal structure, removes the orbital degeneracy. As the $3d$ orbitals have they lobes in different space directions, the X-ray absorption has the same anisotropy and will feel the effect of such a removal.
As explained in the previous paragraphs, different occupation of the e_g or t_{2g} $3d$ orbitals is probed by linear polarized light giving rise to XNLD. For example, a transition to the $3z^2 - r^2$ state is more probable if the light polarisation is along the z axis and conversely transition to the $x^2 - y^2$ is enhanced for polarisation in the xy plane (see figure 3.46).

If all $3d$ orbitals have the same energy and thus are equally occupied, the absorption spectra do not depend on the polarisation but if there is a preferential occupation of some orbitals, because of an electric field, with respect to others, it is possible to know the direction of the free states.
Let us take for example a system with both the e_g states unoccupied and the linear dichroism as the difference between the vertical and horizontal polarisation (figure 3.46). If the $y^2 - x^2$ orbital is more energetic than $3z^2 - r^2$ we will have an XNLD spectra that is reversed with respect to that for a system with the $y^2 - x^2$ orbital at the lowest energy. In figure 3.47 a schematic view

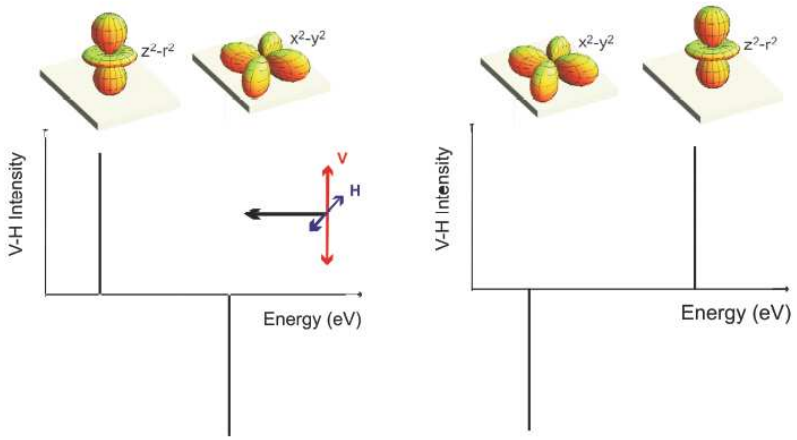

Figure 3.47: the linear dichroism measured as V-H is reversed if the energies of the e_g free orbitals are exchanged. The intensity of a transition towards the $z^2 - r^2$ state will be positive because the density of states is along V, and photoelectrons are excited to this state by V polarized light. Conversely for $x^2 - y^2$, lying in the plane, H polarization gives higher intensity, so that V-H is negative. In the left panel the $3z^2 - r^2$ orbital is the less energetic so the first absorption peak of XNLD is positive. On the right the intensities are opposite. From ref. [43]

of the mechanism is shown[43].

3.6.6 Simulations of X-ray magnetic and orbital dichroism spectra

As explained in §3.6.4, the fine structure of the X-ray absorption spectra near the absorption edges, can be calculated by atomic multiplet theory, but in solid state also the symmetry breaking by crystal field and the electron delocalization have to be taken in account.
In order to perform an atomic multiplet calculation for a metal ion, one of the most known and powerful way is a package of codes, ultimately based on that by Cowan for atomic states. To greatly simplify its use, a user friendly graphical interface has been developed by Riccardo Gusmeroli, in collaboration with Prof. Claudia Dallera: the Missing scientific package [44]. It allows not only a rapid processing and viewing of the calculated data and parameters, but also, with the addition other tools, to introduce a crystal field multiplet evaluation and configurations interactions. The used codes are finally combined together to obtain X-Ray Absorption (XAS) and Resonant Inelastic X-Ray Emission spectra. The further packages introduced are the crystal field multiplet program written by B. T. Thole and based on the point group code by P. H. Butler and the charge transfer multiplet program by B. T. Thole too with the help of B. Searle and in collaboration

with A. Kotani, H. Ogasawara and K. Okada[43].
In our case we are interested in the simulation of Mn $L_{2,3}$ dichroism spectra. In mixed valence manganites, $Mn^{3+/4+}$ coexist. However it has been demonstrated that the Mn^{4+}, while it contributes to the total absorption signal, weakly affects the linear dichroism. As shown by T. Saitoh et al, Mn^{4+} is strongly hybridised and the charge transfer effect realizes a mostly $3d^4$-ligand configuration with one electron coming from oxygen atoms. The contribution to XLD is so strongly reduced[45].
We then focus on the Mn^{3+} dichroism simulations. Using the Missing package, we consider the transition from $2p^6 3d^4$ (Mn^{3+}) to $2p^5 3d^5$ state (Mn^{3+*}). The crystal field effect is taken into account by setting the CFT splitting parameters Δ ($10Dq$), Ds and Dt, related to the splitting if the $3d$ levels as shown in figure 1.2. The magnetic contribution, both in circular and linear dichroism calculations, is introduced by adding the magnetic exchange interaction (Ex. in figure 3.48).
In figure 3.48 the simulated XLD spectra of Mn^{3+} are reported for fixed crystal field splitting and for different values of the magnetic exchange energy. In this case we are considering elongated octahedra ($Ds, Dt > 0$). The Missing package allows to only consider the spin oriented along the z axis. The simulation very well describes (at least in shape) the orbital ordering contribution as observed, for example on compressively strained LSMO thin films on $LaAlO_3$ [46], thus showing a $3z^2 - r^2$ preferential occupation. On the other hand, the magnetic contribution does not always reproduce the observed behaviour, and more complex calculations may be needed, as the ones reported in ref. [43].

3.6.7 Resonant inelastic X-ray scattering (RIXS)

X-ray emission (XES) is a second type of X-ray spectroscopy. It is also divided in normal X-ray spectroscopy (NXES), where an electron is kick from the photon to complete ionization, and resonant X-ray spectroscopy (RXES), where the energy of the photon is large enough to resonantly excite an inner shell electron to a higher unoccupied excited state of the atom (final state of X-ray absorption).
This leaves behind a hole in the core level. Relaxation of the core-hole state takes place with a transition of an inner shell electron, together with the emission of an X-ray photon.
This is the physical process behind the resonant inelastic X-ray scattering. Unlike the usual X-ray absorption and emission processes, RIXS is a second order process; it incorporates both absorption and the subsequent emission. RIXS process is both temporally and spatially coherent. The spatial coherence implies that signal from equivalent atoms in the system are obtained, hence RIXS is element specific. There exist a variety of experimental tech-

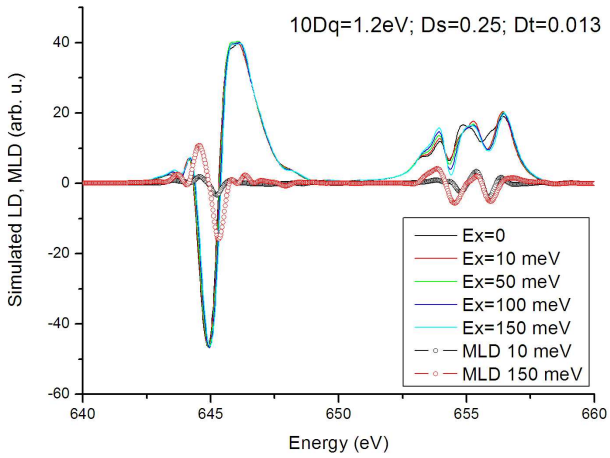

Figure 3.48: XLD simulation of Mn^{3+}. The $10Dq, Ds$ and Dt values are reported. Positive Ds and Dt values indicate that we are considering elongated octahedral environment. MLD curves represent the magnetic-only contribution, obtained by substracting the curve calculated for zero exchange energy from the other curves.

niques which use these advantages of RIXS to give information on the electronic system symmetry, spin and element specifically[47].

3.6.8 The samples

The samples are the $(LaMnO_3)_{2n}(SrMnO_3)_n$ ($(LMO)_{2n}(SMO)_n$) superlattices deposited on $SrTiO_3$ (STO) substrates with $n = 1, 5, 8$, described in section §1.2.4 and in ref.s [16, 28].
The samples have been grown by MBE, by using the shuttered deposition technique with RHEED stoichiometry control[34] described in section §2.1.5, as reported in ref. [16]. The $LMO)_{2n}(SMO)_n$ periods were repeated in each deposition until a total thickness of about 23 nm was reached.
In figure 3.49, the $\theta - 2\theta$ patterns XRD patterns of the superlattices with $n = 1-4$ are reported. The high angle XRD pattern of superlattices is characterized by principal peaks corresponding to the average lattice spacing of the superlattice and by satellite peaks that correspond to the reflections:

$$2\frac{\sin\theta_{peak}}{\lambda} = \frac{1}{\bar{d}} \pm \frac{n_S}{\Lambda}, \tag{3.9}$$

where $\bar{d} = \frac{N_A d_A + N_B d_B}{N_A + N_B}$ is the average lattice spacing ($d_{A,B}$= lattice spacing and $N_{A,B}$= number of unit cell of (A,B) material), Λ is the superlattice wavelength $\Lambda = N_A d_A + N_B d_B$ and n_S is the order of the satellite.
The large number of satellite peaks and their small width indicate that the structural correlation length of the superlattice is large[48].
All superlattices are coherently strained: all of them are forced to the in-

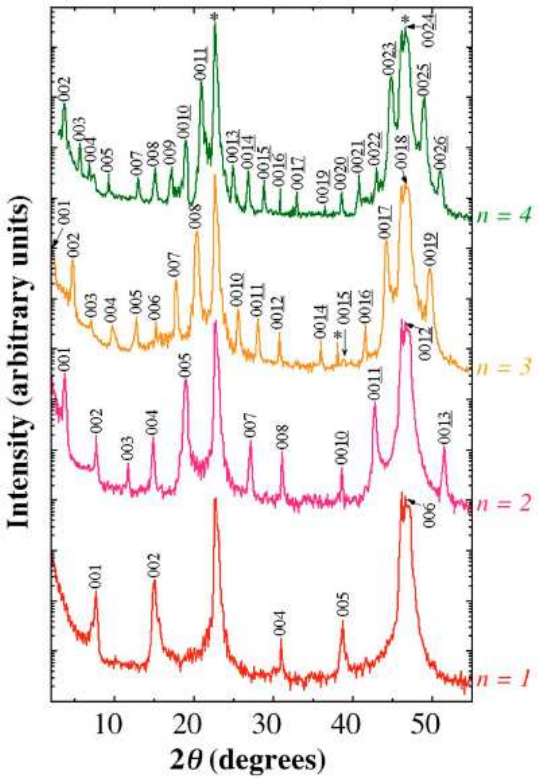

Figure 3.49: X-ray diffraction $\theta-2\theta$ patterns of the $n = 1$, 2, 3, and 4 superlattices grown on (100) SrTiO3. Substrate peaks are marked with (*). The superlattice wavelengths were calculated to be 11.63 ± 0.09 Å, 23.14 ± 0.57 Å, 34.81 ± 0.49 Å, and 46.2 ± 1.1 Å respectively. From ref. [16]

plane lattice parameter a of the STO substrate (3.905 Å) and to an average out-of-plane parameter $\bar{c} \approx 3.87$ Å. As a consequence, the LMO blocks are subjected to compressive strain (+2.2%) and the SMO blocks to tensile strain (-2.6%). Indeed 200 Å thick films of LMO and SMO on STO substrate show c-axis values about 3.93 and 3.78 Å, respectively[21]. The average ratio between out-of-plane and in-plane lattice parameter is $\bar{c}/a < 1$, indicating a compressive tetragonal distortion, while looking at the constituent block, we have an elongation for LMO ($c_{LMO}/a > 1$) and a compression for SMO ($c_{SMO}/a < 1$).

3.6.9 Experimental setting for the XAS experiment.

The XAS measurements have been performed at the ID08 beamline of the European Synchrotron Radiation Facility (Grenoble, France), which is based on AppleII undulator source (allowing a full control of linear and circular polarization) and a high scanning speed spherical grating monochromator (Dragon type).
The sample was mounted in a liquid He cryostat, allowing to vary the temperature to 300K to 4.2K. The sample holder keeps the sample in vertical position in the laboratory reference system, and can rotate in order to have normal and grazing incidence (corresponding to 30° respect to the sample surface) of the X-ray beam.
A magnetic field, parallel to the incident beam direction, was applied by means of a superconducting magnet, and the absorption signal was measured by total electron yield (TEY). The application of the magnetic field is necessary to polarize the spins in the beam direction for the XMCD and XMLD measurements.
In particular the XLD measurement is performed in grazing incidence (GI), by subtracting the XAS signal in vertical (V) and (H) polarization. In the system used, V and H are referred to the laboratory reference, so that in V polarization the electric field lies in the sample plane, while in H polarization it is oriented nearly along the substrate plane (as the GI angle is not zero), as shown in figure 3.50.
For the The XMCD measurements can be performed both in grazing (GI) and normal incidence (NI) configuration. In GI the spins are polarized in plane, while in NI they are out of plane, so that the magnetic easy axis can be identified. As explained in §3.6.2, the XMCD can be obtained as the difference between the absorption between (L = negative helicity) and right polarized (R = positive helicity) photons or by the difference of the absorption of single polarized photons (L or R) by changing the sign of the applied magnetic field (+ or -). In order to have a better statistics, the dichroic signal is calculated as:

$$I_{XMCD} = I(L^+) - I(R^+) + I(R^-) - I(L^-), \tag{3.10}$$

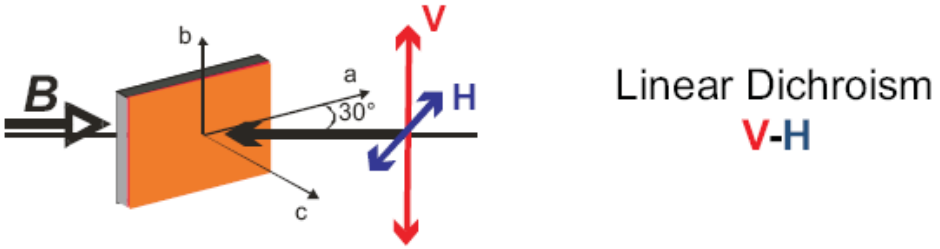

Figure 3.50: Experimental geometry for grazing incidence x-ray absorption spectroscopy: V and H represent the vertical and horizontal linear polarisation, which correspond roughly to investigate the in-plane and the out-of-plane directions in the perovskite structure of the sample. The B vector represents the direction of an external magnetic field that can be applied parallel to the x-ray beam. From ref. [43]

$L(R)^{+(-)}$ indicates left (right) polarized photons with positive (negative) magnetic field. The angle Θ between the magnetic moment and the photon helicity in equation 3.6.2 is always 0 or π as the applied magnetic field polarises the spins in the beam direction.
In order to evaluate the magnetic contribution in linear dichroism spectra, XLD has been measured at 300K (room temperature), where the magnetic contribution of FM and AFM phases is negligible or absent, and at low temperatures (this usually corresponds to above and below the transition temperatures T_C and $T_{Néel}$). The room temperature spectra contains only the XNLD contribution, that can be subtracted from the low temperature data in order to obtain the only magnetic contribution, in the hypothesis that the orbital contribution is not temperature dependent.
Furthermore the XMLD contains the FM and AFM anisotropy contributions. In order to remove the FM contribution, a magnetic field large enough to saturate the FM spins is applied in the beam direction. In the measurement configuration represented in figure 3.50, this corresponds to orient the spins in the direction perpendicular to both V and H polarization, so that the FM spin contribution is removed. The AFM spins are supposed to possess higher anisotropy energy, so that they do not rotate with the application of field. In conclusion, the XMLD measured at B=0T contains both FM and AFM anisotropy contribution, while the one measured at B=1T only contains the AFM contribution.
Prior to any dichroism evaluation, in all the XAS measurements at the Mn $L_{2,3}$ edge, a constant background was fitted to the pre-edge region of the L_3 edge and subtracted from the spectra, which are then normalized to the edge jump set to unity above the L_2 edge. Furthermore, to compare the XMCD and XLD from different samples, the dichroism was normalized to the maximum of the sum of the XAS signals with different polarization.

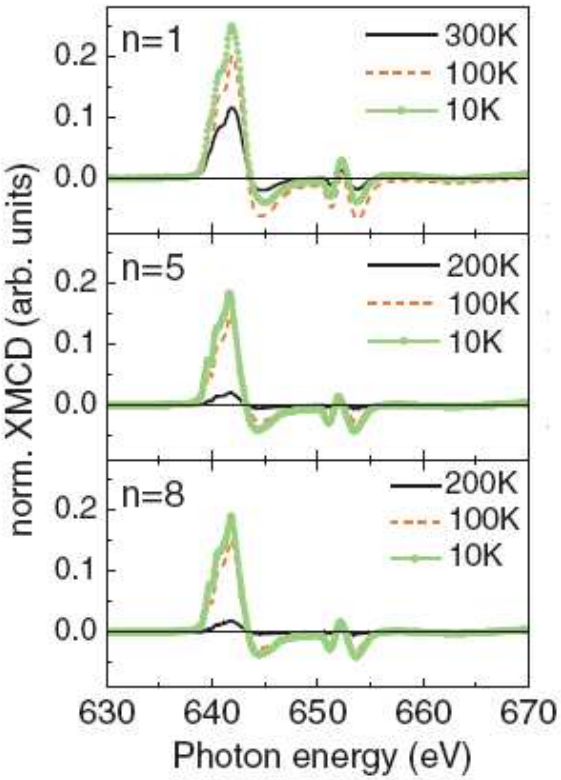

Figure 3.51: XMCD results at grazing incidence with an applied magnetic field of 1 T and at different temperatures for SLs with $n = 1$, 5, and 8. The XMCD results are normalized to the sum of the XAS L_3 peak height signals.

3.6.10 XMCD: magnetic easy axis and coercivity

In figure 3.51 the XMCD spectra of the $n = 1, 5$ and 8 samples are reported for 10, 100 and 300K temperatures. The $n = 1$ samples shows a relevant XMCD intensity also at 300 K, as the Curie temperature of the $n = 1$ sample is above room temperature[16], as shown in figure 1.16.
Without resorting to the sum rules, 3.6 and 3.7, the hysteresis cycles of the samples can be measured by measuring the XMCD at various applied field, and by taking the value of the maximum of the XMCD at any field. This value will be $\propto m$, the Mn magnetic moment. As the sum rules fail in giving a correct quantitative estimation of the magnetic moment of transition metals such as Mn, the obtained hysteresis cycles have been normalized to unity. Indeed in this case we are mainly interested to features of the hysteresis cycle, such as the saturation and the coercive field.
In figure3.52 the magnetic hysteresis cycles, obtained by the XMCD spectra in NI and GI, are reported. In the right panel, the saturation magnetization M_S value for different n is also reported.

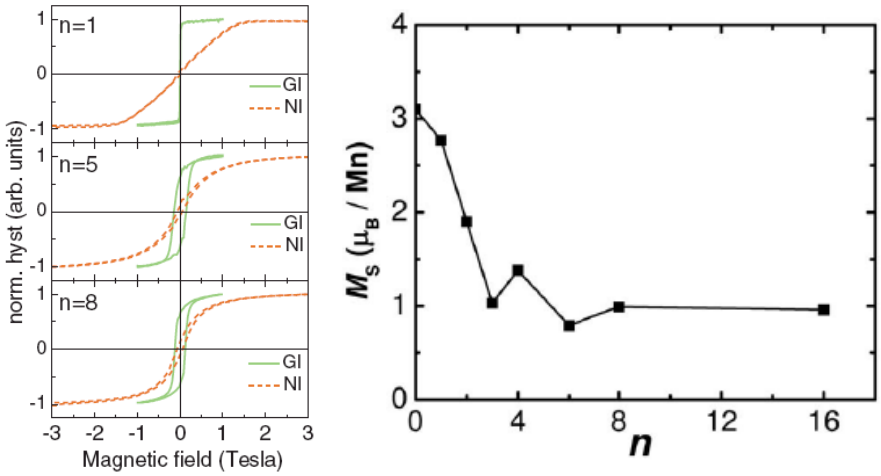

Figure 3.52: Left: Hysteresis loops at 10 K obtained by the maximum peak intensity of the XMCD (about 642 eV) as a function of the applied magnetic field. The curves are normalized to unity for a better comparison of the coercive fields. Right: Saturation magnetization M_S values for the superlattice series as reported by ref. [16]. The $n = 0$ point indicates the M_S of the alloy $La_{2/3}Sr_{1/3}MnO_3$.

It can be observed that FM easy axis is mostly oriented in the *ab* plane. This FM anisotropy resembles that one induced by the magnetocrystalline anisotropy in the LSMO films under tensile strain. The most interesting result is that the anisotropy ratio is larger in the SL with $n = 1$, where the density of FM interfaces is highest, and decreases with n.
Another interesting value is the increase of the coercive field for the samples $n = 5, 8$ respect to the samples with $n = 1$. The increase of the coercive field is not monotonic with n. However also the M_S value is not monotonically decreasing for the $n = 5, 8$ samples.
In the work of Zhao et al.[49] on the same superlattice system, large hysteresis cycles are reported for the samples with $n = 2, 3, 5$. These large hysteresis are interpreted in terms of competing AFM/FM interactions with magnetic pinning, frustration and canted order.
In order to obtain information on the AFM content in the samples, we have to resort to linear dichroism measurements.

3.6.11 XMLD: AFM phase and its anisotropy.

In the left panel of figure 3.53 the XMLD of the samples is reported, obtained as the difference between the low temperature XLD and the high temperature one (300 K for $n = 1$ and 200 K for $n = 5, 8$). In all samples we find an important AFM contribution to XLD. As we can see from the graphs in the left panel, the B=0 T and the B=1 T, for the $n = 1$ sample the curves have similar shape and different intensities, while for the $n = 5$

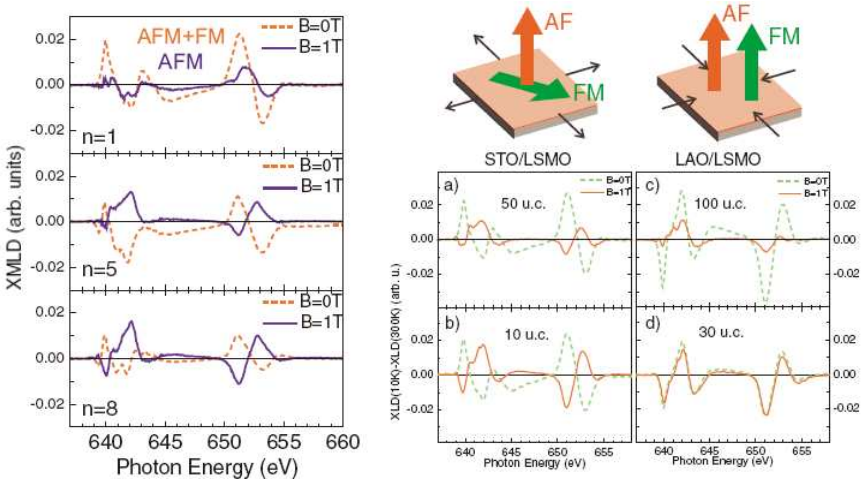

Figure 3.53: Left: Difference between the XLD spectra taken at 10 K and 300 ($n = 1$) or 200 K ($n = 5, 8$), with B=0 T and B=1 T. Only the magnetic contribution is present in the spectra. All spectra are normalized to the sum of the XAS L_3 peak height signal. Right: XMLD spectra of LSMO thin films on STO and LAO, reported for comparison. The FM and AFM easy axes in the two cases are also represented in the upper cartoon. From ref.[46].

and 8 samples the B=0 T is inverted (it changes sign) when the magnetic field is applied.

For comparison the results of the XMLD from the work by Aruta et al. [46] on $La_{0.7}Sr_{0.3}MnO_3$ (LSMO) samples is reported. The authors of ref.[46] interpret their data as shown in the cartoon in the right panel of figure 3.53. The data can be simply interpreted as following: as the FM easy axis of all our samples is in plane (from XMCD measurements) an inversion of the XMLD curves indicates that the AFM easy axis is orthogonal to the FM one. So, in the $n = 1$ sample, the FM and AFM easy axes are in plane, while in the $n = 5$ and 8 samples the AFM easy axes is oriented out of the plane.

This simple interpretation is supported by atomic multiplet simulations of XMLD, as reported, for example, in ref. [43].

Out-of-plane local spin AFM direction has been also observed on LMO single films belonging to the same series of samples of the superlattices (see ref. [16]).

Looking at the XMLD integrated intensities in figure 3.54, we can see that the AFM contribution is increasing with decreasing number of the interfaces. Correspondingly, from the M_S values in figure 3.52, the saturation magnetization is roughly decreasing.

We can then attribute the FM contribution to the interfaces, and the AFM contribution to the bulk of the constituent blocks, that become thicker with increasing n.

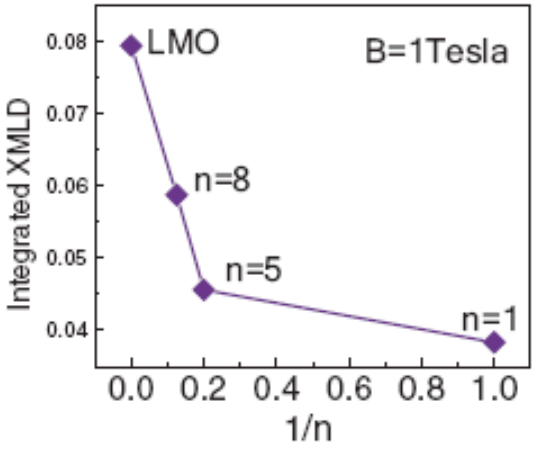

Figure 3.54: Integral of the absolute value of the XMLD curves at B=1 T with respect to $1/n$.

For the $n = 1$ superlattice the SMO layer is reduced to a SrO layer sandwiched between two interface MnO_2 layers. We then deduce that the AFM signal cannot come from the SMO, but rather from the LMO part of the superlattice. The schematic drawing in figure 3.55 depicts that, for very thin constituent blocks such as $n = 1$, the AFM local spin direction is pinned to a mainly in-plane orientation by the interfacial FM anisotropy. The AFM content is responsible for the reduced Bohr magnetons number in the $n = 1$ sample, about $3.0\mu_B$/Mn (from ref [16]) compared with the optimal $3.7\mu_B$/Mn value of the LSMO films.
For higher n, such as 5 and 8, the AFM contribution can come from both the SMO and LMO blocks, as theoretically predicted by Nanda and Satpathy [31] (see figure 1.21).
Here in figure 3.55, we attribute the detected AFM signal to the LMO block, by considerations about the strain and the orbital occupation, and also because the same anisotropy is observed in the LMO single film.
The orbital occupation in the superlattices is discussed in the next section.

3.6.12 Orbital occupation and charge density.

In figure 3.56 the XLD spectra at high temperature of the $n = 1, 5, 8$ samples are reported together with the XLD of the LMO sample.
The XLD of the $n = 1$ sample can be identified with the one of Mn^{3+} in a tetragonally compressed octahedron, when the $x^2 - y^2$ $3d$ orbital is energetically favoured (as represented in figure 3.56). Conversely the $n = 5$ and 8 samples and the LMO film show the features of the $3z^2 - r^2$ preferential occupation, that is stabilised in tetragonally elongated octahedra. This is indeed the case of the single film LMO, that is compressively strained on the

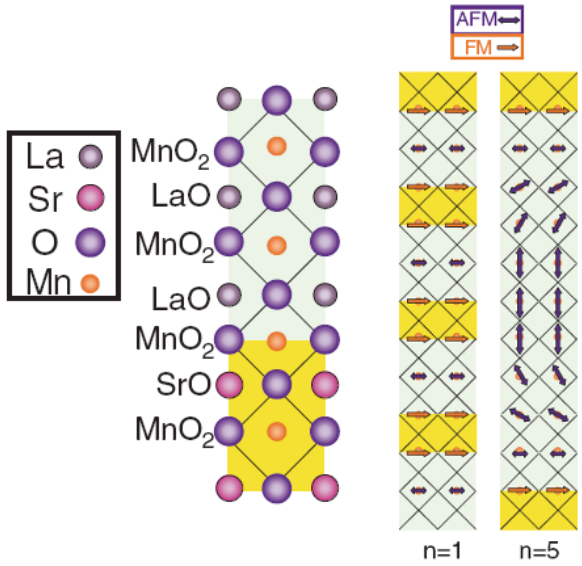

Figure 3.55: Schematic drawing of the local spin orientation hypotized in the superlattices is reported. The length of the arrows is roughly proportional to the magnetic (AF or AFM) content of the MnO_2 layers.

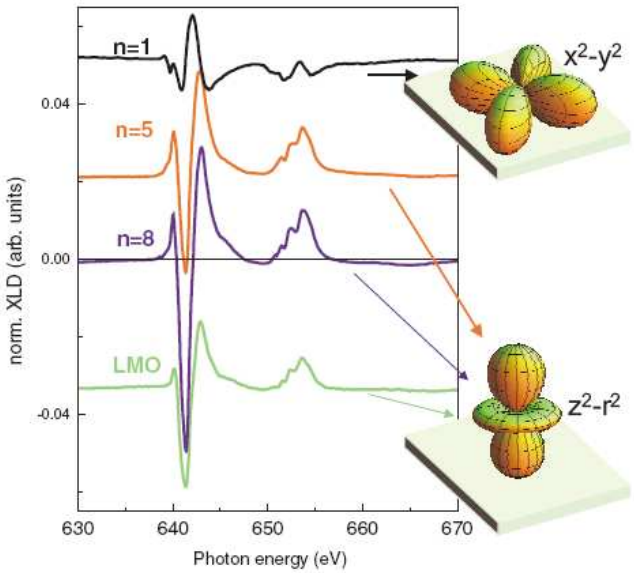

Figure 3.56: XLD spectra at 300 K for $n = 1$ SL and 200 K for $n = 5$ and 8 SLs and the LMO film. The spectra are reported as the difference of the XAS measurements with vertical (v) and horizontal (h) polarizations in grazing incidence configuration and normalized to the sum of the XAS L_3 peak height signals.

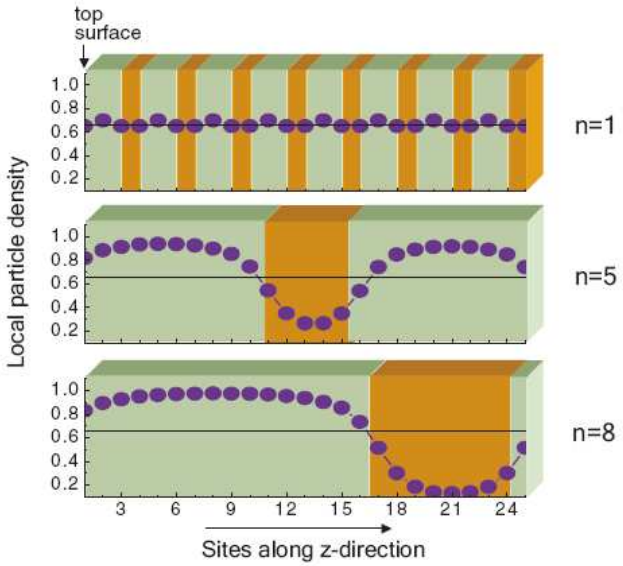

Figure 3.57: Schematic drawing of the top part of superlattices measured by total electron yield, together with the spatial charge density (blue dots) along the samples, calculated as described in the text. Green and orange zones represent LMO and SMO constituent blocks, respectively.

STO substrate, so that the octahedra elongate in the out-of-plane direction. The superlattices, on the other hand, experience a modulated strain, with the LMO compressed in plane, while the SMO experiences an even larger tensile strain (see section §3.6.8).

To better understand the behaviour of the XLD, we resort to theoretical calculation, carried on by the group of Prof. Cataudella of University of Naples, now reported in ref. [21]. In figure 3.57 the calculated particle density as a function of the Mn site are reported. The results are based on density calculations made within a self-consistent Hartree approach for the considered superlattices. In figure only the depth of the samples that can be probed by the TEY measurement is represented.

As we can see from the particle density of $n = 5$ and 8 samples, the Mn ions in the SMO blocks are mainly in a $3d^3$ configuration, i.e. the e_g electron density is nearly zero. As shown by T. Saitoh et al, Mn^{4+} is strongly hybridised and the charge transfer effect realizes a mostly $3d^4$-ligand configuration with one electron coming from oxygen atoms. The contribution to LD is so strongly reduced. Then the XLD signal in these samples mainly comes from the LMO blocks, that are compressively strained.

Another striking characteristic of the XLD spectra is that, counterintuitively, the XLD of the LMO single film is less intense than the one of the $n = 8$ sample. However it has to be considered that the LMO single film

gradually relaxes the substrate induced strain along his thickness, while in the superlattices severely strained interfaces are present, resulting in more strained LMO blocks.
In the $n = 1$ superlattice, conversely, the particle density is homogeneously distributed in all the sample. The contributions from LMO and SMO blocks cannot any longer be distinguished, the e_g electron-density distribution becomes almost constant and equal to the average density. The strain does not act in opposite way on LMO and SMO, but the system responds as a whole to the average strain that is slightly tensile, and the eg $x^2 - y^2$ orbitals get stabilized as in LSMO grown on STO.

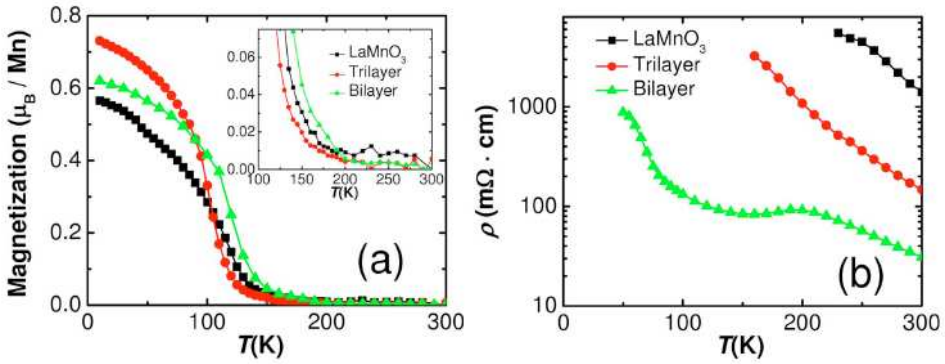

Figure 3.58: Field-cooled magnetization in an in-plane magnetic field of 1000 Oe and (b) resistivity as a function of temperature for an $LaMnO_3$ thin film, an n=16 sample (bilayer), and a $LaMnO_3$ /$SrTiO_3$/$SrMnO_3$ sample (trilayer). Magnetization details are shown in the inset. From ref. [16].

3.7 $La_xMnO_{3-\delta}$ thin films on STO: transport, magnetic and orbital properties.

The data shown in §3.6 clearly indicate that for long-period $(LaMnO_3)_{2n}(SrMnO_3)_n$ superlattices, the magnetic properties and the e_g orbital occupation are mainly determined by the properties of the LMO blocks.
This is also confirmed by data reported in the paper by Adamo et al. [16], that performed an interesting experiment on the $n = 16$ superlattice, that is a $(LaMnO_3)_{32}(SrMnO_3)_{16}$ bilayer. This sample contains only one interface, and its M_S has about the same value respect to the $n = 8$ superlattice (2 interfaces) and the LMO single film (no interfaces). The authors also deposited a trilayer sample, where the $(LaMnO_3)_{32}$ and $(SrMnO_3)_{16}$ blocks are separed by 5 unit cells of STO, so that the charge transfer at the interface is inhibited. The magnetization versus temperature measurements, shown in figure 3.58, indicate that only a slight increase in the T_C distinguish the bilayer from the trilayer behaviour. Furthermore both behaviours are very similar to the LMO single film one. Conversely, the presence of a metallic interface significatively affects the transport properties, as evidenced by the right panel of figure 3.58.
$LaMnO_3$ is an interesting "ingredient" not only in manganite based superlattices, but also in other superlattice systems, such as $LaMnO_3/SrTiO_3$ superlattices. For example, a new kind of Ti^{3+} ferromagnetism at LaMnO3/SrTiO3 interfaces, consequence of the charge transfer, has been recently observed by García-Barriocanal et al.[50].
However, in the study of superlattice systems it is crucial to be able to disentangle the interface effects from the ones arising in the LMO itself as a consequence of strain or stoichiometry defects.

As already pointed out in section §1.2.2 and §1.2.3, even a light hole doping originating either from La:Mn unbalancing or from oxygen non stoichiometry can rapidly cast the LMO to ferromagnetic state.
In order to better understand the behaviour of self-doped LMO, we prepared several series of $La_xMnO_{3-\delta}$ samples, by varying both the La:Mn ratio (i.e. x) and the oxygen content (i.e. δ). The samples were prepared by MBE codeposition on several substrates, here we will focus on the ones deposited on $SrTiO_3$, showing the highest T_C values as a function of doping. La:Mn ratio in our samples is ranging from 0.66 to 1.07. Oxygen content is provided by annealing procedures in air. Different oxygen contents are obtained by varying the annealing temperature. Unfortunately it is not possible to measure the oxygen content in thin films, so that δ remains unknown. However we know that more oxygen is absorbed (i.e. δ decreases) at higher annealing temperature.
Also for these samples X-ray absorption spectroscopy measurements at the Mn (and O) edge were performed at the ID08 beamline of the European Synchrotron Radiation Facility. The experiment were performed using the same experimental setting described in section §3.6. Furthermore resonant inelastic X-ray spectroscopy measurement were also performed, as described in the following.

3.7.1 Issues regarding stoichiometry dependant self-doping

It is useful to present how a variation in the La:Mn ratio and/or in the oxygen content determines the Mn^{4+} concentration in $La_xMnO_{3-\delta}$. In doing so, some information is necessary about the crystalline structure of non stoichiometric LMO compounds; this information is provided by the work of Wołcyrz et al. on powder samples, analyzing the structure of non stoichiometric compositions by neutron diffraction, and measured the corresponding manganese valence by iodometric titration[51].

La:Mn ratio $x < 1$

In samples with $x < 1$ La vacancies are present. If only La vacancies are present, i.e. all Mn and O oxygen sites are occupied, part of Mn^{3+} has to oxidize Mn^{4+}. The average manganese valence y is given by:

$$La_x^{3+}Mn^{y+}O_3^{2-} \Rightarrow 3x + y - 6 = 0 \Rightarrow y = 6 - 3x; \tag{3.11}$$

corresponding to an amount of Mn^{4+} ions equal to $3(1-x)$, i.e. in this situation the Mn^{4+} content increases at three times that of the La vacancy. In this situation a $x = 0.67$ sample would contain no Mn^{3+} at all.
From the work of Wołcyrz et al. we know that when La vacancies are present, in the La_xMnO_3 structure some Mn can occupy the La site, i.e. the

perovskite A site. The authors report on a $x = 0.91$ sample, annealed in air at 1270K. In this sample they find that about the 16% of La vacancies in the A site are occupied by Mn ions, so that the formula of the sample is: $[La_{0.922}\ Mn_{0.013}\ ]MnO_3$. At this high annealing temperature, the authors find that the oxygen sites are fully occupied.
The La-Mn substitution in the A-site allows for a reduction of the oxidation of Mn in the B site, as the authors verify from iodometric titration.

La:Mn ratio $x = 1$

When $x = 1$ the Mn valence should be exactly 3+. However the authors of ref. [51] report findings for this composition, in samples annealed at 830 K, of a Mn valence equal to 3.500.
This high Mn valence is interpreted in terms of oxygen excess. Indeed $LaMnO_3$ is the only perovskite that exhibits a substantial excess oxygen. The only way to accommodate this excess oxygen in the structure is through simultaneous vacancies in the A and B sites.
The formula found for their $x = 1$ sample is $La_{0.941}Mn_{0.941}O_{3.059}$, where some oxygen (0.059) exceeds the perovskite oxygen sites, equal to about 50% of the total cationic vacancies. This oxygen can be located in interstitial sites thanks to the presence of the cationic vacancies[51].
As a consequence of substantial excess oxygen and cationic vacancies, the Mn valence is even higher than that found in the $x < 1$ sample (i.e. the 50% of the Mn^{3+} is converted to Mn^{4+}).

La:Mn ratio $x > 1$

When $x > 1$, manganese vacancies are present. If all the other sites are occupied, the situation would be the following:

$$La_1^{3+}Mn_{1/x}^{y+}O_3^{2-} \Rightarrow 3 + y/x - 6 = 0 \Rightarrow y = 3x, \tag{3.12}$$

i.e. the Mn valence would be three times the La:Mn ratio.
However in ref.[51] an $x < 1$ sample annealed at 1070 K is also found to contain some excess oxygen (equal to the 62% of the nominal deficiency on the Mn site). Mn-La substitution in the B site is not possible due to the fact that the large La ions are unacceptable in the B octahedral sites.
The presence of excess oxygen contributes to an increase in the Mn valence in the following way:

$$La_1^{3+}Mn_{1/x}^{y+}O_{3+\Delta}^{2-} \Rightarrow 3 + y/x - 6 - 2\Delta = 0 \Rightarrow y = 3x + 2\Delta, \tag{3.13}$$

where Δ is the excess oxygen, that may result from either simultaneous cationic vacancies or by interstitial oxygen[51].

Self-doping and magnetic properties: bulk versus film behaviour

Wołcyrz et al. [51] analyze samples with a La:Mn ratio ranging from $x = 0.91 \div 1.11$. In principle, due to the fact that in our samples the x range extends to lower values, we cannot know if the results from ref. [51] can be applied to our samples.
Joy et al. [52] studied the La-deficient compositions of LMO in bulk samples, sintered by MnO_2 and La_2O_3 powders, and identified the limiting value of x in (1-1/8 = 0.875). Beyond this limit, the Curie temperature of the compounds (as these samples show a ferromagnetic ground state) saturates, and Mn_3O_4 impurities are formed via the unreacted MnO_2 (as the samples are sintered at 1200°C in oxygen, and Mn_3O_4 phase is formed from any Mn oxide when heated above 1000-1100°C).
However Gupta et al. [53], obtained quite different results from La_xMnO_3 thin films deposited on $SrTiO_3$ substrates by PLD. Indeed they found an increase of the Curie temperature from 115 K ($x = 1$) up to 240 K for the $x = 0.75$ sample, and a slight decrease for the $x = 0.67$ sample.
This indicates that in this case the self-doping is still effective beyond the limit fixed by Joy et al.[52]. This is most probably a consequence of epitaxial stabilization, allowing the LMO structure to stabilize even in presence of a large number of vacancies.
The T_C=240 K is from an as grown $x = 0.75$ sample, as the other film of the series. However, the authors also show that the T_C values increase when the samples are annealed in O_2 at 850°C. The annealed $x = 0.75$ sample has Curie temperature close to 300 K.
As discussed above, non-stoichiometric LMO composition are all characterized by the presence of Mn^{4+}. As a consequence most of compositions show ferromagnetic properties.
An interesting finding is that the T_C rapidly decreases for $x > 1$, despite a consistent number of Mn^{4+} ions present in these samples. Conversely the $x < 1$ samples show high T_C values[54].
The magnetic interactions in ferromagnetic manganites are usually attributed to the DE mechanism. The concentration of Mn^{4+} ions is a crucial factor, as the Mn^{4+}-O-Mn^{3+} FM interaction must prevail on the Mn^{3+}-O-Mn^{3+} AFM one. When $x > 1$, Mn^{4+} increases as a consequence of Mn vacancies, but at the same time a number of Mn-O-Mn paths are broken, thus reducing the interaction strength[51, 54].
On the other hand, in $x < 1$ samples, vacancies occur in the La sites, not participating in the interaction. Furthermore, the occupation of La sites by Mn ions, reduces the amount of Mn^{4+} necessary to compensate the oxygen charge. Indeed an excess of Mn^{4+} would rather push the system to AFM behaviour, as observed in manganites when hole content (i.e. Mn^{4+} content) is above 0.5.
Epitaxial strain can be helpful in this sense: it allows to stabilise structures

with a lower x value, and may also allow the acceptance of an higher fraction of Mn ions at the A site. At the same time it could act in the opposite way on interstitial oxygen.
The oxygen acts in an opposite way with respect to La-Mn substitution, as it contributes to increase the Mn valence. However in oxygen deficient samples, any magnetic interaction is reduced as there is a reduction in the number of Mn-O-Mn bonds.
Excess oxygen acts in two opposing directions: it increases the Mn^{4+} content, but at the same time it is accompanied by simultaneous vacancies on the A and B sites.

3.7.2 Transport properties of $La_xMnO_{3-\delta}$ thin films: the key role of oxygen content

The transport properties of our $La_xMnO_{3-\delta}$ samples have been studied both as a function of x and as a function of the annealing temperature, that correspond to oxygen content. The results of these studies are resumed by the paper by Orgiani et al. ref. [55].
LMO thin films were fabricated by MBE co-deposition in the University of Salerno MBE deposition system. Such a technique easily allowed us to vary the stoichiometry ratio La/Mn by changing the evaporation rate (i.e. the cell temperature) of the single elements. All the depositions were performed under a O_2+5%O_3 mixture pressure of about 2×10^{-6} mbar for 1 h duration, resulting in about 30 nm thick films. In order to vary the oxygen content, LMO thin films were postannealed in air and/or vacuum, by varying the temperature and the time of postannealing.
According to neutron diffraction analysis, at room temperature, $LaMnO_3$ shows an orthorhombic structure (Pbnm space-group) with lattice parameters $a = 5.5367$ Å, $b = 5.7473$ Å, and $c = 7.6929$ Å. However, non stoichiometric samples (x=0.91 to 1)[51] are found to possess a $R\bar{3}c$ coordination with $a = 5.5401$ Å and $c = 13.3677$ Å (by using hexagonal setting). With respect to this last, along the $[20\bar{4}]$ direction, LMO shows a pseudo-perovskite cell with an in-plane squared coordination of Mn atoms and Mn-Mn distances of $a = b \approx 3.90$ Å.
So, while stoichiometric LMO would experience compressive strain on STO substrates, most of non stoichiometric LMO is expected to experience negligible strain.

In figure 3.59 the $\theta - 2\theta$ scan of the samples annealed at the highest temperature of 1030°C (i.e. with the higher oxygen content) are reported. The out-of-plane pseudo-cubic lattice parameter c decreases with decreasing x. It is worth to remark that in these samples the c axis is always smaller than the substrate one, in contrast with the findings on the LMO samples belonging to the superlattice series described in the previous section.

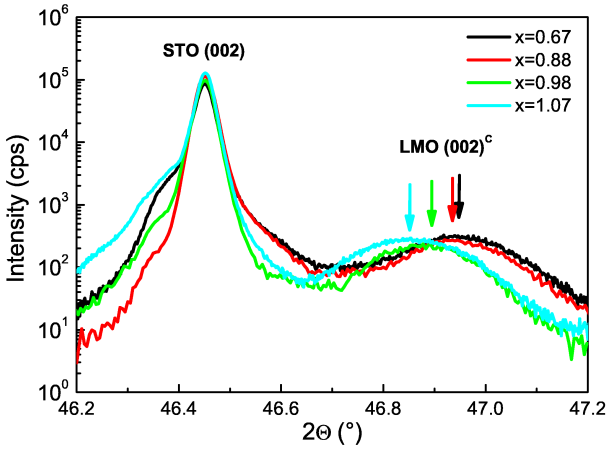

Figure 3.59: $\theta - 2\theta$ scan of LMO samples with $x = 0.67$ to $x = 1.07$ annealed at the highest temperature (1030°C).

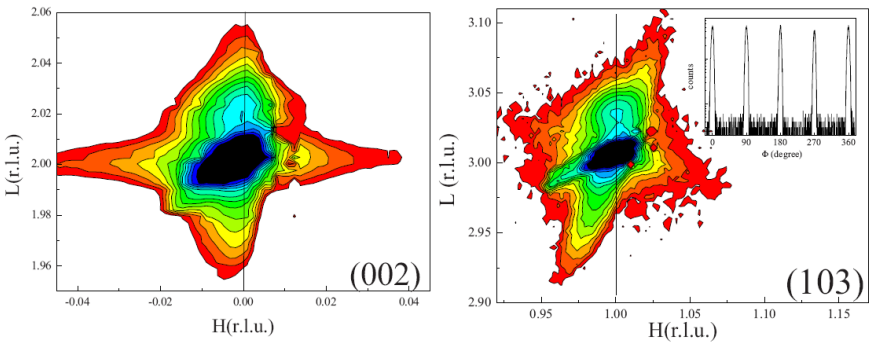

Figure 3.60: Reciprocal space map converted to relative lattice units for the $x = 0.88$ sample, showing the in-plane matching of LMO film on the STO substrate.

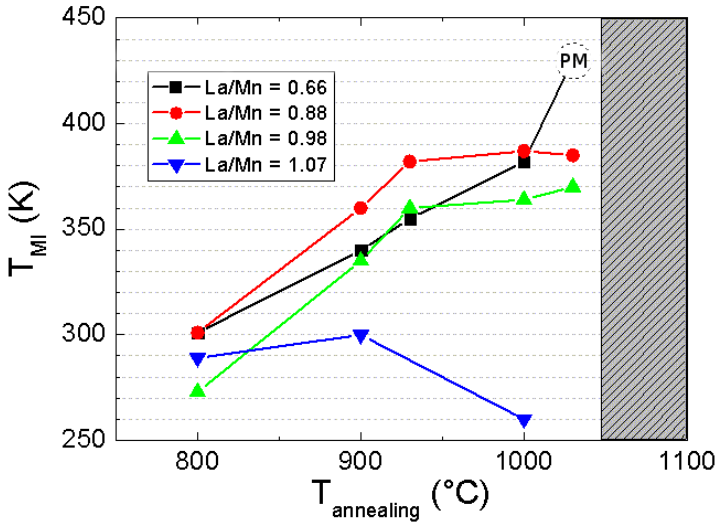

Figure 3.61: Metal-insulator transition temperature (T_{MI}) as a function of the annealing temperature for samples characterized by different La/Mn ratio. The sample $x = 0.66$ annealed at higher temperature (1030°C), becomes paramagnetic metallic (PM). The hatched area represent the temperature above which the samples are decomposed.

In figure 3.60, the reciprocal space map of the $x = 0.88$ sample is reported, showing that the film and substrate are matched in plane.
The c axis is shown to decrease with increasing annealing temperature, indicating oxygen absorption. This is verified by annealing in vacuum a sample: when oxygen is removed, an elongation of the c-axis is found[55].
In figure 3.61, the T_{MI} of the samples is shown as a function of the annealing temperature, for an annealing duration of 54h. The T_{MI} is defined as the maximum temperature of the resistance vs temperature curve R(T). In particular, for the sample $x = 0.66$, the R(T) curve shows no maximum at the higher transition temperature, so that also the high temperature state of the sample is metallic. Conversely, the $x = 1.07$ sample is pushed to insulating state with increasing oxygen content.
It is interesting to note that the T_{MI} values obtained in these samples, thanks to the annealing procedure, are higher than the ones reported by Gupta et al. [53] in their as grown samples.
In order to verify that this correspond to enhanced T_C, we have to resort to magnetic measurements.

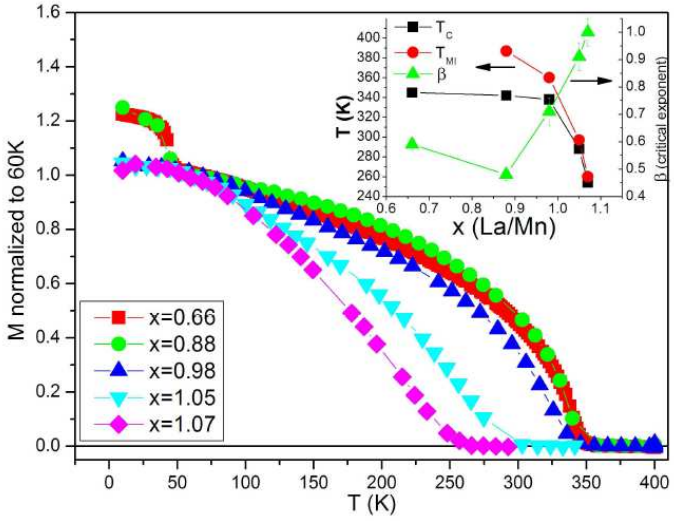

Figure 3.62: Normalized M(T) curves of the samples. The measured magnetic moment has been normalized to the 60 K value after the subtraction of the paramagnetic and instrumental offset contribution (i.e. the magnetic moment measured above the onset temperature of ferromagnetism). In the inset the Curie temperature and critical exponent obtained by the fitting described in the text together with the metal-insulator transition temperature T_{MI} are shown.

3.7.3 Magnetic properties of optimally oxygenated $La_xMnO_{3-\delta}$ thin films

In this section the magnetic measurements on the series of samples annealed at higher temperature are reported. We will refer to this series as the optimally oxygenated one, as the highest T_{MI} values are obtained. The study of the magnetism is mandatory to complete the sample characterization in the framework of DE model of manganites.
The magnetic measurements have been measured in the SQUID magnetometer system of CRISMAT laboratory of the ENSICAEN, thanks to the collaboration of the group of Dr. W. Prellier.

In figure 3.62 the M(T) curves of the samples are reported. In the inset the T_C values are reported. To obtain them, the M(T) curves were fitted by the function:

$$M(T) = M_0(1 - T/T_C)^{\beta}, \tag{3.14}$$

where M_0, β and T_C are fitting parameters. The fit was effectuated in the vicinity of the critical temperature. The parameter β is the critical exponent.
The results of the fittings are reported in the inset of figure 3.62. The highest Curie temperature is 345 K, obtained for the $x = 0.66$ sample. So the magnetic measurements confirm that the enhancement of the T_{MI} (also re-

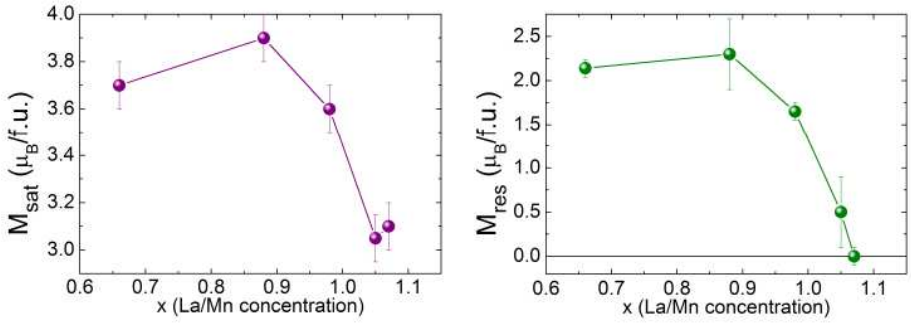

Figure 3.63: Saturation magnetization (M_{sat}) and residual magnetization (M_{res}) as a function of La/Mn content, as obtained by the saturation and remnant values in the hysteresis cycles at 10 K.

ported in the inset of figure 3.62) also corresponds to very high T_C values. As we can see in figure 3.62, the onset of the magnetization is less and less steep for increasing La/Mn ratio, until β reaches the value of 1 for the 1.07 sample. The usual value of β is about 0.33 for ferromagnets, but it has been reported as 0.3-0.4 for LSMO and 0.25-0.28 for the sublattice magnetization in AFM $LaMnO_3$[13]. For the $x = 0.88$ and 0.66 samples, a low temperature anomaly arises in the M(T) curves at about 46K.

In figure 3.63, the saturation magnetization values and the residual magnetization values obtained from the hysteresis cycles is reported. The highest magnetization value is $3.9\mu_B/f.u.$ for the $x = 0.88$ sample. We can observe that the $x = 1.07$ samples, that has $\beta = 1$ shows no residual magnetization. The long-range ferromagnetism in this sample is suppressed.

For the $x = 0.66$ and $x = 0.88$ samples a low temperature anomaly in the magnetization arises at about 46 K (see figure 3.67). This transition is generally attributed to Mn_3O_4 impurities. The issue of impurity phases that might be present in the samples is solved in the next section.

Also the hysteresis cycles of the $x = 0.66$ and 0.88 samples, measured at 10 K, show some peculiar features, as reported in figure 3.64. Following the arrows, we start from fully saturated magnetic moments. By crossing H_c (coercive field), in some interval of field, the magnetization keeps a lower value respect to the saturation one. Then the M further increases, reaching the saturation value at about 10000 Oe. The increase of magnetization is accompanied by a peak in the dM/dH curve at about 4200 Oe for the $x = 0.66$ and 5000 Oe for the $x = 0.88$ samples, as reported in the right panel of figure 3.64. When we go backwards, the M keeps the high value when crossing again 4200/5000 Oe. So, from the peaks in the dM/dH curve, we can distinguish two coercive fields, the first related to the opening of the hysteresis, and the second one to the switch of the magnetization to an higher value. This double coercivity is not observed at 300 K or 100 K.

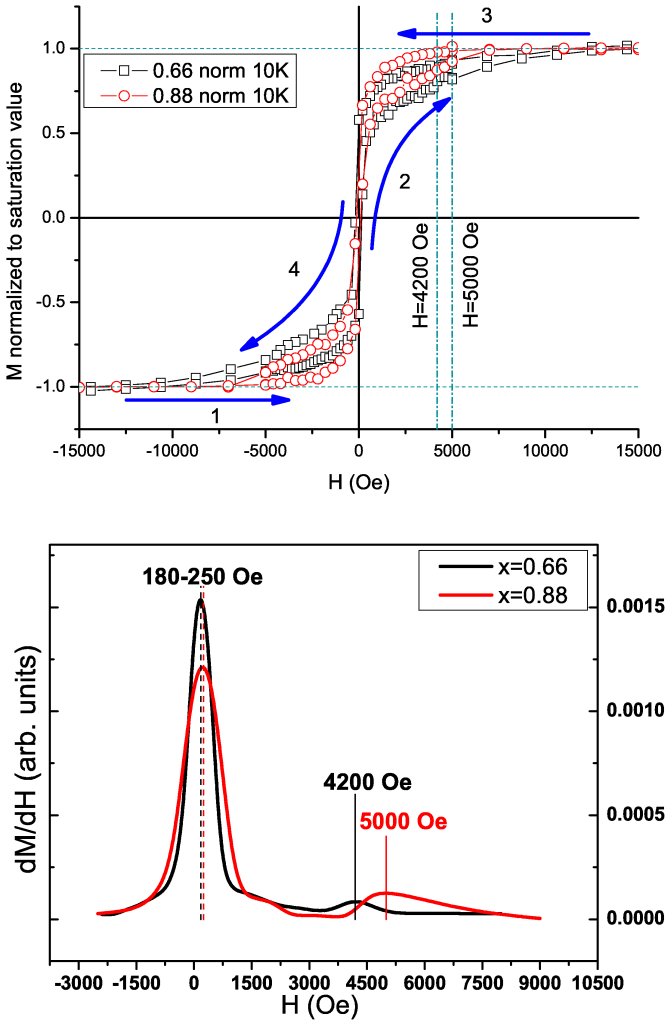

Figure 3.64: Top: hysteresis cycle M(H) of the $x = 0.66$ and 0.88 samples at 10 K , both normalized to the 10 K saturation value. Bottom: the derivatives dM/dH of the hysteresis curves are reported for the branch of the hysteresis cycle labelled by the arrows 1 and 2.

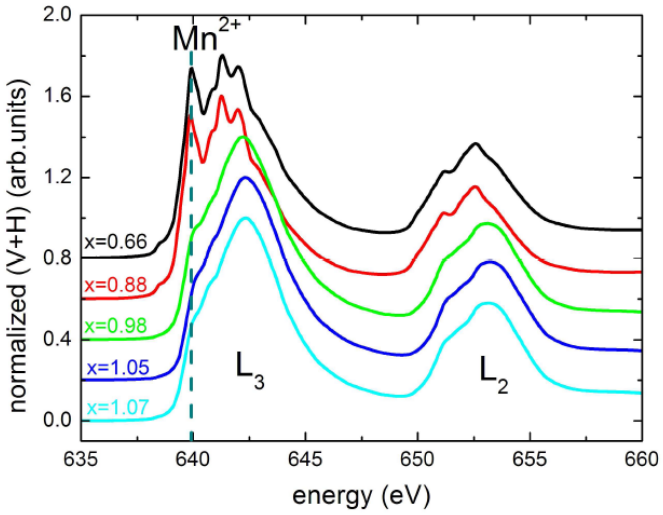

Figure 3.65: Normalized isotropic XAS spectra of our samples, obtained by the sum of the V and H polarization measurements, at 300 K in zero magnetic field. The Mn L_3 and L_2 absorption edges are indexed. The dashed line indicates the position of the peak attributed to the Mn^{2+}.

3.7.4 Isotropic XAS spectra and RIXS: Mn^{2+} and its coordination

Fundamental information to understand the physics of the LMO samples is provided by X-ray spectroscopy.

In figure 3.65 we report the normalized isotropic XAS (V+H) for all the samples. A sharp peak at about 640 eV, indicating the presence of Mn^{2+}[42] (see figure 3.45), is evident in the samples with $x = 0.66$ and $x = 0.88$. As shown in ref.[56] the XAS spectra of the $x = 0.98$, 1.05 and 1.07 are typical of the Mn^{3+}/Mn^{4+}.

The presence of Mn^{2+} is usually associated to impurity phases, such as MnO_2 or Mn_3O_4[52], that are likely to occur in La-deficient samples.

However we know, from ref.[51], that La-Mn substitution is possible in La deficient samples. We then argue that Mn^{2+} can occupy the perovskite A site.

To this aim RIXS measurements have been performed at the European Synchrotron Radiation Facility, as reported by Orgiani et al. in ref.[57]. L-edge RIXS allows to measure the set of the local $d - d$ excitations to assign the crystallographic site of divalent Mn^{2+}-ions and, possibly, to derive some indications on its direct or indirect involvement in the DE ferromagnetism in LMO films. The assignment of the crystalline site of Mn^{2+} ions is based on the measurement of the $d - d$ excitation spectrum. The two possible cation sites have different coordination and ion-oxygen distances : site A is

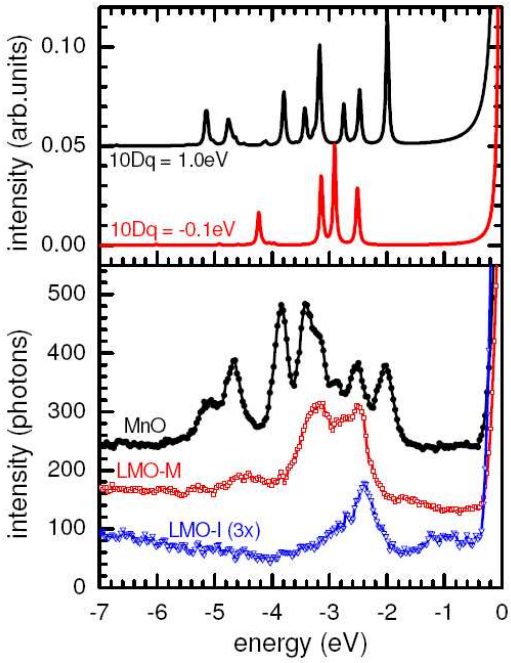

Figure 3.66: (upper panel) Calculated RIXS spectra within a single ion crystal field model and tuned 10Dq and the rescaling of the inter-atomic Slater integrals; (lower panel) Experimental RIXS spectra for an insulating MnO single-crystal (black) and a Mn^{2+}-doped LMO metallic film (red, labelled LMO-M). A RIXS spectra of an insulating LMO thin film is also reported (blue, labelled LMO-I; the intensity is multiplied by a factor of 3). Data refer to RIXS spectra acquired at the selected energy of 640.0 eV (corresponding to Mn^{2+} XAS absorption peak). From ref. [57].

cubo-octahedral (12 O_2 neighbors), with A-O distance $\approx$ 2.7 Å, site B is octahedral (6 O_2 neighbors), with B-O distance $\approx$ 1.9 Å. In a simple point charge crystal field model one thus expects a much smaller splitting of e_g to t_{2g} states at A than B sites (see §1.1).

Moreover the crystal field parameter $\Delta = 10Dq = E(e_g) - E(t_{2g})$ should be negative at A and positive at B. As a reference we use MnO, which has the NaCl structure: Mn^{2+} ion is at octahedral site with Mn-O distance 2.2 Å, i.e., intermediate between sites A and B in LMO. Naming R the cation-ligand distance, and recalling that by crystal field theory[4] the $\Delta \propto R^{-5}$ holds approximately, we expect Δ to be smaller (greater) at site A (B) than in MnO.

We have measured the $d-d$ excitation spectra of Mn^{2+} in LMO and MnO using RIXS excited at the Mn L_3 absorption edge. In particular we have chosen the photon energy 640.0 eV, which is peculiar of Mn^{2+} sites (see XAS spectra of figure 3.65). The RIXS spectra are shown in figure 3.66.

It appears very clearly that in heavily La-deficient LMO metallic films, where XAS demonstrates a strong presence of Mn^{2+}, the $d-d$ excitations are very

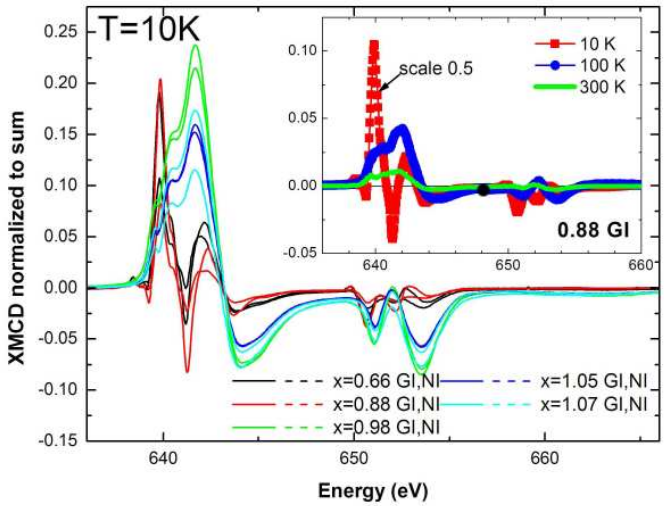

Figure 3.67: Normalized XMCD measured at 10 K in 1T applied magnetic field. In the inset the XMCD of the 0.88 sample in GI is reported for different temperatures, with the intensity of the 10 K curve scaled by a factor of 0.5 to clearly show all the curves with the same vertical scale.

different from those of MnO (lower panel of figure 3.66). To estimate quantitatively the Δ parameter, RIXS spectra have been calculated within a single ion crystal field model, tuning Δ and the rescaling of the inter-atomic Slater integrals to fit the main experimental features. The result is shown in the top panel of figure 3.66.
For MnO we essentially confirm the results of Ghiringhelli et al.[58]: $\Delta = 1.0$ eV, Slater integrals rescaled to 70% of their Hartree-Fock value. For Mn^{2+}-doped LMO films, we find a much smaller crystal field: $\Delta = -0.1$ eV, Slater integrals rescaled to 64%. This indicates univocally that that Mn^{2+} sits at site A and that the Mn-O bond has a non negligible covalent character (indicated by the strong renormalization of Slater integrals). As further support to our interpretation of the RIXS spectra, we show an example of insulating LMO films, excited at the same energy as for the other cases: the spectrum is incompatible with $d-d$ excitations of Mn^{2+}[57].
Analogously we can also deduce from this data that the $d-d$ excitations are not belonging to Mn_3O_4, that could not be measured. In Mn_3O_4, Mn^{2+} sits in a tetrahedral site ($\Delta < 0$), but again considering the Mn-O distance, the expected $\Delta \approx -0.5$ eV.

3.7.5 Magnetic properties studied by X-ray circular and linear dichroism

XMCD: ferromagnetism

We have verified that the Mn^{2+} contained in the $x = 0.66$ and 0.88 samples is not belonging to spurious phases, but it is located in the perovskite A-site. We will now use XMCD to analyze the magnetic properties of the samples, that we will divide in two groups: the samples showing the Mn^{2+} peak in the XAS spectrum will be referred as Mn^{2+} samples, while the other samples (i.e. the samples $x = 0.98, 1.05$ and 1.07) as no-Mn^{2+} samples.
As we can already figure out from figure 3.62 and figure 3.63, these two families of samples show different behaviour in the magnetic and transport properties. For example, looking at the inset of figure 3.62, the Mn^{2+} samples show the highest T_C, that decreases suddenly with increasing La/Mn ratio for the no-Mn^{2+} family.
The XMCD spectra shown in figure 3.67 provide further insight into the magnetic properties of our samples. The circular dichroism of the Mn^{2+} samples has a very different shape from the dichroism of the no-Mn^{2+} samples. The latter is comparable to $La_{0.7}Sr_{0.3}MnO_3$ (LSMO) XMCD and in general to the ferromagnetically ordered Mn^{3+}, the former is a combination of Mn^{3+}/Mn^{2+} circular dichroism (see for example the XMCD data reported by Park et al. [59] and Rader et al. [60]).
In the inset of figure 3.67, the XMCD of the Mn^{2+} sample $x = 0.88$ measured at different temperatures is shown. The Mn^{2+} features appear only at low temperature, and at least up to 100 K the XMCD is similar to the samples where no Mn^{2+} is detected. We can observe that only the 10 K XMCD is measured below the M(T) anomaly shown in figure 3.62.
In this view we can look at the hysteresis cycle of the Mn^{2+} samples. The double saturation (only observed at 10 K) can be interpreted by the existence of two spin populations. By the XMCD measurements we can identify these two population with the DE Mn^{3+}/Mn^{4+} and with the Mn^{2+} that only magnetizes at low temperatures, originating the low temperature anomaly in the M(T).
From the integration of the XMCD curves, by applying the sum rules 3.6 and 3.7, we may calculate separately the spin (m_s) and orbital (m_{orb}) magnetic moment. However, the quantitative analysis with the sum rules is shown to fail in the case of Mn atoms because of the mixing of the L_3 and L_2 core and because of the contribution of the magnetic dipole term. Conversely the ratios m_{orb}/m_s and $m_s(GI)/m_s(NI)$ can be obtained with sufficient accuracy. The former is nearly zero, thus confirming the quenching of the angular momentum, while the latter is reported in figure 3.68. It can be observed that the Mn^{2+} samples have the ferromagnetic easy axis in plane. This is in agreement with the tetragonal compressed symmetry of these samples,

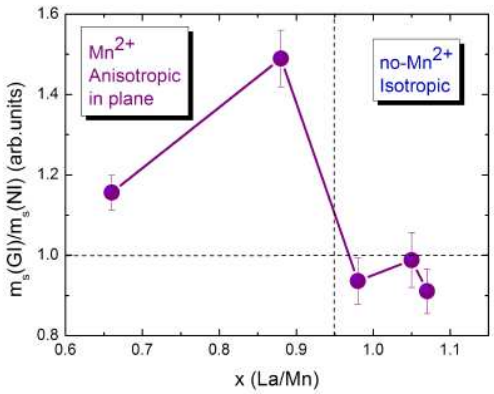

Figure 3.68: Ratio between the out of plane and in plane spin magnetic moments as a function of x. The spin magnetic moments have been obtained by the integration of the magnetic circular dichroism shown in figure 3.67.

showing the out-of-plane pseudo-cubic lattice parameter (c) smaller than the in-plane one (a) that is known to favour the in-plane orientation of the easy magnetization axis[61]. On the contrary, the no-Mn^{2+} samples appear more isotropic. These samples are also less tetragonally distorted, as shown by the XRD in figure 3.59.

XLD and XMLD: orbital occupation and antiferromagnetism

The marked anisotropy of the Mn^{2+} samples is also confirmed by the XLD spectra shown in figure 3.69, showing that the XLD intensity is higher for these samples at all temperatures. The integral of the absolute value of the linear dichroism for the three measurement conditions in figure 3.69 are reported in figure 3.70. At 300 K, even if some of the samples are already ferromagnetic, we do not detect any change in the spectra with the application of 1T magnetic field (not reported here). The XLD then originated solely from the orbital order (OO) component.
The integrated intensities in figure 3.70, confirm that the dominant contribution to the XLD in the Mn^{2+} samples comes from the OO, as at low temperature the magnetic contribution only slightly affects the intensity of the signal. Conversely, the intensity from the no-Mn^{2+} samples is significatively enhanced by the onset of the magnetic order.
In the latter samples, the low temperature XLD is strongly suppressed by the application of the magnetic field, revealing that the main magnetic contribution comes from the ferromagnetic ordering of the spins, and that the AF contribution is weak.
On the other hand the intensity of the Mn^{2+} samples XLD at 10 K,1 T (OO+AF) is higher than that at 10 K,0 T (OO+F+AF). So, when the F

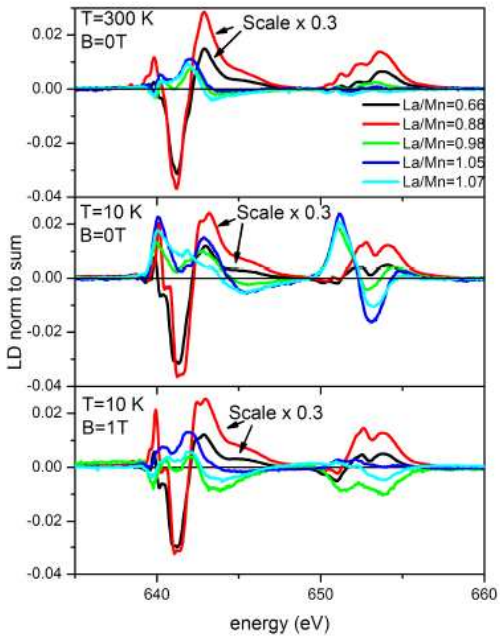

Figure 3.69: Linear dichroism normalized to the maximum of the V+H signal, calculated at 300 K with an applied field of 0T (top panel), at 10 K with an applied field of 0T (middle panel) and at 10 K with an applied field of 1T (bottom panel). The $x = 0.66$ and $x = 0.88$ curves have been rescaled with a factor of 0.3 in order to show all the data with the same scale.

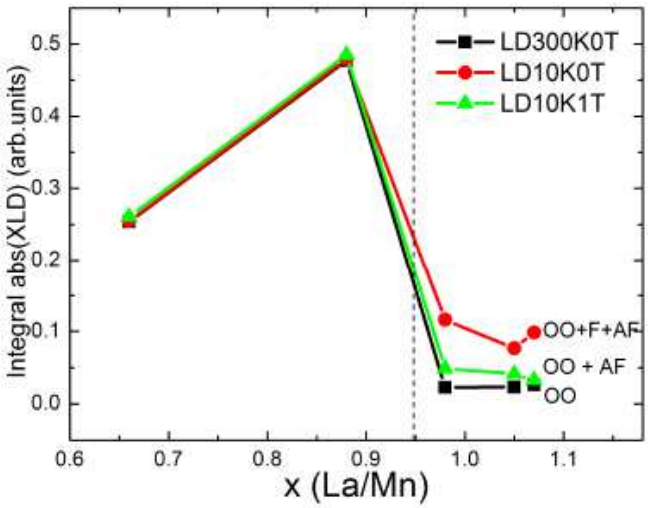

Figure 3.70: Integral of the absolute value of the XLD spectra shown in figure 3.69, as a function of La/Mn ratio. The vertical dashed line ideally separates the Mn^{2+} samples and the no-Mn^{2+} samples behaviour.

contribution is present, the XLD intensity is decreased. This means that the uniaxial anisotropy due to the spin orientation is reduced by the F component, thus indicating that the F and AF spins are mutually orthogonal.
Further information can be extracted from the analysis of the shape and features of the XLD spectra in figure 7. The $x = 0.66$ and $x = 0.88$ curves are typical of the e_g $(3z^2 - r^2)$ preferential occupation. This is apparently in contrast with the observed tetragonal distortion ($c/a < 1$), that is common to all the samples and furthermore it is more relevant in the Mn^{2+} samples, that would give an $(x^2 - y^2)$ preferential occupation (section §1.1).
We can suppose that the lattice distortion, induced by the small Mn^{2+} ion substitution in the A-site, drives the Mn^{3+} in the B-site to orbital order locally. On the other hand no orbital contribution from the Mn^{2+} is detected. When the magnetic contribution sets in, the XLD cannot be described by a single Mn^{3+} ion model with a magnetic exchange energy contribution (from XLD simulations[43]). Hybridization, Mn^{2+} contribution or differently strained phases have to be taken into account for this discrepancy.

3.7.6 Oxygen K-edge absorption spectra

Absorption spectra were also measured at the oxygen K edge. Oxygen K edge consist in the $1s \rightarrow 2p$ transition. Although the transition involves oxygen orbitals, the threshold structure observed at the oxygen K edge is determined by the electronic structure of the $3d$-transition-metal ion. Thus the XAS intensity at the oxygen K edge threshold region directly relates to both the hybridization of oxygen $2p$ with Mn $3d$ orbitals on the one hand and the availability of e_g character oxygen $2p$ orbitals on the other[56]. The 3d transition metal is important because the oxygen 2p shell is full in an ionic picture. Empty oxygen $2p$ orbitals are created through ground-state hybridization between $3d$-transition-metal orbitals and oxygen $2p$ orbitals[63]. In figure 3.71, the O K edge absorption spectra of four of the samples are reported. The XAS evidences different features for the Mn^{2+} and no-Mn^{2+} samples, and a marked anisotropy in the formers.
The edge threshold structure, showing very different features with changing polarization in the 0.88 and 0.66 samples, can be compared with the XAS of several Mn oxides, as it is only related to the Mn $3d$ orbitals. This comparison is reported in figure 3.72. The threshold region ($\sim 530 - 532$ eV) of the spectra in H-polarization ($E||c$-axis) resembles the MnO XAS spectra where only Mn^{2+} is present. The spectra in V-polarization ($E||ab$-plane) cannot be easily compared with the Mn oxide spectra in figure 3.72. However they can be compared with the spectra of Mn^{2+} and Mn^{4+} doped manganites ($La_{0.7}Ce_{0.3}MnO_3$ and $La_{0.7}Ca_{0.3}MnO_3$) reported by Asokan et al. [64], and it can be observed that they are a mixture of the two kind of manganites.
More specifically, the peak at ∼530 eV is assigned to the O $2p$ hybridized

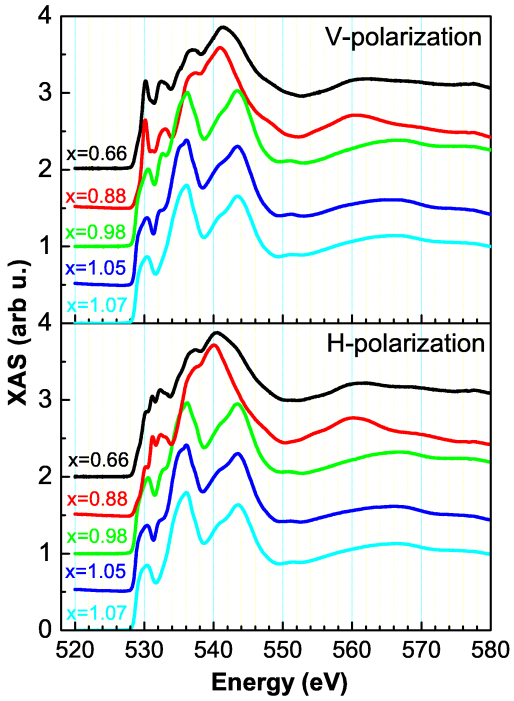

Figure 3.71: Room temperature XAS O K edge of LMO films with different La/Mn ratio: (a) in V-polarization, (b) in H-polarization, (c) LD obtained from the difference between the two XAS (V-H) and normalized to the sum of two XAS (V+H). The data refer to LMO film with La/Mn ratio 0.66 (black), 0.88 (red), 0.98 (green) and 1.07 (blue), respectively. Moreover, the spectra in V- and H-polarization are shifted vertically for clarity.

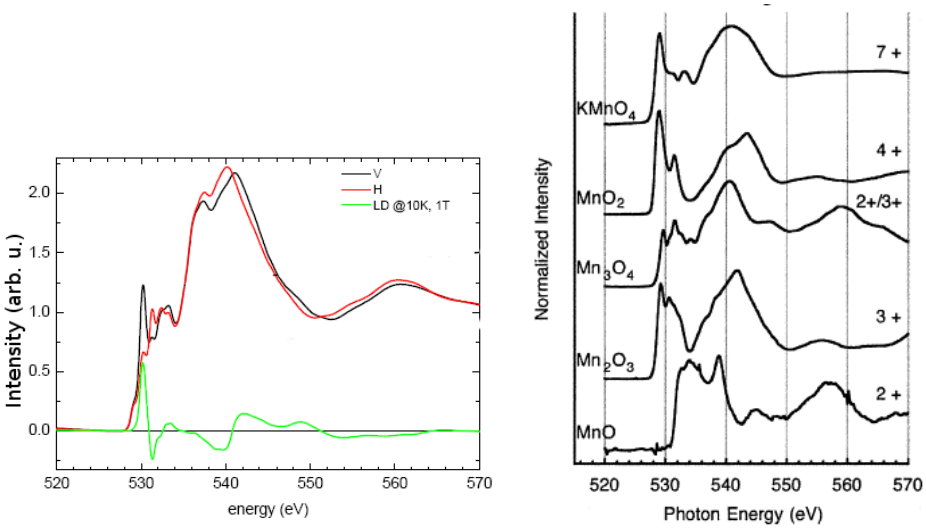

Figure 3.72: Comparison of the threshold region of the O K absorption edge of the $x = 0.88$ sample with the XAS of several Mn oxides, from ref[42].

with Mn t_{2g}-orbitals while the peak at ∼532 eV is assigned to the hybridization with the e_g electrons. The t_{2g} electrons are tightly bound, forming narrow band, and the two e_g electrons are strongly hybridized with the O $2p$ states and, depending upon the doping are either localized or itinerant. XAS spectra measured in H-polarization of the 0.88 and 0.66 samples (see figure 3.71) clearly show that in the c-axis direction the t_{2g} features become less pronounced in favor of the e_g with increasing Mn^{2+} content.

On the contrary XAS spectra of LMO films with La/Mn$\gtrsim$ 1 are more isotropic and similar to the LSMO where the traditional double-exchange Mn^{3+}/Mn^{4+} develops, as the ones reported in figure 3.73. In case of LSMO, the peak at about 536 eV is associated to the bands with La $5d$/Sr $4d$ character and the peak at about 545 eV to the bands with Mn $4sp$ character. It is interesting to notice that those two peaks merge in an almost unique broad region when Mn substitutes La in films with La/Mn$<$ 1[56].
The effect of the Mn^{2+} on the electronic bands is evidenced by the XAS at the O K edge, indicating that the Mn^{2+}-La substitution not only contributes to create new interactions through a lattice distortion but also by modifying the hybridization with the oxygen.

3.7.7 Discussion of the results

All data have shown that La/Mn disproportion with opposite ratios gives rise to different Mn valence states, leading to different magnetic properties. The samples with La/Mn$<$ 1 (the Mn^{2+} samples) are characterized by A-site vacancies because of the La deficiency. According to ref.[51] a fraction of the

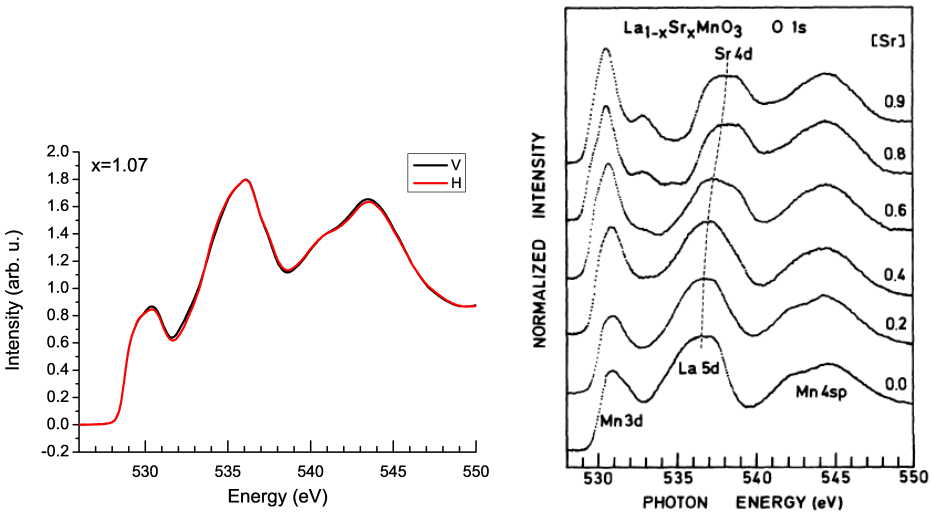

Figure 3.73: Comparison of the threshold region of the O K absorption edge of the $x = 1.07$ sample with the XAS of several LSMO samples with different Sr content, from ref[56].

A-site vacancies can be occupied by the excess Mn, and the correct formula of these samples can be described as $(La_xMn_y)_{Asite}$ $(Mn_{1-y})_{Bsite}O_{3-3y}$. On the basis of the RIXS measurements of ref.[57], we argue that the Mn in the A-site is assuming valence 2+. Conversely for the La/Mn$\gtrsim$ 1, the hole doping is due to Mn deficiency and/or excess oxygen (i.e. simultaneous vacancies on the A and B sites)[51].
In all the samples, to preserve the charge neutrality, part of the Mn in the B-site must oxidize to Mn^{4+}. In the La/Mn$<$ 1 samples, because of some Mn^{2+} at the A-site, a smaller amount of Mn^{4+} is necessary to balance the charge compared to the La/Mn$>$ 1 samples with an equivalent cationic deficiency. Then the doping for the DE mechanism to take place, can be kept in the La/Mn$<$ 1 samples in a wider region of La/Mn disproportion.
DE usually takes place in Mn^{3+}/Mn^{4+} mixed valence systems, but, as realized in $La_{1-x}Ce_xMnO_3$ compounds, it can also take place in Mn^{2+}/Mn^{3+} systems. However, in our samples the Mn^{2+} and Mn^{3+}/Mn^{4+} are not occupying equivalent sites. Mn^{2+} may be involved in a more exotic conduction mechanism[57], whereas the DE part is played by the usual Mn^{3+}/Mn^{4+} actors.
The Mn^{2+} and no-Mn^{2+} samples show different behaviour in the magnetic and transport properties. A robust FM phase is observed in Mn^{2+} samples, while a weakening of the ferromagnetism is induced in the no-Mn^{2+} samples. The observation of two coercive fields in the Mn^{2+} samples can be associated with the existence of two spin populations, belonging to the two magnetic ions populations: DE Mn^{3+}/Mn^{4+} and the Mn^{2+}.

Considering the DE mechanism in these two situations, we conclude that, in the absence of a distortion, this would be more hampered in the no-Mn^{2+} samples because of the reduction of the number of the Mn-O-Mn DE paths. However in the Mn^{2+} samples, the La-Mn substitution in the A-site causes a severe local distortion of the crystal lattice, leading to a $(3z^2 - r^2)$ orbital ordering in the Mn^{3+} octahedra. We have shown that this orbital ordering is accompanied by an AFM phase with spins oriented along the c-axis. It is largely recognized that the orbital ordered phases are related to antiferromagnetic insulating states, whereas ferromagnetism is accompanied by orbital disorder[62]. The spin direction in the AF phase is indeed the one favoured by the observed OO[15]. Conversely the no-Mn^{2+} samples show a weak OO and consequently a weak AF signal (figures 3.69 and 3.70). In both Mn^{2+} and no-Mn^{2+} samples, the ferromagnetic phase can be linked to orbital disorder as in the case of DE in manganites[62].
Despite the observed OO and AF phase, the Mn^{2+} samples show higher T_C and T_{MI} , together with higher magnetic moment. This is of course a consequence of the higher B-site occupation (Mn-O-Mn), but we have also to consider that the Mn^{2+} is a magnetic ion, occupying the A-site instead of the La that has zero magnetic moment. XMCD data demonstrate the F ordering of the Mn^{2+}, that then contributes to enhancement of the ferromagnetism.

3.8 Conclusions

In sections §3.1-§3.5 the developing of deposition and optical lithography techniques are described, for the fabrication of devices for current perpendicular-to-plane measurements and field effect devices.
CPP measurements require to grow the thin film or multilayer to be measured on a conductive substrate or a metallic film.
In our case we decided to use $SrRuO_3$ base electrodes, as this material has several desirable properties: low resistivity, smooth surface films can be grown, elevate thermal and chemical stability. SRO thin films on untreated STO substrates have been grown by PLD and optimized, and their structural and transport properties have been studied as a function of the deposition conditions.
We also deposited thin films of $BaTiO_3$ on STO substrates, on SRO buffered STO and on LSMO/STO bilayers on Si. BTO is a standard ferroelectric material, already employed to engineer ferroelectric capacitors and ferroelectric memories. Our aim was to use it to engineer a ferroelectric field effect device using ultrathin LSMO films.
All the lithographic steps for the fabrication of CPP devices have been optimized. The most delicate part is the ion etching of the film to be measured, that has to be stopped when the base electrode is reached. We found that, in order to correctly perform this step, the etching must be monitored by mass spectrometer.
We tried to use the CPP geometry to perform electrical polarization measurements on ferroelectric or multiferroic films. This is interesting not only in view of measuring the properties of LMO-based multiferroic superlattices by our CPP configuration, but also in order to test the ferroelectric properties of oxides that can be used as ferroelectric gates in field effect devices as the ones described in this work.
In this case the insulation of top and bottom electrode becomes crucial, as high electric fields have to be applied across the thickness of the film.
$BiFeO_3/LaNiO_3$ bilayers have been patterned, but the impossibility to monitor the etching and probably the small BFO thickness prevented us to obtain a good device.
BTO/SRO films have been successfully patterned, but the BTO showed too low resistivity to measure polarization. We argue that oxygen vacancies in the BTO films degrade their resistivity. BTO thin films with thickness lower than 200 nm (our films are 85 nm thick) are often found to be lossy, so that polarization can be measured only at low temperatures.
It has to be considered that the side insulator too (Al_2O_3) may not be suitable to bear high electric fields. However, in case of traditional CPP measurements, with conducting thin films and multilayers, as the ones described in the following, the breakdown of the side insulator is less likely, as low electric fields are involved, and small loss currents can be neglected.

We tried to engineer simple field effect devices in order to study the field effect on LSMO ultrathin films. True field effect in homogeneous phase manganite thin films has only been observed by Pallecchi et al. in planar devices.
We used ultrathin films in order to overcome the problem of the screening of electric field in high carrier density materials. However, when we tried to use Al_2O_3 as gate oxide, the ultrathin film was damaged by the ion beam deposition. Similar problems have been encountered for the gold contacts, and solved by depositing, prior to the ion beam deposition, a protective gold layer at room temperature by PLD.
Quite surprisingly, when we tried to deposit a BTO film over the LSMO/STO bilayers by PLD, using high temperature deposition in low oxygen pressure, the structural and transport properties of the LSMO were not degraded, as demonstrated by the XRD and resistivity.
However, because of the low gate resistance, we were not able to perform field effect measurements.
From our results, we can conclude that high resistive BTO films would be the best choice as gate electrode. The gate resistance can be enhanced by using a thicker BTO layer, or by further optimize the oxygen content in BTO. Thinner films would be more desirable, as this would increase the gate capacitance, i.e. higher electric fields can be applied with lower voltage.
Also the pattern used for the field effect devices is not the best choice, as the use of large area gates increases the possibility of including lossy defects in the insulator. The same mask used for CPP measurements may be a good choice, by using the LSMO film in place of the base electrode and using an insulator in place of the multilayer to be measured. In this case the base electrode two probe resistance has to be measured, while applying a voltage between top and bottom electrode.
Our studies, by dealing with several technical problems, give precious information to fabricate CPP devices for conductive multilayers characterization and to proceed in the developing of MOSFET-like field effect devices. Both measurement geometries may be applied in the transport characterization of the superlattices and of the thin film described in the following of the thesis.
In section §3.6 we report on the orbital and magnetic characterization of LMO/SMO superlattices by X-ray absoption spectroscopy.
The experimental data can be explained by the interplay of charge transfer and delocalization at the interfaces and localized states mainly influenced by the lattice degrees of freedom in the inner part of the LMO and SMO constituent blocks.
When the charge transfer through the interfaces delocalize the e_g electrons into the entire superlattice, such as in the $n = 1$ sample, the system behaves as an homogeneous system. On the contrary, when the interface density is

smaller ($n = 5, 8$) and the distance between interfaces is higher than the Thomas-Fermi length[28, 27], the role played by the strain applied to each constituent block becomes fundamental. As a consequence the electronic localization is accompanied by the preferential out-of-plane e_g orbital occupation. Moreover the in-plane easy axis of the double-exchange FM spin orientation, with the pinned AFM spin orientation, further confirms that the uniform electronic distribution in the $n = 1$ superlattices causes properties dominated by the average strain effects as a whole, thus favoring the in-plane orbital occupation. However, when the thickness of the constituent blocks increases the interfacial FM phase does not extent in the whole superlattices but is confined to the interface. The DE FM phase keeps the in-plane preferential orientation, while the AFM spin direction is dictated by the orbital occupation in the orbital ordered insulating phase.
The results of this study are resumed in the publication by Aruta et. al, ref. [21].
In section 3.7 we report on the properties of non-stoichiometric LMO thin films. The study of such samples is important not only to better understand the properties of superlattice systems, but also from a fundamental point of view, as explained in the following.
We have demonstrated that $La_xMnO_{3-\delta}$ thin films on STO with $x < 1$ have not only good transport properties, but also show enhanced ferromagnetism due to the Mn^{2+} contribution.
The results of this work are reported in the paper by Galdi et al., ref. [65]. The substitution of La^{3+} with a magnetic ion such as Mn^{2+}, contributes to increase the saturation magnetization, despite the OO and AFM induced in the Mn^{2+} samples by the lattice distortions induced by the smaller ion substitution.
It is natural to take in account whether the Mn^{2+} can now contribute also to the electrical transport.
This is indeed possible because the energy levels of Mn^{2+} cross the Fermi's energy level so that they could participate to the hopping process. The need for an alternative conducting mechanism stems from the fact that a smaller tolerance factor depresses the usual DE mechanism, but favour a new hopping path involving Mn^{2+} ions. This issue has been handled by a theoretical point of view in the paper by Orgiani et al.[57]. Beside the hopping mechanism in the traditional DE-framework, two extra possible paths for the added hole were considered: namely, a hopping mechanism between two Mn-ions directly through an intervening Mn^{2+}-ion and a Multiple-DE hopping path through the O-Mn^{2+}-O ions, as shown in figure 3.74.

The hopping parameters $t_{\mathbf{b},\mathbf{c}}$ for the two hopping mechanisms **b** and **c** have been calculated in units of the DE hopping parameter $t_{\mathbf{a}}$, by using the techniques described in ref. [57].
The hopping mechanism **b** is very unlikely, as $t_{\mathbf{b}} \approx 10^{-3} t_{\mathbf{a}}$, while the hopping mechanism **c**, despite its apparent complexity, has $t_{\mathbf{c}} \approx 0.24 t_{\mathbf{a}}$.

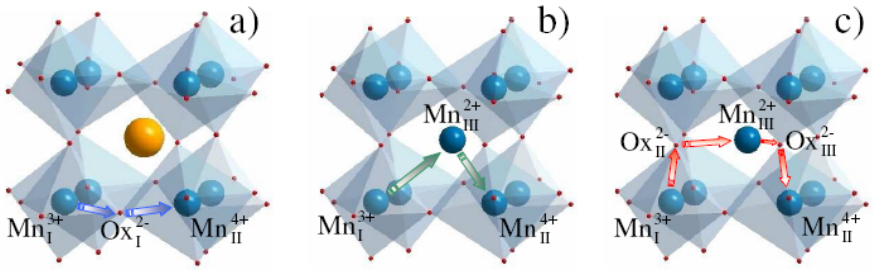

Figure 3.74: Possible hopping mechanisms in conventional and Mn^{2+}-substituted manganites. In panel **a**, the traditional DE-mechanism (blue arrows) between two Mn-ions (MnI and MnII , respectively) through intervening O-ion (OxI) is reported. In panel **b** and **c**, two possible additional hopping paths in Mn^{2+}-doped manganites are reported: a direct hopping (panel **b**) between two Mn-ions (MnI and MnII , respectively) through intervening Mn^{2+}-ion (namely, MnIII) and a Multiple-DE hopping path (panel **c**) through the O-Mn-O ions (OxII , MnIII and OxIII , respectively).

Such a value has been obtained by assuming that all the ions are structurally arranged in an undistorted perovskite. $LaMnO_3$ generally shows a distorted orthorhombic/rhombohedral perovskite unit cell, characterized by O-ions slightly displaced out of the joining lines among the Mn-ions (as showed in section §1.2.1)). In this respect, because of the buckling angle between the Mn-plane and the Mn-O bonds, the superimposition of MnI-OxI-MnII orbitals is actually reduced, thus subsequently reducing the $t_{\mathbf{a}}$ value. Moreover, the smaller size of Mn^{2+}-ionic radius (compared to La^{3+}'s ones) should increase the cubic distortion of the perovskite cells, thus further reducing the $t_{\mathbf{a}}$ value. On the contrary, because of the tilting of the oxygen octahedra, the distance between some oxygen-ions and the central Mn^{2+}-ion should be shortened with respect to the undistorted structure (in which the A-O distance is $\sqrt{2}/2$ times unit cell lattice parameter). As a consequence, the superimposition between O_2-Mn^{2+} orbitals actually increases, thus increasing the $t_{\mathbf{c}}$ value.
The idea of using multiple-valence atoms both as a dopant and as an active element electronically involved in the conduction mechanism (namely, the Mn^{2+} in manganites) opens new scenarios in the study of physical properties of CMR-materials.

Bibliography

[1] E. Dagotto, Science Perspectives (2007);

[2] B.R.K. Nanda, S. Satpathy, Phys. Rev. Lett., **101** 127201 (2008);

[3] Isaac B. Bersuker, *Electronic Structure and Properties of Transition Metal Compounds (introduction to the theory)*, Wiley-Interscience (1996);

[4] Roger George Burns, *Mineralogical Applications of Crystal Field Theory, second edition*, Cambridge University Press (1993);

[5] G. H. Jonker, J. H. Van Santen, Physica **16** 337 (1950);

[6] A. P. Ramirez, J. Phys.: Condens. Matter **9** (1997);

[7] C. Zener, Phys. Rev. **81** 440 (1951);

[8] P. W. Anderson, H. Hasegawa, Phys. Rev. **100** 675 (1955);

[9] A. J. Millis, P. B. Littlewood, B. I. Shraiman Phys. Rev. Lett. **74** 5144 (1955);

[10] Abdelmoula, N. , Dhahri, J. , Guidara, K. , Dhahri, E. and Joubert, J. C., Phase Transitions, **70** 197-210 (1999);

[11] J. L. García-Muñoz, J. Fontcuberta, B. Martínez, A. Seffar, S. Piñol, X. Obradors, Phys. Rev. B, **55** R668 (1997);

[12] B. Dabrowski, O. Chmaissem, J. Mais, S. Kolesnik, J.D. Jorgensen, and S. Short, *unpublished*;

[13] J. M. D. Coey, M. Viret, Advances in Physics **48** 167-293 (1999);

[14] J. Kanamori, J. Phys. Chem. Solids **10** 87-98 (1959).

[15] R. Maezono, S. Ishihara, N. Nagaosa, Phys. Rev. B **58** 11583 (1998);

[16] C. Adamo, X. Ke, P. Schiffer, A. Soukiassian, M. Waru- sawithana, L. Maritato, D. G. Schlom, Appl. Phys. Lett. **92** 112508 (2008);

[17] C. Aruta, M. Angeloni, G. Balestrino, N. G. Boggio, P. G. Medaglia, A. Tebano, B. Davidson, M. Baldini, D. Di Castro, P. Postorino, P. Dore, A. Sidorenko, G. Allodi, R. De Renzi, J. Appl. Phys. **100** 023910 (2006);

[18] T. Hotta, M. Moraghebi, A. Feiguin, A. Moreo, S. Yunoki, and E. Dagotto, Phys. Rev. Lett. **90**, 247203 (2003);

[19] S. Dong, R. Yu, S. Yunoki, G. Alvarez, J.-M. Liu, E. Dagotto, Phys. Rev. B, **78** 201102R (2008);

[20] J. S. Zhou and J. B. Goodenough, Phys. Rev. Lett. **96**, 247202 (2006).

[21] C. Aruta, C. Adamo, A. Galdi, P. Orgiani, V. Bisogni, N. B. Brookes, J. C. Cezar, P. Thakur, C. A. Perroni, G. De Filippis, V. Cataudella, D. G. Schlom, L. Maritato, G. Ghiringhelli , Phys. Rev. B, **80** 140405 (2009);

[22] V. Skumryev, F. Ott, J. M. D. Coey, A. Anane, J-.P. Renard, L. Pinsard-Gaudart, Revcolevschi, Eur. Phys. J. B, **11** 401 (1999);

[23] E. Dagotto, T. Hotta, A. Moreo, Physics Reports **344** 1-153 (2001);

[24] C. Barone, A. Galdi, N. Lampis, L. Maritato, F. Miletto Granozio, S. Pagano, P. Perna, M. Radovic, and U. Scotti di Uccio, Phys. Rev. B **80** 115128 (2009) *and references therein*;

[25] A. Ohtomo, H.Y. Hwang, Nature **427** 423 (2004);

[26] C. Aruta, S. Amoruso, R. Bruzzese, X. Wang, D. Maccariello, F. Miletto Granozio, and U. Scotti di Uccio Appl. Phys. Lett. 97, 252105 (2010);

[27] A. Bhattacharya, S. J. May, S. G. E. te Velthuis, M. Warusawithana, X. Zhai, B. Jiang, J. M. Zuo, M. R. Fitzsimmons, S. D. Bader, and J. N. Eckstein, Phys. Rev. Lett. **100**, 257203 (2008);

[28] C. Adamo, C. A. Perroni, V. Cataudella, G. De Filippis, P. Orgiani, and L. Maritato Phys. Rev. B, **79** 045125 (2009);

[29] M. A. Herman, Vacuum **32** 555 (1982);

[30] M. Naito, H.Yamamoto, H. Sato, Physica C 305 233-250 (1998);

[31] B.R.K. Nanda, S. Satpathy, Phys. Rev. B **79**, 054428 (2009);

[32] M.P. Singh, W. Prellier, Ch. Simon, B. Raveau **87**, 2022505 (2005);

[33] P. Murugavel, W. Prellier, Appl. Phys. Lett. **100** 02350 (2006);

[34] J.H. Haeni, C.D. Theis, D.G. Schlom, Journal of Electroceramics **4** 385-391, (2000);

[35] G. Schütz , W. Wagner, W. Wilhelm, P. Kienle et al., Phys. Rev. Lett. **58** 737 (1987);

[36] B. T. Thole, P. Carra, F. Sette and G. van der Laan, Phys. Rev. Lett. **68** 1943 (1992);

[37] P. Carra, B. T. Thole, M. Altarelli and X.Wang, Phys. Rev. Lett. **70** 694 (1993);

[38] C. T. Chen, Y. U. Idzerda, H.-J. Lin, N. V. Smith et al., Phys. Rev. Lett. **75** 152(1995);

[39] Y. Teramura, A. Tanaka and T. Jo , J. Phys. Soc. Jap. 65, **4** 1053 (1996);

[40] Michael Räkers, *An x-ray spectroscopic study of novel materials for electronic applications*. PhD thesis, Department of Physics University of Osnabrück (2009);

[41] E. Arenholz, G. van der Laan, R. V. Chopdekar and Y. Suzuki, Phys. Rev. Lett. **98** 197201 (2007);

[42] B. Gilbert, B. H. Frazer,A. Belz,P. G. Conrad, K. H. Neal- son, D. Haskel, J. C. Lang, G. Srajer,G. De Stasio, J. Phys. Chem. A, **107** 2839-2847 (2003);

[43] C. Piovera, *Orbital and Magnetic Anisotropy in Manganite Thin Films Studied By X-ray Absorption Spectroscopy*, Tesi di Laurea, Politecnico di Milano (A.A. 2008-2009);

[44] Missing web site: *http://www.esrf.eu/UsersAndScience/Experiments/TBS/SciSoft/OurSoftware/MISSING* ; Riccardo Gusmeroli and Claudia Dallera, *Missing 1.1 Short User Manual*;

[45] T. Saitoh et al. Phys. Rev. B **51** 13942;

[46] C. Aruta, G. Ghiringhelli, V. Bisogni, L. Braicovich, N. B. Brookes, A. Tebano, and G. Balestrino, Phys. Rev. B 80, 014431 (2009);

[47] *Resonant inelastic X-ray scattering (RIXS)*, Trinanjan Datta

[48] E. E. Fullerton, I. K. Schuller, H. Vanderstraeten, Y. Bruynseraede, Phys. Rev.B **45** 9292 (1999);

[49] H. B. Zhao, K. J. Smith, Y. Fan, G. Lüpke, A. Bhattacharya, S. D. Bader, M. Warusawithana, X. Zhai, and J. N. Eckstein, Phys. Rev. Lett. **100**, 117208 (2008);

[50] J. Garcia-Barriocanal, J.C. Cezar, F.Y Bruno, P. Thakur, N.B. Brookes, C. Utfeld, A. Rivera-Calzada, S.R. Giblin, J.W. Taylor, J.A. Duffy, S.B. Dugdale, T. Nakamura, K. Kodama, C. Leon, S. Okamoto, J. Santamaria, Nat. Com- mun. 1:82, DOI:10.1038/ncomms1080 (2010);

[51] M. Wołcyrz, R. Horyń, F. Bourée, and E. Bukowska, J. Alloys Compd., **353** 170 (2003);

[52] P.A. Joy, C.R. Sankar, and S.K. Date,J. Phys. Condens. Matter **14** L663 (2002);

[53] A. Gupta, T. R. McGuire, P. R. Duncombe, M. Rupp, J. Z. Sun, W. J. Gallagher, and Gang Xiao, Appl. Phys. Lett., **67** 3494 (1995);

[54] R. Horyń, A. Sikora, E. Bukowska, J. Alloys Comp. **353** 153 (2003);

[55] P. Orgiani, C. Aruta, R.Ciancio, A. Galdi, L. Maritato Appl. Phys. Lett. **95**, 013510 (2009);

[56] M.Abbate, F.M.F.de Groot, J.C.Fuggle, A.Fujimori, O.Strebel, F.Lopez, M.Domke, G.Kaindl, G.A.Sawatzky, M.Takano, Y. Takeda, H.Eisaki, and S.Uchida, Phys. Rev. B, **46** 4511 (1992);

[57] P. Orgiani, A. Galdi, C. Aruta, V. Cataudella, G. De Filippis, C.A. Perroni, V. Marigliano Ramaglia, R. Ciancio, N.B. Brookes, M. Moretti Sala, G. Ghiringhelli, L. Maritato, Phys. Rev. B **82** 205122 (2010);

[58] G.Ghiringhelli, M.Matsubara, C.Dallera, F.Fracassi, A.Tagliaferri, N.B.Brookes, A.Kotani, and L.Braicovich, Phys. Rev. B **73** 035111 (2003); ibid. **78** 117102 (2008);

[59] J.-H. Park, E. Vescovo, H.-J. Kim, C. Kwon, R. Ramesh, T. Venkatesan, Phys. Rev. Lett. **81** 1953-1956 (1998);

[60] O. Rader, W. Gudat, D. Schmitz, C. Carbone, W. Eber- hardt Phys. Rev. B **56** 5053-5056 (1997);

[61] T. K. Nath, R. A. Rao, D. Lavric, C. B. Eom, L. Wu, and F. Tsui, Appl. Phys. Lett. **74** 1615 (1999);

[62] Y. Konishi, Z. Fang, M. Izumi, T. Manako, M. Kasai, H. Kuwahara, M. Kawasahi, K. Terakura, Y. Tokura, J. Phys. Soc. Jap., **68** 3790 (1999);

[63] K. B. Garg, N. L. Saini, B. R. Sekhar, R. K. Singhal, B. Doyle, S. Nannarone, F. Bondino, E. Magnano, E. Carleschi and T. Chatterji, J. Phys.: Condens. Matter **20** 055215 (2008);

[64] K.Asokan, K.V.R.Rao,J.C.Jan, J.W.Chiou, W.F.Pong, Ravi Kumar, Shahid Husain, J.P.Srivastava, Surface Review and Letters **9** 1053 (2002).

[65] A. Galdi, C. Aruta, P. Orgiani, N. B. Brookes, G. Ghiringhelli, M. Moretti Sala, R. V. K. Mangalam, W. Prellier, U. Lüders, and L. Maritato, Phys. Rev. B *(to be published)*;

[66] I. Pallecchi, L. Pellegrino, E. Bellingeri, A. S. Siri, and D. Marré, J. Appl. Phys. **95** 8082 (2004);

[67] S. Mathews, R. Ramesh, T. Venkatesan, and J. Benedetto, Science **276**, 238 (1997);

[68] T. Wu, S. B. Ogale, J. E. Garrison,B.Nagaraj,A.Biswas, Z. Chen, R. L. Greene, R. Ramesh, T. Venkatesan, and A. J. Millis, Phys. Rev. Lett. **86**, 5998 (2001);

[69] M. A. Seigler, P. A. A. Van der Heijden , A. E. Litvinov, R. E. Rottmayer, IEEE transaction on magnetics, **39** 1855 (2003);

[70] K. Aoshima, N. Funabashi, K. Machida, Y. Miyamoto, N. Kawamura, K. Kuga, N. Shimidzu, F. Sato, Appl. Phys. Lett. **91**, 052507 (2007);

[71] M. Kurakado, X-Ray Spectrom. **29**, 137-146 (2000);

[72] N. Ashkenov, M. Schubert, E. Twerdowski, H. v. Wenckstern, B.N. Mbenkum, H. Hochmuth, M. Lorenz, W. Grill, M. Grundmann, Thin Solid Films **486** 153- 157 (2005)

[73] J. Mannhart, J.G. Bednorz, K.A. Müller, D.G. Schlom, J. Ströbel, Journal of Alloys and Compounds **195** 519-525 (1993);

[74] T. Zhao, S. B. Ogale, S. R. Shinde, R. Ramesh, R. Droopad, J. Yu, K. Eisenbeiser, J. Misewich, Appl. Phys. Lett. **84** 750 (2004);

[75] Y.-G. Park, T. Kanki, H.-Y. Lee, H. Tanaka, T. Kawai, Solid-State Electron. **47** 2221-2224 (2003);

[76] T. Wu, S. B. Ogale, J. E. Garrison, B. Nagara, Amlan Biswas, Z. Chen, R. L. Greene, R. Ramesh, T. Venkatesan, Phys. Rev. Lett. **86** 5998 (2001);

[77] G. Cao, S. McCall, M. Shepard, J. E. Crow, R. P. Guertin, Phys. Rev. B **56** 321-329 (1997);

[78] G. Ornelas-Arciniega, J. Reyes-Gomez, A. G. Castellanos-Guzman, Journal of the Korean Physical Society, 32 S380-S381 (1998);

[79] G. Herranz, B. Martinez, J. Fontcuberta, F. Sanchez, M.V. Garcia-Cuenca, C. Ferrater, M. Varela, Appl. Phys. Lett. **82** 85 (2003);

[80] F. Sanchez, G. Herranz , I.C. Infante , C. Ferrater , M.V. Garcia-Cuenca, M. Varela , J. Fontcuberta, Progress in Solid State Chemistry **34** 213-221 (2006);

[81] L. Klein, J.S. Dodge, T.H. Geballe, A. Kapitulnik, A.F. Marshall, L. Antognazza, K. Char, Appl. Phys. Lett. **66** 2427 (1995);

[82] P. Orgiani, C. Aruta, G. Balestrino, S. Lavagna, P.G. Medaglia, A. Tebano, Eur. Phys. J. B **26** 23-28 (2002);

[83] G. Herranz, B. Martinez, J. Fontcuberta, F. Sanchez, C. Ferrater, M. V. Garcia- Cuenca, M. Varela, Phys. Rev. B **67** 174423 (2003);

[84] C.W. Jones, P.D. Battle, P. Lightfoot, W.T.A. Harrison, Acta Cryst. C **45**, 365-367 (1989);

[85] L Klein, J S Dodge, C H Ahn, J W Reiner, L Mieville, T H Geballe, M R Beasley and A Kapitulnik, J. Phys.: Condens. Matter **8** 10111-10126 (1996) and references therein;

[86] Jon-Paul Maria, H. L. McKinstry, S. Trolier-McKinstry, Appl. Phys. Lett. **76** 3382 (2000);

[87] J. Choi, C. B. Eom, G. Rijnders, H. Rogalla, D. H. A. Blank, Appl. Phys. Lett. **79** 1447 (2001);

[88] F.Ricci, M. F. Bevilacqua, F. Miletto Granozio, U. Scotti di Uccio, Phys. Rev. B **65** 155428 (2002);

[89] Q. Gan, R. A. Rao, C. B. Eom, Appl. Phys. Lett. 70 (15) 1962 (1997);

[90] G. Rijnders, D.H.A. Blank, J. Choi, C-.B. Eom, Appl. Phys. Lett. **84** 505 (2004);

[91] L Klein, J S Dodge, C H Ahn, J W Reiner, L Mieville, T H Geballe, M R Beasley, A Kapitulnik, J. Phys.: Condens. Matter **8** 10111-10126 (1996);

[92] B. J. Kennedy, B. A. Hunter, and J. R. Hester, Phys. Rev. B **65**, 224103 (2002);

[93] B.A. Strukov, A.P. Levanyuk "Ferroelectric Phenomena in Crystals" Physical Foundations, Springer;

[94] J.F. Scott (2000) Ferroelectric Memories. Springer;

[95] R. Resta, Rev. Mod. Phys 66 899-915 (1994);

[96] Y. Yoshimura , M. Morioka , A. Kojima, N. Tokunaga, T. Koganezawa , K. Tozaki, Physics Letters A 367 394-401 (2007);

[97] Ch. Buchal, L. Beckers, A. Eckau, J. Schubert, W. Zander, Mat. Sci. Eng. B 56 234-238 (1998);

[98] D.-Y. Kim, S.-G. Lee, Y.K. Park, S.Y. Park, Mat. Lett. 40 146-150 (1999);

[99] C. Li, D. Cui, Y. Zhou, H. Lu, Z. Chen, D. Zhang, F. Wu, Appl. Surf. Sci. 136 173-177 (1998);

[100] G. Y. Yang, G. D. Lian, E. C. Dickey, C. A. Randall, D. E. Barber, P. Pinceloup, M. A. Henderson, R. A. Hill, J. J. Beeson, D. J. Skamser, J. Appl. Phys. 96 7500 (2004);

[101] S. Picozzi, C. Ederer, J. Phys, Condens. Matter 21 303201 (2009);

[102] W. Prellier, M.P. Singh, P. Murugavel, J. Phys. Condens. Matter 17 R803-R832 (2005);

[103] A. Palewicz, I. Sosnowska, R. Przenioslo and A.W. Hewat, Acta Physica Polonica A 117 296 (2009);

[104] D. Lebeugle, D. Colson, A. Forget, M. Viret, P. Bonville, J.F. Marucco, S. Fusil, Phys Rev. B 76, 024116 (2007);

[105] H. Béa, B. Dupé, S. Fusil, R. Mattana, E. Jacquet, B. Warot-Fonrose, F. Wilhelm, A. Rogalev, S. Petit, V. Cros, A. Anane, F. Petroff, K. Bouzehouane, G. Geneste, B. Dkhil, S. Lisenkov, I. Ponomareva, L. Bellaiche, M. Bibes, and A. Barthélémy, Phys. Rev. Lett. 102, 217603 (2009);

[106] A. J. Hatt, N. A. Spaldin, C. Ederer, Phys. Rev. B 81 054109 (2010);

[107] H. Béa, M. Bibes, A. Barthélémy, K. Bouzehouane, E. Jacquet, A. Khodan, J.-P. Contour, S. Fusil, F. Wyczisk, A. Forget, D. Lebeugle, D. Colson, M. Viret, Appl. Phys. Lett 87 072508 (2009);

[108] A. A. Belik,S. Iikubo, K. Kodama, N. Igawa, S. Shamoto, S. Niitaka, M. Azuma, Y.Shimakawa, M. Takano, F. Izumi, E. Takayama-Muromachi, Chem. Mater. 18 798-803 (2009);

[109] W. Eerenstein, F. D. Morrison, J. F. Scott, N. D. Mathur, Appl. Phys. Lett. 87, 101906 (2005);

[110] A. David, Ph. Boullay, R. V. K. Mangalam, N. Barrier, W. Prellier, Appl. Phys. Lett. 96, 221904 (2010);

[111] A. Sambri, S. Amoruso, X. Wang, F. Miletto Granozio, and R. Bruzzese, J. Appl. Phys. **104**, 053304 (2008);

[112] S. Amoruso, J. Schou, J. G. Lunney, AIP Conf. Proc. **1278**, 665 (2010);

[113] P. Orgiani, R. Ciancio, A. Galdi, S. Amoruso, and L. Maritato, Appl. Phys. Lett. **96**, 032501 (2010);

[114] J-P. Maria, S. Trolier-McKinstry, D.G. Schlom, M.E. Hawley, G.W. Brown, J. Appl. Phys. **83** 4373-4379 (1998);

[115] P. Rundqvist, A.Vorobiev, S. Gevorgian, K. Khamchane, Z. Ivanov, J. Appl. Phys. **93** 1291-1297 (2003);

[116] E. Langenberg, M. Varela , M.V. Garcia-Cuenca, C. Ferrater, F. Sanchez, J. Fontcuberta, Materials Science and Engineering B **144** 138-142 (2007);

[117] W. Eerenstein, F. D. Morrison, J. F. Scott, N. D. Mathur, Appl. Phys. Lett. **87**, 101906 (2005);

[118] Qingyu Xu, Haifa Zai, D. Wu, T. Qiu, M. X. Xu, Appl. Phys. Lett. **95**, 112510 (2009);

[119] M.P.Singh, K.D.Truong, P.Fournier, P.Rauwel, E.Rauwel, L.P.Carignan, D.Menard, J. Magn. Magn. Mater. **321** 1743-1747 (2009) ;

[120] R. Ranjit, B. Kundys, and W. Prellier, Appl. Phys. Lett. **91** 222904 (2007);

[121] D. Bao, N. Mizutani, X. Yao, and L. Zhang, Appl. Phys. Lett. **77**, 1041 (2000);

[122] J.L. Garcia-Munoz, J. Rodriguez-Carvajal, P. Lacorre, and J.B. Torrance, Phys. Rev. B **46**, 4414 (1992);

[123] Y.P. Wang et a.l , J. Phys. D: Appl. Phys. **39** 2019 (2006);

[124] The Poisson ratio ν is defined by the expression:$\varepsilon_{zz} = \frac{-\nu(\varepsilon_{xx}+\varepsilon_{yy})}{(1-\nu)}$ where ε_{zz} is the deformation of the c-axis $(c - c_{bulk})$ and $\varepsilon_{xx}, \varepsilon_{yy}$ are the deformations of the in-plane lattice parameters. $\nu = 0.5$ implies volume conservation. Real values of Poisson ratio are about 0.3-0.4.

[125] O. Trithaveesak, J. Schubert, Ch. Buchal, J. Appl. Phys. **98**, 114101 (2005);

[126] M. Okano, D. Sawamura, and Y. Watanabe, Jpn. J. Appl. Phys., Part 1 **37**, 5101 (1998);

Chapter 4

Résumé en langue Française

4.1 Propriétés magnétiques, orbitales et de transport d'hétérostructures basées sur $LaMnO_3$

Les oxydes fonctionnels avec la structure de perovskite combinent beaucoup de propriétés intéressantes (supraconductivité, ferroélectricité, ferromagnétisme, piézoélectricité) avec une structure cubique relativement simple.
Les perovskites sont des oxydes ternaires avec la formule ABO_3, où un métal de transition B est entouré par des octaèdres d'oxygène partageants les coins. Les propriétés du matériau sont déterminées par l'hybridation entre le métal de transition et les orbitales de l'oxygène.
Grâce à leur structure simple et leur paramètres de maille très proches, la croissance heteroepitaxial des films minces de perovskite peut être employée afin de fabriquer des hétérostructures. Des matériaux avec la fonctionnalité différente peuvent donc être assemblés. Grâce aux avancées récentes dans la fabrication des matériaux sous forme de couche mince, l'épaisseur de chaque couche individuelle peut être diminuée jusqu'à une ou quelques cellules unitaires. De tels systèmes sont appelés super-réseaux, et ils peuvent être vus comme des hétérostructures ou comme nouveaux composés (P. Zubko et al., Annu. Rev. Condens. Matter Phys., 2 141-165 (2011)).
Les interfaces entre les oxydes constituant les hétérostructures et les super-réseaux peuvent fournir de nouvelles fonctionnalités à ces matériaux grâce à la redistribution des charges et à des phénomènes de reconstruction électronique. Par exemple un gaz d'électrons 2D avec haute mobilité, et avec un état fondamental supraconducteur, est formé aux interfaces $LaAlO_3/SrTiO_3$, alors que les deux blocs constitutifs sont des isolants.
Les manganites (B=Mn) sont depuis longtemps profondément étudiées grâce à l'existence du phénomène de magnéto-résistance colossale (CMR) dans plusieurs de ces composés. En particulier, les composés de LaMnO3 (LMO) dopés avec des alcalins sont les plus étudiés à cause de leurs propriétés

métalliques.
La motivation de ce travail est de comprendre la physique des super-réseaux basés sur LMO présentant la même composition que la manganite $La_{0.7}Sr_{0.3}MnO_3$ qui est métallique et avec la plus haute température de Curie. qui est métallique et ferromagnétique avec une température de Curie d'environ 360K. Ces super- réseaux se composent de 2n cellules de LMO et de n cellules de SrMnO3 (SMO), répétées plusieurs fois jusqu'à une épaisseur fixe(230 Å) (C. Adamo et al., Appl. Phys. Lett. 92 112508 (2008)).
Sans considérer l'effet des interfaces, il est également important de comprendre comment les blocs constitutifs sont modifiés par les contraintes, par la teneur en oxygène et par les défauts de stoechiométrie. Puisque le LMO est plus sensible à de telles perturbations que le SMO, notre travail s'est concentré sur les propriétés des couches minces non-stoechiométriques de LMO avec différents degrés d'oxygénation (P. Orgiani et al., APPL. Phys. Lett. 95, 013510 (2009)).
Le manuscrit est organisé de la façon suivante :

- étude des propriétés de transport : afin d'étudier profondément les propriétés de transport des couches minces et des super-réseaux, nous avons développé un procédé lithographique afin d'effectuer des mesures avec courant perpendiculaire-au-plan (CPP) et des mesures de modulation de résistance par le champ électrique (effet de champ).

- étude de l'ordre orbital et des moments magnétiques : cette information a été obtenue grâce aux techniques spectroscopiques dans le domaine des rayons X mous. En particulier a été utilisée la spectroscopie d'absorption des rayons X (XAS) et son dichroïsme linéaire et circulaire en correspondance des énergies d'excitation du manganèse et de l'oxygène. En outre nous avons tiré profit des mesures de diffusion résonnante non élastique des rayons X (RIXS) pour déterminer la coordination du manganèse dans la cellule perovskite.

La première partie a été développée au laboratoire GREYC - ENSICaen. Au-delà de l'optimisation du processus lithographique elle-même, le dépôt de plusieurs oxydes a été également effectuée. En particulier le dépôt d'un oxyde métallique est nécessaire pour les mesures CPP, et des oxydes ferroélectriques ont été déposés pour la technologie des dispositifs à effet de champ. En particulier des couches ferroélectriques ont été déposées au laboratoire CRISMAT A l'ENSICaen, grâce à une collaboration avec le groupe de Dr. W. Prellier.
La deuxième partie du travail a exigé l'utilisation de la source de synchrotron pour les mesures de XAS et de RIXS. En particulier, deux expériences, une sur des super-réseaux et la deuxième sur des couches minces de LMO, ont été effectuées au European Synchrotron Radiation Facility (ESRF à Grenoble), sur la ligne de faisceau ID08. L'intensité du rayonnement de synchrotron et le plein contrôle de la polarisation sont cruciaux afin d'effectuer des mesures

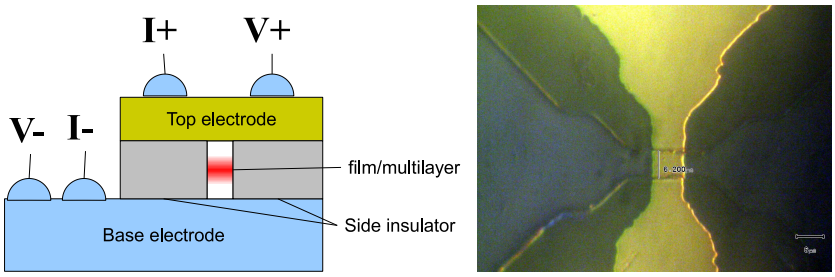

Figure 4.1: Gauche: Schéma d'un dispositif CPP Droite: Image au microscope optique d'un dispositif CPP réalisé dans ce travail de thèse.

de dichroïsme et de diffusion inélastique de haute résolution.

4.1.1 Dispositifs CPP

Les dispositifs CPP permettent de mesurer les propriétés de transport avec le courant perpendiculaire au plan du film. Dans le cas des super- réseaux, cela permet de faire passer le courant à travers les interfaces. Avec les mesures dans la configuration expérimentale habituelle, ce dispositif per- met de distinguer entre les contributions de transport dans le plan et perpendiculairement au plan. Dans la figure 4.1, le schéma d'un dispositif CPP est représenté. Ce dispositif exige que la multicouche à mesurer est fabriquée sur une couche métallique ou un substrat conducteur, pour constituer l'électrode de base. En outre, la surface de mesure doit être définie afin de mesurer la résistivité et d'éviter l'inclusion de beaucoup de défauts. Quand la surface de mesure est plus petite que des centaines de micron, il faut définir une électrode supérieure de surface plus grande afin de placer les sondes de mesure. L'électrode supérieure doit alors être isolée de l'électrode de base par un insolant de flanc.
Nous avons décidé d'utiliser des couches minces de $SrRuO_3$ (SRO) en tant qu'électrode de base, car ce matériau a un paramètre de maille compatible avec les super-réseaux étudiés, et permettant donc leur croissance épitaxiale. En outre le SRO est un oxyde métallique de faible résistivité, avec une stabilité chimique et thermique élevée.
J'ai optimisé la croissance par dépôt par laser pulsé des couches minces de SRO sur substrats de STO(001). La morphologie des films a été mesurée par AFM (Microscope à Force Atomique en mode tapping). Cela a permis la mesure de la rugosité des films et l'identification du mode de croissance. Puisque ces films doivent être utilisés comme première couche, notre but est d'obtenir des films de faible rugosité. La struc- ture des films à été étudiée par XRD (Diffraction de Rayons X).

Les mesures $\theta - 2\theta$ et les mesures en espace réciproque ont permis de déterminer l'orientation, le paramètre de maille et l'alignement dans le plan

des films. Enfin les propriétés de transport ont été sondées par des mesures de résistance en fonction de la température, qui ont indiquées que tous les films ont un comportement métallique avec des basses valeurs de résistivité. De plus les caractéristiques des courbes de R(T) et de dR(T)/dT semblent être étroitement liées à la structure cristalline et aux taux de dépôt des couches.
Une image d'un vrai dispositif CPP est reportée dans la partie droite de figure 4.1. Une couche d'Al_2O_3 déposée par canon ionique a été employée comme isolant de flanc. Les contacts en or ont été déposées par la même tech- nique.
Afin d'obtenir une définition précise de la surface de mesure et d'éviter des courts-circuits, une technique de gravure anisotrope (gravure ionique), a été employée.
La géométrie CPP a été fabriquée sur des bicouches $BaTiO_3$/SRO (BTO/SRO) et $BiFeO_3/LaNiO_3$. Le choix de la couche de SRO est crucial afin de contrôler la gravure ionique, car pas toutes les espèces peuvent être détectées par le spectromètre de masse afin d'identifier la couche gravée et définir l'arrêt de la gravure.
En cas de films ferroélectriques, nous nous intéressons à la polarisation électrique. Malheureusement, l'existence de petites pertes nous a empêché de mesurer les cycles ferroélectriques, mais la structure con- vient aux mesures de résistivité des échantillons conducteurs, où un faible champ électrique est appliqué et les pertes sont négligeables.

4.1.2 Dispositifs à effet de champ

Des dispositifs à effet de champ avec une structure similaire aux MOSFET ont été fabriqués avec des couches minces de $La_{0.7}Sr_{0.3}MnO_3$ sur des substrats de Si avec une couche de STO (100). Des couches d'Al_2O_3 et de BTO ont été déposé sur les couches minces de LSMO comme oxydes de grille. En particulier la couche Al_2O_3, avec une épaisseur comprise entre 200 et 300 nanomètres a été déposée par canon à ions, alors que le BTO a été déposé par ablation laser pulsé.

Afin d'augmenter la modulation de résistance induite par le champ électrique, j'a employé des films ultra-minces de LSMO (20-15 nanomètres), puisque la modulation de champ électrique dans des matériaux métalliques est réduite à peu de cellules élémentaires. Malheureusement, nous avons constaté que l'étape de dépôt d'Al_2O_3 a endommagé le LSMO. De plus, la couche de BTO de 85 nm présente des pertes, empêchant donc l'application du champ électrique, mais dans ce cas-ci le LSMO n'a pas été endommagé. La basse résistivité de BTO peut également expliquer les mesures non réussies lors des cycles de polarisation dans la configuration CPP.

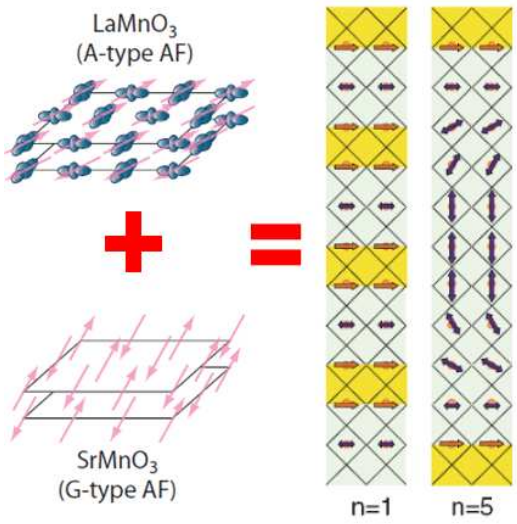

Figure 4.2: Schéma des moments magnetiques dans des super-réseaux de differente périodicité obtenu par le données de XMCD et XMLD

4.1.3 Magnétisme et ordre orbital dans les super-réseaux

Dans ce travail, j'ai étudié les propriétés magnétiques et orbitales des super-réseaux de LMO/SMO développés par C. Adamo comme décrit dans C. Adamo et al., Appl. Phys. Lett. 92 112508 (2008). Ces propriétés ont été entièrement mesurées par XAS et dichroïsme. Les résultats des mesures spectroscopiques ont été aussi interprétés grâce aux mesures d'aimantation et de transport présentées dans des travaux précédents (voyez par exemple C. Adamo, C.A. Perroni et al. Phys. Rev. B, 79 045125 (2009)). Les mesures de dichroïsme linéaire à la température ambiante (XLD ou XNLD) au seuil d'absorption du manganèse $L_{3,2}$, nous ont fourni les informations sur l'ordre orbital préférentiel des ions de manganèse. En particulier grâce aux mésures XLD nous pouvons déterminer si les orbitales occupées se trouvent préférentiellement dans le plan du couche ou hors plan.

Nous avons constaté que pour le super-réseau n=1 les orbitaux occupés sont en plan, comme trouvé pour les couches minces de LSMO sur STO (C. Aruta et al., Phys. Rev. B 80, 014431 (2009)), alors que pour n=5 et 8, l'ordre préférentiel dans les blocs de LMO est hors plan.
Ce changement d'occupation orbital est interprété en raison de la concurrence du transfert de charge aux interfaces et de la localisation électronique dans les blocs constitutifs des super-réseaux de longue période. L'ordre magnétique a été étudié par le dichroïsme circulaire magnétique (XMCD), qui sonde directement le moment ferromagnétique des ions, et par le dichroïsme linéaire magnétique (XMLD), qui est la modification des spectres de XLD

quand induite par les moments magnétiques des ions. Cette technique est sensible au ferromagnétisme et au antiferromagnétisme. La contribution des deux peut être distinguée par la réponse à l'application du champ magnétique.
Ces mesures ont été également effectuées au seuil du manganèse $L_{3,2}$. Les cycles d'hystérésis mesurés par XMCD ont indiqué que l'axe de facile aimantation se situe dans le plan pour tous les échantillons, et que le champ coercitif est très haut pour les super-réseaux de grande période. Cette augmentation est expliquée par la présence d'une grande composante antiferromagnétique dans ces échantillons, comme les mesures de XMLD l'indiquent. En particulier dans les échantillons n=5,8, l'axe facile antifer- romagnétique suit l'occupation orbitale dans les blocs de LMO, étant hors plan. Inversement, dans le super-réseau n=1 l'axe antiferromagnétique est parallèle à l'axe ferromagnétique. Dans ce cas, le comportement des super-réseaux de grande période semble être également dicté par l'interaction entre charge et structure cristalline dans le bloc de l'isolateur LMO, alors que pour le cas n=1 le ferromagnétisme lié aux interfaces détermine également l'axe facile antiferromagnétique.

4.1.4 Proprietés des couches minces de $La_xMnO_{3-\delta}$

Le LMO est le composant des super-réseaux qui est le plus sensible aux pertur- bations. Par conséquent, il faut étudier l'influence des défauts d'oxygénation et de stoechiométrie afin d'exclure qu'ils sont à l'origine du comportement des super-réseaux.
Les couches minces non stoechiométriques de LMO ont été déposées dans le système de dépôt par épitaxie de faisceau moléculaire (MBE) de l'université de Salerno. Les films ont été déposés sur substrats de STO (001) en variant le rapport La:Mn = x avec x entre $x = 0.66$ à $x = 1.07$. Alors nous avons divisé les films en plusieurs séries, et chaque série a été recuite en air pour 54h aux différentes températures afin de fournir un contenu d'oxygène différent.
Nous avons divisé les films en plusieurs séries, et chaque série a été recuite à l'air pendant 54h à différentes températures afin d'obtenir différents concentration en oxygène. Des mesures de XRD et R(T) ont été effectuées sur tous les échantillons. Les mesures ont indiquées que la plupart des échantillons sont métalliques à basse température et qu'en dépit du procédé de recuit, ils ont le même paramètre de maille du substrat dans le plan, et un paramètre de maille hors plan plus petit (P. Orgiani et al., Appl. Phys. Lett. 95, 013510 (2009)). Ces résultats sont opposés à ce qui est prévu sur le LMO stoechiométrique, c'est à dire dans un état isolant et en contrainte compressive.
Pour compléter notre analyse, nous avons effectué des mesures magnétiques sur les échantillons plus riches en oxygène. Le magnétisme est fort dans les

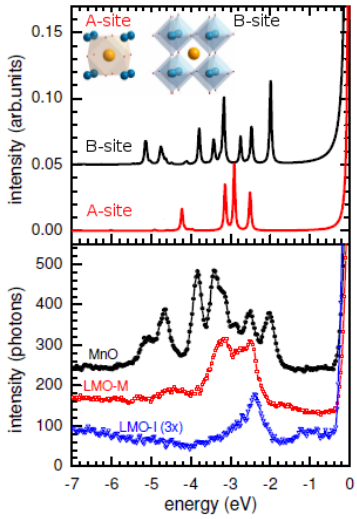

Figure 4.3: Mesure RIXS (en bas) démontrant que les excitations orbitales de l'échantillon $x = 0.88$ (LMO-M) sont compatibles avec une simulation (en haut) impliquant que le Mn^{2+} est dans l'emplacement du ion La (nommé A-site), e que les excitations de l'oxyde de Mn MnO_2 et des échantillons isolantes sont très différent de celles-là

échantillons avec $x < 1$ et affaibli dans ceux avec $x > 1$.
Enfin nous avons employé les mêmes techniques spectroscopiques employées sur les super-réseaux pour déterminer l'ordre orbital et les directions de facile aimantation dans nos échantillons.
LLes mesures ont indiqué que les échantillons non-stoechiométriques et riches en oxygène de LMO ont des propriétés nettement différentes par rapport au LMO dans les super-réseaux.
En outre les échantillons montrant des propriétés très semblables au LSMO, c'est à dire les échantillons x=0.66 et 0.88, ont montré une proportion significative de Mn^{2+}. Le Mn^{2+} est habituellement associé à des impuretés d'oxyde de manganèse, alors que dans ce cas-ci, les mesures de RIXS ont indiqué que les excitations orbitales du Mn^{2+} sont plutôt compatibles avec cet ion occupant l'emplacement du ion La (P.Orgiani et al., Phys. Rev. B 82 205122 (2010))(voyez fig. 4.3).

Donc le Mn^{2+} réduit le nombre de vacances sur l'emplacement du La et agit comme dopant.
Les données de XMCD indiquent qu'à 10 K le Mn^{2+} est aussi ferromagnétique.
Le XLD indique que la substitution La-Mn induit un ordre orbital qui est tout le contraire de celui prévu vue la déformation induite par contrainte.
Les mesures XMLD indiquent un composant antiferromagnétique fort dans les échantillons de Mn^{2+}, qui suit l'orientation de l'ordre orbital (hors plan) (A. Galdi et al., Phys. Rev. B. 83 064418 (2011)).

Les bonnes propriétés métalliques ferromagnétiques de ces échantillons contrastent avec l'ordre antiferromagnétique et orbital observés. Les calculs théoriques indiquent qu'il est possible qu'un nouveau mécanisme de conduction est à l'oeuvre dans ces échantillons, grâce à la substitution de l'ion La avec un ion Mn qui peut participer à la conduction. Ce mécanisme peut fonctionner même en présence de l'ordre orbitale et de l'arrangement antiferro- magnétique observés (P.Orgiani et al., Phys. Rev. B 82 205122 (2010)).